Nonlinear optical responses of phthalocyanines in the presence of nanomaterials or when embedded in polymeric materials

A thesis submitted in fulfilment of the requirements for the degree of

DOCTOR OF PHILOSOPHY

Of

RHODES UNIVERSITY

By

OWOLABI MUTOLIB BANKOLE

November 2016

DEDICATIONS

To

Almighty Allah for HIS blessings over me

To

My beloved mother, Omolola Tutulola Bankole

for her prayers and support.

To

My wife Bankole Rofiah Omolola and
My children Bankole Aaqeelah Oluwadamilare
Bankole Abdul-akeem Omobolaji

for their sacrifices, prayers and support.

ACKNOWLEDGEMENTS

The completion of this thesis was not only due to my dedication and perseverance, but also to the assistance and contributions from different individuals. I would like to appreciate the following people for their contributions to the success of this thesis.

Distinguished Professor Tebello Nyokong, my esteemed supervisor who worked tirelessly to ensure all her students, irrespective of your race or background, succeed in their research works. Her constructive criticisms and comments, research ideas, patience are all I needed to complete this PhD program within the stipulated time.

S22/F26 lab members

I want to appreciate all the S22/F26 members of Department of Chemistry, Rhodes University, for the good relationship I have enjoyed with everyone in the course of my research work. The following people are my worthiers;

- Drs. Ogunbayo and Akinbulu for their recommendations to do my PhD under the supervision of Prof. T. Nyokong.
- Drs. Amuhaya, Sanusi and Fashina for their encouragements and moral supports in my first year.
- Ms. Gail Cobus for ensuring smooth running of DST/Mintek NIC Sensors group.
- Mr. Francis Chindeka for the running and analyses of XPS and CHNS experiments.
- Dr. Gertrude Fomo for helping me during the arrangement of this thesis. Thank You!

Funding

- Adekunle Ajasin University, Akungba, (AAUA), Ondo State, Nigeria; my employer.
- Tertiary Education Trust Fund (TETFund), for the financial support.
- DST/MINTEK for financial support through my supervisor, Prof. Tebello Nyokong.

Family and friends

I would like to appreciate my wife, Mrs Rofiat Bankole, and my kids; Aaqeelah and Akeem, for their support and the sacrifices they were forced to make while I was away. Also, my appreciation to Asst. Prof. N.A. Oladoja for his guidance in the course of my academic career.

ABSTRACT

This work describes the synthesis, photophysical and nonlinear optical characterizations of alkynyl Pcs (**1**, **2**, **3**, **8** and **9**), 1,2,3-triazole ZnPc (**4**), mercaptopyridine Pcs (**5**, **6** and **7**) and amino Pcs (**10** and **11**). Complexes **1**, **2**, **4**, **7**, **8**, **9** and **11** were newly synthesized and characterized using techniques including ^{1}H-NMR, MALDI-TOF, UV-visible spectrophotometry, FTIR and elemental analysis. The results of the characterizations were in good agreement with their molecular structures, and confirmed the purity of the new molecules. Complex **10** was covalently linked to pristine graphene (GQDs), nitrogen-doped (NGQDs), and sulfur-nitrogen co-doped (SNGQDs) graphene quantum dots; gold nanoparticles (AuNPs); poly(acrylic acid) (PAA); Fe_3O_4@Ag core-shell and Fe_3O_4-Ag hybrid nanoparticles via covalent bonding. Complex **11** was linked to $Ag_x Au_y$ alloy nanoparticles via NH_2-Au and/or Au-S bonding, 2 and 3 were linked to gold nanoparticles (AuNPs) via clicked reactions. Evidence of successful conjugation of **2**, **3**, **10** and **11** to nanomaterials was revealed within the UV-vis, EDS, TEM, XRD and XPS spectra.

Optical limiting (OL) responses of the samples were evaluated using open aperture Z-scan technique at 532 nm and 10 ns radiation in solution or when embedded in polymer mixtures. The analyses of the Z-scan data for the studied samples did fit to a two-photon absorption mechanism (2PA), but the Pcs and Pc-nanomaterial or polymer composites also possess the multi-photon absorption mechanisms aided by the triplet-triplet population to have reverse saturable absorption (RSA) occur. Phthalocyanines doped in polymer matrices showed larger nonlinear absorption coefficients (β_{eff}), third-order susceptibility ($I_m[\chi^{(3)}]$) and second-order hyperpolarizability (γ), with an accompanying low intensity threshold (I_{lim}) than in solution. Aggregation in DMSO negatively affected NLO behaviour of Pcs (**8** as a case study) at low laser power, and improved at relatively higher laser power. Heavy atom-substituted Pcs (**6**) enhanced NLO and OL properties than lighter atoms such as **5** and **7**. Direct relationship between enhanced photophysical properties and nonlinear effects favoured by excited triplet absorption of the **2**, **3**, **10** and **11** in presence of nanomaterials was established. Major factor responsible for the enhanced nonlinearities of **10** in the presence of NGQDs and SNGQDs were fully described and attributed to the surface defects caused by the presence of heteroatoms such as nitrogen and sulfur. The studies showed that phthalocyanines-nanomaterial

composites were useful in applications such as optical switching, pulse compressor and laser pulse narrowing.

TABLE OF CONTENTS

ABBREVIATIONS

BE	–	binding energy
DBU	–	1,8-diazabicyclo-[5.4.0]-undec-7-ene
DCM	–	dichoromethane
DCC	–	dicyclohexycarbodimide
DMAE	–	dimethylaminoethanol
DMAP	–	4-dimethylaminopyridine
DMF	–	dimethyl formamide
DMSO	–	dimethyl sulfoxide
EDC	–	1-ethyl-3-(3-dimethylaminopropyl carbodiimide)
ESA	–	excited state absorption
FRET	–	Förster resonance energy transfer
FT-IR	–	Fourier transform infra-red
FCA	–	free-carrier absorption
FWHM	–	full width at half-maximum
GQDs	–	graphene quantum dots
HOMO	–	highest occupied molecular orbital
IC	–	internal conversion
IUPAC	–	International Union of Pure and Applied Chemistry
ISC	–	intersystem crossing
JCPDS	–	Joint Committee on Powder Diffraction
LUMO	–	lowest unoccupied molecular orbital
MS	–	mass spectroscopy
MALDI	–	matrix-assisted laser desorption ionization
MPA	–	3-mercaptopropionic acid
MPcs	–	metallophthalocyanines
NPs	–	nanoparticles
Nd-YAG	–	neodymium-doped yttrium aluminium garnet
NHS	–	N-hydroxysuccinimide
N-GQDs	–	nitrogen-doped quantum dots
NLA	–	nonlinear absorption

NLO	–	nonlinear optics
NLR	–	nonlinear refraction
NLS	–	nonlinear scattering
OL	–	optical limiting
PDT	–	photodynamic therapy
PL	–	photoluminescent
Pcs	–	phthalocyanines
PAA	–	poly(acrylic acid)
PMMA	–	poly(methyl methacrylate)
PBC	–	poly(bisphenol A carbonate)
PSU	–	polysulfone
^{1}H-NMR	–	proton nuclear magnetic resonance
QDs	–	quantum dots
RSA	–	reverse saturable absorption
SA	–	saturable absorption
SPR	–	surface plasmon resonance
SN-GQDs	–	sulfur and nitrogen co-doped quantum dots
TCSPC	–	time correlated single photon counting
THF	–	tetrahydrofuran
TF	–	thin films
TOABr	–	tetraoctylammonium bromide
TOF	–	time-of-flight
TEM	–	transmission electron microscopy
TMAOH	–	tetramethylammonium hydroxide
2PA	–	two-photon absorption
3PA	–	three-photon absorption
UV-vis	–	ultraviolet visible
VR	–	vibrational relaxation
XRD	–	x-ray diffraction
XPS	–	x-ray photoelectron spectroscopy

SYMBOLS

A	–	absorbance
k	–	absorption cross-section ratio
F	–	area under fluorescence curve
τ_{avF}	–	average fluorescence lifetime
N_A	–	Avogadro constant
w_o	–	beam waist
β_{eff}	–	effective nonlinear absorption coefficient
L_{eff}	–	effective path length
L_{eff}	–	effective path length for 3PA
Eff	–	efficiency of energy transfer
σ_T	–	excited state absorption cross section
$\mathbf{S_1}$	–	first excited singlet state
$\mathbf{T_1}$	–	first excited triplet state
τ_F	–	fluorescence lifetime
Φ_F	–	fluorescence quantum yield
k_F	–	fluorescence rate constant
σ_{FCA}	–	free-carrier absorption cross-section
$\mathbf{S_0}$	–	ground singlet state
σ_0	–	ground state absorption cross section
I_O	–	input irradiance
τ_{ISC}	–	intersystem crossing lifetimes
I_{lim}	–	limiting threshold intensity
α	–	linear absorption coefficient
T(z)	–	linear transmittance
f	–	Lorentz local field factor
$\mathbf{S_n}$	–	nth excited singlet state
$\mathbf{T_n}$	–	nth excited triplet state
I_{00}	–	on-focus peak input irradiance
I_{out}	–	output intensity
L	–	path length (thickness of sample holder)

ε_o	–	permittivity of free space
δ_H	–	proton nmr chemical shift
k_{ISC}	–	rate constant for intersystem crossing
z_0	–	Rayleigh length
z	–	sample position
F_{sat}	–	saturation fluence
γ	–	second-order hyperpolarizability
$I_m[\chi^{(3)}]$	–	third-order susceptibility
τ_T	–	triplet lifetime
Φ_T	–	triplet quantum yield
β_2	–	two-photo absorption coefficient
β_3	–	three-photon absorption coefficient

FIGURES

SCHEMES

TABLES

CHAPTER 1
INTRODUCTION

1.1 Phthalocyanines

1.1.1 Discovery of Phthalocyanines (Pcs)

The phthalocyanine (Pc), **Figure 1.1**, was first accidentally observed as a dark bluish material by von Braun and Tcherniac in 1907 [1]. The first attempt at the isolation of the coloured product was made by Henri de Diesbach and van der Weid in 1927, during the reaction of orthodibromobenzene with copper(I)cyanide in pyridine [2]. The exceptionally stable blue pigment obtained was not properly characterized. Inspired by this attempt, further studies on the elucidation of the molecular structures of metal-free phthalocyanines (H_2Pc) and its metal derivatives (MPcs) were carried out and documented in the literature by Linstead and Robertson, and co-workers from Imperial College, London, U.K. [3-10].

1.1.2 Structure of Phthalocyanine (Pcs) Complexes

Phthalocyanines are synthetic tetrapyrrolic macrocycles containing four iminoisoindoline rings with a conjugated 18 π-electron system. They are structurally related to other macrocylic pigments such as porphyrins. Metal-templated phthalocyanines are referred to as metalophthlocyanines [11]. The central cavity of phthalocyanine can accommodate sizeable numbers of metals without any form of distortion to the Pc ring [12,13], while inclusion of heavier metals like lead have been reported to distort the shapes of the MPc ring [14,15].

The numbering system of phthalocyanine is broadly divided into two (**Figure 1.1**), depending on the location of the substituents on the phthalocyanine macrocylces. The ease of modification of Pcs allow for possible attachment of substituents either on α (non-peripheral) or β (peripheral) positions of the phthalocyanine ring. According to nomenclature of tetrapyrroles [3], α−substituents are positioned at 1, 4, 8, 11, 15, 18, 22, and 25 on the phthalocyanine ring, while substituents located at 2, 3, 9, 10, 16, 17, 23, and 24 are called β-substituents, **Figure 1.1A** and **B**. The extensive π-π conjugative system of the Pc ring causes aggregation and make them insoluble in many organic solvents [16-18]; this problem can be easily overcome by attaching bulky substituents on the peripheral and/or non-peripheral positions of Pc ring [19-21].

The unique spectroscopic, photophysical and photochemical properties [22-24] of Pcs have made them the most studied organic macrocyles. These properties are critical to

their performances in diverse state-of-the-art technological applications such as photosensitizers, liquid crystals, dye-sensitized solar cells, electrochemical sensors, organic photovoltaic (OPV) devices, and as nonlinear optical (NLO) materials [25-33].

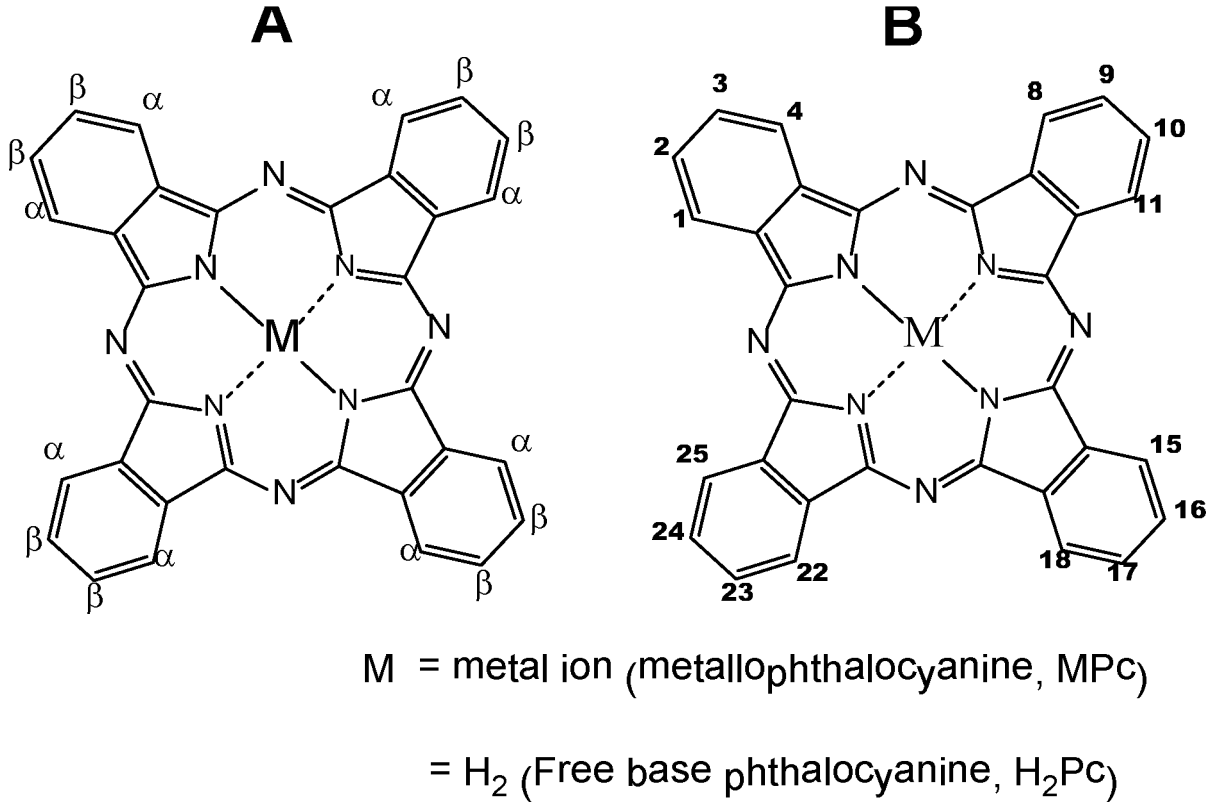

Figure 1.1: Phthalocyanine ring showing (A) peripheral (B) and non-peripheral position substitutions for IUPAC numbering systems.

1.1.3 General synthesis of symmetrical and unsymmetrical Phthalocyanines

Symmetrically tetra-substituted MPcs can be prepared by cyclotetramerization of substituted phthalonitrile precursors in the presence of metal salts, high boiling solvents and catalysts [34], **Scheme 1.1**. High boiling solvents such as dimethyl formamide (DMF), dimethylaminoethanol (DMAE), pentanol and quinolone are commonly used for cyclization of Pcs in the presence of catalysts such as 1,8-diazabicyclo-[5.4.0]-undec-7-ene (DBU) or urea. When Li metal is used during the cyclization reaction, a metallated LiPc with loosely held Li metal is obtained which can be easily demetallated to give metal-free Pcs when treated with acids [4,35]. This method is employed for the synthesis of metal-free phthalocyanines reported in this thesis.

In the case of tetra substituted triazole-functionalized phthalocyanines (also reported in this work) using Huisgen cycloaddition "click chemistry" reaction [36-38], two synthetic strategies are usually employed, **Scheme 1.2**. The first strategy involves the cyclization of triazole ring substituted-phthalonitrile precursor in the presence of suitable solvent such as DMAE, routes i/ii (**Scheme 1.2**) [39]. The second strategy followed post-modification approach in which the reactive alkyne phthalocyanines are converted to the triazole-functionalized molecules via click reactions, routes iii (**Scheme 1.2**) [40-42]. Both strategies are reported in this thesis; the former was employed to afford 1,2,3 triazole-fused nitrophenyl zinc phthalocyanines; and the later was employed to prepare nanocomposites of indium or zinc phthalocyanines-gold nanoparticles.

Asymmetrical phthalocyanines (Pcs) are essential molecules, particularly in the design of optical limiting materials [43,44] and liquid crystals [45,46] due to their unique photophysical properties and reduced symmetry. The presence of single anchor group on asymmetrical Pcs provide specific point of attachment to form stable covalent linkage to other organic molecules or nanoparticles for improved functionalities [47,48]. Synthetic methods of preparation of asymmetrical substituted Pcs include sub-phthalocyanine routes [49,50], polymer support method [51], and conventional statistical mixed condensations of dinitriles [52,53]. For the mixed condensations approach, two different substituted phthalonitriles or 1,3-diiminoisoindolines are mixed in ratio 3:1 and in the presence of metal salt to give six possible constitutional isomers with varying percentage yields, **Scheme 1.3** [52]. Though the AB_3 type isomer is favoured with about 40% yield, its Isolation and purification are complicated due to the presence of other isomers. The formation of other isomers can be suppressed by increasing the ratio of the dinitrile precursors to 10:1 or above [54]. Asymmetrical substituted (A_3B-type) ZnPcs covalently linked to nanomaterials such as gold, Fe_3O_4@Ag core-shell, Fe_3O_4-Ag heterodimer, graphene quantum dots (GQDs); nitrogen-doped quantum dots (N-GQDs), sulfur and nitrogen co-doped quantum dots (SN-GQDs), and polyacrylic acid for photophysical and nonlinear applications, are reported in this work.

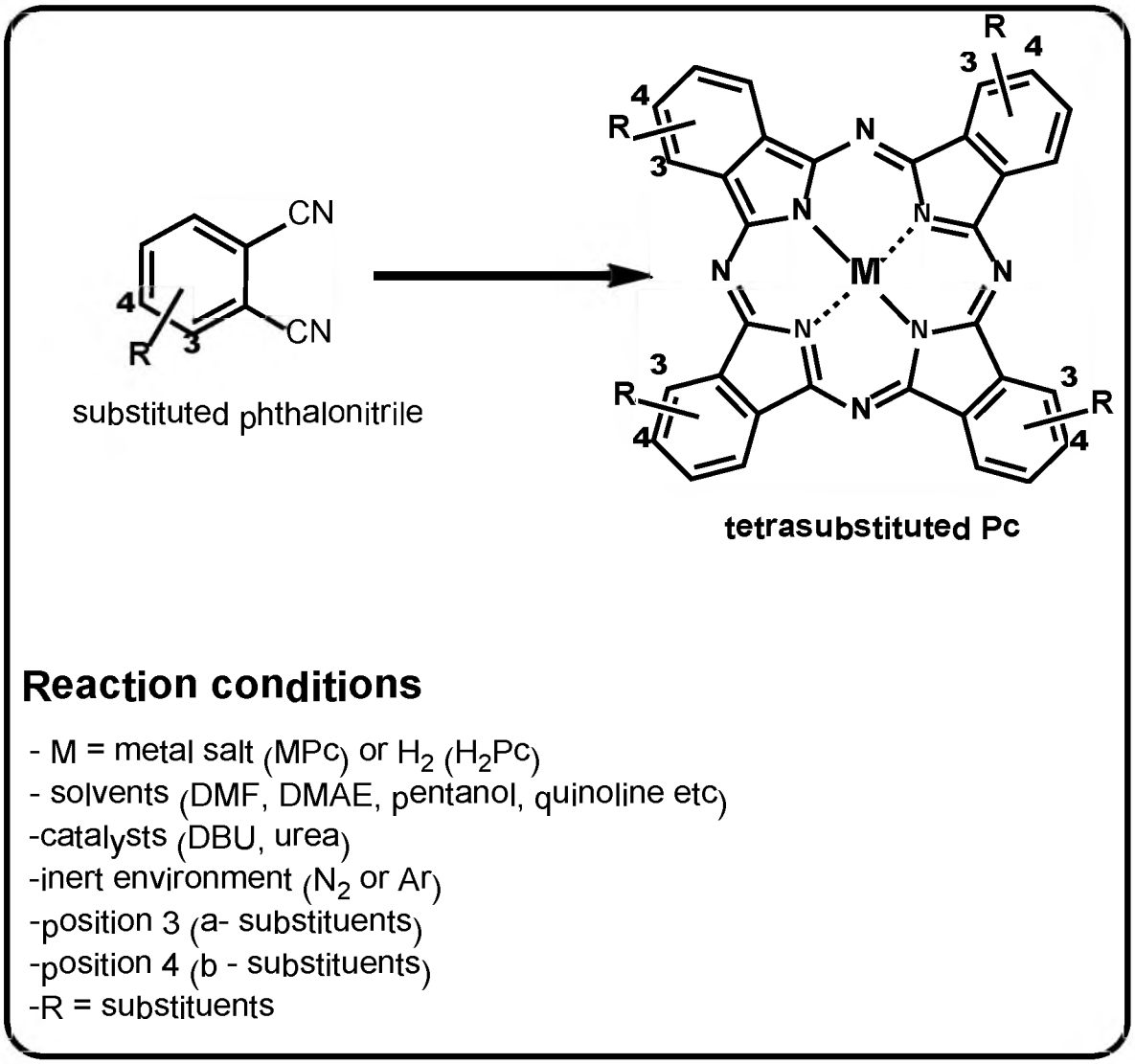

Scheme 1.1: Synthetic routes to preparation of symmetrically substituted MPcs from substituted 4 or 3-nitrophthalonitriles. DMF = dimethyl formamide, DMAE = dimethylaminoethanol, DBU = 1,8-diazabicyclo-[5.4.0]-undec-7-ene

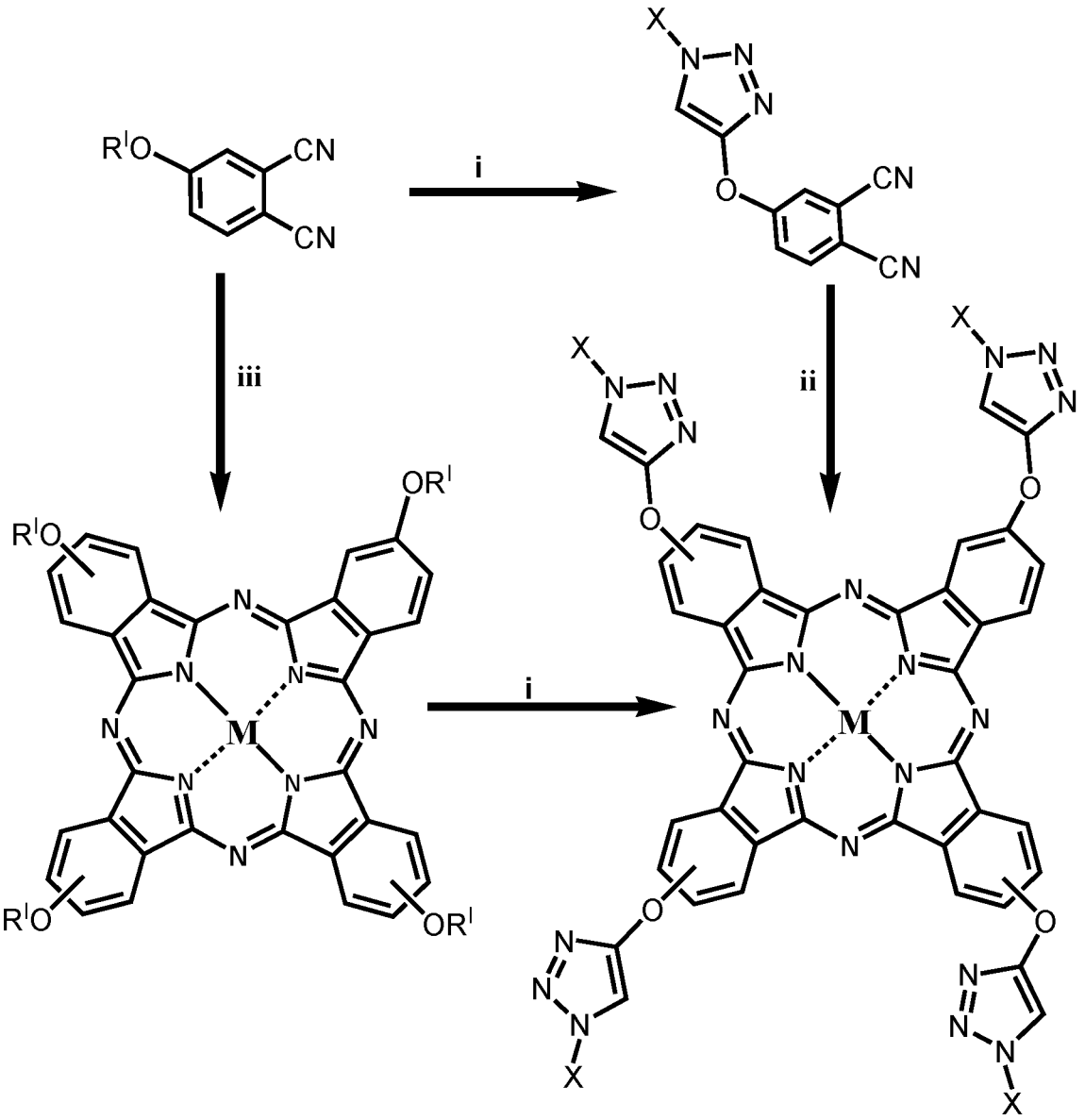

Reaction conditions

M = metal salt
i = $CuSO_4.5H_2O$, sodium ascorbate, THF/H_2O, rt
ii- DMAE, reflux, Ar or N_2, 18-24 h
iii- n-Pentanol, DBU, Ar or N_2, 18-24 h
R^I = alkynyl group
X = alkyl group, benzyl or nanoparticles etc.

Scheme 1.2: General Synthetic routes to triazole-functionalized tetra substituted MPcs at peripheral positions. THF = tetrahydrofuran, $CuSO_4.5H_2O$ = copper (II) sulfate pentahydrate. DMAE and DBU as described above

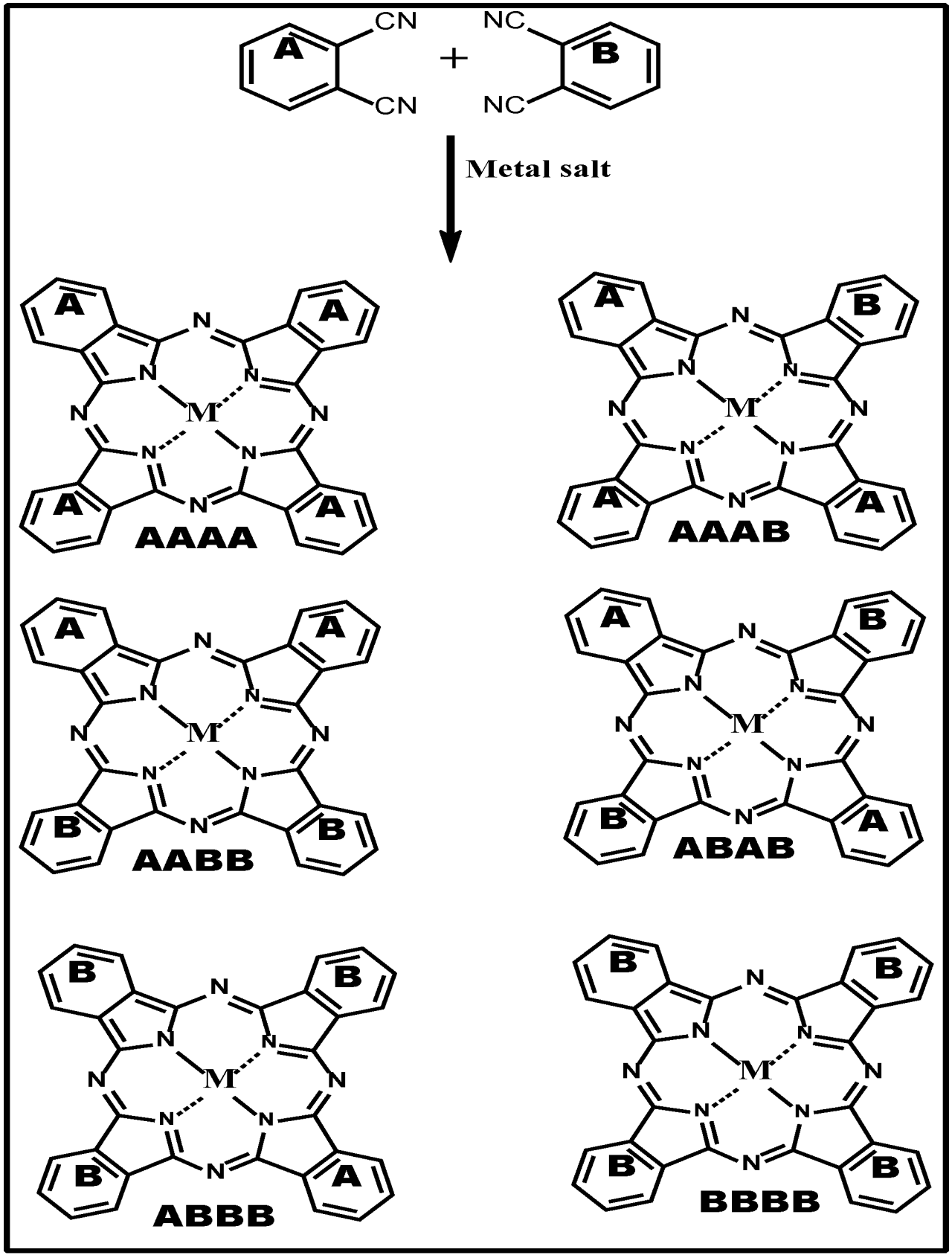

Scheme 1.3: Method of preparing asymmetrical phthalocyanines [17,24].

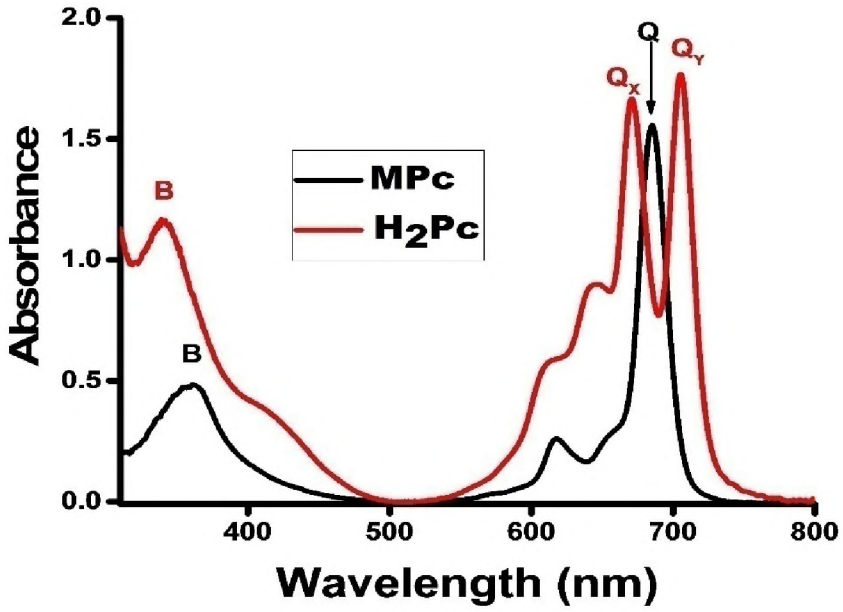

Figure 1.2: Electronic absorption spectra of MPc and H_2Pc.

1.1.4 UV/Vis Absorption Spectra of phthalocyanines

The UV/Vis absorption spectrum of MPc is characterized by the presence of single intense Q band corresponding to D_{4h} symmetry; while electronic absorption spectrum of H_2Pc show split Q bands attributed to lower D_{2h} symmetry, **Figure 1.2**. The increase in symmetry for MPc compared to H_2Pc is as a result of the change in geometry resulting in the reduction of number of allowed transitions. According to four-orbital model proposed by Gouterman and coworkers [55-57], the split Q bands of H_2Pc are due to electronic transitions from a_{1u} of the highest occupied molecular orbitals (HOMO) to the non-degenerate b_{2g} and b_{3g} of the lowest unoccupied molecular orbitals (LUMO), **Figure 1.3**. The characteristic Q band of MPc is due to π (a_{1u}) $\rightarrow\pi^*$ (e_g) electronic transitions, **Figure 1.3**. The less-intense Soret or B-band (in both spectra) appears at around 350 nm in the ultraviolet (UV) region, it originates from two transitions; B_1 and B_2 which corresponds to $a_{2u}\rightarrow e_g$ and $b_{2u}\rightarrow e_g$ respectively, **Figure 1.3**.

The position of Q band absorption in MPc complexes can be influenced by the parameters which include; nature of central metal, peripheral or non-peripheral substitution of substituents, nature of the substituents etc. Any of these parameters can

also be used to tune the nonlinear absorption (NLA) and/or optical limiting (OL) properties of phthalocyanines for enhanced activities.

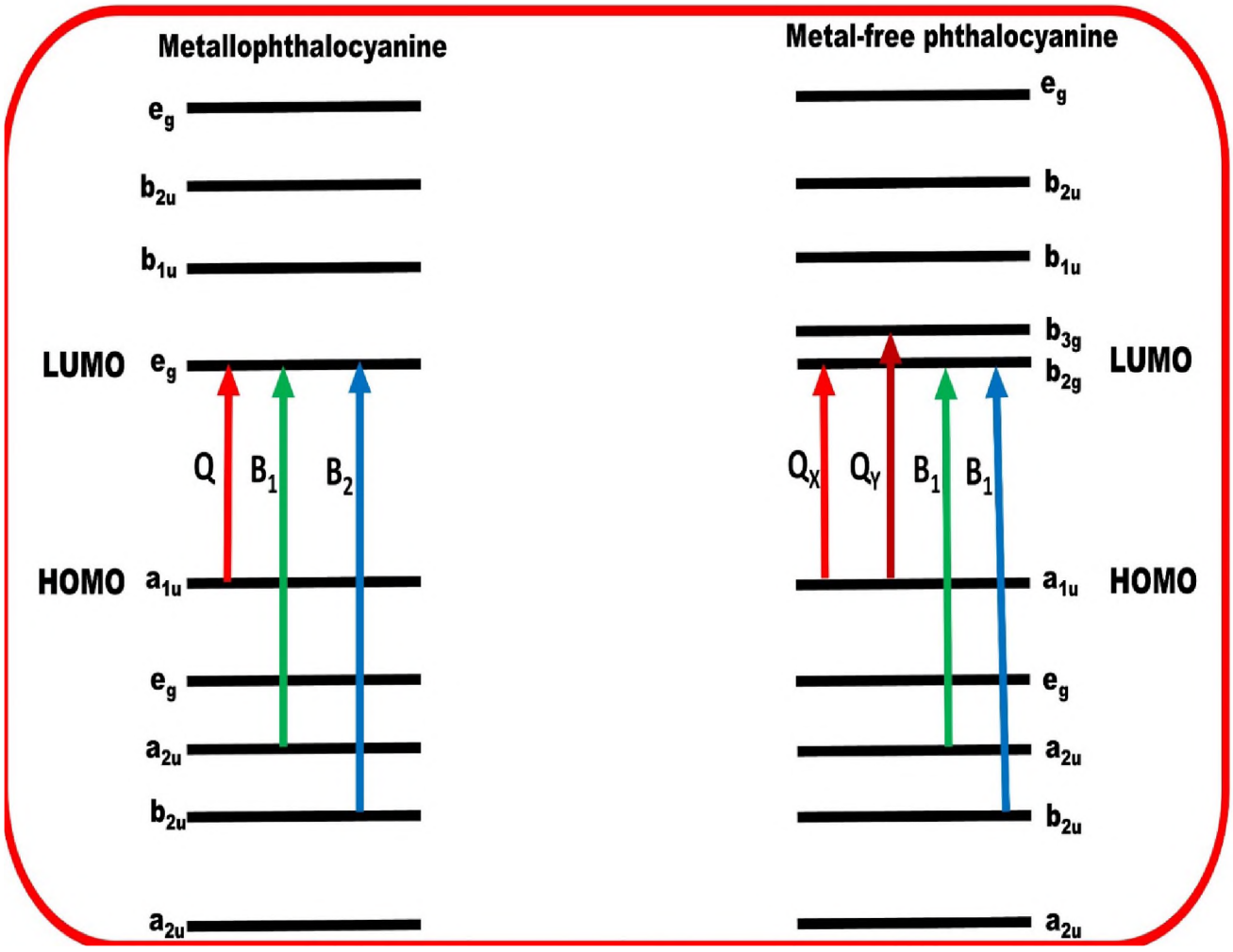

Figure 1.3: Gouterman's four-orbital model of electronic transitions in metallophthalocyanine and metal-free phthalocyanine.

1.1.5 Photophysical properties of phthalocyanines

Photophysical properties are the physical changes induced when a fluorophore interacts with photons without formation of new product. Photoexcitation of phthalocyanine usually result in radiative and radiationless transitions as depicted in the modified Jablonski diagram, **Figure 1.4** [58-60]. Pc molecule absorbs a photon to undergo transition (A) from the ground state (S_0) to the highest vibrational level of excited singlet excited state (S_1), and subsequently relaxed (VR) to the lowest vibrational level of S_1 upon collision with other molecules. Due to the limited life times of the excited states of S_1, Pc

molecule can either return to the ground states (S_0) through fluorescence (F) and internal conversion (IC), or by undergoing intersystem crossing (ISC) to populate the triplet excited states (T_1). Enhanced triplet-triplet absorption in a molecule is important for photo driven applications in bio-medicine, catalysis, organic solar cells and optical limiting devices [61-64]. Estimation of the photophysical parameters obtained during photoexcitation processes of MPcs such as fluorescence quantum yields, lifetimes, triplet quantum yields and lifetimes are discussed further.

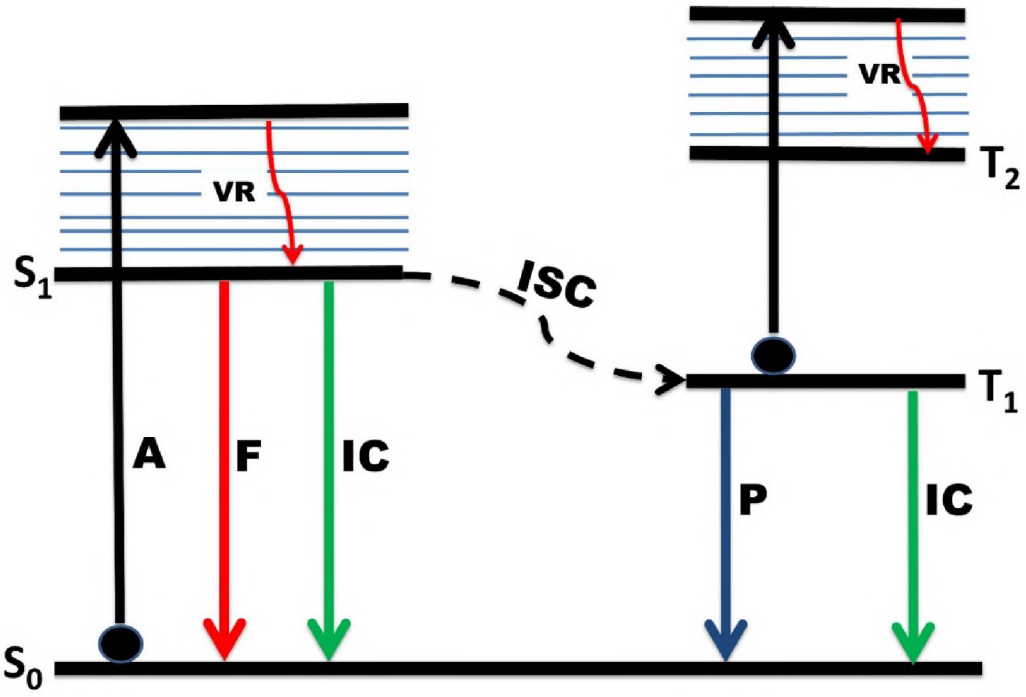

Figure 1.4: Modified Jablonski diagram showing the photoexcitation processes in MPcs. S_0 = singlet ground state, S_1 = singlet excited state, A = absorption, F= fluorescence, IC = internal conversion, VR = vibrational relaxation, ISC = intersystem crossing, P = phosphorescence and T_1 = triplet excited state.

1.1.5.1 Fluorescence quantum yield (Φ_F) and life-time (τ_F)

Fluorescence quantum yields denoted as Φ_F, measure the ratio of photons absorbed to the photons emitted by the fluorophores (MPcs) through fluorescence emission. Factors such as size of the central metal, extent of aggregation, nature of solvents, type and position of substituents on the Pc ring, extended π-π conjugative system, temperature, pH

as well as presence of nanoparticles have been reported to influence the quantum yields of fluorophores [65,66]. The Φ_F values for the studied complexes in dimethyl sulfoxide (DMSO) or tetrahydrofuran (THF) were determined using previously reported comparative methods (**Eq. (1.1)**) [67,68]. Unsubstituted ZnPc in DMSO was employed as standard for all the studies conducted in this thesis. The samples and ZnPc standard were excited at the same excitation wavelengths and the emission spectra recorded from ~610 nm to 800 nm.

$$\Phi_F = \Phi_F^{std} \frac{F\, A_{std}\, n^2}{F_{std} A\, n_{std}^2} \quad (1.1)$$

where Φ_F^{std} is the fluorescence quantum yield of the ZnPc standard, (= 0.2 [69]), F and F_{std} are the areas under the fluorescence emission curves of the MPcs and the ZnPc standard, respectively. A and A_{std} are the respective absorbance of MPcs and standard at the excitation wavelengths. n and n_{std} are the refractive indexes of the solvents (DMSO or THF) used for the samples and the standards, respectively.

The fluorescence lifetimes (τ_F) for all the samples were obtained from Time Correlated Single Photon Counting (TCSPC) technique [70,71] by fitting their fluorescence decay dataset to mono or bi-exponential functions using OriginPro programs.

1.1.5.2 Förster resonance energy transfer (FRET)

Förster resonance energy transfer (FRET) is a non-radiative energy transfer process through which a photo-excited fluorescent donor molecule (e.g. quantum dots) transfers energy to an acceptor molecule (MPcs) through dipole-dipole coupling [72-75]. The fluorescence quantum yields and lifetimes of acceptor molecule are increased following energy transfer process, while fluorescence quantum yields and lifetimes of donor molecules are reduced [74,76-78]. Förster resonance energy transfer between MPcs (acceptors) and graphene quantum dots (donors) were evaluated in this work. The fluorescence quantum yields of the donor in presence of acceptor ($\Phi_F^{(Pc-QDs)}$) were estimated using **Eq. 1.2**:

$$\Phi_F^{(Pc-QDs)} = \Phi_F^{QDs} \frac{F^{(Pc-QDs)}}{F_{QDs}} \quad (1.2)$$

where $F^{(Pc-QDs)}$ and F_{QD} are the fluorescence intensities of donor in presence and absence of acceptor, respectively. Φ_F^{QDs} represents fluorescence quantum yield of the donor alone and was used as a standard. Fluorescence quantum yields (Φ_F^{QDs}) of the donor in absence

of acceptor was determined using comparative methods described above (**Eq. 1.1**), and rhodamine 6G in ethanol used as a standard (Φ_F= 0.94 [73]). The conjugates were all excited at the wavelengths where only the donor absorbs.

FRET efficiencies (Eff) were determined from the fluorescence quantum yields of the donor in the presence ($\Phi_F^{(Pc-QDs)}$) and in the absence ($\Phi_F^{(QDs)}$) of the acceptor using **Eq. 1.3** [73,77]:

$$\text{Eff} = 1 - \frac{\Phi_F^{(Pc-QDs)}}{\Phi_F^{(QDs)}} \quad (1.3)$$

Eff can also be calculated in terms of lifetime of the donor in the presence ($\tau_F^{(Pc-QDs)}$) and in the absence ($\tau_F^{(QDs)}$) of the acceptor according to **Eq. 1.4** [77,79]:

$$\text{Eff} = 1 - \frac{\tau_F^{(Pc-QDs)}}{\tau_F^{(QDs)}} \quad (1.4)$$

1.1.5.3 Triplet quantum yield (Φ_T) and lifetime (τ_T)

The values of Φ_T and τ_T provide necessary information for determining the magnitude of multi-photon absorption processes responsible for positive nonlinear absorption effects in organic molecules [80-83]. Samples for triplet quantum yields were first de-gassed with argon and irradiated at the Q band maxima in a spectrophotometric fluorescence cell using nanosecond flash photolysis laser system. The triplet quantum yields were determined using a comparative method, **Eq. 1.5** [84,85];

$$\Phi_T = \Phi_T^{std} \frac{\Delta A_T \varepsilon_T^{std}}{\Delta A_T^{std} \varepsilon_T} \quad (1.5)$$

where Φ_T^{std} is the triplet quantum yield for the unsubstituted ZnPc standard ((Φ_T)= 0.65 for ZnPc in DMSO) [86], ΔA_T and ΔA_T^{std} are the changes in the triplet state absorption of the sample and standard, respectively, and ε_T and $\varepsilon_T^{std}$are the triplet state molar extinction coefficients of the sample and the standard, and can be determined using **Eqs. 1.6** and **1.7** [86]

$$\varepsilon_T = \varepsilon_S \frac{\Delta A_T}{\Delta A_S} \quad (1.6)$$

$$\varepsilon_T^{std} = \varepsilon_S^{std} \frac{\Delta A_T^{std}}{\Delta A_S^{std}} \quad (1.7)$$

where ε_S and ε_S^{std} are the singlet state molar extinction coefficients of the sample and the standard, respectively.

The triplet lifetimes of a molecule measure the average time an already excited molecule remains in the triplet excited state. Triplet lifetimes were determined by exponential fitting of the triplet decay curves (**Figure 1.5**) [87] using OriginPro 8.0 program.

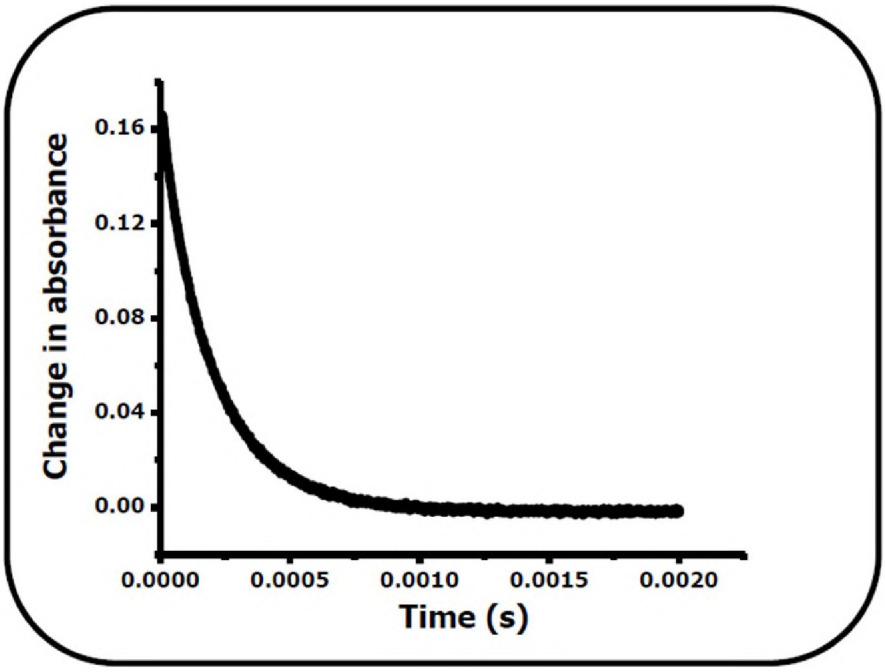

Figure 1.5: Typical triplet decay curve for MPc [87]

1.1.6 Phthalocyanines used in this work for NLO

Metallophthalocyanines and their derivatives have been extensively studied macrocycles for the development of nonlinear optical devices used for protecting light sensitive materials [88,89] from dangerous laser radiations, and to manipulate or process optical signals in telecommunication systems [90,91]. MPcs have numerous advantages over other macrocycles as passive optical limiters due to their degree of aromaticity, low di-electric constant, large third-order nonlinear susceptibility and polarizability, and their facile processing to optical components [92-95]. Optical limiting effects of MPcs are based on reverse saturable absorption (RSA) in which the nonlinear absorption coefficient increases as the optical input intensity increases [96]. The mechanism of RSA in MPcs is due to strong absorption in the triplet excited states mediated by already excited

molecules [15,80,97,98]. The structures and naming of phthalocyanine molecules used in this work are summarized in **Table 1.1.**

Table 1.1: Summary of phthalocyanine complexes and names used in this work

Molecular structure	Name	Complex number
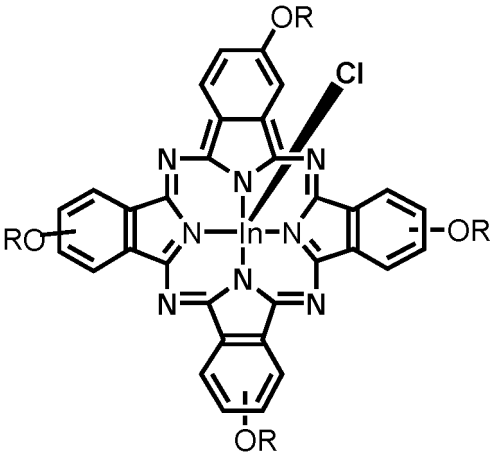	**R =** 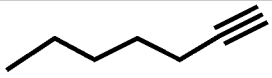 2,9(10),16(17),23(24)-tetrakis(hex-5-ynoxy)phthalocyanatoindium (III) chloride. Studies: photophysics and nonlinear optics.	1 (New)
	R = 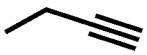 2,9(10),16(17),23(24)-tetrakis(prop-2-ynoxy) phthalocyanato indium(III) chloride. Linked to AuNPs Studies: photophysics and nonlinear optics	2 (New)
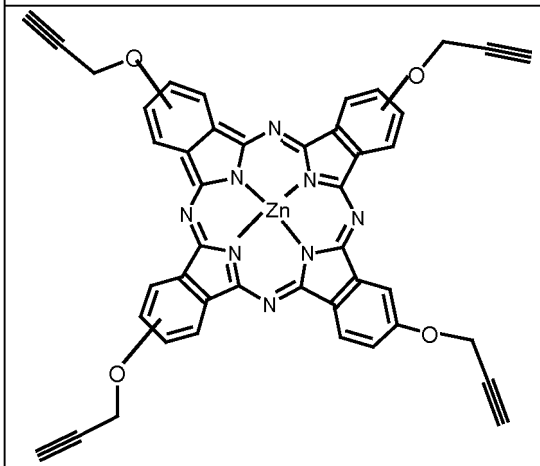	2,9(10),16(17),23(24)-tetrakis(prop-2-ynoxy) phthalocyanine zinc(II) Linked to AuNPs Studies: photophysics and nonlinear optics.	3

Molecular structure	Name	Complex number
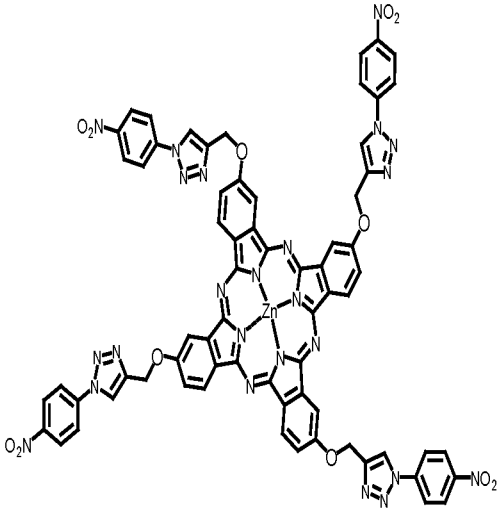	2,9(10),16(17),23(24)-tetrakis 4-nitro-1-benzyl-4-(3,4-dicyanophenoxymethyl)-1H-1,2,3-triazole Studies: photophysics and nonlinear optics	4 (New)
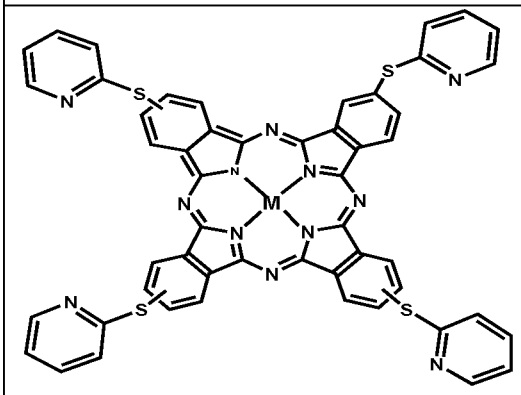	M = Zn 2,9(10),16(17),23(24)-tetrakis(2-mercaptopyridiny)Phthalocyanine zinc (II) Studies: nonlinear optics in solution and thin films (PBC). M = In 2,9(10),16(17),23(24)-tetrakis(2-mercaptopyridiny) phthalocyanine indium (III) Studies: nonlinear optics in solution and thin films (PBC).	5 6

Molecular structure	Name	Complex number
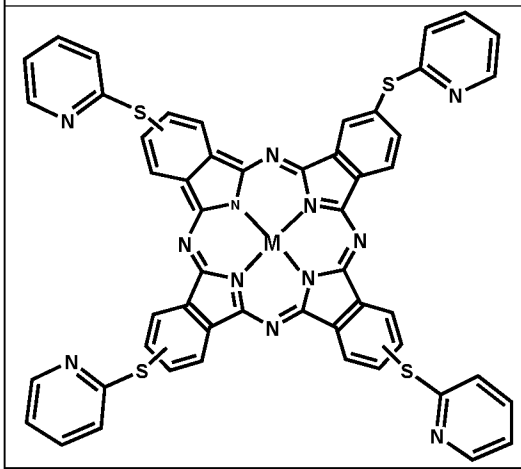	M = H_2 2,9(10),16(17),23(24)-tetrakis(2-mercaptopyridiny) phthalocyanine Studies: photophysics and nonlinear optics in solution and thin films (PBC).	7 (New)
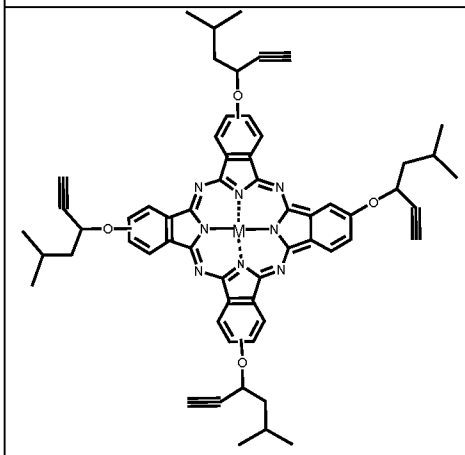	M = H_2 2,9(10),16(17),23(24)-tetrakis-(4-(5-methylhex-1-yn-3-yloxy)) phthalocyanine Studies: photophysics and nonlinear optics in solution and thin films (PSU).	8 (New)
	M = Zn 2,9(10),16(17),23(24)-tetrakis-(4-(5-methylhex-1-yn-3-yloxy)) phthalocyanine zinc (II) Studies: photophysics and nonlinear optics in solution and thin films (PSU).	9 (New)
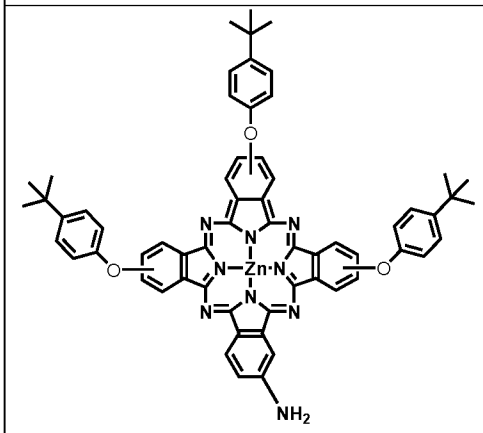	2,9(10),16(17)-trikis-(4-tertbutylphenoxyl)-4-aminophthalocyaninato zinc (II) Linked to AuNPs, Fe_3O_4@Ag, Fe_3O_4-Ag, GQDs, NGQDs and SNGQDs Studies: photophysics and nonlinear optics in solution and thin films (PAA).	10

Molecular structure	Name	Complex number
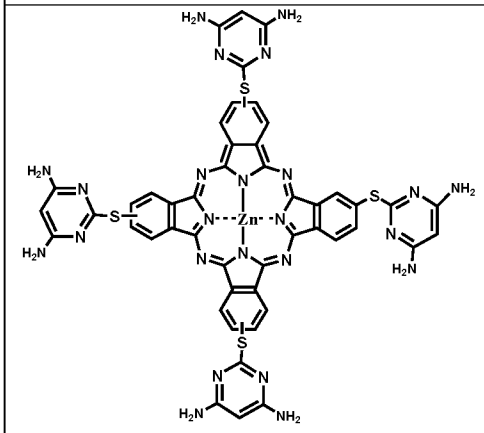	2,9(10),16(17),23(24)-tetrakis-(4-(4,6-Diaminopyrimidin-2-ylthio) zinc (II) phthalocyanine Linked to Ag_xAu_y nano-alloys. Studies: photophysics and nonlinear optics.	11 (New)

AuNPs = gold nanoparticles, Fe_3O_4@Ag = magnetite-silver core-shell nanoparticles, Fe_3O_4-Ag = magnetite-silver hybrid nanoparticles, GQDs = graphene quantum dots, NGQDs = N-doped graphene quantum dots and SNGQDs = S, N co-doped graphene quantum dots, Ag_xAu_y= silver and gold Nano alloys, PSU = polysulphone, PBC = poly(bisphenol A) carbonate, PAA = polyacrylic acid.

The Pcs used in this work are broadly classified into three (3) major groups as;

(i) Alkynyl and/or 1,2,3-triazole functionalized indium, zinc and metal-free Pcs (**1, 2, 3, 4, 8, 9**);

(ii) Mercaptopyridine-substituted indium, zinc, and metal-free Pcs (**5, 6, 7**); and

iii) Tetra (**11**) or mono-substituted (**10**) amino Zn-centered Pcs.

1.1.6.1 Group i: Alkynyl Pcs (1, 2, 3, 8, 9) and 1,2,3-triazole functionalized ZnPc (4)

Table 1.2 lists alkynyl Pc complexes which have been studied for photophysics, and electrochemical studies only [99-108]. No heavy atoms such as In have been employed, hence this work explored the photophysics of In containing Pcs for enhanced intersystem crossing required for the multi-photon absorption processes in nonlinear optics. It can be seen in **Table 1.2**, that the Φ_T values recorded for the selected Pcs are generally low, suggesting quenching of the excited states of the molecules by fluorescence rather than

intersystem crossing. It is shown in this work that the Φ_T values can be significantly improved using In as central metals.

Table 1.2: A selection of some of the alkynyl or triazole functionalized Pc molecules that have been reported in literature

A selection of MPc + NPs	Photophysical parameters				Application	Ref	Complex/ conjugate number
	Φ_F	τ_F (ns)	Φ_T	τ_T (μs)			
PANI-N3/TA-CoPc	-	-	-	-	Electrochemistry	99	**12**
ZnPAI/ZnPTr	-	-	-	-	Semiconductor/ electrochemistry	100	**13** **14**
FePc	-	-	-	-	Electrocatalysis	101	**15**
TEZnPc	0.21	0.7	-	-	Fluorescence sensing	102	**16**
TEZnPc-6AH	0.15	0.04	-	-	Fluorescence sensing	103	**17**
3HB$_3$ZnPc-SiNPs	0.20	2.92	0.40	352	Photophysical studies	104	**18**
4HB$_3$ZnPc -SiNPs	0.22	3.00	0.49	373			**19**
3HB$_4$ZnPc-SiNPs	0.20	2.90	0.37	484			**20**
MnTHOPc	-	-	-	-	Electrochemistry	105	**21**
TBZnPc	0.4	3.92	-	-	Electrochemistry/ fluorescence studies	106	**22**
TBBNZnPc	0.01	3.34	-	-			**23**
SWNT-ZnPc	-	-	-	-	Photovoltaic device	107	**24**
FePc-QDs	-	-	-	-	Electrocatalysis	108	**25**

PANI-N$_3$/TA-CoPc= tetrakis(pent-4-ynoxy) phthalocyaninato cobalt(II)-azido aniline, ZnPAI = tetrakis (propyn-3-yloxy) phthalocyanine zinc (II), ZnPTr=tetrakis (1-Benzyl-4-(3,4-dicyanophenoxymethyl))-1H-1,2,3-triazole, FePc = tetrakis(5-hexyn-oxy) Fe(II) phthalocyanine, TEZnPc = tetrakis(2-ethynylcyclohexyloxy)phthalocyaninatozinc(II), TEZnPc-6AH = tetrakis(2-ethynylcyclohexyloxy)phthalocyaninatozinc(II) clicked to 6-azido-hexanoic acid, 3HB$_3$ZnPc = 3-(hex-5-ynyl 3-hydroxybenzoate)phthalocyaninato zinc (II), 4HB$_3$ZnPc = 4-(hex-5-ynyl 3-hydroxybenzoate)phthalocyaninato zinc (II), 3HB$_4$ZnPc = 3-(hex-5-ynyl 4-hydroxybenzoate)phthalocyaninato zinc (II), MnTHOPc = Mn tetrakis(5-hexynoxy)phthalocyanine, TBBNZnPc = 1,4-Bis(1-(tri-tert-butylphthalocyaninate zinc(II))-1H-1,2,3-triazol-4-yl)benzene, TBZnPc = 23-ethynyl-2(3),9(10),16(17)-tri-tert-butylphthalocyaninate zinc(II), SWNT-ZnPc = single-wall carbon nanotubes-Zn(II) azidophthalocyanine, QDs =azide-funtionalised CdSe/ZnS, SiNPs = silica nanoparticles.

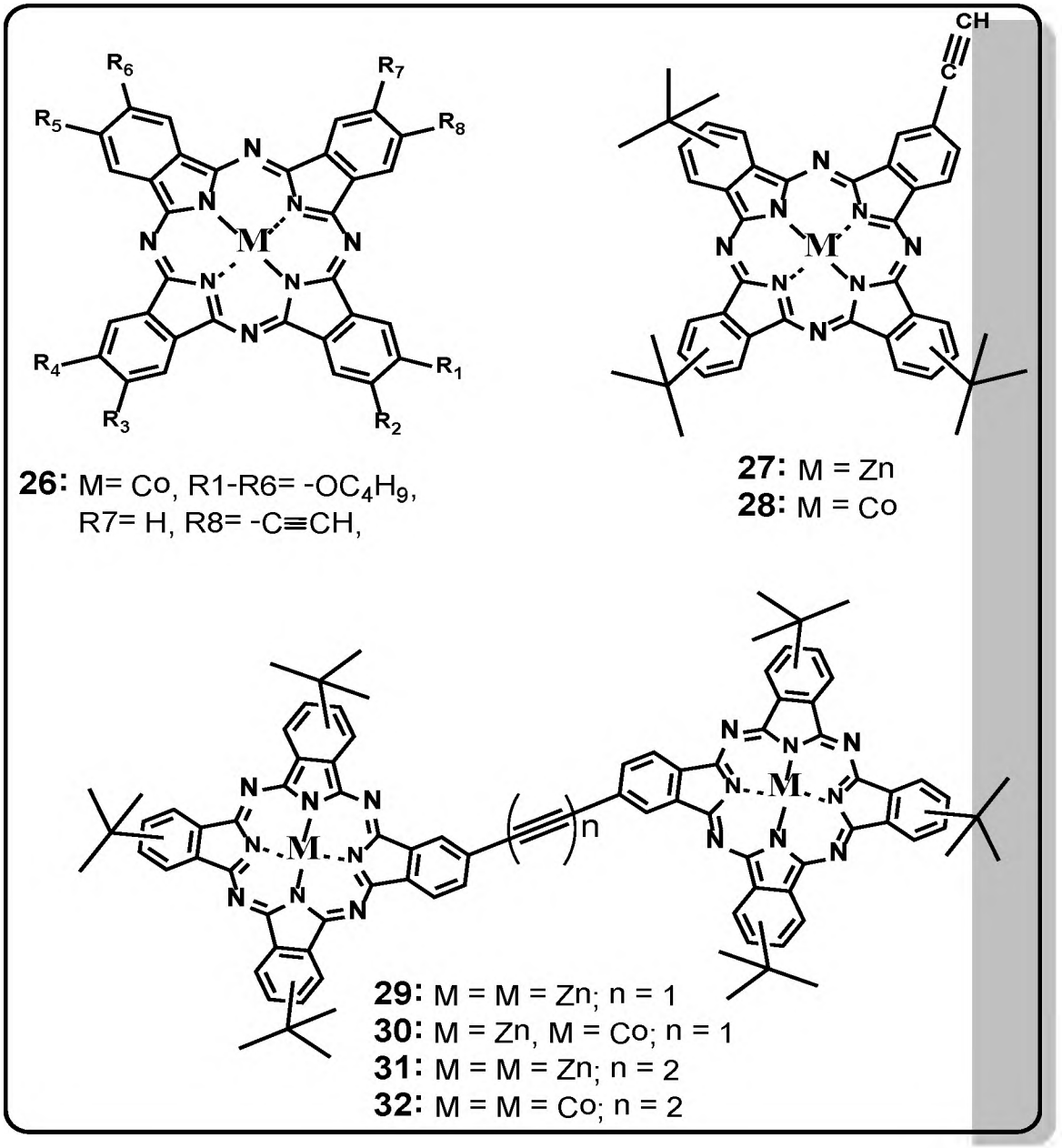

Figure 1.6: Selection of alkynyl Pc molecules that have been reported for nonlinear optical characterizations in literature.

Table 1.3 lists a selected Co or Zn alkynyl MPcs [108,109] (structures shown in **Figure 1.6**) which have been used for nonlinear optics (NLO). It is surprising that despite the number of alkynyl or triazole-functionalized phthalocyanines reported (**Table 1.3**) so far in literature only few of them have been reported for nonlinear optical characterizations. Asymmetrical alkynyl Pcs have been used, but with central metals

such as Co which are not good for NLO due to their paramagnetic nature, which shortens the triplet excited states.

Table 1.3: Summary of NLO parameters for selected alkynyl phthalocyanines that have been reported in literature. The nonlinear optical characterizations were monitored under nanosecond laser pulse durations using Z scan technique in Toluene

Pc	Conc. (g/L)	λ_{max} Q_{band} (nm)	α (cm^{-1})	I_{oo} (GW/cm^2)	β_{eff} (cm/GW)	$I_m[\chi^{(3)}]$ (esu) x 10^{-11}	γ (esu)x 10^{-33}	k (σ_T/σ_0)	Ref
26	0.5	677	1.8	1.0	7.2±1.4	0.27±0.05	2.3±0.4	4.9±0.3	108
27	0.5	684	1.95	0.5	35.0±7.0	1.3±0.2	8.3±1.6	8.9±0.3	108
28	0.5	673	1.76	2.0	1.4±0.3	0.05±0.01	0.32±0.06	3.3±0.8	108
29	0.5	678	1.06	0.2	12.0±2.0	0.46±0.08	5.8±1.1	3.0±0.1	108,109
30	0.5	677	1.22	0.5	5.6±1.1	0.21±0.04	2.6±0.5	1.8±0.1	108
31	0.5	709	1.19	0.5	23.0±5.0	0.87±1.6	11.0±2.0	5.4±0.2	108,109
32	0.5	691	1.60	0.5	35.0±7.0	1.3±0.2	17.0±3.0	11.0±0.1	108,109

Alkynyl moieties on the peripheral positions of complexes **1**, **2**, **3**, **8** and **9** were chosen for improved solubility and to allow for future modification with azide containing nanoparticles or molecules using Huisgen cyclo-addition "click" reactions. Increased intersystem crossing (ISC) has been reported for triple bonds containing groups [27]. Hence improved population of triplet states required for reverse saturable absorptions are expected for complexes **1**, **2**, **3**, **8** and **9**. Indium and Zinc were chosen as the central metal for complexes **1** and **2** because of its heavy atom effect which can induce increased

rate of intersystem crossing to triplet states via spin-orbit coupling, and consequently, enhance the optical limiting (OL) performances of the Pcs [90,110,111].

Enhanced OL characterizations of 1,2,3 triazole-fused nitrophenyl ZnPc (**4**) was explored for the first time in this report and the results were compared to complex **3**. It is noteworthy to mention that no optical limiting (OL) parameter (I_{lim}) was reported in **Table 1.3**. Also, the reported β_{eff}, $I_m[\chi^{(3)}]$, and γ are lower than those that will be reported in this thesis.

1.1.6.2 Group ii: Mercaptopyridine substituted Pcs (5 - 7)

Table 1.4 lists Pcs in general which have been used for NLO/OL in solution or in thin films [112-122]. The structures are shown in **Figure 1.7.** From **Table 1.4**, it is evident that poly (methyl methacrylate) (PMMA) is preferred as host polymer for Pc complexes for NLO characterizations. Other polymers such as poly(vinylchloride) (PVC) [123], polyacrylic acid (PAA) [117] and poly(bisphenol A carbonate) (PBC) [124] have also been investigated to host phthalocyanine molecules for practical OL applications. Recently, improved optical limiting behaviour of MPcs-doped in PBC compared to PMMA have been reported [125]. The enhancement of MPcs in presence of PBC was attributed to its higher mechanical strength and improved stability compared to PMMA. Encouraged by the improved NLO responses of MPcs-doped PBC above, nonlinear optical properties for complexes **5**, **6** and **7** are investigated in solution and in PBC. The NLO parameters such as β_{eff}, $I_m[\chi^{(3)}]$, and γ are highly improved in this work when PBC is employed coupled with the use of In as the central metal for **6**.

The choice of mercaptopyridine substituents for complexes **5**, **6** and **7** was due to good spectroscopic, photochemical and improved optical limiting properties of sulfur-substituted phthalocyanines [126-130]. The tuning of NLO properties of Pc complexes **5**, **6** and **7** was achieved in this work by varying the central metal atom of the complexes. As stated above, Pcs containing heavy metals such as indium and zinc are expected to show improved NLO behavior compared to metal-free Pcs. However, good OL properties of metal-free Pcs have also been reported in the literature [131,132], hence they are studied in this work and compared to metal Pc analogues.

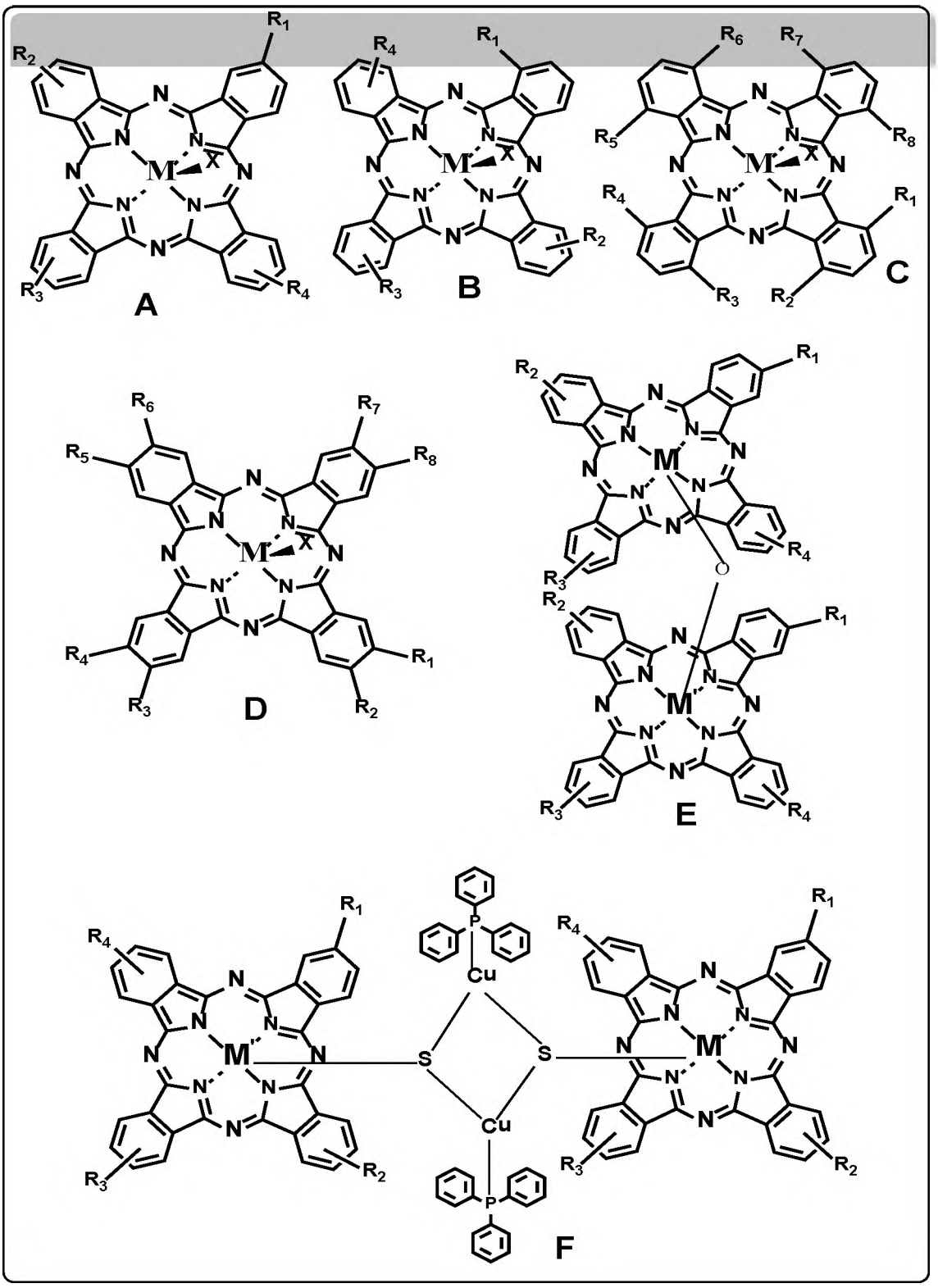

Figure 1.7: Selected Pc molecules doped in polymer matrices or in solution that have been characterized for optical limiting applications. They have been grouped into 6 categories based on their structures and/or points of substitutions on Pc rings.

Legends for Figure 1.7

CATEGORY A

33: M = In, X = Cl, R_1-R_4 = 1-(benzyloxy)benzene

34: M = In, X = Cl, R_1-R_4 = -C(CH$_3$)$_3$

35: M = In, X = Cl, R_1-R_4 = 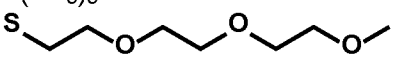

36: M = In, X = Cl, R_1-R_4 = 4-((pyren-1-yl)methyleneamino)-phenoxy)

37: M = In, X = Cl, R_1 = 4-aminophenoxyl, R_2=R_3=R_4= 4-((pyren-1-yl)methyleneamino)-phenoxy)

38: M = In, X = Cl, R_1-R_4 = 4-aminophenoxyl

39: M = In, X = Cl, R_1-R_4 = 1-(2,3-Dihydro-1H-inden-1-yloxy)

40: M = In, X = Cl, R_1-R_4 = 4-tert-butylphenoxyl

41: M = In, X = Cl, R_1-R_4 = OC_6H_5

42: M = Zn, X = nil, R_1-R_4 = H

43: M = Zn, X = nil, R_1-R_4 = -C(CH$_3$)$_3$

44: M =2H, X = nil, R_1-R_4 = -C(CH$_3$)$_3$ 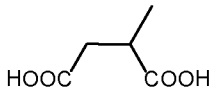

45: M = Zn, X = nil, R_2=R_3=R_4 = -C(CH$_3$)$_3$, R_1=

CATEGORY B

46: M = In, X = Cl, R_1-R_4 = 4-tert-butylphenoxyl

47: M = In, X = Cl, R_1-R_4 = OC_6H_5

48: M = In, X = Cl, R_1-R_4 = 1-(benzyloxy)benzene

49: M = In, X = Cl, R_1-R_4 = 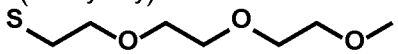

CATEGORY C

50: M = In, X = Cl, R_1-R_8 = -C_6H_{13}

51: M = In, X = F, R_1-R_8 = -C_6H_{13}

CATEGORY D

52: M = In, X = Cl, R_1-R_8 = 1-(benzyloxy)benzene

53: M = In, X = Cl, R_1-R_8 = 4-tert-butylphenoxyl

54: M = In, X = Cl, R_1-R_8 = OC_6H_5

55: M = Zn, X = nil, R_1-R_8 = OC_7H_{15}

56: M = 2H, X = nil, R_1-R_8 = OC_7H_{15}

57: M = In, X = Cl, R_1-R_8 = 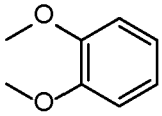

CATEGORY E

58: M = M' = In, R_1-R_4 = -C(CH$_3$)$_3$

59: M = In, M' =Ga, R_1-R_4 = -C(CH$_3$)$_3$

CATEGORY F

60: [Cu_2(tBu4PcGa)(tBu4PcIn)S_2TPP$_2$]

Table 1.4: Pc molecules doped in polymer matrices or in solution that have been reported for optical limiting characterizations in the literature. Laser excitations varied from 532 to 800 nm in the nanosecond region using Z scan technique

Sample	Solv	Conc. (g/L)	α (cm^{-1})	I_{oo} (GW/cm^2)	β_{eff} (cm/GW)	$I_m[\chi^{(3)}]$ (esu) x 10^{-11}	γ (esu)	k (σ_T/σ_o)	I_{lim}(J/cm^2)	Ref
33	C	1.0	0.30	0.5	59.0±11.0	NA	NA	23.1±0.8	NA	112
33/PMMA	TF	NA	201.4	0.2	1.0×10^5	NA	NA	8.6±0.6	NA	112
34	T	0.5	0.53	0.5	44.0±9.0	1.6±0.3	13.0×10^{-33}	27.4±0.6	NA	110
34/PMMA	TF	NA	176.6	0.2	89.7	335	NA	3.68±0.1	1.64	113
35	C	NA	1.4	0.15	398	NA	NA	NA	NA	114
35/PMMA	TF	NA	115	0.15	NA	NA	NA	NA	NA	114
36	D	1.5	NA	0.3	9.9	0.35	2.63×10^{-28}	NA	2.93	115
37	D	1.5	NA	0.3	53.8	1.89	1.02×10^{-27}	NA	0.54	115
38	D	1.5	NA	0.26	221.6	7.80	3.9×10^{-27}	5.9×10^2	0.28	116
38/PMMA	TF	NA	NA	0.1	10000	NA	NA	1.8×10^4	0.006	117
38/PAA	TF	NA	NA	0.1	11500	NA	NA	1.6×10^4	0.005	117
39	D	1.5	NA	0.1	650	22.9	1.16×10^{-26}	4.18×10^3	0.095	117
39/PAA	TF	NA	NA	0.1	7000	NA	NA	3.49×10^5	0.009	117
39/PMMA	TF	NA	NA	0.1	3300	NA	NA	2.30×10^5	0.019	117
40	D	NA	NA	NA	NA	3.23	1.41×10^{-35}	1.24	1.71	118

Sample	Solv	Conc. (g/L)	α (cm^{-1})	I_{oo} (GW/cm^2)	β_{eff} (cm/GW)	$I_m[\chi^{(3)}]$ (esu) x 10^{-11}	γ (esu)	k (σ_T/σ_o)	I_{lim} (J/cm^2)	Ref
41	D	NA	NA	NA	NA	9.19	4.01 x 10^{-35}	2.58	1.93	118
42/PMMA	TF	0.15	19.46	12.7	43.0	NA	NA	NA	NA	119
43/PMMA	TF	0.1	NA	200	15	2.10	NA	NA	0.55	120
44/PMMA	TF	0.1	NA	200	60	3.71	NA	NA	0.131	120
45/PMMA	TF	0.1	1.2	200	200	16.2	NA	NA	0.112	120
46	D	NA	NA	NA	NA	8.40	3.66 x 10^{-35}	5.24	1.81	118
47	D	NA	NA	NA	NA	1.12	4.83 x 10^{-35}	2.12	2.11	118
48	C	1.0	0.18	0.5	41.0±8.0	NA	NA	25.7±0.8	NA	112
48/PMMA	TF	NA	159.4	0.2	4100	NA	NA	9.1 ±0.6	NA	112
49	C	NA	1.4	0.15	237	NA	NA	NA	NA	114
49/PMMA	TF	NA	265	0.15	NA	NA	NA	NA	NA	114
50	T	1.0	0.93	0.15	32.0±6.0	1.2±0.2	(7.3±1.4) x 10^{-33}	16.1±0.3	NA	110
51	T	1.0	0.93	0.5	35.0±0.6	1.2±0.2	(8.1±1.6) x 10^{-33}	16.2±0.3	NA	121
52	C	1.0	0.62	0.5	130±4.0	NA	NA	20.0±0.9	NA	112
52/PMMA	TF	NA	378.95	0.2	70000	NA	NA	7.5±0.5	NA	112
53	D	NA	NA	NA	NA	2.87	3.07 x 10^{-35}	53.4	1.92	118
54	D	NA	NA	NA	NA	4.59	2.00 x 10^{-35}	41.4	1.16	118
55/PMMA	TF	0.1	NA	200	180	11.3	NA	NA	0.137	120

Sample	Solv	Conc. (g/L)	α (cm^{-1})	I_{oo} (GW/cm^2)	β_{eff} (cm/GW)	$I_m[\chi^{(3)}]$ (esu) x 10^{-11}	γ (esu)	k (σ_T/σ_o)	I_{lim}(J/cm^2)	Ref
56/PMMA	TF	0.1	NA	200	60	4.86	NA	NA	0.164	120
57	DF	1.01	1.1	NA	34	NA	NA	NA	0.43	122
58	T	0.5	1.13	0.5	46.0±9.0	1.5±0.3	24.0 x 10^{-33}	12.4±0.3	NA	110
59	T	0.5	1.02	0.5	29.0±5.0	1.1±0.2	15.0 x 10^{-33}	10.0±0.2	NA	110
60	T	NA	0.95	0.2	23.7	0.89	NA	18.24±2	23	113
60/PMMA	TF	NA	145.35	0.2	3310	184	NA	4.41±0.14	3.2	113

T= toluene, TF = thin films, D = DMSO, C = chloroform, PMMA = poly (methyl methacrylate), PAA = polyacrylic acid, DF = DMF, NA= not available, Solv = solvent or medium which the studies occurred.

1.1.6.3 Group iii: Amino groups containing Pcs (10 and 11)

The presence of NH_2 groups on complexes **10** and **11** allows for possible covalent or $\pi - \pi$ linking to nanoparticles. Phthalocyanine complexes substituted with tert-butyl and/or amino groups have been studied extensively for optical limiting applications. Statistical mixing of the two groups will give rise to material (complex **10**) with significant enhanced optical limiting properties compared to tetra-tert-butyl or amino substituted Pcs.

1.2 Introduction to nanomaterials

Improved optical and electronic properties of nanomaterials compared to bulk material [133-135] are attributed to increased ratio of surface area-to-volume of the nanostructures; and quantum confinement effects of the particles which have the same size scale as the wavelengths of electrons [135-142]. Because of their shapes and tiny sizes, nanomaterials such as Au, Ag, Fe_3O_4 and graphene quantum dots have been found useful in many state-of-the-art technological applications such as in the development of electronic and optical limiting devices [143-148].

Recent studies have shown that photophysical and photochemical properties of MPcs can be greatly enhanced in the presence of metallic nanoparticles such as AuNPs, AgNPs and Fe_3O_4 NPs) [149-154]; and carbon-based nanostructures [155-158]. Optical limiting of MPcs in presence of graphene quantum dots have not received enough attention, hence are also a subject of this thesis. Enhanced photophysical properties of MPcs-nanomaterial composites have been attributed to increased rate of ISC to the excited triplet states favoured by diminished fluorescence of MPcs in presence of nanomaterials [150,151,155].

MPcs are good passive optical limiting materials due to their good photo-thermal stability against laser radiation [159]; and the ease at which they undergo reverse saturable absorptions even at low laser power. Unlike MPcs, metallic NPs are known to alternate between saturable absorption (SA) at low laser input intensity, and reverse saturable absorption (RSA) at higher laser intensity [160-163]. Hence, at the appropriate concentrations and laser input intensities, exciting functional molecular materials composed of metallic nanoparticles (SA) and MPcs (RSA) could be generated for potential applications in optical switching, optical pulse compressor and for narrowing laser pulses [161,164].

In this thesis, comparative studies on the photophysical and nonlinear optical responses of phthalocyanine-nanoparticle composites explored; and the studies are broadly classified into two as follows (**Table 1.1** lists the studies conducted in this thesis):

Phthalocyanines conjugated to metallic nanoparticles

- low symmetry ZnPc (**10**) with mono-amino group was covalently linked to the mercaptopropionic acid (MPA) capped gold AuNPs to form amide linkage;
- low-symmetry ZnPc (**10**) was covalently linked to mercaptopropionic acid (MPA) capped Fe_3O_4@Ag core-shell or Fe_3O_4-Ag heterodimer nanoparticles;
- Alkynyl moieties on complexes **2** and **3** were coupled to azide-derivatized AuNPs using Huisgen cyclo-addition "click" reactions.
- complex **11** was conjugated to AgAu nano-alloys. Unlike **10** with single point of attachment, complex **11** was used to form Pc-AgAu conjugates through amine or thiol-metallic plasmonic bondings depending on the orientation of the Pcs on the nano-alloys.

Phthalocyanines conjugated to non-metallic nanoparticles (graphene QDs)

- low-symmetry ZnPc (**10**) was covalently linked to graphene quantum dots (GQDs), N-doped (N-GQDs) and S, N co-doped graphene (S, N-GQDs) quantum dots.

It is noteworthy to mention that this is the first time plasmonic metallic nanoparticles and graphene quantum dots are linked to MPcs complexes for OL studies. OL characterizations of tetra-substituted MPc covalently linked to polyacrylic acid (PAA) has been reported before [165]. However, OL characterizations of low symmetry analogues linked to PAA is reported here for the first time. In order to ensure ideal optical limiting material with high stability capable of withstanding long term laser irradiation [166-169], studies were also done where MPc (complex **10** as an example) covalently linked to AuNPs or PAA blended into thin-films for practical purposes.

1.2.1 Gold (AuNPs) and Silver (AgNPs) Nanoparticles

What differentiates AuNPs and AgNPs from other metallic nanoparticles is the presence of intense surface plasmon bands caused by the interaction of the "free electrons" within the conduction band (**Figure 1.8**) [170,171]. The surface plasmon of AuNPs and AgNPs exhibit interesting scattering and absorbance properties that are primarily dictated by the

particle size, interparticle distance, shape, and refractive index of the medium [172-175]. As **Table 1.5** shows [116,176-182], no conjugates of asymmetrical Pcs [structures in **Figure 1.9**] with AuNPs and/or AgNPs have been reported before, hence a subject of this thesis.

The colloidal Au nanospheres synthesized are either functionalized with MPA prior covalent linkage to Pc **10**, or functionalized with azidopropylamine for Huisgen cycloaddition reactions with complexes **2** and **3**. This is the first time AuNPs are linked to Pc via click reactions.

Extensive investigations into optical limiting characterizations of metallic nanoparticles [183-185] and MPcs have been reported separately. Gowda et al [181] recently reported on enhanced nonlinear optical absorption of silver and gold nanoparticles in a metal-free phthalocyanine liquid crystalline matrix. However, nonlinear optical absorption response of metal-based phthalocyanine conjugated to gold or silver nanoparticles have not been reported in the literature. Herein, enhancement of optical limiting responses of MPc complex (**11**) in presence of nanoalloys of AgAu nanoparticles prepared at different molar ratios was described for the first time. Also, comparative photophysical and optical limiting characterizations of Pc **10** covalently linked to Fe_3O_4@Ag core-shell or Fe_3O_4-Ag heterodimer nanoparticles are reported in this thesis.

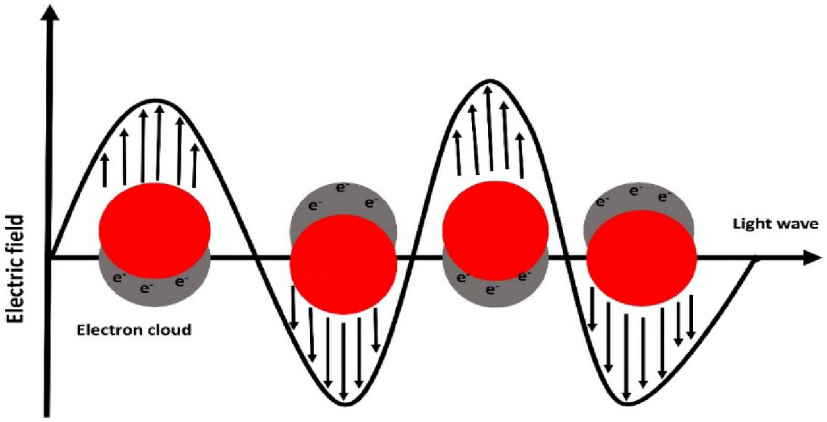

Figure 1.8: Localized SPR collective Oscillations of free electrons due to applied electric field.

Table 1.5 shows [116,176-182] MPc complexes (structures shown in **Figure 1.9**) which have been studied for NLO in the presence of nanomaterials; and confirms there have been no

studies of asymmetrical MPcs in presence of Ag NPs, only symmetrical MPc in presence of magnetite nanoparticles have been reported before [176].

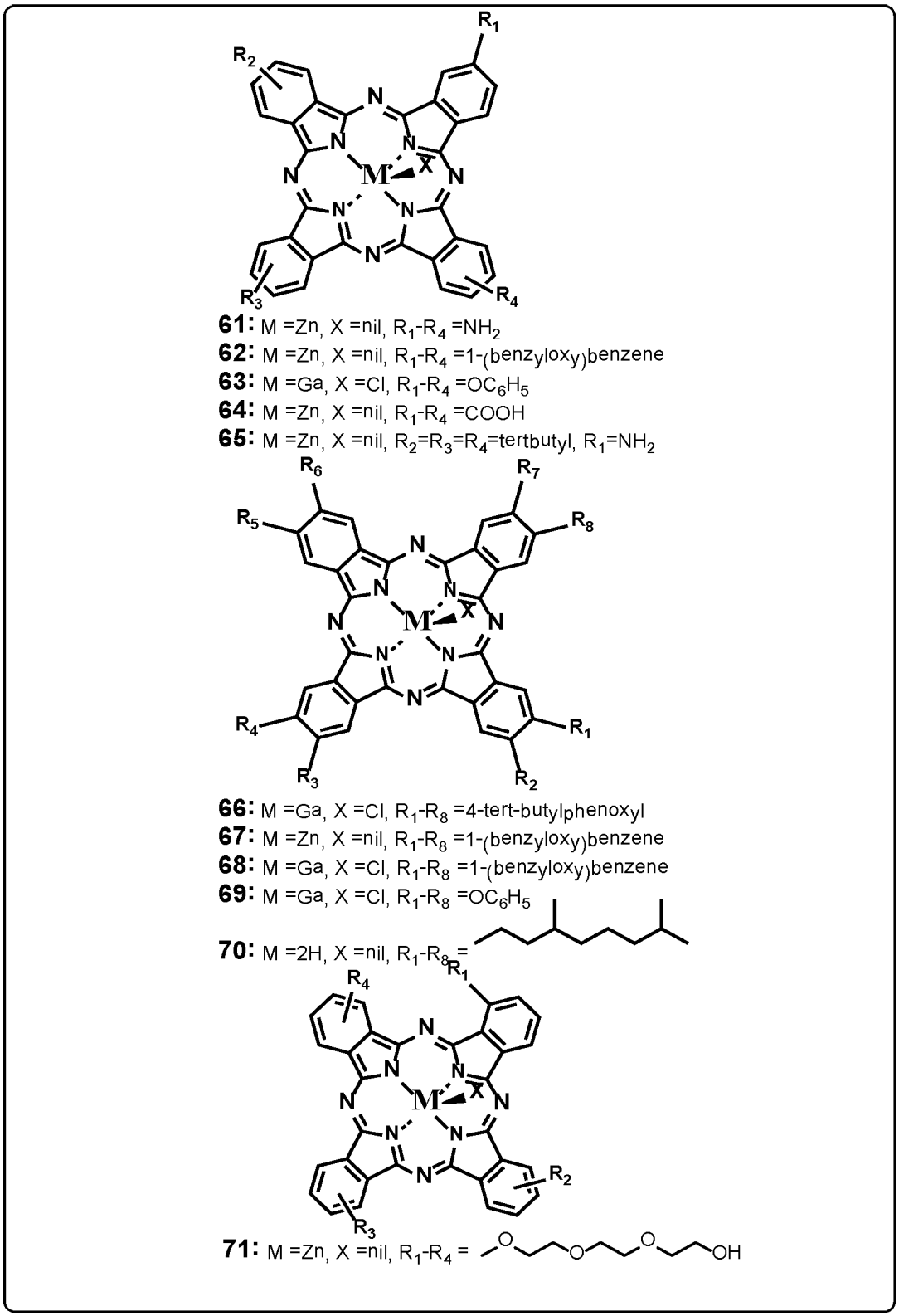

Figure 1.9: MPc complexes conjugated to nanomaterials for NLO applications (Data presented in Table 1.5).

Table 1.5: Lists of some Pc-nanomaterial composites that have been reported for NLO characterizations in the literature. Laser excitations conditions at 532 nm and ns-regime unless otherwise stated

Sample	Solv	Conc. (g/L)	α (cm^{-1})	I_{oo} (GW/cm^2)	β_{eff} (cm/GW)	$I_m[\chi^{(3)}]$ (esu) x 10^{-11}	γ (esu)	k (σ_T/σ_o)	I_{lim} (J/cm^2)	Ref
38+SiMNP	D	NA	1.5	0.122	400	14.1	7.03×10^{-27}	NA	0.16	176
38+SiNP	D	NA	1.5	0.122	200	7.04	3.51×10^{-27}	NA	0.30	176
38+CdSe/ ZnS QDs	D	0.1	1.5	0.141	700	24.6	1.24×10^{-26}	NA	0.092	177
38+CdSe QDs	D	0.1	1.5	0.141	310	10.9	5.47×10^{-27}	NA	0.21	177
38+SWCNT	D	NA	1.5	0.260	300	6.25	2.93×10^{-27}	NA	0.34	116
38+SWCNT	DF	NA	1.5	0.260	120	3.95	1.85×10^{-27}	NA	0.57	116
40+CdTe-TGA QDs	D+H	NA	NA	NA	6.87	2.39	1.19×10^{-30}	NA	0.049	178
61+CdTe-TGA QDs	D+H	NA	NA	NA	11.7	0.142	0.149×10^{-30}	NA	0.043	178
62+CdTe-TGA QDs	D+H	NA	NA	NA	14.5	5.04	1.34×10^{-30}	NA	0.039	178
63+CdTe-TGA QDs	D+H	NA	NA	NA	6.94	2.41	1.16×10^{-30}	NA	0.062	178
64-GO	D	0.13	NA	0.326	200	NA	NA	NA	NA	179
64-NGO	D	0.13	NA	0.326	370	NA	NA	NA	NA	179

Sample	Solv	Conc. (g/L)	α (cm^{-1})	I_{oo} (GW/cm^2)	β_{eff} (cm/GW)	$I_m[\chi^{(3)}]$ (esu) x 10^{-11}	γ (esu)	k (σ_T/σ_o)	I_{lim} (J/cm^2)	Ref
65-GO	DF	1.0	6.28	NA	51.2±11.7	1.7±4.03	NA	NA	NA	180
65-GO[a]	DF	1.0	6.83	NA	31.0±6.3	2.1±4.33	NA	NA	NA	180
52+CdTe-TGA QDs	D+H	NA	NA	NA	43.3	15.0	6.55×10^{-30}	NA	0.036	178
66+CdTe-TGA QDs	D+H	NA	NA	NA	109	38.0	23.2×10^{-30}	NA	0.03	178
67+CdTe-TGA QDs	D+H	NA	NA	NA	17.8	6.18	3.31×10^{-30}	NA	0.034	178
68+CdTe-TGA QDs	D+H	NA	NA	NA	96.1	33.4	15.3×10^{-30}	NA	0.03	178
69+CdTe-TGA QDs	D+H	NA	NA	NA	14.2	4.93	1.3×10^{-30}	NA	0.047	178
40+CdTe-TGA QDs	D+H	NA	NA	NA	3.49	1.21	0.514×10^{-30}	NA	0.051	178
70+Ag	LCM	NA	NA	0.51	30	NA	NA	NA	0.101	181
70+Au	LCM	NA	NA	0.51	50	NA	NA	NA	0.082	181
71+GO	D	0.13	NA	0.43	300	NA	NA	NA	1.74	182
71+RGO	D	0.13	NA	0.43	1500	NA	NA	NA	0.98	182

[a] studies at 1064 nm, SWCNT = single-walled carbon nanotubes, GO = graphene oxide, RGO = reduced graphene oxide, NGO = amino-functionalization graphene oxide, TGA = thioglycolic acid, SiMNP = silica coated magnetic nanoparticles, SiNP = silica nanoparticles, QDs = quantum dots, Ag = silver nanoparticles, Au =gold nanoparticles, D+H = DMSO + H_2O, LCM = liquid crystalline matrix, others as stated above.

1.2.2 Iron Oxide Nanoparticles, Fe_3O_4 (Magnetite)

Magnetite are black magnetic mineral containing both divalent (ferrous oxide) and trivalent (ferric oxide) iron species as shown in the simplified chemical reaction for the preparation of magnetite (**Figure 1.10**) [186,187]. Like any other nanoparticles, particle sizes and controllable morphologies are the intriguing features through which the magnetic properties of magnetite can be tuned from ferromagnetic to superparamagnetic properties [188].

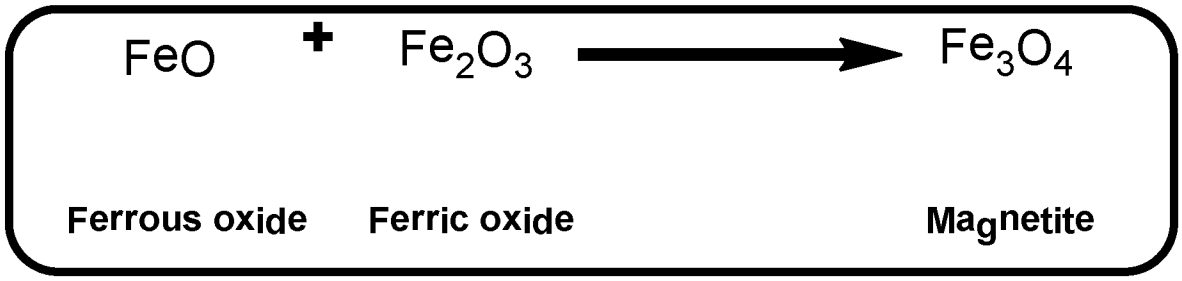

Figure 1.10: Simplified chemical reaction for the preparation of magnetite.

Two-photon absorptions and other nonlinear optical phenomena have been reported for superparamagnetic iron oxide NPs [189-192]. These nonlinear optical responses can be enhanced further when iron oxide NPs are in nano-contact with plasmonic NPs like Au and Ag [185,193]. Bare magnetic nanoparticles are susceptible to aggregation due to their high surface energies. They easily undergo oxidation when exposed to air which could result in loss of dispersibility and magnetism [187]. Hence, coating the nanoparticles with non-magnetic NPs such as Au, Ag etc., is required to reduce the aggregation tendency of bare NPs, improve the stability and enhance the dispersibility of colloidal NPs in common organic solvents [187,194], hence the magnetites were coated with Ag in this thesis.

In this study, iron oxide nanoparticles with average size of 7 ± 2 nm were successfully prepared through polyol method; the resulting NPs were either coated with Ag shells or formed hybrid nanoparticles with Ag domains. Both core-shell and hybrid nanoparticles were functionalized with mercaptopropionic acid (MPA) prior covalent linking to complex **10**. Nonlinear optical characterizations of low symmetry MPcs linked to plasmonic and/or metallic nanoparticles such as Ag or Fe_3O_4 have not been reported before.

1.2.3 Graphene Quantum Dots (GQDTs)

Graphene quantum dots (QDs) are zero dimensional (0D) sp^2-hybrid carbon systems that have attracted tremendous attention for a wide range of applications [195]. In contrast to other carbon based nanostructures, such as graphene (2D), nanotubes (1D), graphene oxides (2D), or graphite (3D), GQDs have lateral dimensions less than 100 nm with enhanced quantum confined electronic state and unique edge effects which confer superior optical and electronic properties on GQDs [195,196]. GQDs with new or improved intrinsic properties can be prepared by selective surface functionalization with heteroatoms such as N and S, **Figure 1.11** [197,198]. N and/or S/N doped GQDs analogues have been found useful in many state-of-the-art technological applications such as photocatalysis, fuel cells and many more [198-200].

Recently, Bourlinos et al [148] reported enhanced optical limiting responses of nitrogeneuos boron doped carbon dots at pico and nanosecond laser excitation conditions. The origin of the OL responses was believed to be similar to that of conventional semiconductor QDs. This is the only optical limiting characterizations of GQDs reported in the literature to date. However, extensive studies on nonlinear optical characterizations of MPcs in the presence of other carbon-based materials have been reported [116,179-182].

Encouraged by the improved NLO responses reported for MPcs in presence of carbon-based nanostructures, photophysical and nonlinear optical characterizations of graphene quantum dots (GQDs), N-doped (N-GQDs) and S, N co-doped graphene (S, N-GQDs) quantum dots conjugated to complex **10** are reported for the first time. It is evident from **Table 1.5** that no MPcs linked to GQDs have been reported before, hence they are studied in this work.

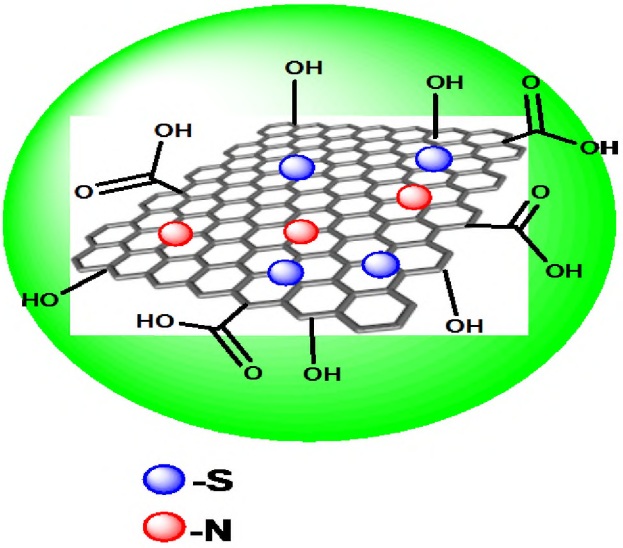

Figure 1.11: Representative of N, S co-doped graphene quantum.

1.3 Nonlinear optics (NLO)

1.3.1 Basics

Optics is an area of research in science which studies the interaction of light with molecular materials [201]. The interactions can be either linear optics (LO), where the properties of the molecular material exhibit linear optical response with increasing input intensity, **Figure 1.12A** [201], or nonlinear optics (NLO), where there is induced nonlinear optical response of the molecular materials to the transmitted optical intensity, **Figure 1.12B** [201]. The latter process, specifically, has led to the development of nonlinear optical materials which can be used to manipulate the phase, polarization, frequency and/or the path of laser fluence for variety of technological applications [90,91,146-148,202].

The first nonlinear optical effects of induced second harmonic generation (SHG) by a Ruby laser in crystal quartz at 347.1 nm was successfully demonstrated in 1961 by Franken et al [203]. The success of this experiment sparked intense research efforts related to the development of optical limiting materials like conjugated organic molecules, polymers and nanomaterials against potentially dangerous laser radiations [88-95]. Optical limiting materials protect optical sensors and human eyes by absorbing potentially harmful high intensity laser radiation and transmit at low intensity below the damage thresholds [90-95].

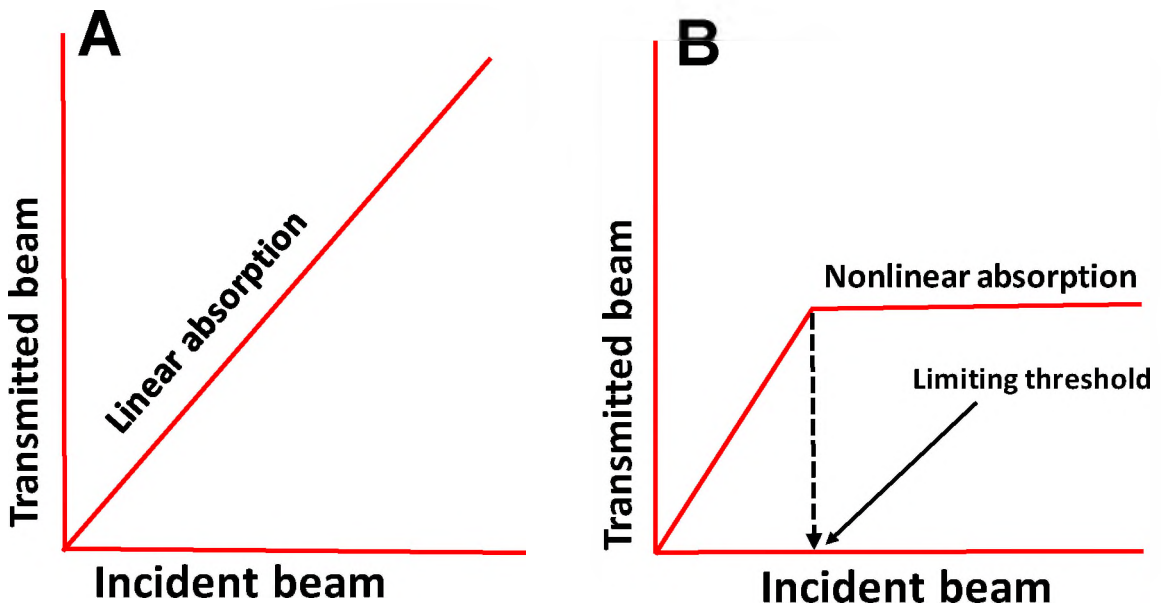

Figure 1.12: Schematic representation showing (A) linear optical transmission for linear optics and (B) nonlinear optical transmission for nonlinear optics.

The primary NLO process which best describes OL behaviour of molecular material for protecting light sensitive material is that which result from nonlinear absorption (NLA) while nonlinear scattering (NLS) and nonlinear refraction (NR) are secondary processes. Hence, only nonlinear absorption parameters and the associated nonlinear absorption coefficients are considered in this report. NLA can give rise to either reverse saturable absorption (RSA), when the absorption coefficient increases as input intensity increases [160,204,205] (**Figure 1.13A**), or saturable absorption (SA), when absorption coefficients of the material decreases with increasing input intensity [160,205] (**Figure 1.13B**). RSA is a multiphoton process that occurs when the excited states absorption cross-sections are larger than the ground state cross sections [90-95]. SA on the other hand is a one-photon absorption process which occurs when the ground states are more populated than the excited cross-section states [160,205].

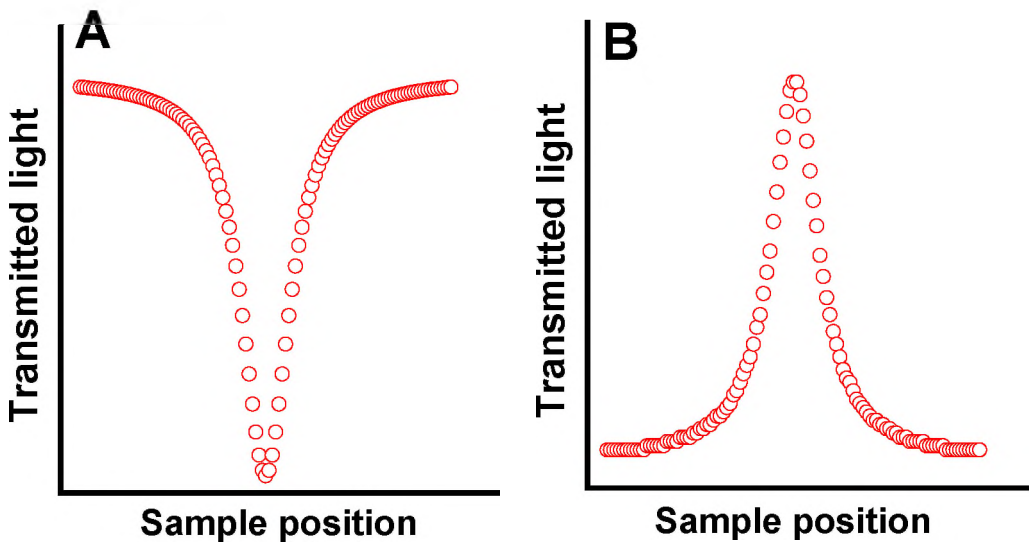

Figure 1.13: Typical open aperture (OA) Z-scans for (A) reverse saturable absorption (RSA) profile and (B) saturable absorption (SA) profile. Unpublished work.

1.3.2 Nonlinear optical (NLO) parameters

Optical limiting characterizations of complexes and composites studied in this thesis were carried out using the open-aperture (OA) Z-scan technique that has been described by Sheik-Bahae and coworkers [206,207]. The basic working principle of the technique involve measuring the transmitted light (transmittance) by the samples due to the passage of the sample under tightly focused Gaussian laser beam. The magnitude of nonlinear interactions (nonlinear absorption coefficients) between the samples and the incident laser irradiance were estimated as function of sample position (z) relative to the focus (z = 0). Transmittance (T(Z)) is related to sample position (z) and nonlinear absorption coefficient β_{eff} by Eq. 1.8:

$$T(Z) = \frac{1}{1+\beta_{eff}L_{eff}(I_{00}/(1+(z/z_0)^2))} \quad (1.8)$$

where I_{00} is the intensity of the light on focus, β_{eff} is the effective nonlinear absorption coefficient, z_0 is the diffraction length of the beam, z is the sample position with respect to input intensity, L_{eff} is the effective length, respectively. L_{eff} in the sample of length L is defined in terms of the linear absorption coefficient, α, in Eq. 1.9:

$$L_{eff} = \frac{1-e^{-\alpha L}}{\alpha} \quad (1.9)$$

A simpler numerical form of **Eq. 1.8** which is well suited to the experimental data directly was employed as shown in **Eq. 1.10**:

$$T(Z) = 0.363e^{\frac{-q(z)}{5.60}} + 0.286e^{\frac{-q(z)}{1.21}} + 0.213e^{\frac{-q(z)}{24.62}} + 0.096e^{\frac{-q(z)}{115.95}} + 0.038e^{\frac{-q(z)}{965.08}} \quad \textbf{(1.10)}$$

where q(z), the dependence of the nonlinear absorption parameter on the normalized transmittance $T(Z)$, is calculated for above equation using **Eq. 1.11**:

$$q(z) = \frac{\beta_{eff} L_{eff} I_{00}}{1+(z/z_0)^2} \quad \textbf{(1.11)}$$

The imaginary part of the third-order susceptibility ($\mathrm{I_m}[\chi^{(3)}]$) is related to the nonlinear absorption coefficient, β_{eff}, and can be calculated using **Eq. 1.12** [208]:

$$\mathrm{I_m}[\chi^{(3)}] = n^2 \varepsilon_0 c^2 \lambda \beta_{eff} / 4\pi^2 \quad \textbf{(1.12)}$$

where, n and c are the linear refractive index (n = 1.479 for DMSO), and speed of light respectively. ε_0 is the permittivity of free space and λ is the wavelength of the laser.
The relationship between second order hyperpolarizability (γ) and imaginary third-order susceptibility ($I_m[\chi^{(3)}]$) of the samples is expressed in equation **Eq. 1.13** [208]:

$$\gamma = \frac{\mathrm{I_m}[\chi^{(3)}]}{f^4 C_{\mathrm{mol}} N_A} \quad \textbf{(1.13)}$$

where C_{mol} is the molar concentration of the active species in the triplet state, f is the Lorentz local field enhancement factor defined as $f = (n^2 + 2)/3$; n is the refractive index of the sample and N_A is the Avogadro constant.

The oscillating free electrons on the surface of metallic plasmonic NPs like AuNPs are known to generate free carriers around 500-550 nm, corresponding to the localized SPR bands of AuNPs. Hence possible interference due to strong absorption of MPc-NPs composites at the region of the excitation laser wavelengths are expected. The free carrier absorption (FCA) mechanisms contributing to OL of MPc-AuNPs conjugates are estimated using, (**Eq. (1.14)**) [209]:

$$\mathrm{T(z)} = F_o(F_c/F_o)In(1 + F_o/F_c) \quad \textbf{(1.14)}$$

where: $F_c = \frac{4\mathrm{h}\pi\nu}{\sigma_{FCA}\,(1 - To)}$

where T_o and F_c are the linear transmission and incident fluence, respectively, $\hbar = \mathrm{h}/2\pi$(where h is the Planck's constant), ν is the frequency of the laser, and σ_{FCA} is the FCA cross-section.

1.4 Summary of aims of thesis

1. Synthesis of peripherally tetra-substituted alkynyl terminated indium phthalocyanines (complexes **1** and **2**); the effects of the carbon chain length of the substituents on the photophysical and nonlinear optical behaviour of the complexes were described.

2. Comparative studies of the photophysical, spectroscopic and nonlinear optical characterizations of tetraakynyl ZnPc and when "clicked" to nitrophenyl azide (complexes **3** and **4**).

3. Nonlinear optical characterizations and optical limiting properties of complexes **5**, **6** and **7** are investigated in solution ($CHCl_3$) and when doped on poly (bisphenol A carbonate) (PBC) thin films.

4. Synthesis, Spectroscopic, photophysical and NLO studies of complexes **8** and **9** in solution and when embedded in polysulfone (PSU) as thin films: effects of aggregation were investigated in THF and DMSO.

5. Spectroscopic, photophysical and NLO studies of synthesized asymmetric ZnPc (complex **10**) when:

i. covalently linked to gold nanoparticles (AuNPs) and polyacrylic acid (PAA). The composites were also blended in PAA and results compared to those in solution.

ii. covalently linked to Fe_3O_4@Ag core-shell, Fe_3O_4-Ag hybrids nanoparticles studied in DMSO.

iii. covalently linked to graphene quantum dots (GQDs), N-doped (N-GQDs) and S, N co-doped graphene (S, N-GQDs) quantum dots; studies were carried out in DMSO.

6. Synthesis, spectroscopic, photophysical and NLO characterizations of diaminopyrimidin-2-ylthio tetra-substituted Zn(II) phthalocyanine (complex **11**) conjugated to Ag_xAu_y nano-alloys.

7. Spectroscopic, photophysical and optical limiting comparative studies of complexes **2** and **3** conjugated to azide-derivatized gold nanoparticles (AuNPs) via Huisgen cycloaddition "click" reactions. The studies were carried out in DMSO.

CHAPTER 2
EXPERIMENTAL SECTION

2.1 Materials

2.1.1 Solvents

The following solvents were supplied by Merck: Ethanol, acetone, methanol, toluene, n-hexane, dichloromethane (DCM), chloroform, diethylether, N, N-dimethyl formamide (DMF) and dimethyl sulphoxide (DMSO). Deuterated dimethyl sulphoxide (DMSO-d_6) and chloroform ($CDCl_3$) were supplied by SAARCHEM. Sigma Aldrich supplied spectroscopic dimethyl sulfoxide (DMSO), tetrahydrofuran (THF) and chloroform for photophysical characterizations. Ultra-pure water was obtained from Milli-Q water system (Millipore Corp., Bedford, MA, USA).

2.1.2 Nanomaterials, polymers and their conjugation to MPcs

Gold (III) chloride trihydrate (99.9%), silver acetate ($Ag(ac)_3$; 99.99%), oleic acid (OA), oleylamine (technical grade), diphenyl ether (99%), tetraoctylammonium bromide (TOABr), 3-mercaptopropionic acid (MPA), 1,2-dodecanediol, tert-butanol, citric acid, sodium hydroxide (NaOH), thiourea, urea, poly(bisphenol A carbonate) (PBC) (Mw ~45,000 by GPC), Poly acrylic acid (PAA) (Mw ~450,000 by GPC), N,N'-dicyclohexylcarbodiimide (DCC), polysulfone (PSU) (Mw ~35,000 g/mol by GPC), and tetramethylammonium hydroxide (TMAOH) were purchased from Sigma–Aldrich. N-hydroxysuccinimide (NHS) and N-(3-dimethylaminopropyl)-N-ethylcarbodiimide hydrochloride (EDC) were from Fluka. 4-dimethylaminopyridine (DMAP) was obtained from SAARCHEM. 4-Nitrophthalonitrile (**1a, Scheme 3.1**) from Sigma Aldrich.

2.1.3 Phthalocyanines syntheses and precursors

5-Hexyn-1-ol, 5-methylhex-1-yn-3-ol, n-pentanol, 2-dimethylaminoethanol (DMAE), n-hexanol, anhydrous potassium carbonate, 1,8-diazabicyclo[5.4.0]undec-7-ene (DBU), lithium metal, copper sulfate pentahydrate, sodium ascorbate (NaAsc), Zn (II) acetate, zinc phthalocyanine (ZnPc), and indium (III) chloride were all obtained from Sigma Aldrich. Hydrochloric acid, silica gel for column chromatography and glacial acetic acid were purchased from Merck or SAARCHEM.

2.2 Instrumentation and methods

- Ground state electronic absorption spectra for the samples either in solution or as thin films were recorded on a Shimadzu UV-2550 UV/Vis spectrophotometer.
- Infra-red spectra were collected on a Perkin-Elmer or Bruker ALPHA FT-IR Spectrometer with Universal ATR Sampling accessory spectrum 100 FT-IR spectrometer.
- ^{1}H-NMR spectra were analysed using either a Bruker AMX400 MHz NMR or a Bruker AVANCE II 600 MHz spectrometer in deuterated ($CDCl_3$ or DMSO-d_6) Solvents.
- Elemental analyses were done using a Vario-Elementar Microcube ELIII.
- Mass spectra data were collected on a Bruker AutoFLEX III Smart-beam TOF/TOF mass spectrometer using α-cyano-4-hydrocinnamic acid as the matrix in the positive ion mode.
- Fluorescence emission spectra were recorded on a Varian Eclipse spectrofluorimeter.
- Time Correlated Single Photon Counting (TCSPC) setup (FluoTime 200, Picoquant GmbH) was used for the fluorescence decay studies. The excitation source was a diode laser (LDH-P-670 driven by PDL 800-B, 670 nm (or 485 nm for quantum dots), 20 MHz repetition rate, 44 ps pulse width, Picoquant GmbH), **Figure 2.1**. A monochromator with a spectral width of about 4 nm was used to select the required measured emission wavelength. The response function of the system, which was measured with a scattering Ludox solution (DuPont), had a full width at half-maximum (FWHM) of about 300 ns. The ratio of stop to start pulses was kept low (below 0.05) to ensure good statistics. All luminescence decay curves were measured at the maxima of the emission peak. The data were analysed with the program FluoFit (Picoquant GmbH).
- Energy dispersive X-ray spectroscopy (EDS) was done on an INCA PENTA FET coupled to the VAGA TESCAM using 20 kV accelerating voltage.

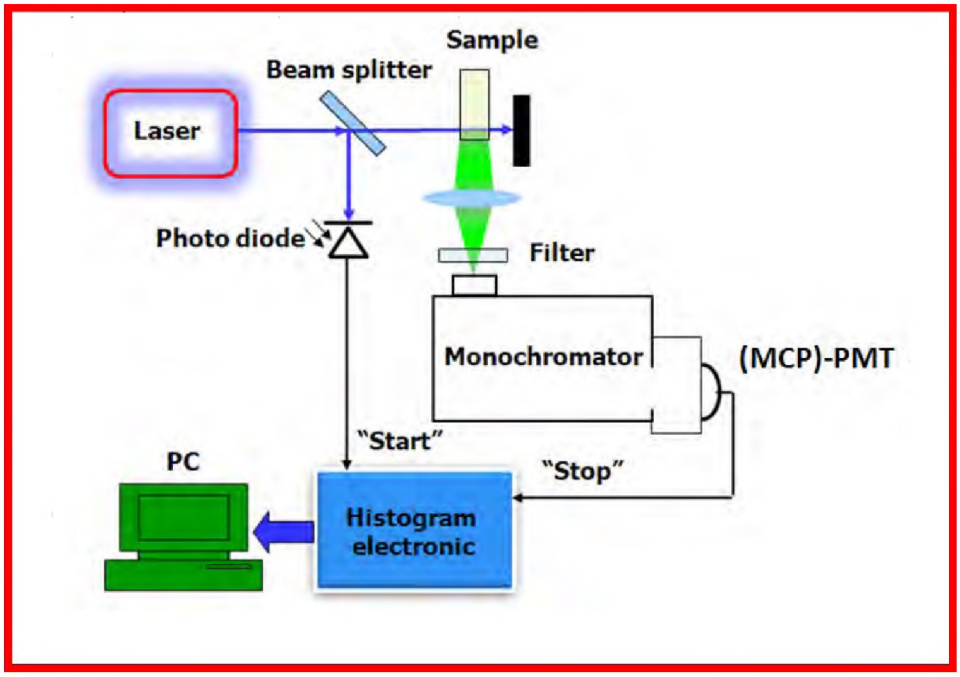

Figure 2.1: Schematic diagram of time-correlated single photon counting (TCSPC) setup. (MCP)-PMT = (Multi channel plate detector)-Photomultiplier tube, PC = Personal computer.

- Transmission electron microscope (TEM) images were obtained using a JEOL TEM 1210 transmission electron microscope at 100 kV accelerating voltage. TEM samples were prepared by placing a drop of conjugates or nanoparticle solution on the sample grid and allowing it to dry before measurements.
- Laser flash photolysis (nanosecond absorption spectroscopy) experiments, **Figure 2.2**, were performed with light pulses produced by a Quanta-Ray Nd:YAG laser providing 400 mJ, 9 ns pulses of laser light at 10 Hz, pumping a Lambda-Physik FL3002 dye laser (Pyridin 1 dye in methanol). Single pulse energy ranged from 2 to 7 mJ. The analysing beam source was from a Thermo Oriel Xenon arc lamp, and photomultiplier tube (a Kratos Lis Projekte MLIS-X3) was used as a detector. Signals were recorded with a two-channel 300 MHz digital real time oscilloscope (Tektronix TDS 3032C); the kinetic curves were averaged over 256 laser pulses.

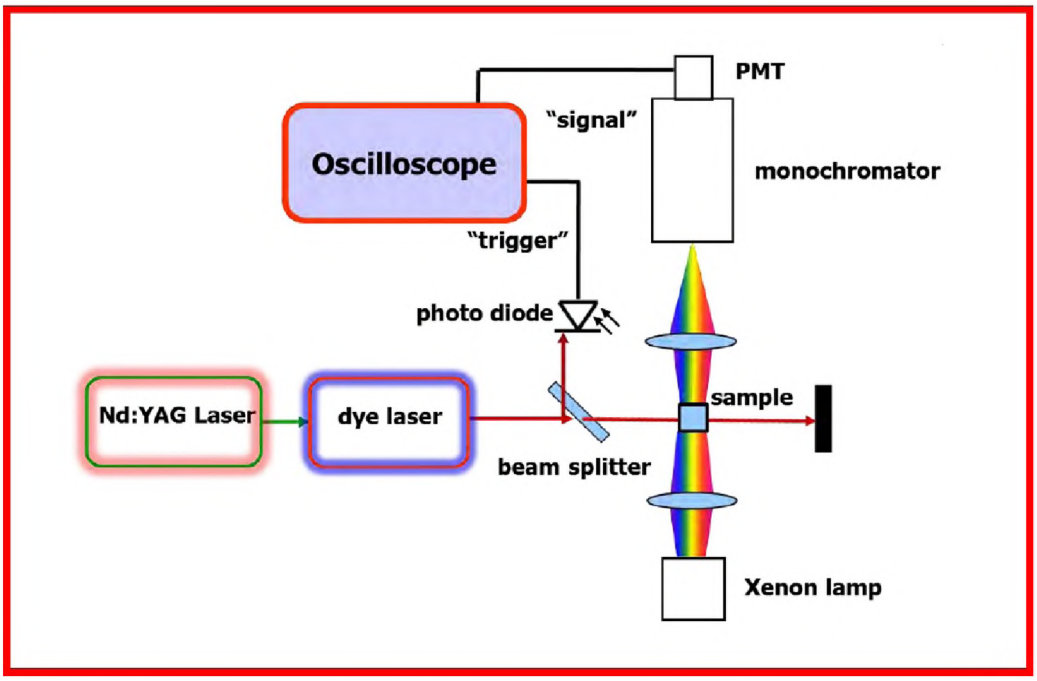

Figure 2.2: Schematic representation for laser flash photolysis setup. PMT = Photomultiplier.

- X-ray powder diffraction patterns were recorded on a Bruker D8 Discover equipped with a LynxEye detector, using CuKα radiation (λ = 1.5405 Å, nickel filter). Data were collected in the range from 2θ = 5° to 100°, scanning at 1° min^{-1} with a filter time-constant of 2.5 s per step and a slit width of 6.0 mm. Samples were placed on a zero background silicon wafer slide. The X-ray diffraction data were treated using Eva (evaluation curve fitting) software. Baseline correction was performed on each diffraction pattern.
- X-ray photoelectron spectroscopy (XPS) analysis was done using an AXIS Ultra DLD, with Al (monochromatic) anode equipped with a charge neutraliser, supplied by Kratos Analytical. The following parameters were used: the emission was 10 mA, the anode (HT) was 15 kV and the operating pressure below 5 x 10^{-9} torr. A hybrid lens was used and resolution to acquire scans was at 160 eV pass energy in slot mode. The centre used for the scans was at 520 eV with a width of 1205 eV, with steps at 1 eV and dwell time at 100 ms as reported before [210]. The high resolution scans were acquires using 80 eV pass energy in slot mode.
- All Z-scan analyses were performed using a frequency-doubled Nd:YAG laser (Quanta-Ray, 1.5 J/10 ns fwhm pulse duration) as the excitation source. The laser was operated in a near Gaussian transverse mode at 532 nm (second harmonic),

with a pulse repetition rate of 10 Hz and energy range of 0.1 μJ – 0.1 mJ, as limited by the energy detectors (Coherent J5-09). The low repetition rate of the laser prevents cumulative thermal nonlinearities. The beam was spatially filtered to remove the higher order modes and tightly focused with a 15 cm focal length lens. The Z-scan system size (l × w × h) used was 600 mm × 300 mm × 350 mm (excluding the computer, energy meter, translation stage driver and laser system). The liquid samples were placed in a cuvette (internal dimensions: 2 mm × 10 mm × 55 mm, 0.7 mL) and a path length of 2 mm (Starna 21-G-2).

- Thin-films of MPc-polymer composites were measured using knife edge attachment of the Bruker D8 Discover X-ray diffraction (XRD).

2.3 Synthesis

2.3.1 Synthesis of phthalonitriles

Substituted phthalonitriles such as 4-(2-propynyloxy)-phthalonitrile (**1b(ii)**, **Scheme 3.1**) [102], 4-(2-mercaptopyridine) phthalonitrile (**7a, Scheme 3.4**) [211], and 4-(4-6-Diaminopyrimidin-2-ylthio) phthalonitrile (**11a, Scheme 3.5**) [212] were synthesized and purified as outlined by previous reports.

2.3.1.1 4-hexy-5-ynyloxy-phthalonitrile, 1b(i) (Scheme 3.1)

Nitrophthalonitrile (**1a**, 2g, 11.5 mmol) and 5-hexyn-1-ol (**1b(i)**, 1.69g, 11.5 mmol) were dissolved in dry DMSO (20 ml) and stirred for 10 min; finely ground anhydrous K_2CO_3 (2.16 g, 15.56 mmol) was added in portions over 2 h and stirred at 40 °C for 48 h under nitrogen. Then product was poured into 300 ml of cold water. The precipitate was filtered off and washed with water, until the filterate was neutral. The recrystalization from hexane and methanol gives the desired compound as a yellow crystalline powder. Yield: 1.74 g (60%). IR (KBr*)* ν_{max}/cm^{-1}: 3281.88 (≡ C-H); 2228.24 (CN); 2221.56 (C≡C); 1557.31, 1488.16 (C=C phenyl); 1287.31 (Ar-O-C); 1307.74, 1250.93, 1002.56, 839.99, 660.14 . Anal. Calcd for $C_{14}H_{12}N_2O$: C 74.98 , H 5.39, N 12.49%; found: C 73.66, H 5.522, N 12.88%. ^{1}H NMR (600 MHz, DMSO-d_6): δ, ppm: 8.02 (Ar-H,s, 1H), 7.75 (Ar-H,d, 1H), 7.43 (Ar-H,d, 1H), 4.15 (CH_2-O-, t, 2H), 2.77 (C≡CH, s, 1H), 2.22 (CH_2, t, 2H), 1.81 (CH_2, m, 2H), 1.58 (CH_2, m, 2H).

2.3.1.2 5-Methylhex-1-yn-3-yloxy phthalonitrile (8b) (Scheme 3.2)

A mixture of 4-nitrophthalonitrile (**1a**, 1.00 g, 5.77 mmol) and 5-methylhex-1-yn-3-ol (**8a,** 0.65 g, 5.77 mmol) was stirred at 50 °C in DMF (15 mL) under nitrogen for 15 min. While still under continuous and efficient stirring, finely ground anhydrous K_2CO_3 (1.60 g, 11.59 mmol) was added portion-wise during a 2 h period at room temperature, after which, the reaction mixture was heated again to 50 °C and was allowed to stand for further 36 h at this temperature. The crude product was cooled to room temperature, poured into ice water (150 mL) and extracted with DCM. The organic phase was washed several times with water, and the solvent evaporated under reduced pressure to afford compound **8b** (yellow viscous liquid). Yield: 0.60 g (44%). FT-IR (ATR): ν (cm^{-1}): 3292 (H-C≡C-), 3084-3050 (CH, aromatic), 2959-2872 (CH, aliphatic), 2232 (C≡N), 2119 (C≡C). ^1H NMR (400 MHz, $CDCl_3$), δ (ppm): 0.98 (d, J= 3 Hz, 6H, CH_3), 1.84 (m, J= 3 Hz, 2H, CH_2), 1.96 (m, J= 3 Hz, 1H, CH), 2.60 (d, J = 2 Hz, 1H, C≡CH), 4.82 (dt, J = 2 Hz, J = 3 Hz, 1H, CH), 7.31 (dd, J = 3 Hz, J = 6 Hz, 1H, Ar-H), 7.39 (d, J = 3 Hz, 1H, Ar-H), 7.73 (d, J = 6 Hz, 1 H, Ar-H). ^{13}C NMR (400 MHz, $CDCl_3$), δ (ppm): 22.6, 24.8, 44.1, 67.7, 76.9, 77.3, 80.0, 108.0, 115.4, 115.8, 117.5, 120.6, 120.8, 135.2, 160.7. MS, m/z: calcd 238; found 238 $[M]^+$. Anal. for $C_{15}H_{14}N_2O$ %: calcd C 75.61, H 5.92, N 11.76; found C 74.51, H 5.72, N 12.20.

2.3.1.3 4-Nitro-1-benzyl-4-(3,4-dicyanophenoxymethyl)-1H-1,2,3-triazole (4b) (Scheme 3.3)

4-Nitrophenyl azide (**4a**) was synthesized following a procedure reported by Pagoti et al. [213]. A mixture of 4-(2-propynyloxy)-phthalonitrile (**1b(ii)**, 131.6 mg, 0.72 mmol), 4-nitrophenyl azide (**4a**, 130.0 mg, 0.792 mmol), $CuSO_4.5H_2O$ (14.3 mg, 0.072 mmol, 0.1eq) and sodium ascorbate (8.9 mg, 0.036 mmol, 0.05 eq) in 10 mL of THF/H_2O (1:1) was stirred at room temperature for 48 h under Ar, then poured into 100 mL of cold water. The precipitate was filtered off and washed with water, until the filtrate was neutral. The crude residue was crystallized from THF-methanol (1:1) to give the desired product **4b** as brown powder. Yield: 79%. IR (KBr*)* ν_{max}/cm^{-1}: 3155.53 (triazole N_3); 2232.36 (CN); 1525.98 (As-NO_2); 1593.15, 1503.63 (C=C phenyl); 1341.44 (Sym-NO_2); 1316.49 (Ar-O-C); 1305.94, 1255.95, 1010.76, 828.96, 669.64. Anal. Calcd for $C_{17}H_{10}N_6O_3$: C 58.96, H 2.91, N 24.27%; found: C58.77, H 3.61, N 24.13%. ^1H NMR

(600 MH z, DMSO-d_6): δ, ppm: 9.21 (s, 1H, $H_{triazole}$), 8.25 (Ar-H, d, 2H), 8.25 (Ar-H, d, 2H), 8.12 (Ar-H, d, 1H), 7.95 (Ar-H, d, 1H), 7.62 (Ar-H, dd, 1H), 5.50 (CH_2-O-, t, 2H).

2.3.2 Syntheses of phthalocyanines

The syntheses of zinc centred phthalocyanine complexes **3**, **5** and **10**, and ClInPc (**6**) have been reported [102,214-218].

2.3.2.1 Hex-5-ynoxy phthalocyanine indium (III) chloride (1, Scheme 3.1)

A mixture of 4-hexy-5-ynyloxy-phthalonitrile (**1b(i)**, 0.25g, 1.11 mmol), indium (III) chloride (0.246 g, 1.11 mmol) and few drops of catalytic DBU in n-pentanol (1.5 mL) was stirred under reflux at 140 °C for 20 h under argon atmosphere. The crude dark blue product (**1**) was cooled to room temperture and washed with methanol, ethanol, acetone, 1 M HCl and acetone in succession. Column chromatography on silica gel as stationary phase and THF:methanol as eluent was used for final purification. The blue-green indium phthalocyanine obtained was thereafter concentrated and dried.

Yield: 64.55 %, UV-Vis (DMSO): λ_{max}/nm: 699, 629, 358 . FT-IR [KBr disc (ν_{max}/cm-1)]: 3284.87 (C-H); 2934.29 (CH aliphatic); 3088.56 (Ar-H); 2221.56 (C≡C); 1227.75, 1117.90, 1081.06, 1045.03 (C-O-C), 966.22, 824.45, 740.93, 650 (Pc-Skeleton). Anal. Calc. for $C_{56}H_{52}N_8O_4InCl.H_2O$: C 63.31, H 4.70, N 10.52; Found: C 63.26, H 4.91 N 10.68. MS (MALDI-TOF) m/z: Calcd. 1046.36; Found: 1049.22 $[M+3H]^+$. ^{1}H NMR (600 MH z, DMSO-d_6): δ, ppm: 8.53 (Ar-H, d, 4H), 7.62 (Ar-H, s, 4H), 7.18 (Ar-H, dd, 4H), 4.09 (CH_2-O-, t, 8H), 2.11 (C≡CH, s, 4H), 1.75 (CH_2, m, 8H), 1.48 (CH_2, m, 8H), 1.09 (CH_2, t, 8H).

2.3.2.2 Prop-2-ynoxy phthalocyanine indium(III) chloride (2, Scheme 3.1)

The synthesis and purification of complex **2** was similar as outlined for complex **1** except that 4-propy-2-ynyloxy-phthalonitrile (**1b(ii)**, 0.3g, 1.64 mmol) was employed instead of 4-hexy-5-ynyloxy-phthalonitrile (**1b(ii)**. Complex **2** yield: (75%). UV-Vis (DMSO): λ_{max}/nm (log ε): 693 (5.01), 625 (4.35), 360 (4.75). FT-IR [KBr disc (ν_{max}/cm^{-1})]: 3286 (≡C-H); 2929 (CH aliphatic); 3077 (Ar-H); 2161 (C≡C); 1604 (Ar C-C), 1280, 1215, 1084, 1011 (C-O-C), 939, 825, 742, (Pc-Skeleton). Anal. Calc. for $C_{44}H_{24}N_8O_4InCl$: C 60.12, H 2.75, N 12.75%; Found: C 60.01, H 2.74, N 12.01. MS (MALDI-TOF) m/z: Calcd.

878.86; Found: 879.36 $[M+H]^+$. ^1H NMR (600 MH z, DMSO-d_6): δ, ppm: 8.44 (Ar-H, d, 4H), 7.78 (Ar-H, s, 4H), 7.36 (Ar-H, dd, 4H), 4.45 (CH_2-O-, t, 8H), 2.70 (C≡CH, s, 4H).

2.3.2.3 5-Methylhex-1-yn-3-yloxy phthalocyanine zinc (II) (9, Scheme 3.2)

A mixture of 4-(5-methylhex-1-yn-3-yloxy) phthalonitrile (**8b**, 200 mg, 0.84 mmol), excess zinc (II) acetate (160 mg, 0.87 mmol), DBU (0.25 mL) and n-pentanol (2 mL) were refluxed under nitrogen atmosphere at 140 °C for 6 h. The crude product was washed in MeOH before the final purification on a silical gel stationary phase, using THF as eluent. The pure compound **9** was obtained as shining green solid.

2.3.2.4 5-methylhex-1-yn-3-yloxy phthalocyanine (8, Scheme 3.2)

The synthesis and purification of compounds **9** and **8** were similar, except that **8** required no metal salt instead of excess zinc acetate used in **9**.

Complex **8** yield: 70 mg (35%). UV-vis, λ_{max}/nm(log ε): (THF) 704 (5.21), 668 (5.18), 646 (4.92), 610 (4.74), 334 (4.85). IR (ATR): ν (cm^{-1}): 3644 (N-H), 3286 (H-C≡C-), 3070 (CH, aromatic), 2955-2870 (CH, aliphatic), 2114 (C≡C). ^1H NMR (400 MHz, $CDCl_3$), δ (ppm): 1.44 (d, 24H, CH_3), 1.54 (t, J = 3 Hz, 8H, CH_2), 1.75 (m, J = 3 Hz, 4H, CH), 2.27 (s, 4H, C≡CH), 5.0 (t, J = 3 Hz, 4H, CH), 6.98-7.70 (m, 12H, Ar-H). MS, m/z: calcd. 955; found 955 $[M]^+$. Anal. for $C_{60}H_{58}N_8O_4$ %: calcd C, 75.45; H, 6.12; N, 11.73; found C, 74.92; H, 5.45; N, 12.15.

Complex **9** yield: 90 mg (42%). UV-vis, λ_{max}/nm (log ε): (DMSO) 687 (4.99), 616 (4.30), 322 (4.83); (THF) 680 (5.00), 616 (4.25), 352 (4.70). IR (ATR): ν (cm-1): 3285 (H-C≡C-), 3070 (CH, aromatic), 2955-2870 (C-H, aliphatic), 2114 (C≡C). ^1H NMR (400 MHz, $CDCl_3$), δ (ppm): 1.25 (d, 24H, CH_3), 1.50 (t, J = 3 Hz, 8H, CH_2), 1.72 (m, J = 3 Hz, 4H, CH), 2.15 (s, 4 H, C≡CH), 4.96 (t, J = 3 Hz, 4H, CH), 7.15-7.76 (m, 12H, Ar-H). MS, m/z: calcd. 1016; found 1016 $[M]^+$. Anal. for $C_{60}H_{56}N_8O_4Zn$ %: calcd C, 70.74; H, 5.54; N, 11.00; found C, 69.90; H, 6.49; N, 10.95.

2.3.2.5 4-Nitro-1-benzyl-4-(3,4-dicyano phenoxy methyl)-1H-1,2,3-triazole ZnPc (4, Scheme 3.3)

A mixture of 4-nitro-1-benzyl-4-(3,4-dicyanophenoxymethyl)-1H-1,2,3-triazole (**4b**, 0.065 g, 0.187 mmol) and $Zn(CH_3COO)_2$ (0.011 g, 0.052 mmole) in DMAE (5 mL) was heated to 180 °C for 18 h under nitrogen. The dark green coloured product was cooled to room temperature and washed with methanol and ethanol. The residue was further purified by Soxhlet extraction using methanol-water (1:1) for 72 h. The blue-green zinc phthalocyanine obtained was thereafter concentrated, dried and ground. Yield: (75%). UV-Vis (DMSO): λ_{max}/nm (log ε): 683, 625, 360.50. FT-IR [KBr disc (ν_{max}/cm^{-1})]: 3096.53 (triazole N_3); 2931.83 (CH aliphatic); 3076.86 (Ar-H); 1525.98 (As-NO_2); 1593.15, 1503.63 (C=C phenyl); 1341.44 (Sym-NO_2); 1316.49 (Ar-O-C); 1279.87, 1214.91, 1083.84, 1011.45 (C-O-C), 939.47, 825.16, 741.93, 85 (Pc-Skeleton). Anal. Calcd for $C_{68}H_{40}N_{24}O_{12}Zn$: C 56.30, H 2.78, N 23.17%; found: C55.90, H 2.54, N 23.95%. MS (MALDI-TOF) m/z: Calcd. 1450.6; Found: 1453.56 $[M+ 3H]^+$. ^{1}H NMR (600 MH z, DMSO-d_6): δ, ppm: 9.38 (s, 4H, $H_{triazole}$), 8.41 (Ar-H, d, 8H), 8.35 (Ar-H, d, 8H), 8.62 (Ar-H, d, 4H), 8.2 (Ar-H, d, 4H), 7.70 (Ar-H, dd, 4H), 5.82 (CH_2-O-, t, 8H).

2.3.2.6 4-(2-Mercaptopyridine) phthalocyanine (7, Scheme 3.4)

4-(2-Mercaptopyridine) phthalonitrile (**7a**, 2.0 g, 8.44 mmol) and lithium metal (3.80 g, 54.7 mmol) were suspended in 20 mL of dry n-pentanol and heated at 140 °C in a sealed glass tube for 5 h under a nitrogen atmosphere. The crude product was heated under reflux with glacial acetic acid (50 mL) at 100 °C for 2 h. On cooling to room temperature, the product was precipitated with methanol and washed several times with distilled water and dried under vacuum. The solid residue was purified on a silica gel column chromatography with chloroform/methanol (9:1) solvent system as eluent to afford metal-free phthalocyanines (**7**). Yield: 51%. UV/Vis ($CHCl_3$): λ_{max}/nm (log ε): 705 (4.97), 671 (4.96), 649 (4.70), 615 (4.52), 342 (4.81). MS (MALDI-TOF) m/z: Calcd: 950.2; Found: 950.5 $[M]^+$. FT-IR ν_{max}/cm^{-1}: 3286 (N–H, stretch), 3040 (Ar–H), 1602 (NH, bend), 1557 (C=N), 1571 (C=C), 1007, 695 (C-S-C). Anal. Calcd for $C_{52}H_{30}N_{12}S_4$: %C 65.66, %H 3.18, %N 17.67, %S 13.48; found: %C 65.40, %H 3.21, %N 17.20, %S 13.20.^{1}H NMR (600 MHz, $CDCl_3$) δ, ppm: 9.20–7.92 (pyridyl-H, 16H, m), 8.64 (Pc-H, 4H, m), 7.78-7.50 (Pc-H, 8H, m).

2.3.2.7 4-(4,6-Diaminopyrimidin-2-ylthio) Zn (II) phthalocyanine (11, scheme 3.5)

A mixture of 4-(4-6-diaminopyrimidin-2-ylthio) phthalonitrile (**11a**, 1.0 g, 1.467 mmol), $Zn(CH_3COO)_2$ (0.081 g, 0.368 mmol) and 0.3 mL of catalytic DBU in n-hexanol (5 mL) was refluxed under nitrogen for 6 h. The reaction mixture was cooled to room temperature. The product was precipitated with methanol and subsequently washed with methanol and acetone. The crude green product was subjected to silica gel column chromatography and eluted with diethyl ether/DMF (5:1) as eluents, to isolate the required product **11**. Yield: (48%). UV-Vis (DMSO): λ_{max}/nm (log ε): 689 (5.21), 622 (4.51), 356 (4.91). FT-IR [KBr disc (ν_{max}/cm^{-1})]: 3320, 3189 (N−H str.), 2929 (C−H aromatic), 1613, 1572 1572 (N−H bend), 1348 (C−N aryl). Anal. Calc. for $C_{48}H_{32}N_{24}S_4Zn$: C 50.63, H 2.83, N 29.52, S 11.26%; Found: C 50.05, H 3.75, N 28.96, S 11.25. MS (MALDI-TOF) m/z: Calcd. 1138.1; Found: 1141.82 [M+ 3H]$^+$. ^{1}H NMR (400 MH z, DMSO-d_6): δ, ppm: 5.20 (s, 16H, NH), 8.97 (s, 4H, pyrimidinyl-H), 7.77–7.89 (m, 12H, Ar-H).

2.3.3 Preparation of nanomaterials

2.3.3.1 MPA capped AuNPs

Tetraoctylammonium bromide (TOABr) stabilized AuNPs was prepared according to known procedure [219]. The synthesis of MPA-capped AuNPs was adapted from a previously reported procedure for glutathione (GSH)-capped AuNPs [220]. Briefly, 2.87 μL of MPA in 15 mL of degassed ethanol:water (1:1) solution was added to 15 mL of TOABr-stabilized AuNPs in toluene. The mixture was vigorously stirred under N_2 atmosphere for 24 h to allow ligand exchange to take place. The dark brown water soluble MPA-capped AuNPs was precipitated and washed with ethanol. Finally, about 70 mg product was obtained after drying at room temperature.

2.3.3.2 Synthesis of azide-derivatized gold nanoparticles

The synthesis of 3-azido-1-propylamine has been reported before [221]. A mixture of concentrated toluene (4.5 mL) solution of as-synthesized TOABr-AuNPs and 459 mg (4.6 mmol) of azidopropanamine were stirred in an air-tight vial under argon atmosphere overnight to allow ligand exchange between TOABr and azidopropanamine to take place. At the completion of the reaction, the solvent was removed by rotary evaporator,

centrifuged once (15, 000 rpm, 10 min) in absolute ethanol; and dispersed in minimum amount of toluene for further use in click reactions. Yield: 63 mg.IR (KBr) ν_{max}/cm^{-1}: 2102 (As-N_3); 2926, 2857 (alkyl chains).

2.3.3.3 Synthesis of Ag_xAu_y alloy nanoparticles

Figure 2.3 shows the typical preparation of Ag_xAu_y alloy nanoparticles. The synthesis and purification of the Ag_xAu_y nano-alloys at different mole ratios were similar, and followed the method reported by Liu et al [222] with slight modification. In a typical reaction, 0.3 mmol of silver acetate and $HAuCl_4 \cdot 3H_2O$ mixture at 3:1 (Ag_3Au_1) and 1:3 (Ag_1Au_3) ratios were separately added to 100 mL round bottom flask containing 20 mL diphenyl ether, 4 mL oleylamine and 2 mL oleic acid. Each mixture was refluxed at 150 °C for 5 h under argon atmosphere. The reaction mixture was cooled to room temperature, washed several times with dry ethanol, dried at room temperature under vacuum, and dried re-dispersed in hexane.

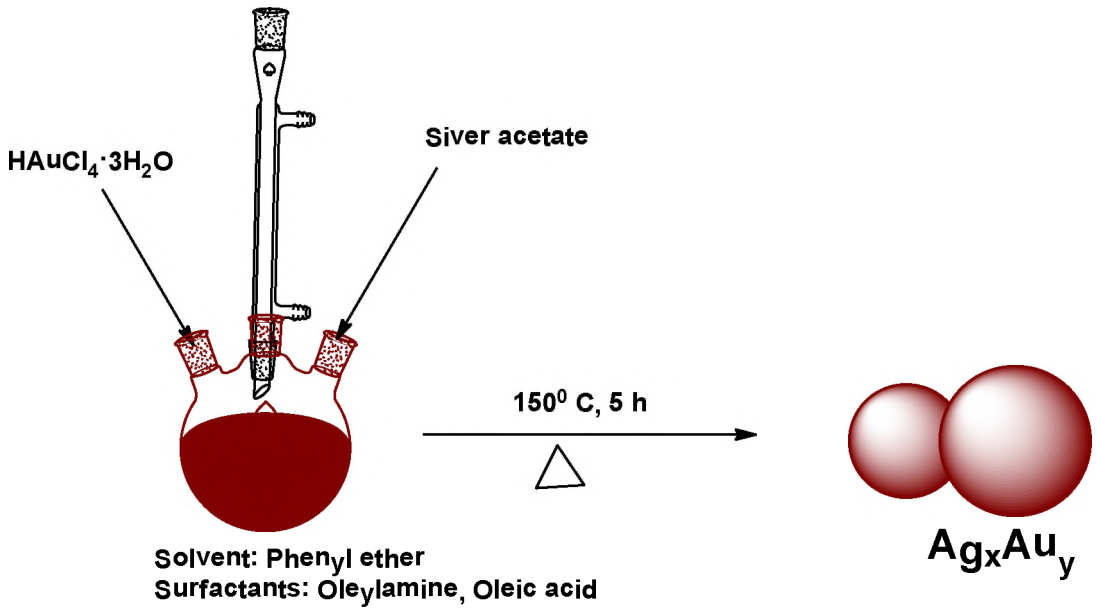

Figure 2.3: Typical synthetic pathway for preparation of Ag_xAu_y alloy nanoparticles. The subscripts x and y are the mole ratios of the precursors.

2.3.3.4 Preparation of MPA capped Fe_3O_4@Ag Core-Shell NPs

Fe_3O_4@Ag core-shell NPs was prepared following similar procedure reported for Fe_3O_4@Au core-shell NPs but with silver acetate as precursor for AgNPs [223]. Briefly, as-prepared Fe_3O_4 NPs (0.33 mmol) [223] dispersed in phenyl ether (10 mL) solution,

$Ag(ac)_3$ (367 g, 2.2 mmol), oleic acid (1 mL) and oleylamine (4 mL) were added to diphenyl ether (20 mL). The solution was refluxed to ~200 °C under nitrogen atmosphere for 2 h. After cooling to room temperature, the crude product (Fe_3O_4@Ag NPs) was precipitated with ethanol, washed several times with ethanol and magnetically decanted. The pure Fe_3O_4@Ag NPs were dried under vacuum, and re-dispersed in toluene. MPA capped Fe_3O_4@Ag NPs were prepared following similar procedures in literature [224] with some modifications. Briefly, as-synthesized Fe_3O_4@Ag NPs were first precipitated from a mixture of toluene (5 mL) and 30 mL absolute ethanol three times and re-dispersed in solution of TMAOH (0.5 M). MPA (400 μL) in 2 mL degassed H_2O was added to the NPs solution and sonicated for 15 min for ligand exchange to take place. Water soluble MPA-capped Fe_3O_4@Ag NPs were precipitated and washed with ethanol to remove unbounded MPA from the surface of the NPs. The MPA-capped Fe_3O_4@Ag NPs were finally dried under vacuum.

2.3.3.5 Preparation of MPA capped Fe_3O_4-Ag heterodimer NPs

The synthesis and purification of Fe_3O_4-Ag heterodimer NPs was similar to the method report for Fe_3O_4@Ag except that the synthesis of Fe_3O_4-Ag NPs carried out in toluene under mild conditions [224]. As-prepared Fe_3O_4 NPs (0.05 mg) [223], 0.05 mg of $Ag(ac)_3$, 0.1 g of 1,2-dodecanediol and 1 mL of oleylamine were mixed in 20 mL toluene and heated to 80-100 °C for 2 h. The reaction mixture was cooled to room temperature, and the product (Fe_3O_4-Ag NPs) was precipitated with ethanol, washed several times with ethanol and magnetically decanted. The purified product was dried at room temperature under vacuum, and re-dispersed in toluene prior to surface functionalization. Surface modifications and purification of as-prepared Fe_3O_4-Ag NPs with MPA was similar as outlined for Fe_3O_4@Ag NPs.

2.3.3.6 Fabrication of pristine, N-doped and S, N, co-doped graphene quantum dots (Scheme 3.8A)

Fabrication and purification of GQDs, NGQDs and SNGQDs were similar and followed bottom-up approach as reported by Qu et al [198,225]. Briefly, citric acid (2.8 g, 0.67 mmol) and NaOH (1.6 g, 2 mmol) for GQDs or thiourea (3.06 g, 2 mmol) for SN-GQDs or urea (2.4 g, 2 mmol) for N-GQDs, were separately dissolved and stirred in 100 mL Millipore water to form a clear solution. The respective homogenous mixture was transferred into a 400 mL Teflon lined stainless autoclave and heated to 160 °C for 4 h.

The crude quantum products were re-dispersed in water and dialyzed for 48 h to remove the excess salts. The final solid products were precipitated with dry absolute ethanol and centrifuged at 15000 rpm for 10 min. The obtained graphene quantum dots were re-dispersed in water prior to conjugation to phthalocyanine.

2.3.4 Preparation of MPc-nanomaterials/polymer conjugates

Formation of amide linkage between complex **10** and carboxyl-containing nanomaterials and polymer were prepared using either EDC/NHS or DDC/DMAP coupling reactions [220,226].

2.3.4.1 Covalent linking of complex 10 to MPA-capped AuNPs and poly acrylic acid (PAA) (Schemes 3.6A and 3.7)

Covalent linking of **10** to PAA was carried out by dissolving 0.15 g of PAA in 10 mL of DMF; this was followed by addition of 50 mg (0.24 mmol) of DCC and 20 mg (0.16 mmol) of DMAP. For amide linkage of **10** to AuNPs, MPA-AuNPs (20 mg) were first dissolved in 2 mL water, then 15 mg (0.078 mmol) of EDC and 10 mg (0.087 mmol) of NHS were added to the solution of MPA-AuNPs. Both solutions (PAA and MPA-AuNPs) were stirred separately at room temperature for 48 h to convert the carboxylic groups (–COOH) of the PAA (**Scheme 3.7**) or MPA-AuNPs (**Scheme 3.6A**) into active carbodiimide ester groups. Complex **10** (30 mg, 0.028 mmol for PAA) and (10 mg, 9.6 $x10^{-3}$ mmol for MPA-AuNPs) was then separately added to solutions of activated PAA and MPA-AuNPs. The stirring continued for another 48 h while monitoring the amide bond formation by FTIR. The resulting crude products were collected and washed several times by centrifugation using absolute ethanol. The pure composite of MPc-AuNPs was dried at room temperature, while MPc-PAA was oven-dried at 100 °C. Both composites gave good yields ranging from 88 to 90% yields

2.3.4.2 Covalent linking of complex 10 to MPA capped Fe_3O_4@Ag Core-Shell and Fe_3O_4-Ag heterodimer NPs, Schemes 3.9 and 3.10

A mixture of EDC (0.02 g, 0.1043 mmol) and NHS (0.015 g, 0.130 mmol) in 200 μL of deionized water were separately added to solution of MPA capped Fe_3O_4@Ag NPs (0.05 g) or Fe_3O_4-Ag NPs (0.05g) dissolved in 3 mL of deionized water. Both solutions were stirred at room temperature for 24 h to activate the (–COOH) of the nanoparticles. Then compound **10** (0.05 g, 0.0481 mmol) in 3.2 mL DMF was added to the activated

Fe_3O_4@Ag and Fe_3O_4-Ag NPs, and further stirred for another 24 h. The resulting crude products were purified as above. The pure conjugates were oven-dried at 60 °C.

2.3.4.3 Covalent linking of complex 10 to GQDs, NGQDs and SNGQDs, Scheme 3.8B

GQDs (50 mg), NGQDs (50 mg) or SNGQDs (50 mg) were separately dissolved in a vial containing 3 mL Millipore water. EDC (20 mg, 0.1043 mmol) and NHS (15 mg, 0.130 mmol) were added to each of the GQDs solution followed by stirring at room temperature for 24 h to activate the carboxylic groups (–COOH) of the GQDs. Then, 10 mg (9.63×10^{-6} mol) of complex **10** in 3 mL DMF was added to each QD solution and stirred for 24 h. The pure conjugates were oven-dried at 60 °C.

2.3.4.4 Conjugation of complex 11 to Ag_xAu_y alloy nanoparticles via NH_2-Au or S-Au bonds, scheme 3.11

The conjugation of complex **11** to Ag_xAu_y nano alloys was adapted from previously reported methods for Pcs conjugated to AgNPs and AuNPs [149,227]. Briefly, to two separate clean vials containing 10 mg each of **11** dissolved in 1.5 mL DMSO was added 2 mL of THF solution containing 5 mg each of the Ag_xAu_y alloyed nanoparticles. Each solution was magnetically stirred at room temperature for 48 h. The resulting crude conjugates were washed several times by centrifugation in dry ethanol, dried under vacuum at room temperature to obtain pure conjugates.

2.3.4.5 Conjugation of compounds 2 and 3 to AuNPs via click reactions (Scheme 3.6B)

Azide-derivatized gold nanoparticles were clicked with **2** or **3** as follows: To 2.5 mL of tert-buty alcohol in a small vial, was added 25 mg of azide-derivatized AuNPs and 20 mg (2.3×10^{-5} mol) of **2** or 20 mg (2.52×10^{-5} mol) of **3** and the mixture stirred for 10 min. Thereafter, $CuSO_4.5H_2O$ (2.8 mg, 1.14×10^{-5} mol) and sodium ascorbate (2.3 mg, 1.14×10^{-5} mol) in 2.5 mL of deionized water were added to the mixture and stirred for 4 days. At the completion of the reaction, the brown-green product was precipitated with abs. ethanol and subsequently washed with ethanol/water (1:1, v/v) to remove $CuSO_4$ and sodium ascorbate. The pure conjugates of MPc-AuNPs obtained were dried under vacuum at room temperature.

2.4 Fabrication of MPc-polymer thin films using compounds 5 - 10

2.4.1 Blending of compounds 5, 6 and 7 with PBC into thin films

Thin films of **5**, **6** and **7** with PBC were prepared according to the reported methods [124,125]. Briefly, PBC (110 mg) and **5** (4.9×10^{-4} M), **6** (4.5×10^{-4} M), or 2.5 mg of 2 (5.3×10^{-4} M), were, respectively, dissolved in chloroform (5 mL) and sonicated for 30 min until a homogeneous mixture of MPc-polymer solutions were obtained. The composites were dropped on glass substrates placed in a Petri dish and the solvent was allowed to evaporate at room temperature. The prepared thin films from **5**, **6**, and **7** are represented as **5-PBC**, **6-PBC**, and **7-PBC**, respectively.

2.4.2 Blending of compounds 8 and 9 with PSU into thin films

polysulfone (PSU) (0.11 g) was weighed into clean vials containing DMF (4 mL) and sonicated until homogeneous mixtures of PSU/DMF solutions were obtained. Thereafter, 4.7 mg of **8** (0.98×10^{-3} M) or 5 mg of **9** (0.98×10^{-3} M) in 1 mL of DMF were added to the polymer/DMF solutions. The solutions were stirred at room temperature for 24 h to dissolve the Pcs. A few drops of Pc-polymer solutions were carefully coated on clean glass slides and baked in an oven at 100 °C for 2 h to remove DMF. The prepared thin films **8** and **9** are labelled as **8-PSU**, and **9-PSU**, respectively.

2.4.3 Preparation of polymer thin films of compound 10 or 10-AuNPs composites with PAA

Thin film preparation of **10** (5 mg) or **10-AuNPs** composites (5 mg) were dissolved in 2 mL of DMF and each separately mixed with PAA (0.1 g in 3 mL DMF) and the mixture stirred in an airtight vial for 48 h at room temperature. A few drops of sample-polymer solutions were coated on clean glass slides baked in an oven at 100 °C for 2 h to give good compact coating surfaces. The prepared thin films (TF) are designated as **10/PAA-TF** and **10-AuNPs/PAA-TF**.

CHAPTER 3
SYNTHESIS & CHARACTERIZATION

PUBLICATIONS

The submitted or published manuscripts in peer-reviewed journals discussed in this thesis are listed below. These articles have not been cited in this thesis:

1. O. M. Bankole, J. Britton, T. Nyokong
   Photophysical and non-linear optical behaviour of novel tetra terminated alkynyl indiumphthalocyanines: Effects of the carbon chain length, **Polyhedron 88** (2015) 73-80.
2. O. M. Bankole, T. Nyokong
   Photophysical and nonlinear optical studies of tetraakynyl zincphthalocyanine and its "clicked" analogue, **J. Mol. Str. 1089** (2015) 107-115.
3. O.M. Bankole, T. Nyokong
   Mercaptopyridine) substituted indium, zinc and metal-free phthalocyanines: nonlinear optical studies in solution and on polymer matrices, **J. Coord. Chem. 68** (20) (2015) 3727-3740.
4. O.M. Bankole, Y. Yılmaz, T,Nyokong
   Nonlinear optical behaviour of alkyne terminated phthalocyanines in solution and when embedded in polysulfone as thin films: Effects of aggregation, **Opt. Mat. 51** (2016) 194-202.
5. O. M. Bankole, T. Nyokong
   Nonlinear optical response of a low symmetry phthalocyanine in the presence of gold nanoparticles when in solution or embedded in poly acrylic acid polymer thin films, **J. Photochem. Photobiol. A: 319** (2016) 8-17.
6. O. M. Bankole, O. Osifeko, T. Nyokong
   Enhanced nonlinear optical responses of zinc diaminopyrimidin-2-ylthio phthalocyanine conjugated to Ag_xAu_y alloy nanoparticles, **J. Photochem. Photobiol. A.329** (2016) 155-166.
7. O.M. Bankole, T. Nyokong
   Comparative studies on photophysical and optical limiting characterizations of low symmetry phthalocyanine linked to Fe_3O_4-Ag core-shell or hybrid nanoparticles, **New J. Chem.**, in press.

8. O. M. Bankole, T. Nyokong
   Azide-derivatized gold nanosphere "clicked" to indium and zinc phthalocyanines for improved nonlinear optical limiting, **J. Mol. Str.** submitted 18-10-2016.
9. O. M. Bankole, O. J. Achadu, T. Nyokong
   Nonlinear interactions of zinc phthalocyanine-Graphene quantum dots nanocomposites: Investigation of effects of surface functionalization with heteroatoms, **J. Fluorescence**, submitted, 24-10-2016.

3.1 Synthesis and characterization of Pcs

This chapter reports on the detailed syntheses, structural and spectroscopic characterizations of MPc (or H_2Pc) complexes and MPc-nanomaterial composites studied in this work. Pc-polymer composites are also discussed in this section.

Figure 3.1 shows the summarized molecular structures of previously reported complexes (**3**, **5**, **6** and **10**) that are used in this work [102,214-218]. Discussions on their syntheses and other characterizations are excluded in this report, only those that have not been reported before are presented.

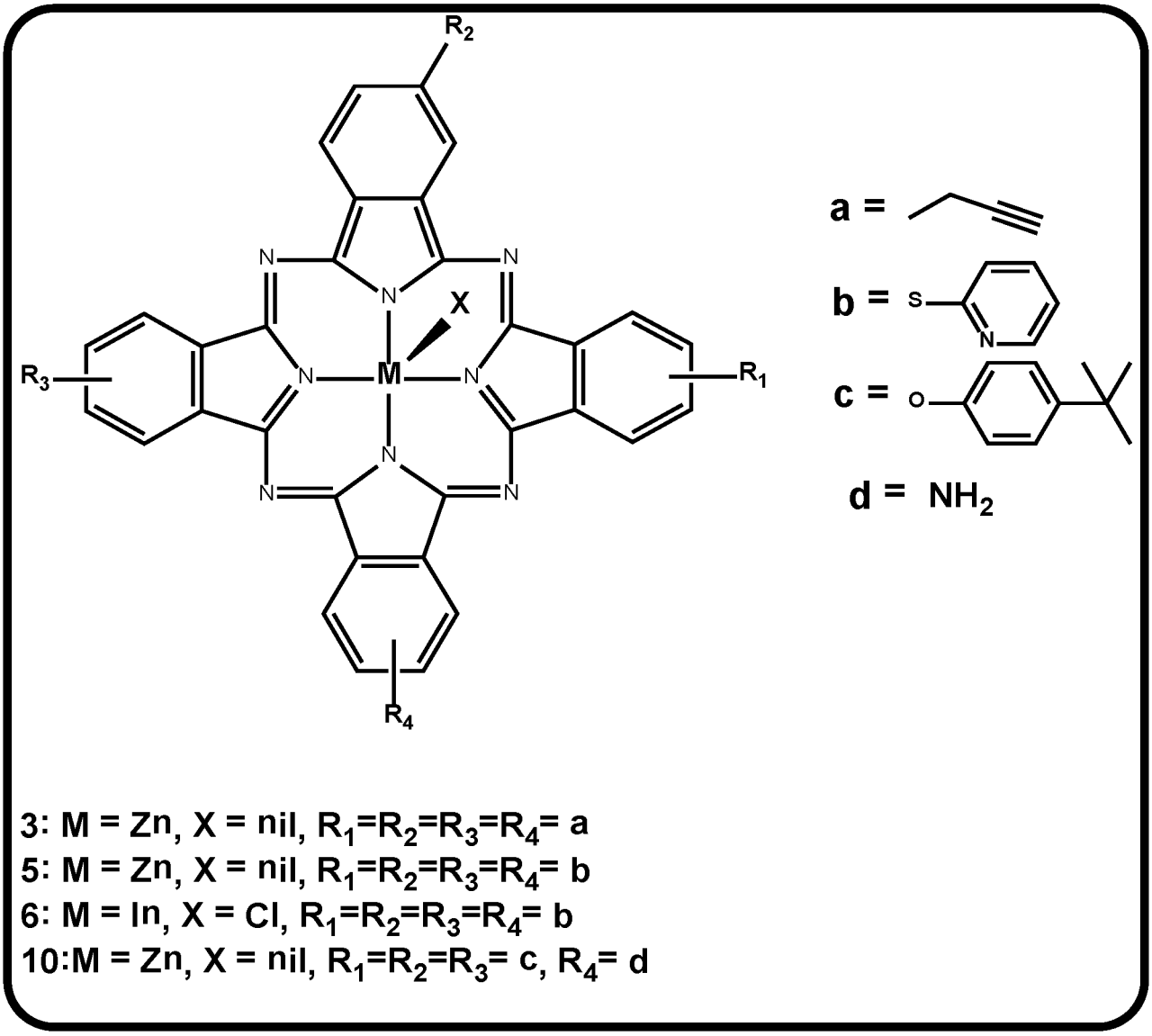

Figure 3.1: Molecular structures of previously reported MPcs that are used in this work

3.1.1 Alkynyl and triazole-functionalized Pc derivatives, complexes 1, 2, 4, 8 and 9, Schemes 3.1 - 3.3

3.1.1.1 Synthesis

The synthesis of alkyne-substituted phthalonitrile precursor (**1b(ii)**), for the preparation of complex **2** has been reported before [102]. Substituted phthalonitriles precursors for complexes **1**, **8** and **9** were synthesized via base catalyzed nucleophilic aromatic displacement reactions [228,229] between 4-nitrophthalonitrile (**1a**) and 5-hexy-1ol for complex **1**, and 5-methylhex-1-yn-3-ol (**8a**) for complexes **8** and **9**, **Schemes 3.1** and **3.2**. The metal assisted ($(Zn(OAc)_2$ or $InCl_3$) cyclotetramerization reactions of **1b(i)**, **1b(ii)**) and **8b** in the presence of catalytic amount of DBU and n-pentanol afforded peripherally tetra-substituted Zn (**9**) or In (**1** and **2**) phthalocyanines, **Schemes 3.1** and **3.2**. The synthesis of metal-free Pc derivative **8** was similar to other alkyne MPcs, except that **8** required no metal salt during the cyclization of **8b**. The compounds were obtained in satisfactorily high yields and were characterized by elemental analysis, UV–Vis, FT-IR, ^{1}H NMR spectroscopies and MALDI-TOF. The characterization results are consistent with the predicted structures as shown in the experimental sections. All the complexes are effortlessly soluble in common organic solvents such as $CHCl_3$, DMF, THF, DCM and DMSO.

The mass spectral are definitive and gave expected masses of all the complexes. Molecular ion peaks of 1049.22 $[M+3H]^+$ and 879.36 $[M+H]^+$ were observed for **1** and **2**, respectively. Similarly, observed molecular ion peaks at m/z: 955 $[M+H]^+$ and 1016 $[M+H]^+$ were respectively recorded for complexes **8** and **9**. Fragmentation of m/z peaks as $[M+nH]^+$, or $[M-nH]^+$ have been reported [230]. Elemental analyses gave percentage C, N and O values that were within 1% in all cases, which are within acceptable range for Pc complexes. ^{1}H NMR spectra confirmed the purity and the expected structures of the synthesized complexes. ^{1}H NMR spectra of the complexes are very similar, except that the two inner core protons (NH) of complex **8** lie in the negative regions of the spectrum and were not observed due to aggregation [231,232].

Synthetic method for the preparation of complex **4** is shown in **Scheme 3.3**. Substituted phthalonitrile precursor **4b** was obtained in good quantitative yield using 1,3-dipolar cycloaddition reaction method between **4a** and **1b(ii)**. Cyclotetramerization of **4b** in the presence of zinc acetate and DMAE at reflux temperature for 18 h gave the desired

complex **4** as an intense blue–green solid. Complex **4** was obtained in satisfactorily high yields and is readily soluble in organic solvents such as DMF, THF, dioxane and DMSO.

The ^{1}H NMR of the precursor **4b** and complex **4** gave the expected protons at the appropriate resonances and integrated correctly. For **4**, the triazole H signal in the dinitrile precursor (**4b**) lies furthest downfield due to its close proximity to the azide nitrogens. Upon formation of complex **4**, the triazole H and CH_2 protons experienced shifts of 0.17 and 0.32 ppm respectively, due to the influence of the Pc ring. The molecular ion peaks for complex **4** was found at m/z = 1453.56 $[M + 3H]^+$.

3.1.1.2 FT-IR

FTIR spectrum of substituted phthalonitrile precursor **8b** (as a representative of phthalonitriles) shows characteristic intense peak due to C≡N stretch at ~2230 cm^{-1}, **Figure 3.2**. Upon cyclization of the precursor, the peak disappeared to confirm successful formation of alkynyl Pcs for complexes **8** and **9** (as representatives for **1** and **2**), **Figure 3.2**. Vibrational signals around ~3285-3292 cm^{-1}, 2114-2119 cm^{-1}, 3050-3084 cm^{-1} and 2870-2955 cm^{-1} due to C≡C-H, C≡C, CH aromatic and CH aliphatic groups respectively, are consistent in the spectra of the substituted phthalonitrile **8b** as well as in the synthesized alkynyl MPc complexes **8** and **9**. In addition to the vibrational bands observed for metallated alkynyl Pcs, unmetallated Pc complex **8** revealed vibrational band at ≈3644 cm^{-1} attributable to the presence of N-H (secondary amine) stretching in the Pc cavity, **Figure 3.2**. The presence of C≡C peak at 3285–3295 cm^{-1} could be responsible for the shifting of NH signal to 3647 cm^{-1} in complex **8**. Also, IR peak value as high as 3555 cm^{-1} for NH stretching have been reported in literature [233].

The characteristic IR peaks around 2123 cm^{-1}, 3286 cm^{-1} and 2122 cm^{-1} due to N_3 (for **4a**), C≡CH (for **1b(ii)**), and C≡C (for **1b(ii)**), respectively disappeared, and a new peak around 3156 cm^{-1} appeared upon successful click reaction between **4a** and **1b(ii)**) to form **4b**, **Figure 3.3**. Disappearance of the sharp C≡N vibrational peak at 2232 cm^{-1} in the IR spectrum of **4b** showed successful formation of triazole-functionalized ZnPc **4**.

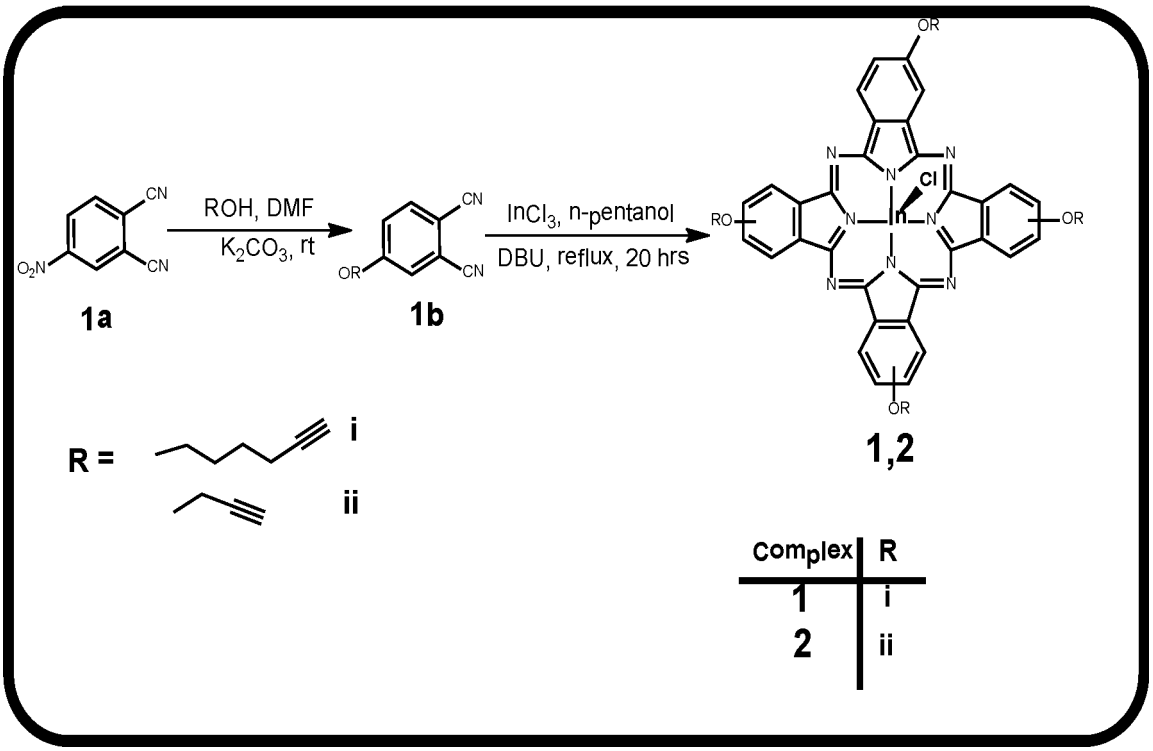

Scheme 3.1: Synthetic pathways for alkynyl complexes of 1 and 2.

3.1.1.3 Ground state electronic absorptions

The electronic absorption spectral of complexes **1**, **2**, **3**, **4** and **9** showed monomeric behaviour in DMSO (and THF for **9**) evidenced by the single Q band of the complexes, this is typical of metallated phthalocyanine [234], with D_{4h} symmetry, **Figure 3.4A**. The observed Q bands for the complexes shifted to higher wavelengths as the central metal is changed from Zn (**3**) to In (**2**); the red shifting of the Q band is ascribed to the larger size of In compared to Zn [235]. The Q band for complexes **3** and **4** were observed at 683 and 684 nm, respectively (**Table 3.1**), showing no shift in the Q band positions. The Q band for **9** was observed at 687 and 680 nm in DMSO and THF, respectively. The 7 nm spectrum shift observed in DMSO is attributed to the higher refractive index of DMSO compared to THF [22]. Q band absorption of complex **1** (696 nm) was red-shifted by 3 nm, compared to **2** (693 nm). Increased carbon chain-length of the substituents in complex **1** gives room for both σ and π bonded electrons in the alkynyl groups to interact [236]. This results in slight destabilization of highest occupied molecular orbital (HOMO) level in **1** than **2**, hence a shift in the Q band to longer wavelength was observed for the former [236].

The UV–vis absorption spectra of metal-free Pc **8** in THF showed distinct (Q_x and Q_y) bands at 701 and 668 nm, respectively, **Figure 3.4B**. In DMSO, the absorption spectrum showed broadness in the Q band region due to aggregation at the concentration ($\approx 10^{-5}$ M) used in **Figure 3.4B**. At low concentration of $\approx 2.5 \times 10^{-7}$ M, the Q bands of complex **8** are more resolved in DMSO due to reduced aggregation, **Figure 3.5**. Aggregation in Pcs is judged by broadening or the presence of two main bands in the Q band region [234].

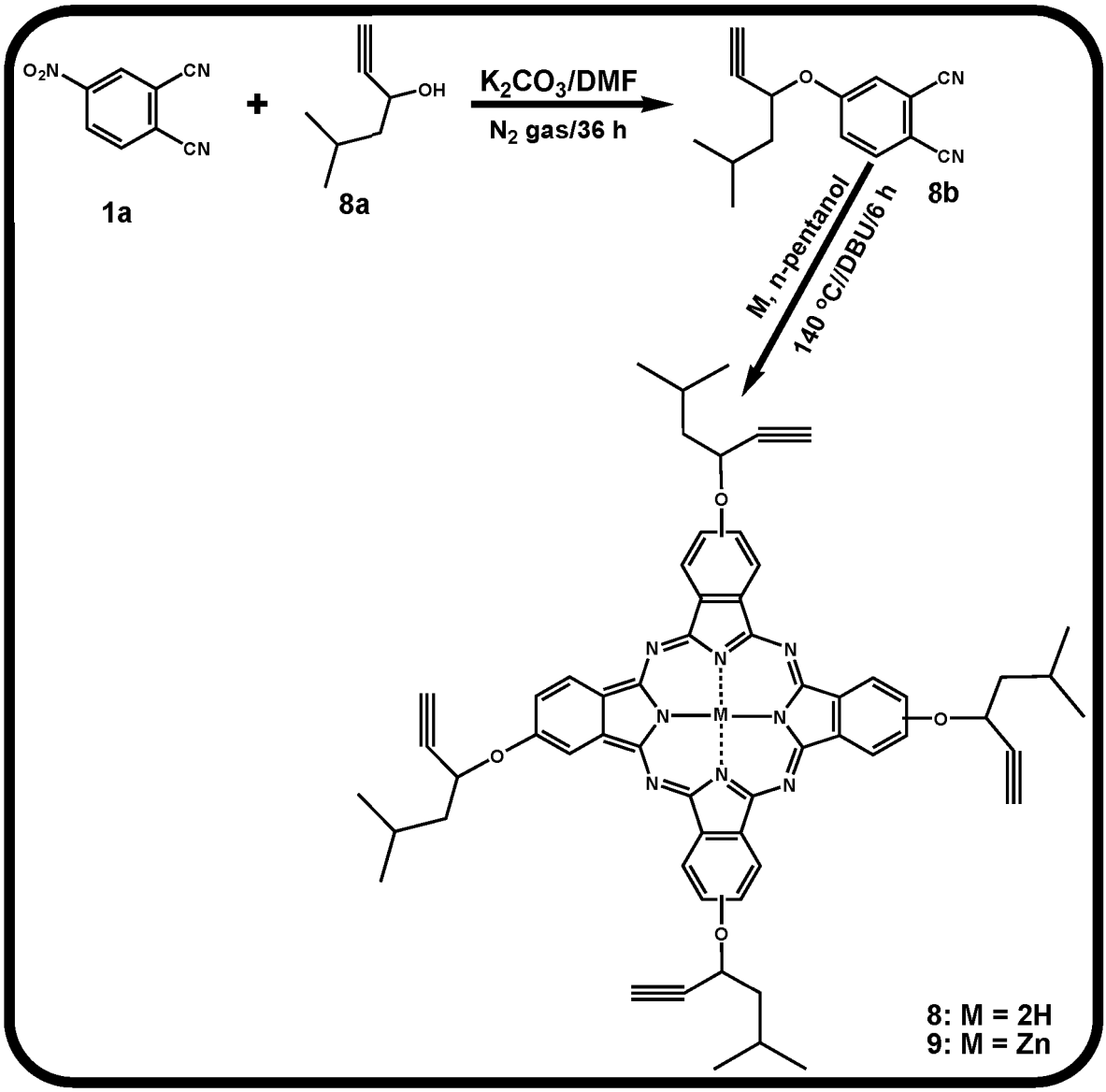

Scheme 3.2: Synthetic pathway for the formation of complexes 8 and 9.

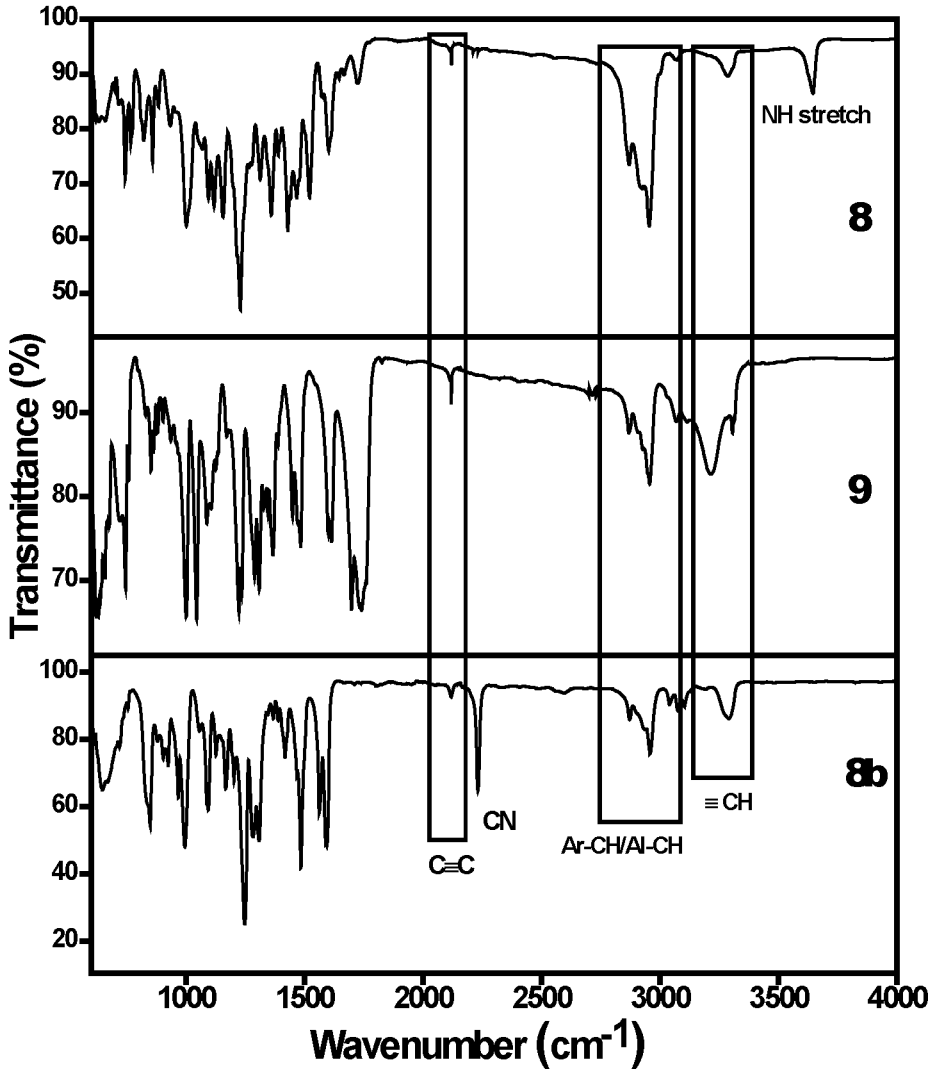

Figure 3.2: FTIR spectra of 8, 9, and 8b

Figure 3.5 shows the normalized absorption, fluorescence emission and excitation spectra of **3** (as a representative of **3**, **4** and **9**) and **2** (as representative of **1** and **2**), respectively, measured in DMSO (**Table 3.1**). The emission and absorption spectra of **3** were mirror images of each other, **Figure 3.5**. Fluorescence spectrum of **2** (indium Pcs) is weak compared to **3** (ZnPcs) due to the heavy atom effect of In, **Figure 3.5**. Also, loss of symmetry in complex **2** is possible due to the large size of indium metal which is more displaced from the cavity of the phthalocyanines ring, and become more pronounced upon excitation [237].

Figure 3.5 shows normalized absorption, fluorescence emission and excitation spectra of metal-free phthalocyanine **8** in DMSO (similar to THF), as stated above complex **8** is monomeric at this concentration used for emission studies (2.5×10^{-7} M). As is typical of metal free phthalocyanines, emission occurs with one peak assigned to 0–0 transition for complex **8** [238].

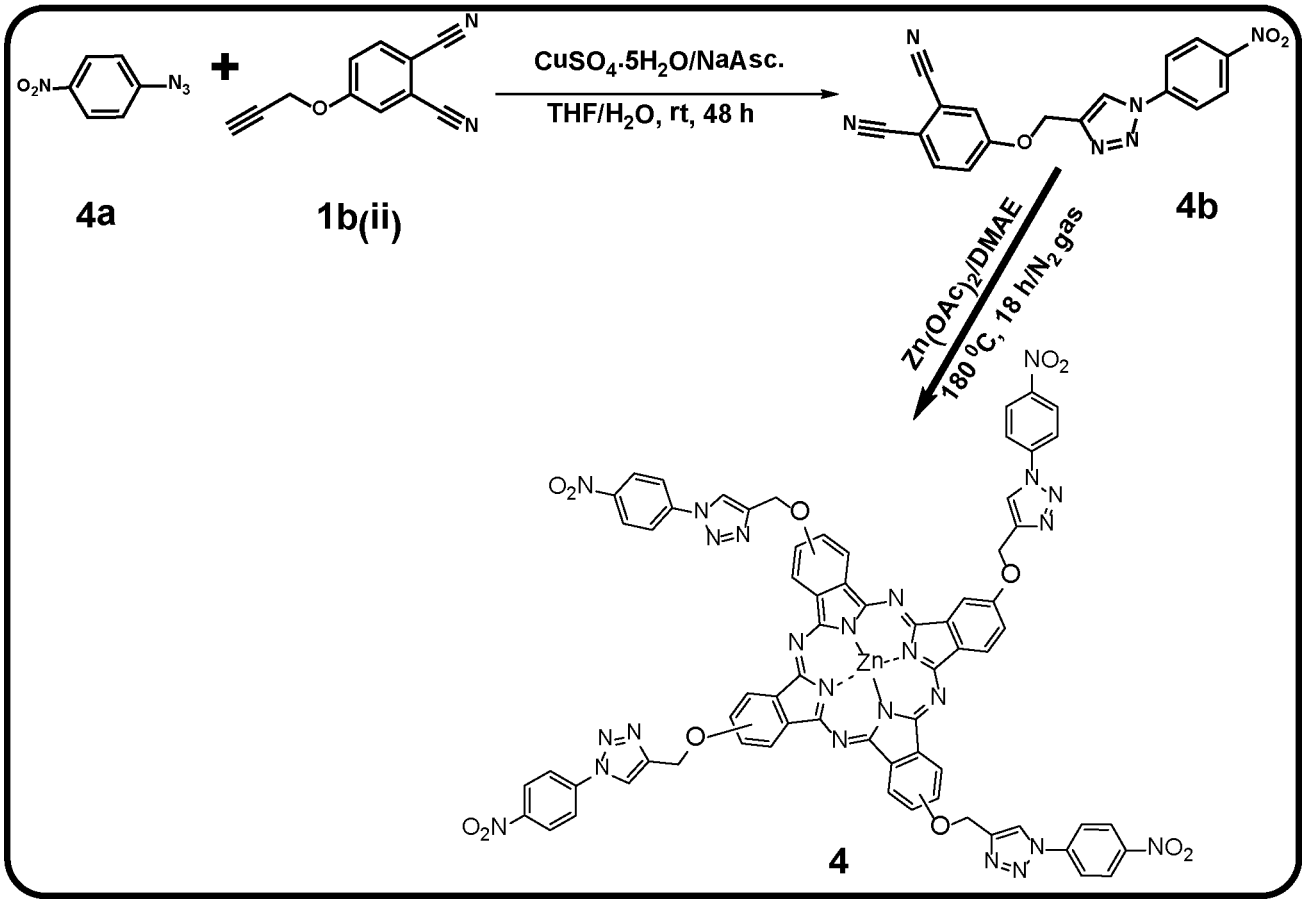

Scheme 3.3: Synthesis of 1,2,3-triazole-functionalized Zn phthalocyanine (4).

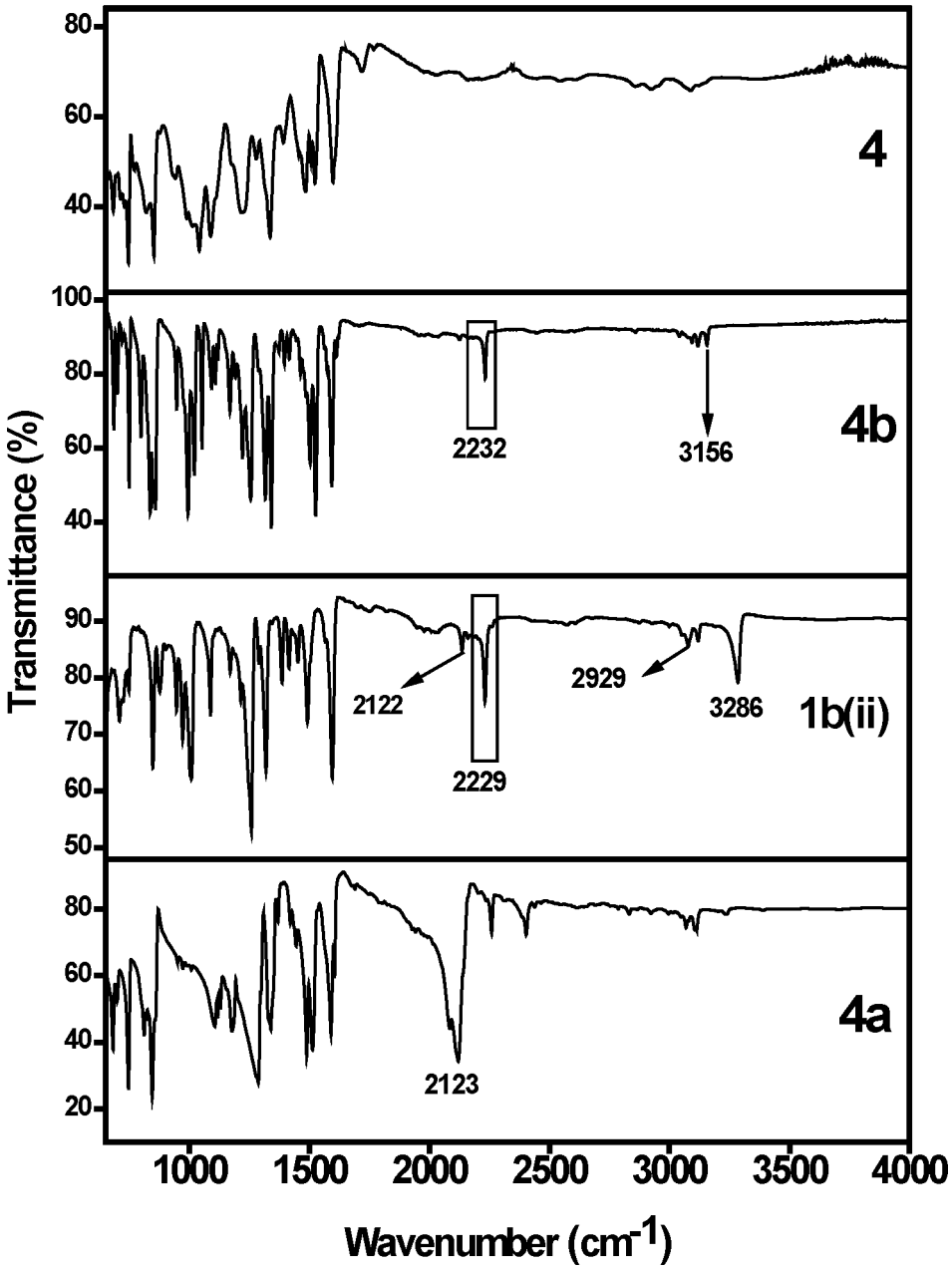

Figure 3.3: FTIR spectra of 4a, 1b(ii), 4b and complex 4.

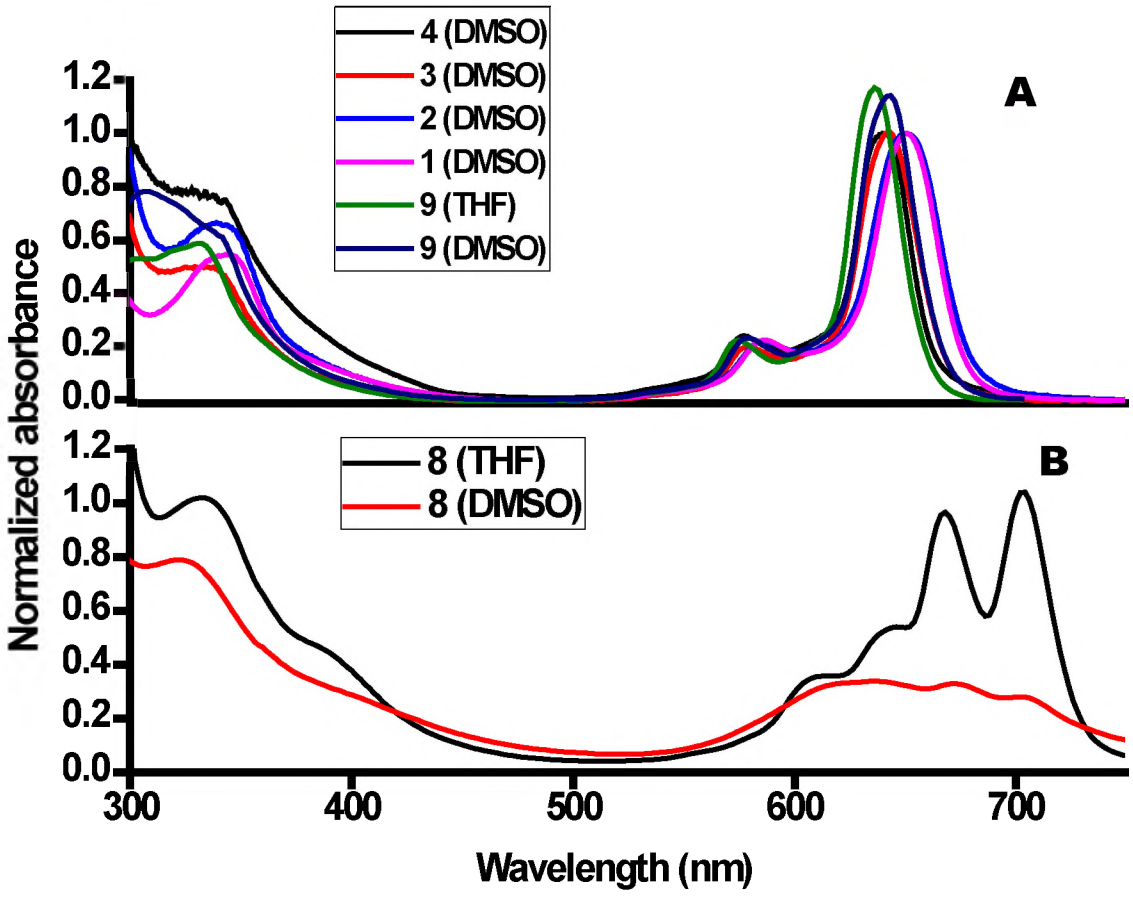

Figure 3.4: Electronic absorption spectral of (A) 1, 2, 3, 4, (in DMSO) 9 (in THF and DMSO) (Concentration ≈2 x 10^{-6} M), and (B) 8 in THF and DMSO at concentration of 1.5 x 10^{-5} M.

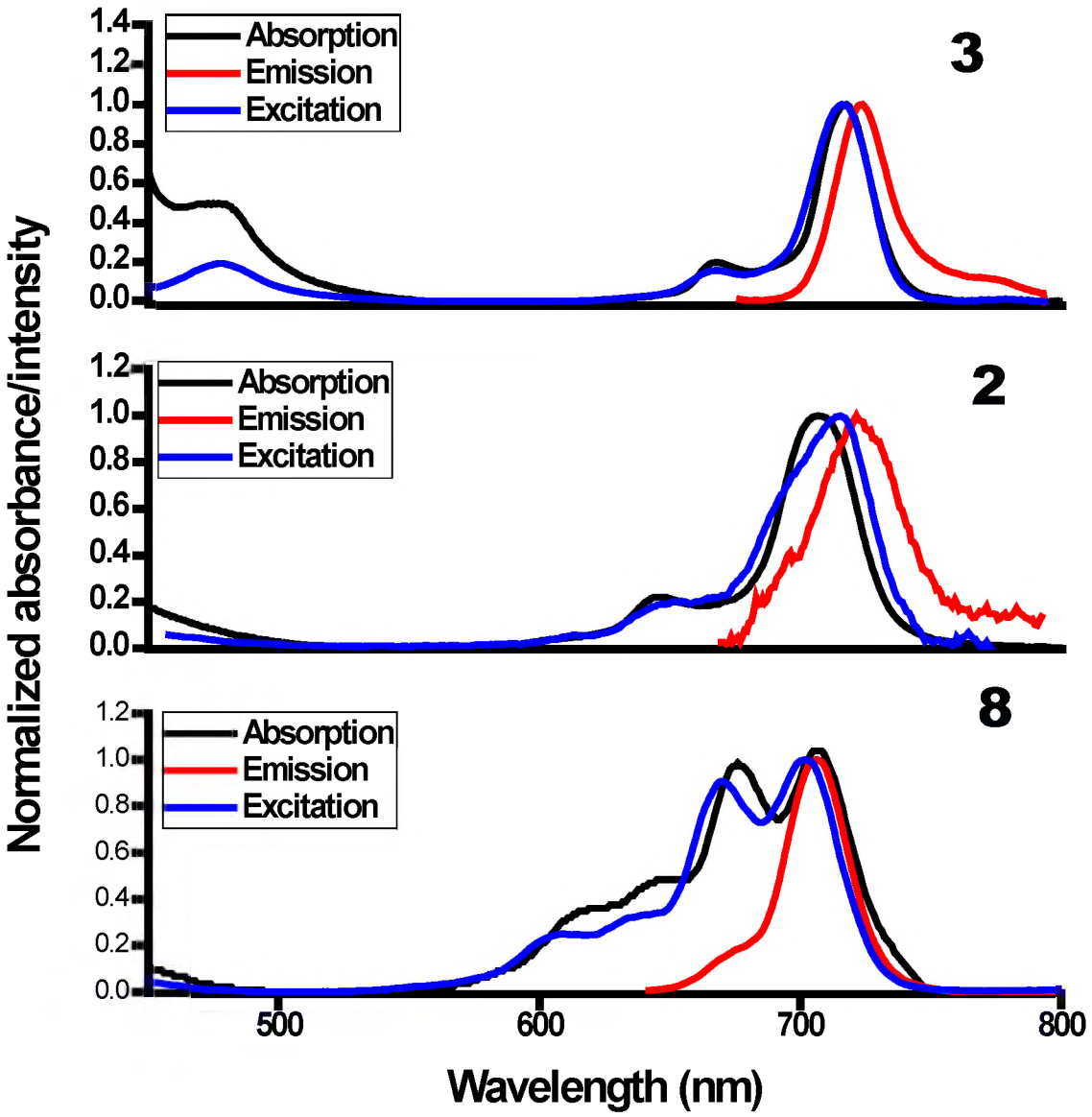

Figure 3.5: Absorption, fluorescence emission and excitation spectra of 3, 2 and 8 (Concentration < 10^{-6} M. Excitation wavelength = 605 nm) in DMSO. Excitation wavelength = 610 nm.

Table 3.1: Absorption, emission, and excitation spectral data for 1, 2, 3, 4, 5, 6, 7, 8, 9, 10 and 11 in DMSO, unless otherwise stated

Compound	Q band, λ_{Q-band} (nm)	Emission, λ_{em} (nm)	Excitation, λ_{exc}(nm)
1	696	710	702
2	693	710	706
3	684	695	684
4	683	695	683
9	687	695	684
9 (THF)	680	688	681
8	672,704	710	698
8 (THF)	668,701	672,701	707
5[a]	685	698	686
6[b]	695	712	697
7 ($CHCl_3$)	705,671	680,709	714
10	691	697	687
11	689	698	689

[a] Data from reference [215], [b] Data from reference [216].

3.1.2 4-(2-Mercaptopyridine) phthalocyanine (7, Scheme 3.4)

Scheme 3.4 represents the route for the synthesis of unmetallated phthalocyanine **7**. The precursor to the synthesis of metal-free phthalocyanine is 4-(2-mercaptopyridine) phthalonitrile (**7a**) whose synthesis has been previously reported [211]. The cyclotetramerization of **7a** with excess lithium metal in the presence of n-pentanol under nitrogen atmosphere results in the formation of lithium phthalocyanine (LiPc, not shown). Complex **7** was synthesized by refluxing LiPc in glacial acetic acid for 2 h to remove the loosely held Li metal in the Pc cavity. The crude product was purified by column chromatography and characterized by FTIR, elemental analyses, ^{1}H NMR, electronic absorption, and MALDI-TOF mass spectroscopies. The obtained data were consistent with the predicted structure. FTIR investigations on the metal-free Pc confirmed the absence of the sharp C≡N vibration at 2230 cm^{-1} observed in **7a**. The presence of single N–H (secondary amine) stretching vibrational band at 3286 cm^{-1} of the inner core of the metal-free Pc further proved the successful conversion of mercaptopyridine phthalonitrile derivative to Pc. In the ^{1}H NMR spectra, the pyridyl-H was observed as a multiplet

between 9.20 and 7.92 ppm, which was integrated to give 16 protons. The proton signals of the Pc ring were observed as multiplet between 8.64 and 7.50 ppm and integrated to 12 protons. The two inner core protons of the Pc lie in the negative region of the spectrum and were not observed [231,232]. The mass spectrum gave the expected value of the synthesized molecule at m/z: 950.5 $[M]^+$, and therefore confirmed the proposed structures. Elemental analysis of the compound was in agreement with the calculated values. The synthesized molecule showed good solubility in most organic solvents, such as chloroform, DMF, dichloromethane, and THF.

The normalized absorption, fluorescence emission and excitation spectra of **7** in $CHCl_3$ is shown in **Figure 3.6**. The Q bands were observed at 705 and 671 nm (**Table 3.1**) with shoulders around 649 and 615 nm, while the B-band was observed at 342 nm. The Q band absorptions of metal-free phthalocyanines possess D_{2h} symmetry, hence the splitting pattern was observed in the spectrum. Both absorption and excitation spectra of complex **7** have similar splitting patterns but with different intensities of the Q band components, **Figure 3.6**, suggesting no form of decomposition to the molecule during fluorescence study.

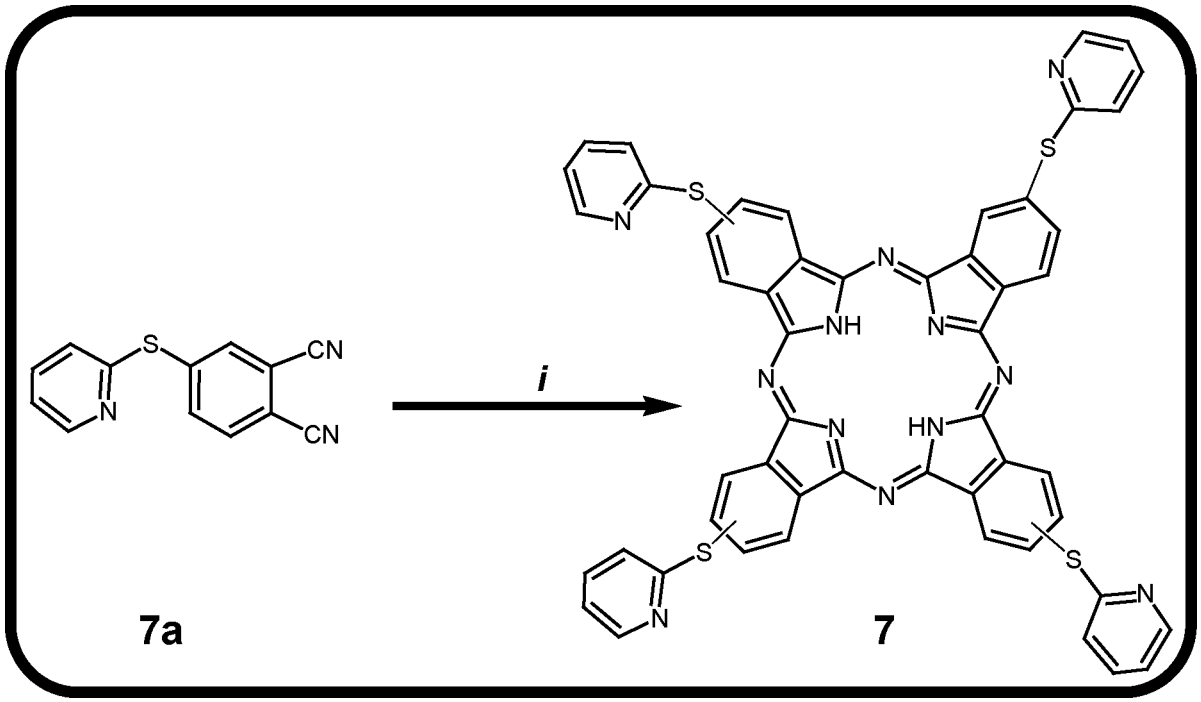

Scheme 3.4: Synthetic route for the preparation of 7: (i) Li metal, n-pentanol, glacial acetic acid, 140 °C, N_2.

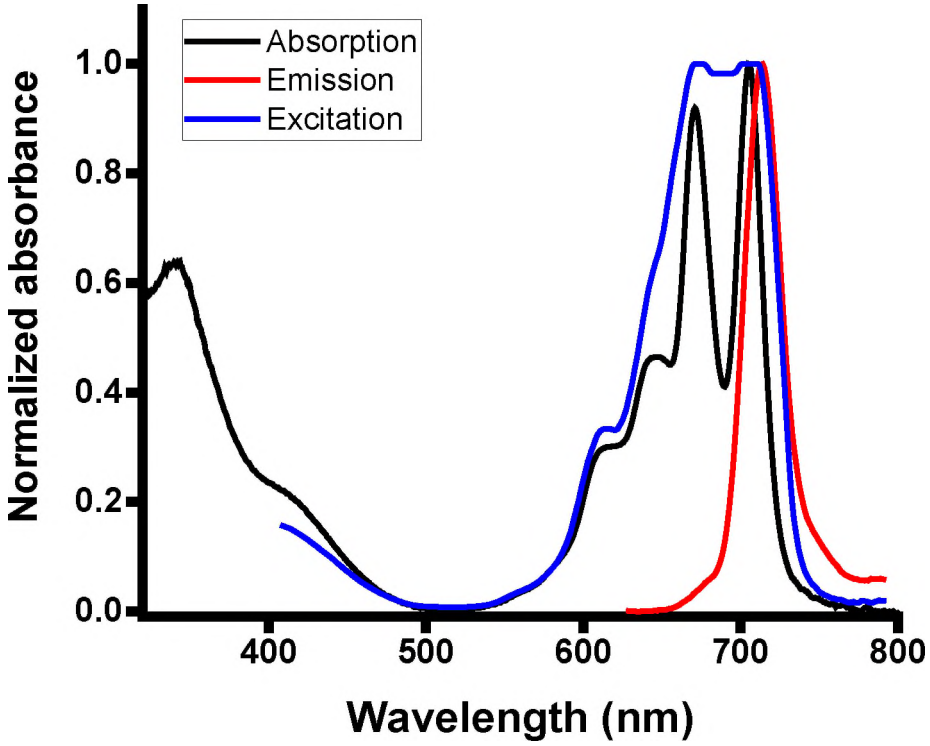

Figure 3.6: Absorption, fluorescence emission and excitation spectra of 7 in $CHCl_3$ (1×10^{-5} M). Excitation wavelength = 610 nm.

3.1.3 4-(4-6-Diaminopyrimidin-2-ylthio) Zn (II) phthalocyanine (11, Scheme 3.5)

Scheme 3.5 represents the pathway for the synthesis of complex **11** via cyclization of compound **11a** in the presence of Zn acetate, n-hexanol, catalytic DBU for 6 h. The pure product (**11**) was obtained in satisfactorily high yield (48%) and characterized by FTIR, elemental analysis, UV–vis, ^{1}H NMR spectroscopies and MALDI-TOF. In the FTIR, the characteristics intense peak around 2232 cm^{-1} due to C≡N stretch in diaminopyrimidin-2-ylthio phthalonitrile (**11a**) disappeared to show the successful formation of complex **11**. Vibrational signals around 3320 and 3189 cm^{-1} due to aromatic primary amines, are consistent in the spectra of the starting material (**11a**) as well as the synthesized molecule **11**. This is an indication that the diaminopyrimidine substituents were retained after cyclization. Vibrational band at ~2929 cm^{-1} is due to CH aromatic stretching, while band around 1613 cm^{-1} is attributable to NH bend of primary amine. The mass spectrum gave expected value of the synthesized molecule at m/z: 1141.82 $[M + 3H]^+$ and therefore

confirmed the proposed structure. Elemental analysis of the compound was in good agreement with calculated values. All the ring and substituent protons of the as-synthesized complex **11** in DMSO were observed in their respective regions as revealed by the ^{1}H NMR. The 12 protons of the Pc ring were observed as singlet between 7.77–7.89 ppm. The singlet pyrimidinyl-H at 8.97 ppm were integrated to give 4 protons, while the broad singlet NH_2 protons were observed around 5.20 ppm.

Figure 3.7 shows the normalised absorption, fluorescence emission and excitation spectra of **11** measured in DMSO. The Q of **11** showed monomeric behaviour in DMSO and was observed at 689 nm, **Table 3.1**. The proximity of the wavelength of the Q band maxima absorption to the excitation Q band spectrum suggests that the excited state and the ground state of the molecule have similar molecular geometries, **Table 3.1** [239], an indication that the excited state is similar, and not affected by excitation.

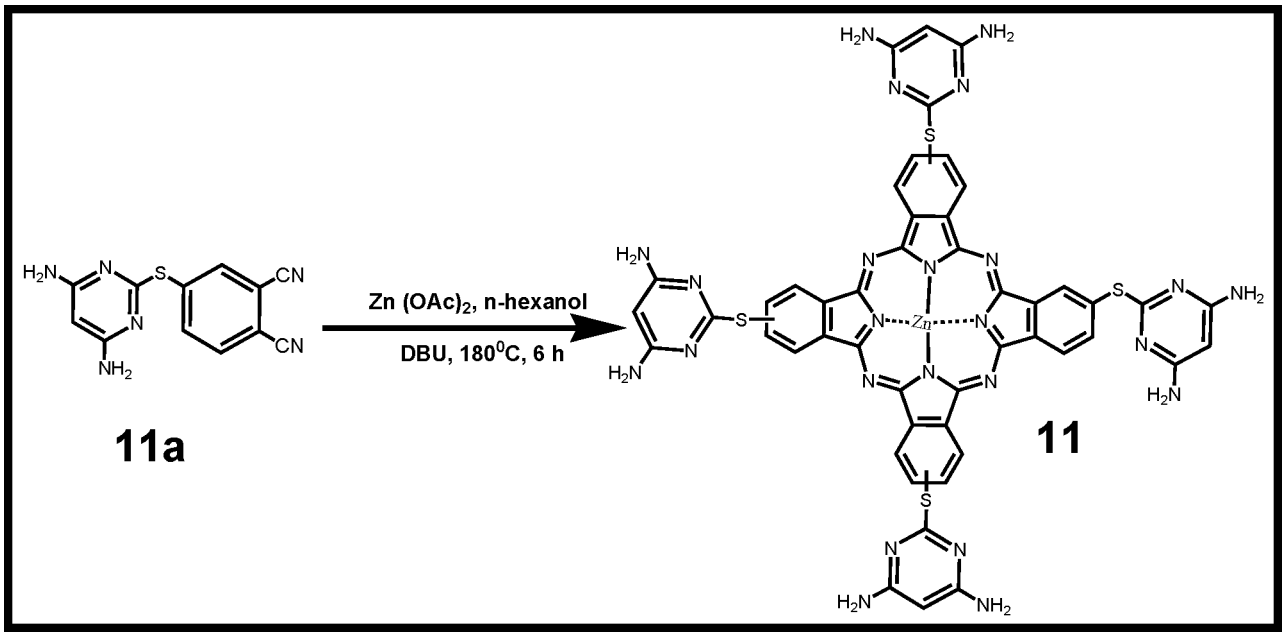

Scheme 3.5: Synthetic pathway for the preparation of 11.

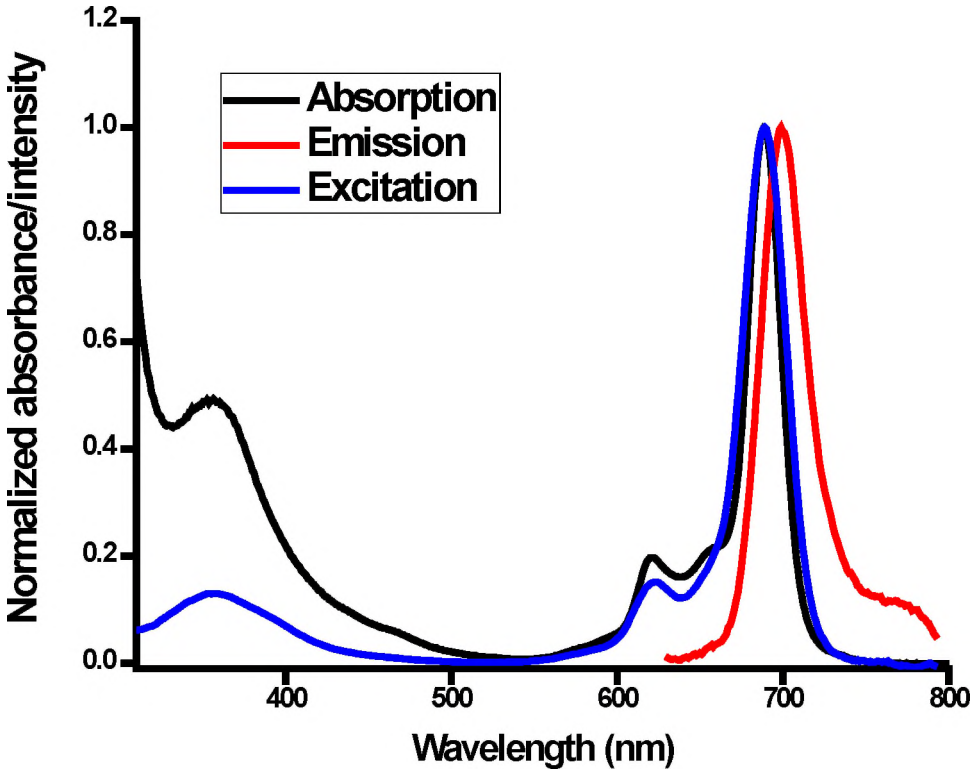

Figure 3.7: Absorption, fluorescence emission and excitation spectra of 11. Conc. in DMSO ≈ 1.6 × 10^{-6} M. Excitation wavelength = 612 nm.

3.2 MPc-Nanomaterial/polymer conjugates - Schemes 3.6 - 3.11

The composites of MPcs-nanomaterials used in this work are summarized below;

- Complexes **2** and **3** were both coupled to azide-derivatized gold nanoparticles (AuNPs) using Huisgen cyclo addition "click" reactions.
- Complex **10** with mono-amino group was covalently linked to the activated carboxyl-groups of MPA-capped gold nanoparticles (AuNPs); MPA capped Fe_3O_4@Ag core-shell and Fe_3O_4-Ag heterodimer nanoparticles; polyacrilic acid (PAA); graphene quantum dots (GQDs), N-doped (N-GQDs) and S, N co-doped graphene (S, N-GQDs) quantum dots via amide bonding.
- Complex **11** was conjugated to Ag_1Au_3 and Ag_3Au_1 alloy nanoparticles via amine-Au or thiol-Au bonds.

3.2.1 Conjugates of 2 and 3 with gold nanoparticles via click reactions (2-AuNPs, 3-AuNPs, Scheme 3.6B)

Clickable azide-derivatized AuNPs were synthesized by using conventional ligand exchange between the loosely held TOABr and azidopropylamine via the stable amine-Au bond. The azide-derivatized AuNPs and alkyne-terminated phthalocyanines (**2** and **3**) were coupled via [3 + 2] Huisgen cycloaddition reaction between the azide and alkyne end groups, using $CuSO_4.5H_2O$ as a catalyst and sodium ascorbate as the reducing agent, **Scheme 3.6B**. The reaction was carried out in tertbutanol:H_2O (1:1 v/v) at room temperature for 96 h to afford triazole products in quantitative yields. The conjugates obtained were purified and characterized by FT-IR, UV-Vis, TEM, XRD and XPS. The compounds are readily soluble in organic solvents such as DMF and DMSO.

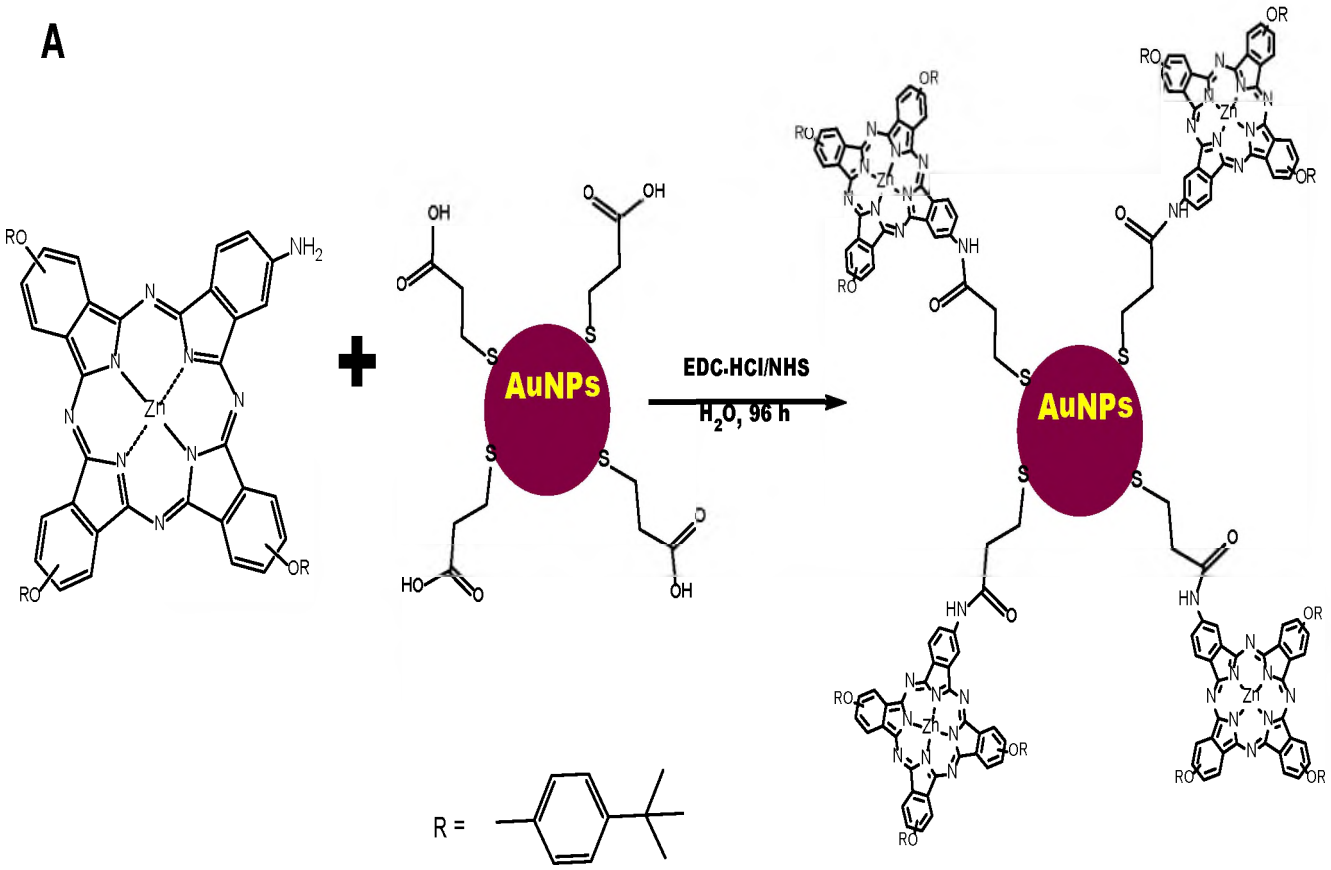

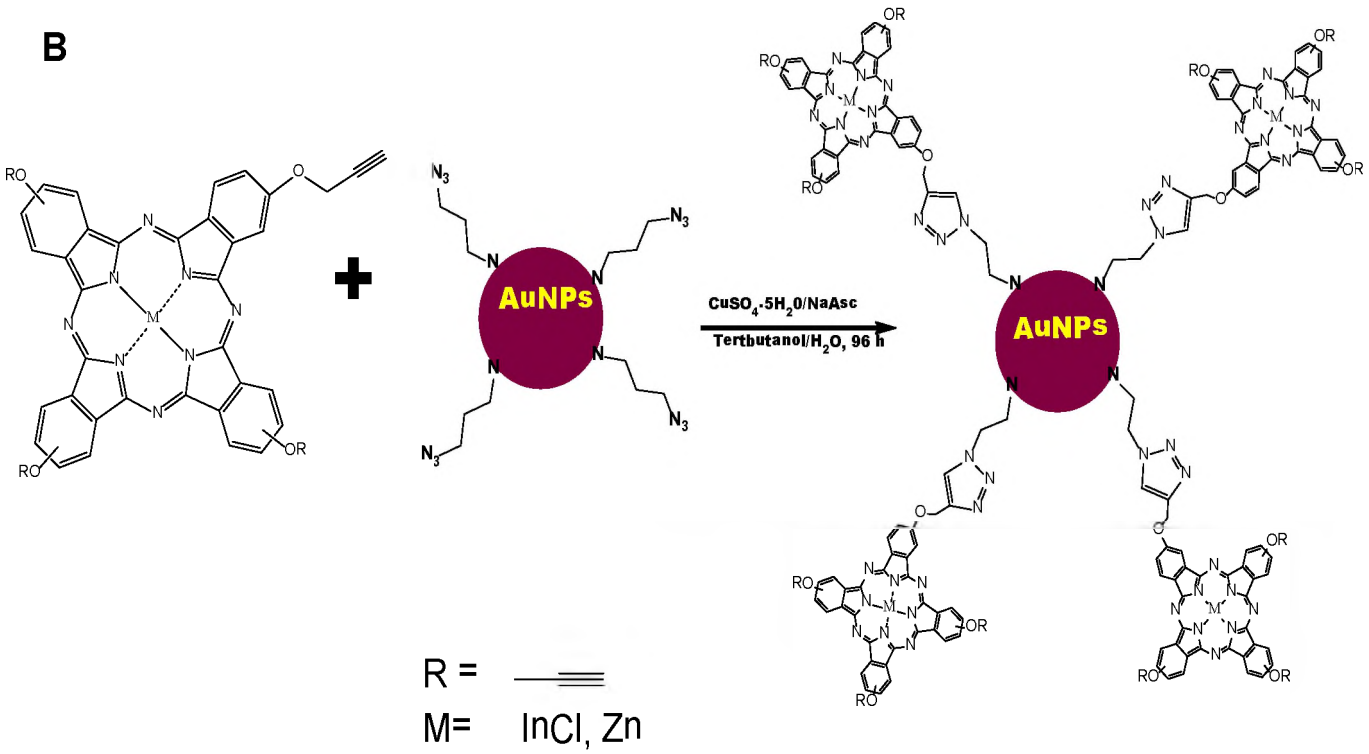

Scheme 3.6: Synthesis of (A) 10-AuNPs via amide bond, and (B) 2-AuNPs and 3-AuNPs via "clicked" reactions.

3.2.1.1 FTIR Spectra

Figure 3.8A depicts the IR spectrum of azidopropylamine. The presence of strong intense peak at 2098 cm^{-1} generally assigned to asymmetric N_3. The presence of azidopropylamine functionality on the surface of AuNPs were confirmed by the small but clearly visible peak at 2102 cm^{-1}, **Figure 3.8B**. The slight shift and reduction in intensity of the azide peak on AuNPs also confirmed interaction between the azidopropylamine and AuNPs. **Figure 3.8C** for alkyne-terminated zinc phthalocyanine **3** (as a representative) shows vibrational signals at 3282 cm^{-1}, 2229 cm^{-1} and 2875-2965 cm^{-1} attributed to C≡C-H, C≡C and CH aliphatic groups, respectively. The characteristic peaks around 2102 cm^{-1}, 3282 cm^{-1} and 2229 cm^{-1} due to N_3 (on AuNPs), C≡C-H, and C≡C (on the ZnPc) disappeared; and new peaks around ~3140 cm^{-1} and ~1730 cm^{-1} [221] due to triazole ring vibrations appeared upon successful Huisgen cycloaddition click reaction, as observed in **3-AuNPs** (**Figure 3.8D**) and **2-AuNPs** (**Figure 3.8E**).

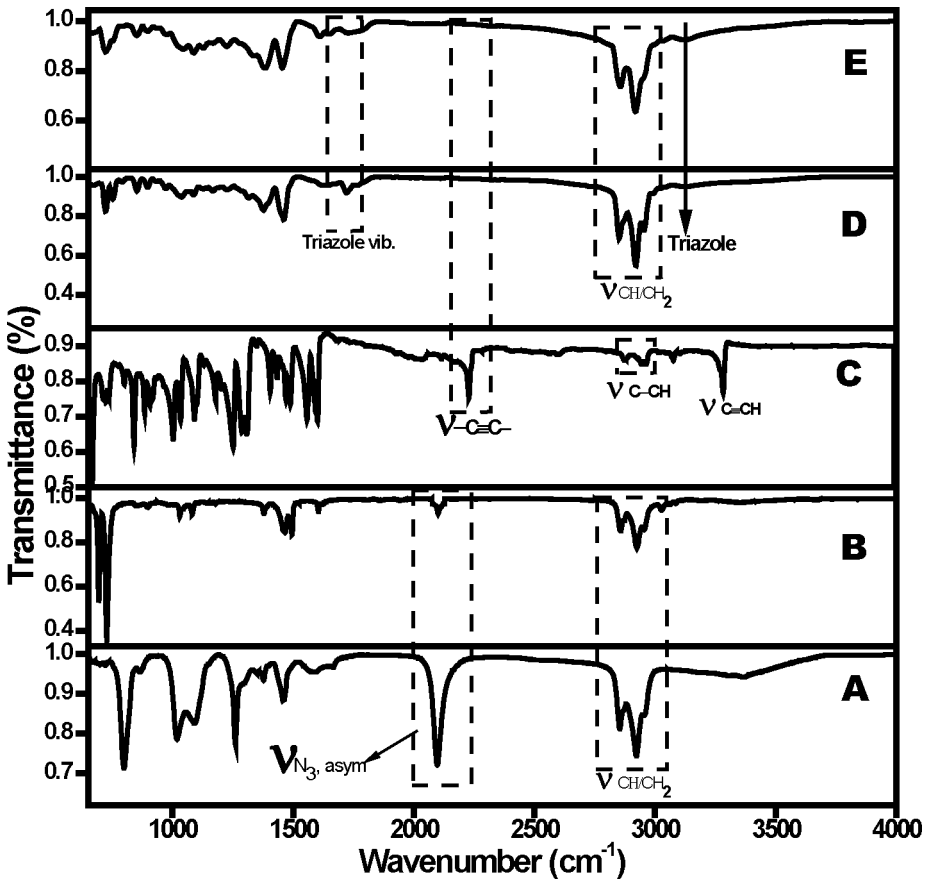

Figure 3.8: FT-IR spectra of (A) azidopropylamine, (B) azide functionalized AuNPs, (C) 3 (as a representative) (D) 3-AuNPs and (E) 2-AuNPs.

3.2.1.2 XRD Data

The X-ray diffraction patterns of as-prepared gold nanoparticles before and after Huisgen cycloaddition click reaction to complexes **2** and **3** are shown in **Figure 3.9**. Five diffraction peaks were observed in the XRD spectra of both TOABr-AuNPs (A) and azide functionalized AuNPs (B). These peaks are positioned at 2θ= 38.38° (111), 44.67° (200), 64.91° (220), 77.89° (311) and 82.32° (222), and were indexed to face-centred cubic structure of pure gold [240]. Phthalocyanine is a carbon-based-amorphous organic molecule, hence broad peaks around 2θ = 23-25° (using

2 (**Figure 3.9C**) as a representative) correspond to the 002 reflection plane of carbon which is the major constituent of phthalocyanines [241]. Successful click reaction between azide functionalized AuNPs and the phthalocyanines was confirmed by the presence of additional broad peak covering 2θ = 17-25° in the XRD patterns of **3-AuNPs** (D) and **2-AuNPs** (E). Also, reduction in the crystallinity of AuNPs was observed after click reactions as evidenced by the broadening of the peaks, **Figure 3.9**.

3.2.1.3 TEM images

Shape and size distribution of the gold nanoparticles and the conjugates were confirmed by transmission electron microscopy (TEM) analysis as shown in **Figure 3.10A-D**. **Figure 3.10A** shows TOABr-protected AuNPs as monodispersed spherical AuNPs with an average particle size of 5 ± 2 nm. After surface modification with 3-azido-1-propylamine, the average particle size of AuNPs was observed to increase to 9 ± 2 nm due to reduction in the interparticle distance between the NPs (hence increased agglomeration) as shown in **Figure 3.10B** [242]. The TEM images of **3-AuNPs** and **2-AuNPs** (**Figure 3.10C, D**) revealed highly aggregated particles after coupling of AuNPs to phthalocyanines; the aggregation can be attributed to the coalescence of neighbouring nanocrystals to form large single or twinned crystals [242,243]. Also, aggregation due to π–π stacking interaction of the aromatic ring of phthalocyanine on nanoparticles has been reported in the literature [220].

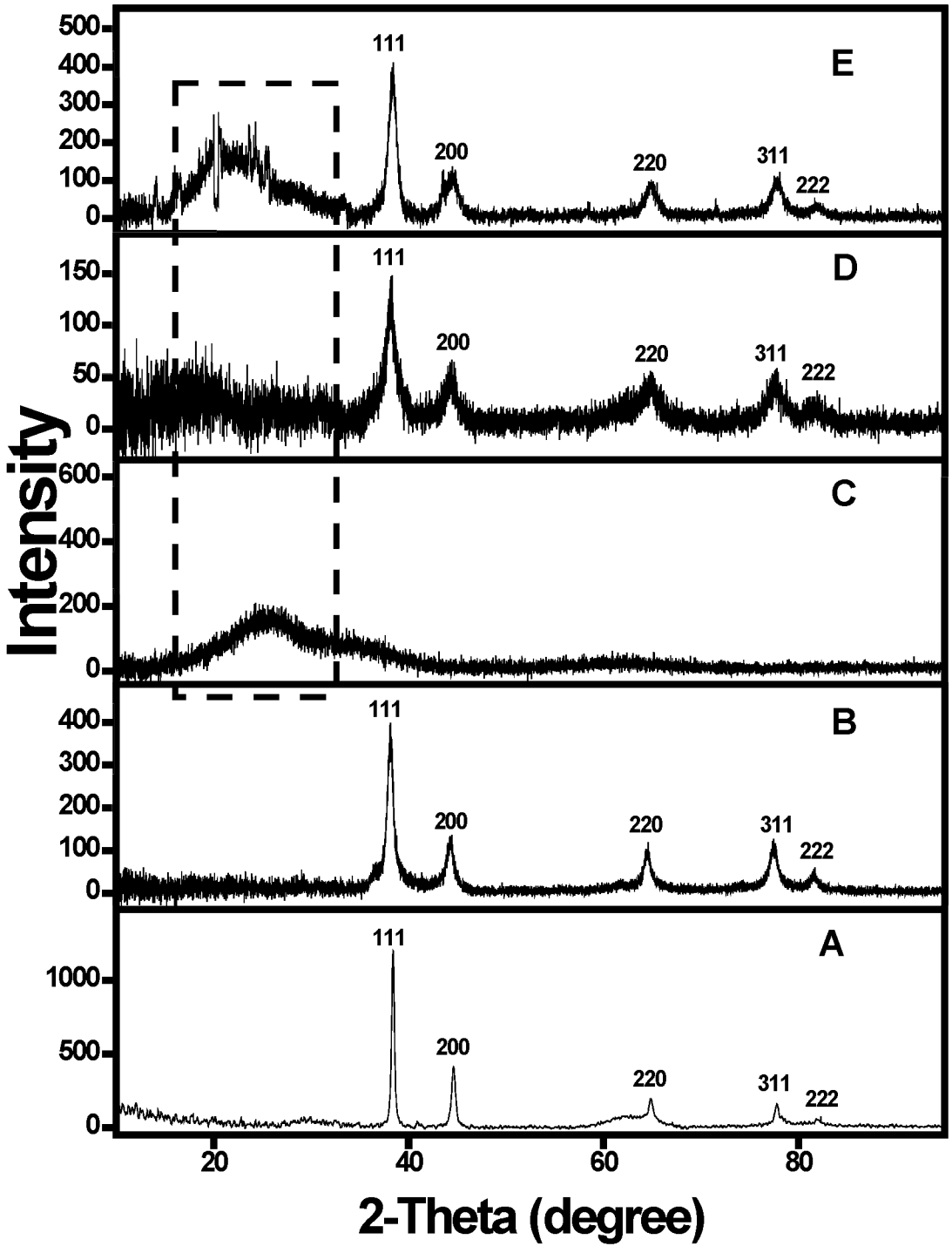

Figure 3.9: X-ray diffraction patterns of (A) TOABr-AuNPs, (B) azide functionalized AuNPs, (C) 2 (as representative), (D) 3-AuNPs, and (E) 2-AuNPs

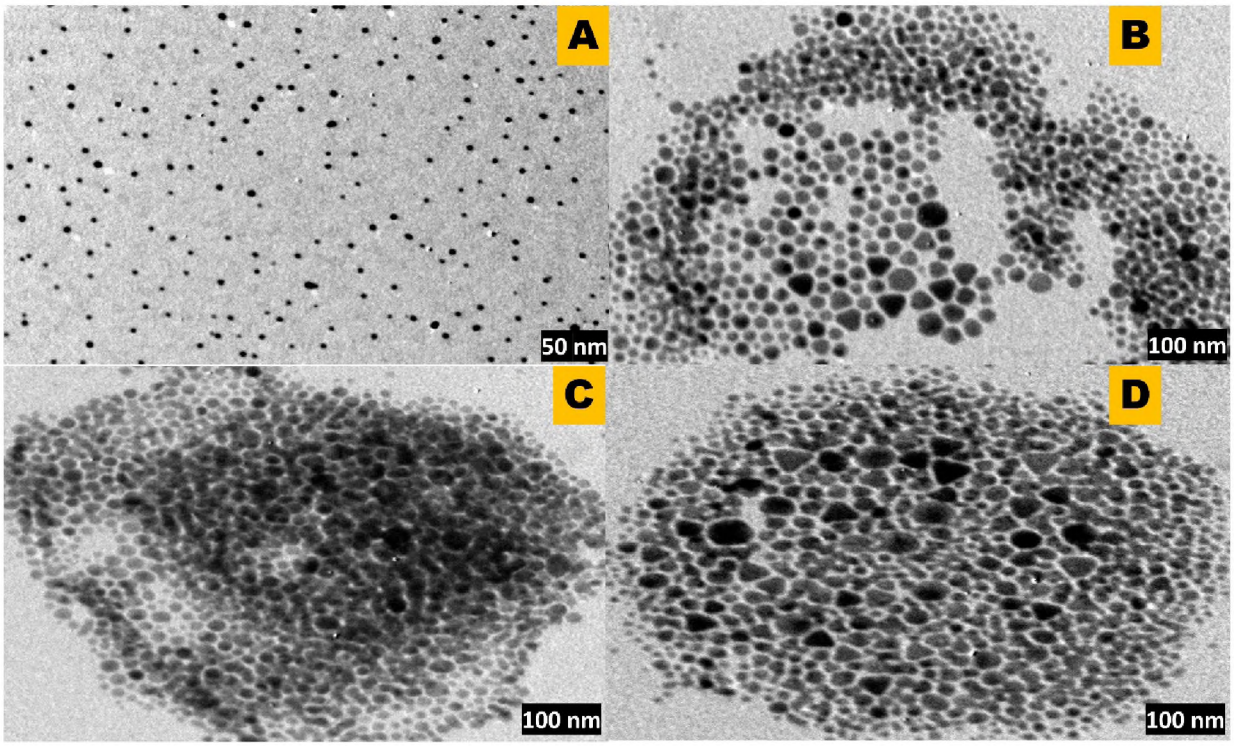

Figure 3.10: Transmission electron microscope (TEM) images of (A) TOABr-AuNPs, (B) azide functionalized AuNPs, (C) 3-AuNPs and (D) 2-AuNPs.

3.2.1.4 Ground state electronic absorption and fluorescence studies

Figure 3.11 shows the UV-vis absorption spectra of as-prepared TOABr protected AuNPs (**a**, black curve) and when ligated to azidopropylamine (**b**, red curve) measured in toluene. The surface plasmonic resonance (SPR) which is size and shape dependent was observed to peak at 523 nm for TOABr-AuNPs, while the slightly broadened SPR peak for azide-derivatized AuNPs was red-shifted at 530 nm. The shift to longer wavelength of azide functionalized AuNPs indicates increase in size of the AuNPs after surface modification due to reduction in the interparticle distance between the gold nuclei [174,175,242]. The increase in size was as also confirmed by TEM results above.

The Q band of **3** blue-shifted from 684 nm to 681 nm after the click reaction with AuNPs, **Table 3.2**. No shift in the Q band of **2** in presence of AuNPs was observed. Broad absorption peaks at around 543 nm for **2-AuNPs** (**d**) and 535 nm for **3-AuNPs** (**c**) are due to the SPR of AuNPs. This confirms the successful coupling of AuNPs to the phthalocyanines.

Normalized absorption, fluorescence emission and excitation spectra of **2-AuNPs** and **3-AuNPs** in DMSO are shown in **Figure 3.12 A** and **B**. The fluorescence of **2-AuNPs** is weak due to the combined heavy atom effects of In and AuNPs, **Figure 3.12 A**. The excitation spectrum appeared broadened and slightly shifted to longer wavelength compared to its absorption spectrum. This is due to possible displacement of In metal from the centre of the phthalocyanines ring upon excitation [237]. Unlike **2-AuNPs**, the ground and excited states of **3-AuNPs** have similar molecular geometries after excitation as seen from the monomeric Q bands of the absorption and excitation spectra, **Figure 3.12B**. However, both **2-AuNPs** and **3-AuNPs** have broad absorption bands around 520-550 nm in their absorption spectra due to the SPR of the coupled AuNPs which are conspicuously absent in their excitation spectra.

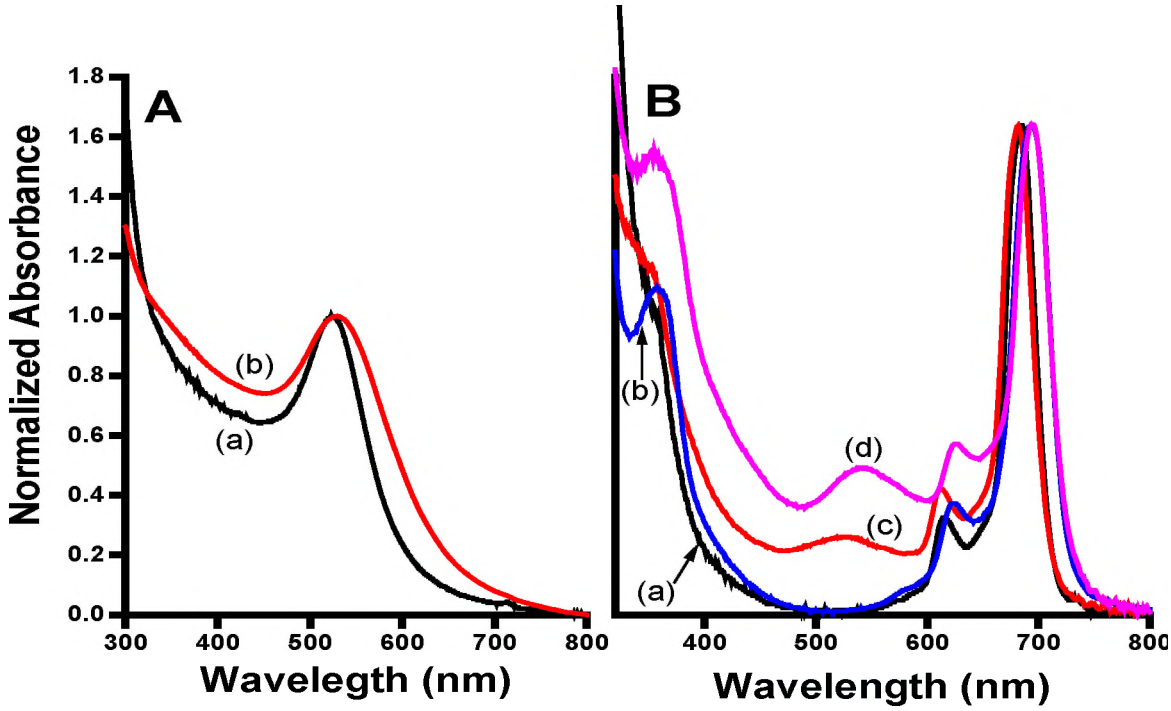

Figure 3.11: Absorption spectral of (A) TOABr-AuNPs (a), azide functionalized AuNPs (b) (in toluene); and (B) 3 (a), 2 (b), 3-AuNPs (c), and 2-AuNPs (d) in DMSO.

Table 3.2: Photophysical parameters for 2, 3, 3-AuNPs and 2-AuNPs recorded in DMSO.

Parameter	2	3	2-AuNPs	3-AuNPs
λ_{abs} (nm)	693	684	693	681
λ_{em}(nm)	710	695	706	694
λ_{exci} (nm)	706	684	703	682

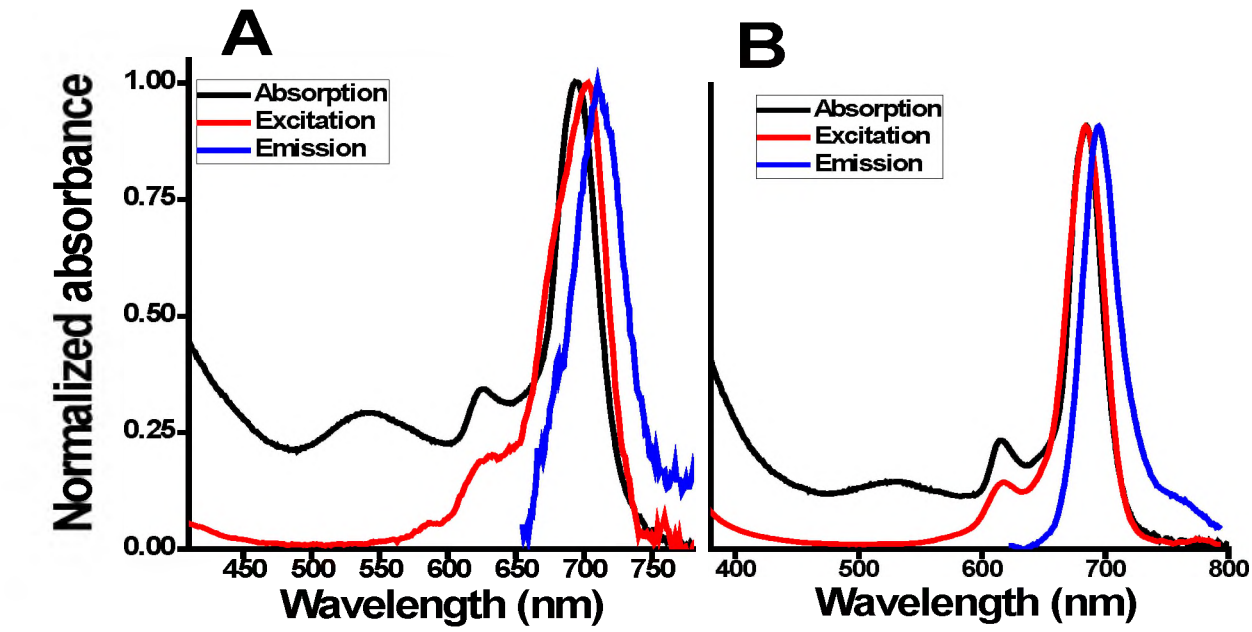

Figure 3.12: Absorption, fluorescence emission and excitation spectra of (A) 2-AuNPs (λ_{exc} = 610 nm) and (B) 3-AuNPs (λ_{exc} = 610 nm). Concentration 1.56 × 10-6 M in DMSO.

3.2.1.5 XPS spectra

Surface chemical compositions of as-prepared azide-derivatized AuNPs and the MPc-AuNPs conjugates were investigated by X-ray photoelectron spectroscopy (XPS), and presented in **Figure 3.13**. Full scan XPS spectra of azide functionalized AuNPs revealed peaks at ≈83.3 eV (Au $4f_{7/2}$) and ≈87.1 eV (Au $4f_{5/2}$) with a spin-orbit splitting (3.8 eV) corresponding to elemental gold (Au^0) [244], **Figure 3.13A**.

The presence of N1s peaks at ca. 401.6 eV on the XPS spectrum of AuNPs confirm successful immobilization of 3-azido-1-propylamine on AuNPs. XPS spectra of **3-AuNPs** and **2-AuNPs** confirmed the presence of Zn at 1022 ($Zn2p_{3/2}$) and 1045.6 ($Zn2p_{1/2}$) eV; and In at 442 ($In3d_{5/2}$) and 453.3 ($In3d_{3/2}$) eV, respectively. Intensities of C1s at 285 eV significantly increased after coupling of Pcs to AuNPs. Reduction in the signal strengths of Au after coupling was observed due to the loading of phthalocyanine macrocycles on the AuNPs, **Figure 3.13B**.

The success of click reactions between azide functionalized AuNPs and the phthalocyanines was verified by comparing the N1s spectra of the conjugates to free phthalocyanines and azide functionalized AuNPs. **Figure 3.13C** shows the deconvoluted N1s spectrum of azide-derivatized AuNPs which deconvoluted into two chemically distinct peaks at 400.54 eV and 402.12 eV, these peaks correspond to N–**N**=**N** and **N**–N=N, respectively, confirming the presence of azide molecules on AuNPs. The absence of the C–NH_2 peak at 400 eV proves the participation of the amine in conjugation with gold surface [149]. The N1s core level spectrum of phthalocyanine (**2** as representative) shows only one peak due to N-C positioned at 399.14 eV. N1s core level spectrum of the **3-AuNPs** were independently deconvoluted into three binding energies at 399.43 eV, 402.30 eV and 403.30 eV corresponding to N-C, N–**N**=**N** and **N**–N=N, respectively. Similarly, N1s spectra of **2-AuNPs** for N-C, N–**N**=**N**and **N**–N=N were positioned at 399.84 eV, 402.55 eV and 403.65 eV. The average ratio of the peak areas of N–**N**=**N** to **N**–N=N is about 2.5:1, and close to stoichiometric ratios of 3:1 reported in the literature [245-247]. Both N–**N**=**N** and **N**–N=N peaks of the conjugates shifted from ca. 400.54 eV and 402.12 eV of AuNPs to higher binding energies after click reactions. This suggests possible change in chemical environments from linear N_3 to triazole ring structures formation. Also, the change in the shapes of the deconvoluted N1s spectra of the conjugates compared to the free phthalocyanines and azide functionalized AuNPs confirmed successful click interactions between azide functionalized AuNPs and the phthalocyanines.

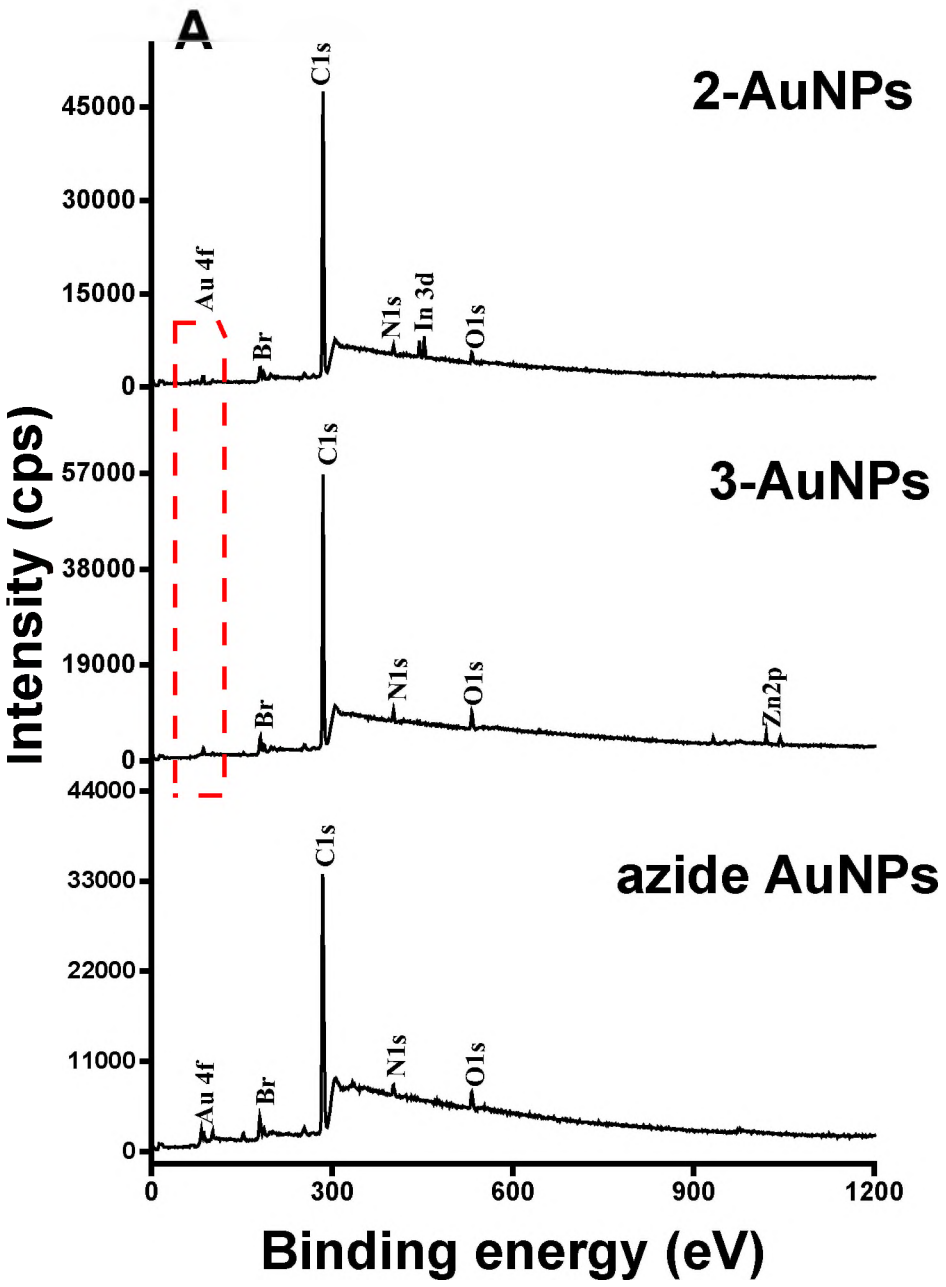
A
2-AuNPs
3-AuNPs
azide AuNPs
Intensity (cps)
Binding energy (eV)
C1s
Au 4f
Br
N1s
In 3d
O1s
Zn2p
45000
30000
15000
0
57000
38000
19000
44000
33000
22000
11000
300
600
900
1200

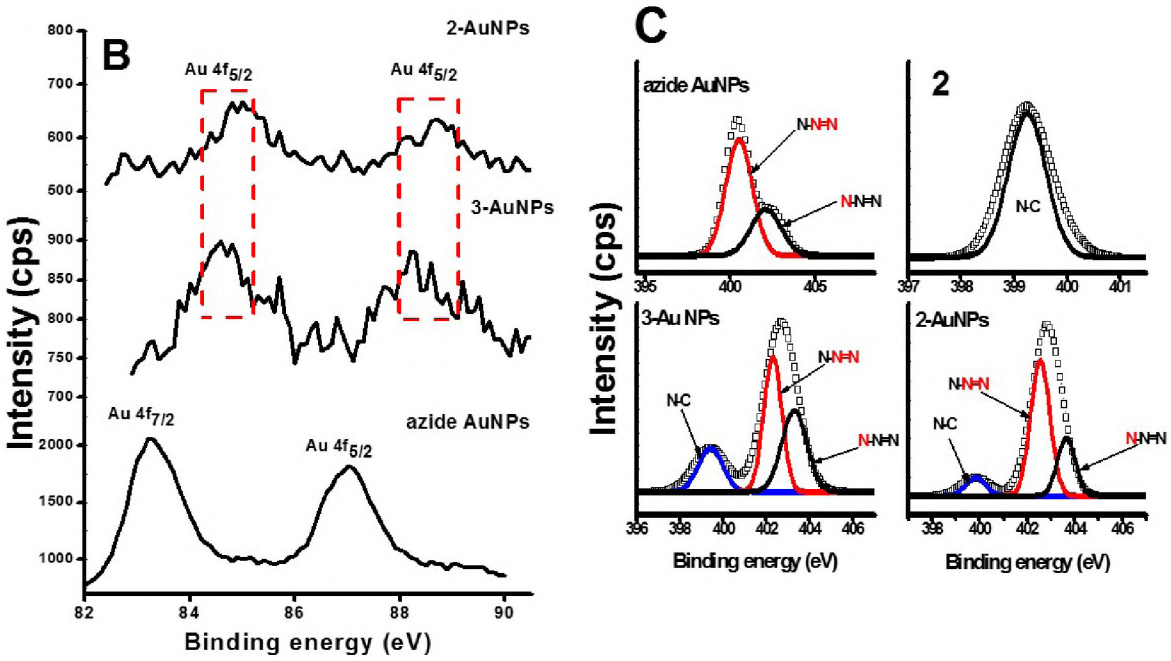

Figure 3.13: (A) Wide scan XPS spectra for (A) azide functionalized AuNPs, 3-AuNPs and 2-AuNPs, (B) expansion of the $Au4f_{7/2}$ and $Au4f_{5/2}$ doublet for AuNPs in azide functionalized AuNPs, 3-AuNPs and 2-AuNPs and (C) High resolution of N1s component for azide functionalized AuNPs, 2, 3-AuNPs and 2-AuNPs.

3.2.2 C covalent linking of complex 10 to nanomaterials or polymer via amide bonding (Schemes 3.7 - 3.10)

The formation of amide bonds between **10** and the nanomaterials were carried out using EDC/NHS [226,248] coupling reactions in a mixture of DMF/H2O (1:1 v/v); **10** was complexed to polyacrilic acid (PAA) in DMF using mixture of DCC and DMAP [220,249]. EDC/NHS (or DCC/DMAP) were used to protonate (or activate) the carboxylic groups (–COOH) of the nanomaterials (or PAA), and make them susceptible to amidation with the amino substituent on complex **10**.

3.2.2.1 Preparation of 10-AuNPs and 10-PAA (Scheme 3.7)

Synthetic pathways for the preparation of **10-PAA** (as representative) via amidation is shown in **Schemes 3.7**, and **3.6A** shows preparation of **10-AuNPs.**

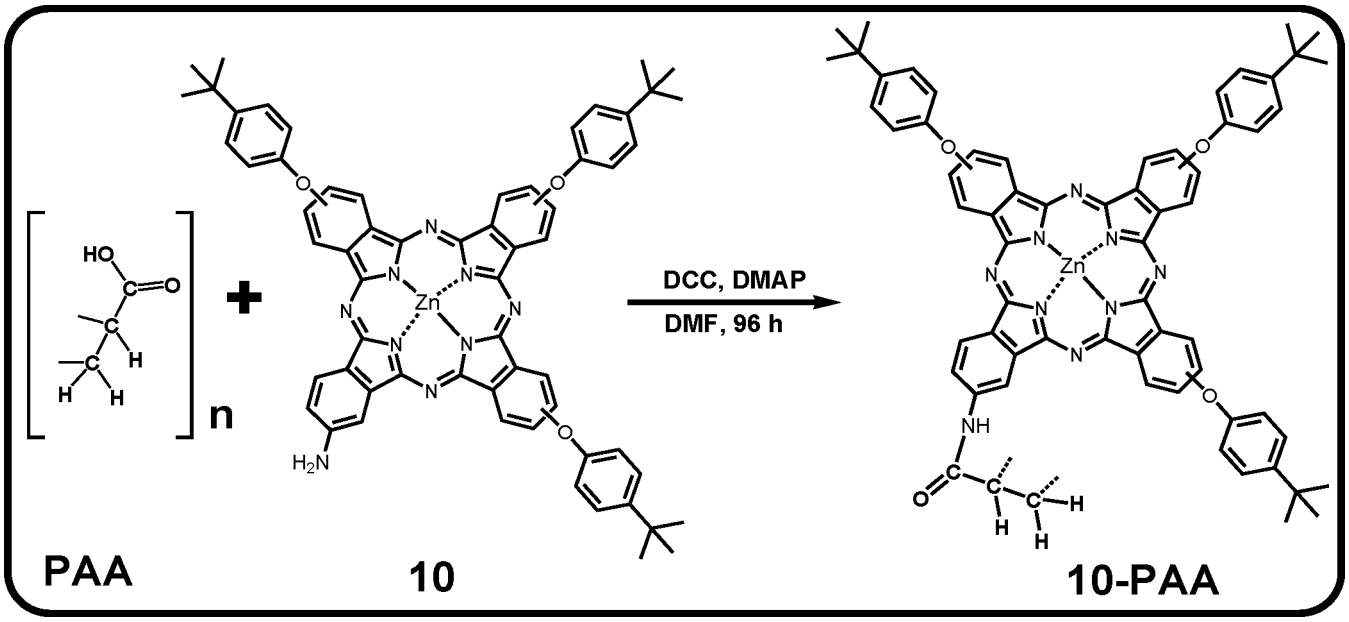

Scheme 3.7: Covalent linking between complex 10 and PAA.

3.2.2.1.1 FTIR Spectra

FTIR spectrum of **10** shows the presence of intense N-H bending mode at 1598 cm^{-1}, with corresponding broad N-H stretching modes between 3360 and 3230 cm^{-1} (**Figure 3.14**). The broad OH absorption bands of MPA-capped AuNPs and PAA, and the corresponding carbonyl stretching were respectively observed around 3100–3500 cm^{-1} and 1690–1700 cm^{-1}, prior to the covalent linking with **10**. The IR spectrum of **10-PAA** composite revealed strong N-H stretching mode at 3326 cm^{-1} due to secondary amide. Other notable peaks for **10-PAA** conjugates are the N-H bending and carbonyl group of amide at 1569 cm^{-1} and 1625 cm^{-1}, respectively. The spectrum of **10-AuNPs** composites showed that -C=O (1655 cm^{-1}) stretching overlapped with the N-H (1629 cm^{-1}) bending modes of amide composites. The shift in the positions of carbonyl positions after covalent functionalization confirmed electronic interactions between the **10** and PAA or AuNPs. When **10** and PAA or AuNPs are mixed with no chemical bond, these changes were not observed.

3.2.2.1.2 TEM images and XRD patterns

Figure 3.15 shows the TEM images of nanospherically shaped MPA-capped AuNPs alone and when covalently linked to **10**. The nanosphere shaped gold particles have estimated particle size of 5 nm (average). There is significant aggregation for the conjugate which may be attributed to the $\pi - \pi$ stacking interaction of the aromatic rings of the phthalocyanines.

Structural characterization of the synthesized phthalocyanine and its conjugates were verified using powder X-ray diffraction (**Figure 3.16**). The AuNPs showed well-defined patterns with experimental 2Θ values at 38.5° (111), 44.1 (200), 65.1°(220), 78.0°(311) and 82.3° (222), as also observed in **Figure 3.9 A** and **B**. The peaks are consistent with the reported Bragg's reflections of pure crystalline gold [240]. Amorphous nature of **10** and poly acrylic acid (PAA) revealed broad peaks in the range of 2Θ = 17–26° (002) and 17–38° (002), respectively. For **10**, the XRD pattern is typical of phthalocyanines [241,250]. Conjugation of **10** to PAA resulted in the formation of single broad peak suggesting low crystallinity in the **10-PAA** conjugate. XRD pattern of **10-AuNPs** shows weak extra peak at 24.4°due to the Pc in addition to AuNPs peaks.

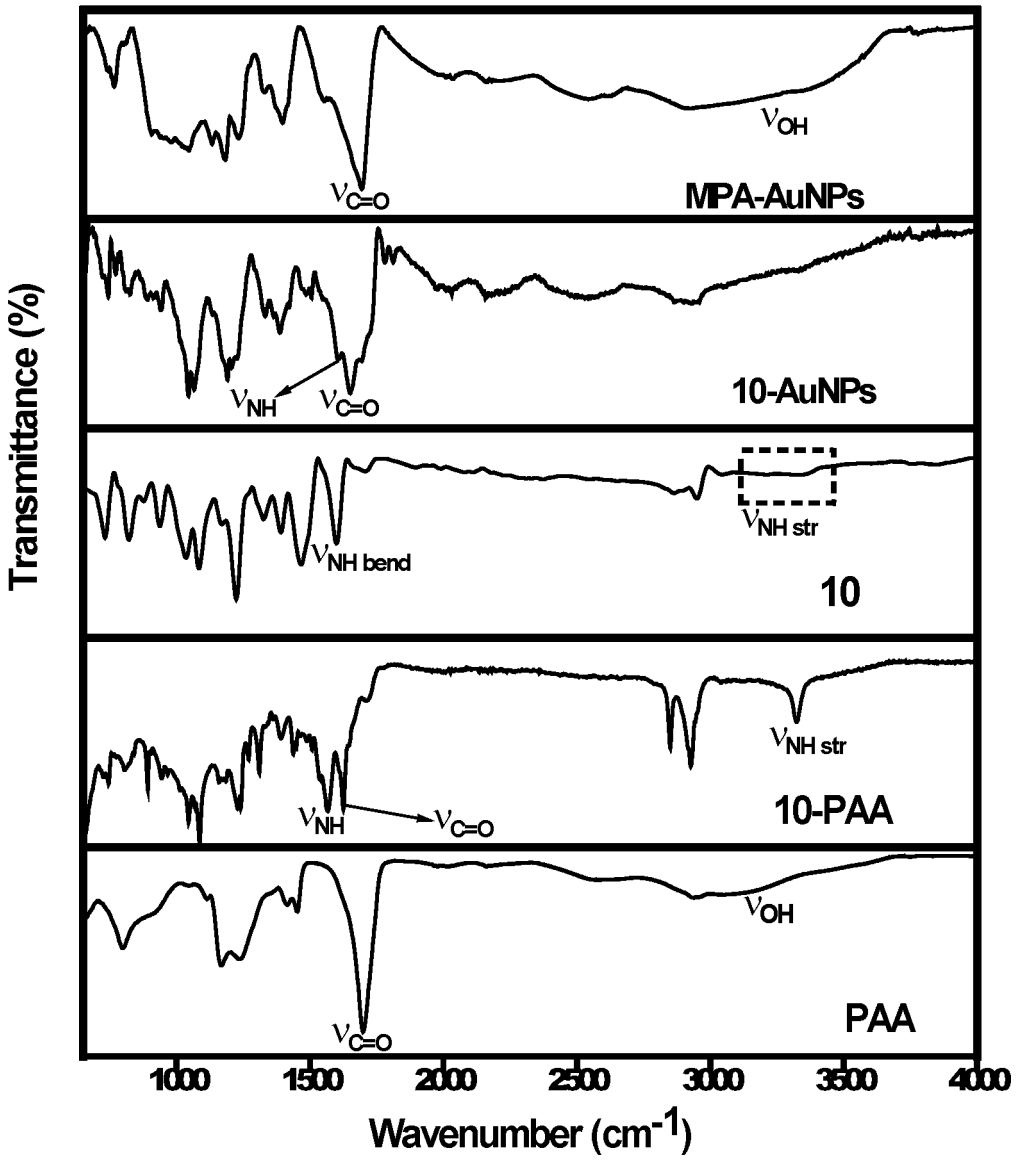

Figure 3.14: FTIR spectra of PAA, 10-PAA, 10, 10-AuNPs and MPA-capped AuNPs

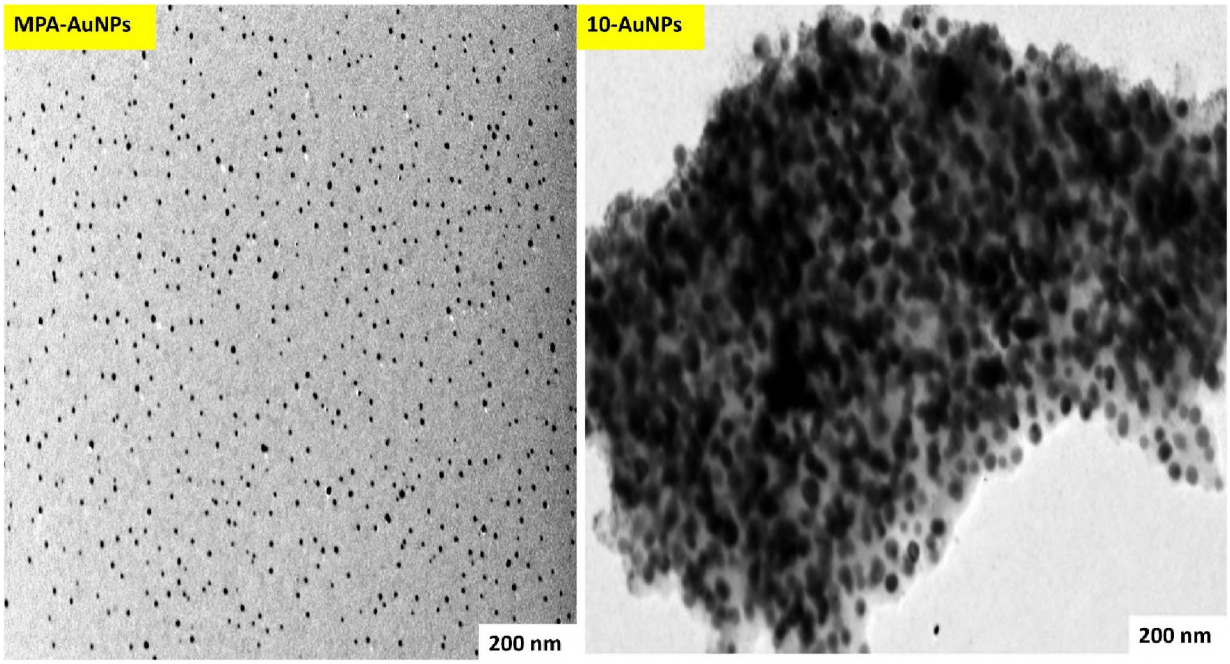

Figure 3.15: Transmission electron microscope (TEM) images of MPA-capped AuNPs and 10-AuNPs.

Table 3.3: Absorption, emission, and excitation spectral data for 10 and 10-nanomaterial composites in DMSO

Sample	Absorption (nm)	Emission, λ_{em} (nm)	Excitation,λ_{exc} (nm)
10	691	697	687
10-AuNPs	690	697	687
10-PAA	688	697	686
10-GQDs	686	698	686
10-NGQDs	687	697	687
10-SNGQDs	687	697	687
10-Fe_3O_4@Ag	683	693	685
10-Fe_3O_4-Ag	685	691	684

3.2.2.1.3 UV–vis absorption and emission

Electronic absorption spectra of **10** and **10-AuNPs** conjugates (in DMSO) alongside unconjugated MPA-capped AuNPs (in aqueous solution) are shown in **Figure 3.17**. The spectrum of MPA-capped AuNPs revealed a surface plasmon resonance absorption (SPR) band at 530 nm. The Q band absorption of **10** showed monomeric behaviour in DMSO at 691 nm, **Table 3.3**. The broadened Q band of **10** before conjugation is typical of NH_2 containing phthalocyanines [111]. Q band absorption of **10** (**Table 3.3**) was slightly red shifted compared to when conjugated to PAA. No significant shift was obtained for the Q band of **10-AuNPs** conjugates. The increase in intensity for **10–AuNPs** below 600 nm is due to the AuNPs SPR band contribution.

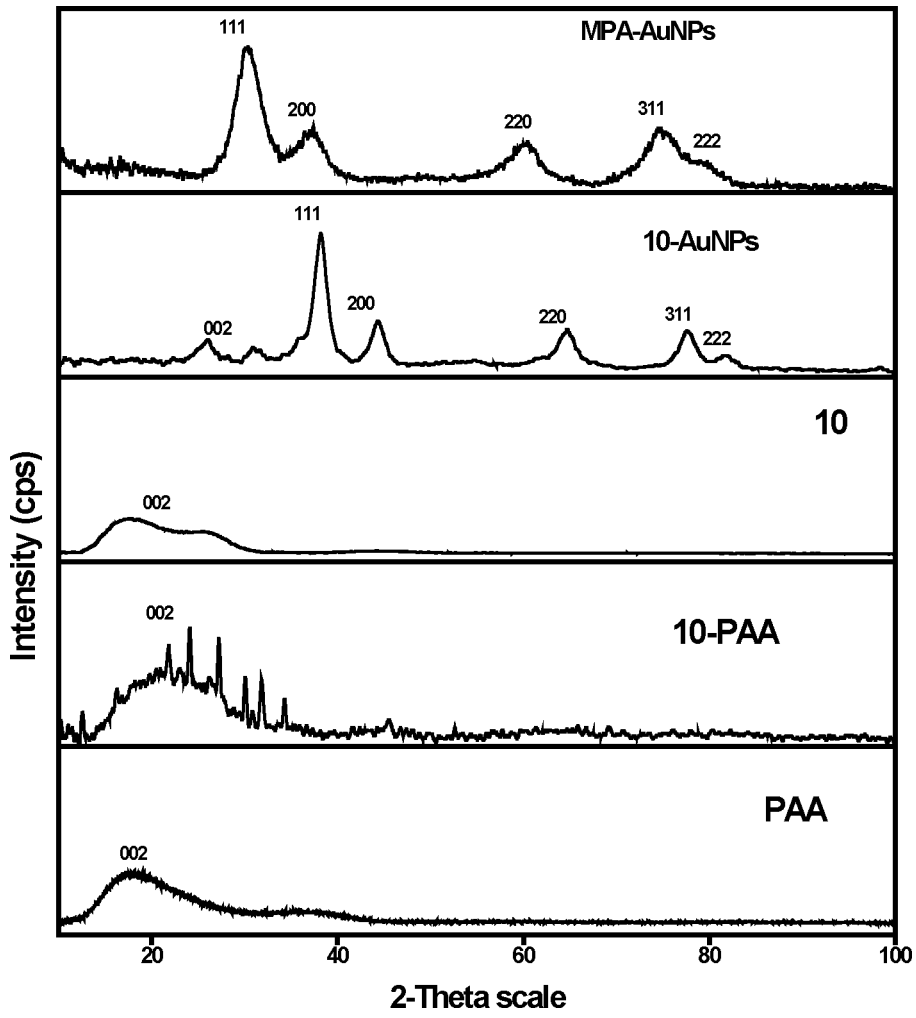

Figure 3.16: X-ray diffraction patterns of PAA, 10-PAA, 10, 10-AuNPs and MPA-capped AuNPs.

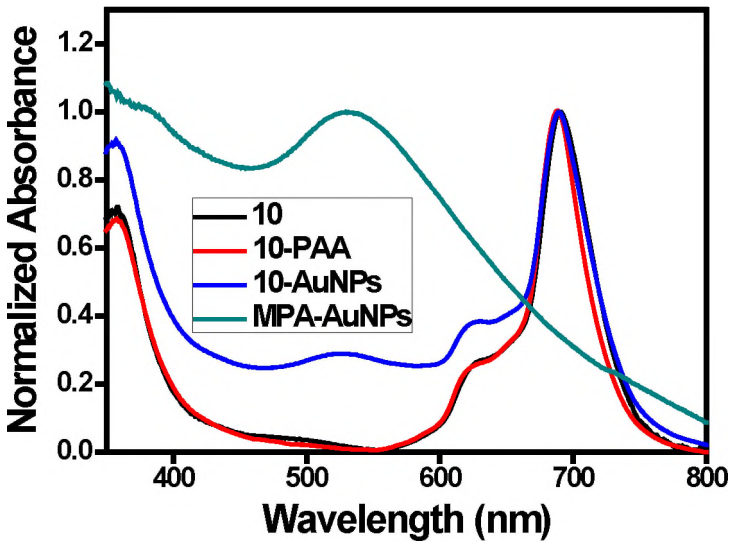

Figure 3.17: Absorption spectra of 10, 10-PAA, 10-AuNPS (in DMSO), and MPA-capped AuNPS (in water).

Normalized absorption, fluorescence emission and excitation spectra of **10-AuNPs** are shown in **Figure 3.18**. The Q band absorption, and excitation spectra are mirror images of each other. The slight shift in Q band maxima between the excitation and absorption wavelength may be due to different equipment used. The SPR contribution is absent in the excitation spectra.

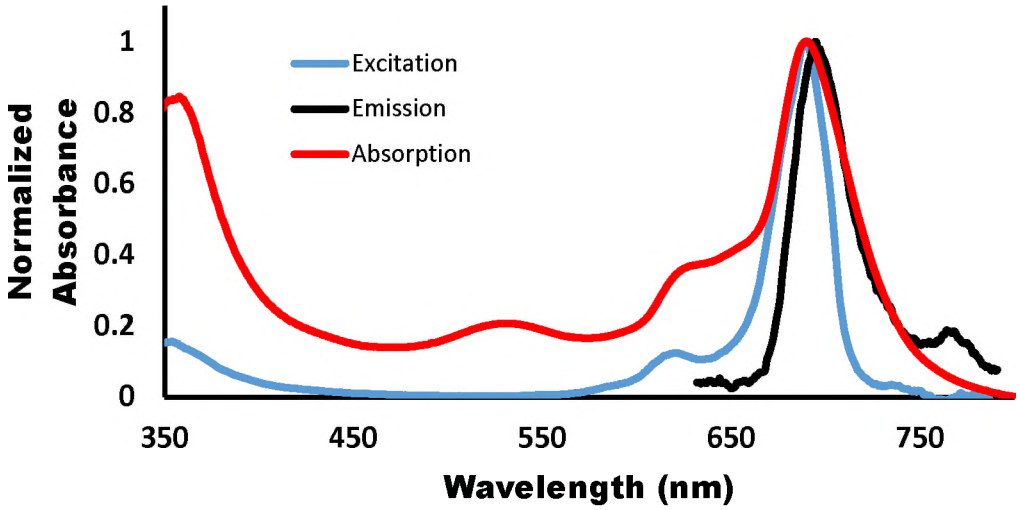

Figure 3.18: Absorption, fluorescence emission and excitation spectra of 10-AuNPs in DMSO. Conc. 1.2 x 10^{-6} M. Excitation wavelength = 613 nm.

3.2.2.2 Preparation of 10-GQDs, 10-NGQDs and 10-SNGQDs (Scheme 3.8B)

Scheme 3.8A shows the synthesis of GQDs, SNGQDs and NGQDs. The -COOH groups on the QDs were converted to active COO^- via EDC/NHS mediated coupling reaction, and linked to amino group of the phthalocyanine (**Scheme 3.8B**) to form amide bonds between **10** and the respective QDs. Depending on orientation, π-π interaction is also possible between **10** and the QDs. The conjugates obtained were purified and characterized by FT-IR, UV-Vis, TEM, XRD and EDX. The conjugates were soluble in DMF, DMSO.

A

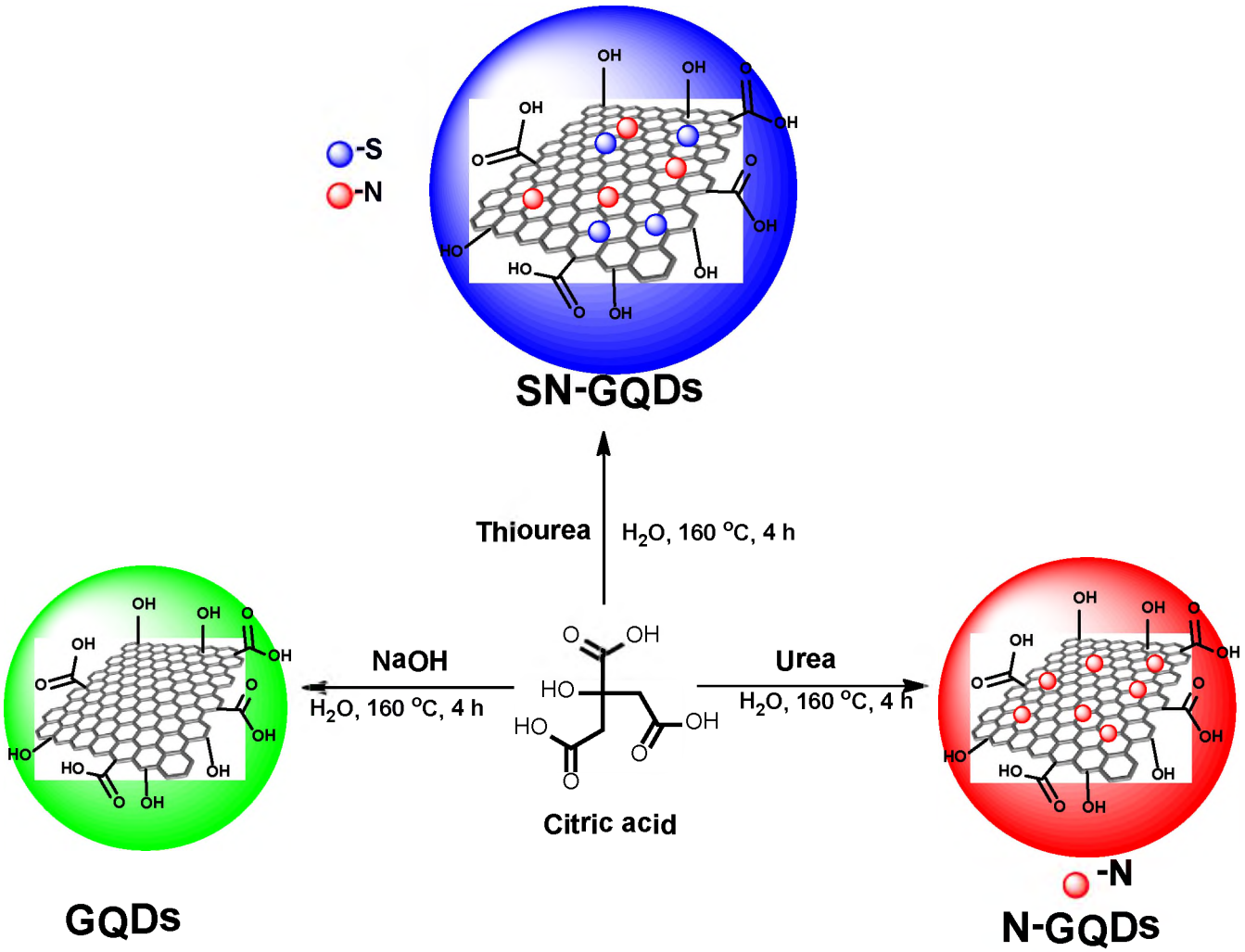

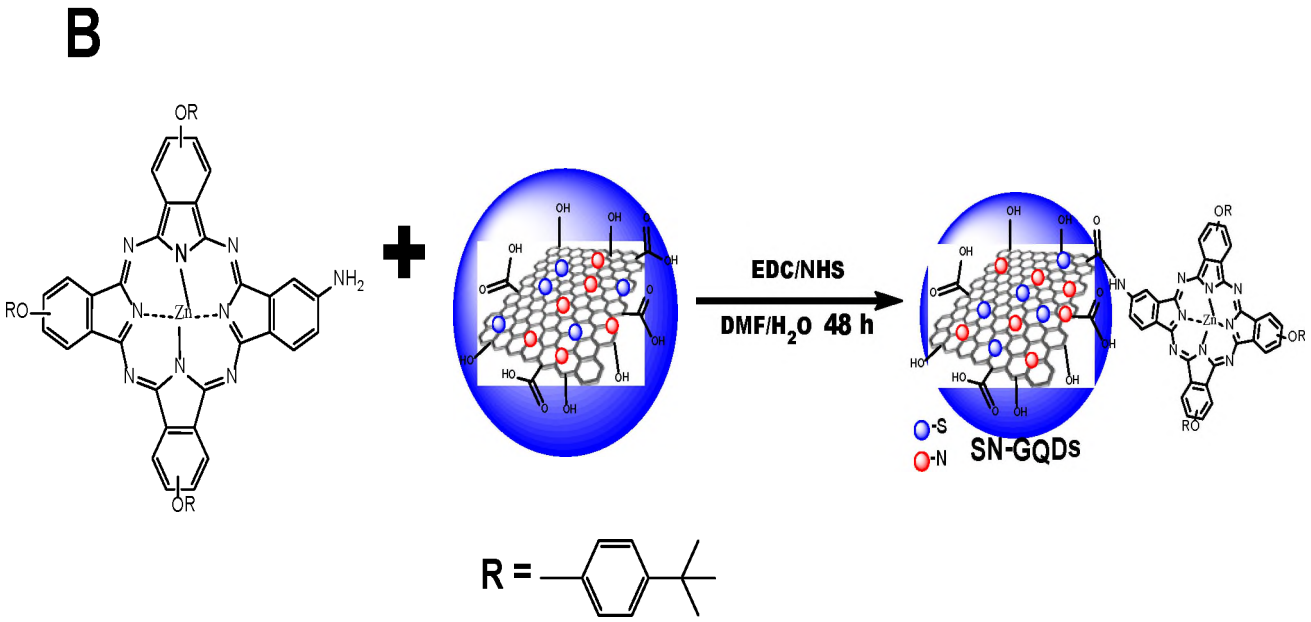

Scheme 3.8: (A) Synthesis of graphene quantum dots (GQDs), N-doped (N-GQDs) and S, N co-doped graphene (S, N-GQDs) and (B) Covalent linking of graphene quantum dots to 10.

3.2.2.2.1 FTIR spectra

The surface functional groups on the QDs as well as the amide bonding to **10** were verified by the FTIR spectra as shown in **Figure 3.19**. FTIR spectrum of pristine GQDs shows characteristic OH peak around 3400 cm^{-1} which is due to COOH on the surface of GQDs. For NGQDs and SNGQDs, the broad characteristic peaks due to OH/NH stretch around 2930-3400 cm^{-1} confirmed the presence of hydroxyl and secondary amine functional groups which co-existed on the surface of NGQDs and SNGQDs. These stretching vibrations of OH/NH were complemented by the presence of overlapped peaks of C=O (≈1705 cm^{-1}), and NH (≈1654 cm^{-1}) bending due to COOH and CONH, respectively, for NGQDs and SNGQDs. FTIR spectra of the conjugates (**10-GQDs**, **10-NGQDs** and **10-SNGQDs**) revealed intense characteristic bands at ≈ 1695-1702 cm^{-1}, ≈1647 cm^{-1} and 3340 cm^{-1} that are attributable to the amide vibrational bands of C=O, NH bending and NH stretch, respectively. This is an indication that the covalent linkages between carboxyl-functionalized QDs and amine of **10** were successful. Also, the shift in the vibrational modes of OH and/or NH and C=O positions before and after covalent

linking confirmed covalent interactions between the amine of phthalocyanine and carboxylic of QDs.

3.2.2.2.2 XRD data

The X-ray diffraction patterns of the as-prepared quantum dots and their phthalocyanine-QDs conjugates are shown in **Figure 3.20**. The diffraction patterns of the graphene quantum dots (GQDs, NGQDS and SNGQDs) appeared between 2Θ = 15° and 31° which corresponds to the graphitic structure [251,252]. The broadness of their diffraction peaks is an indication of the small size of the quantum dots. Like graphene quantum dots, the broad peak observed for **10** positioned between 2Θ = 18° and 27° is close to the 002 reflection plane of carbon which is the major constituent of phthalocyanines and QDs [241,250,253], see also **Figure 3.16**. Conjugation of the **10** to QDs resulted in slightly sharper peaks suggesting possible increase in the size of the conjugates which could arise due to π-π stacking layers of the conjugates. Also, noticeable reduction in the intensity of diffraction of **10** following conjugations to the graphene quantum was also observed.

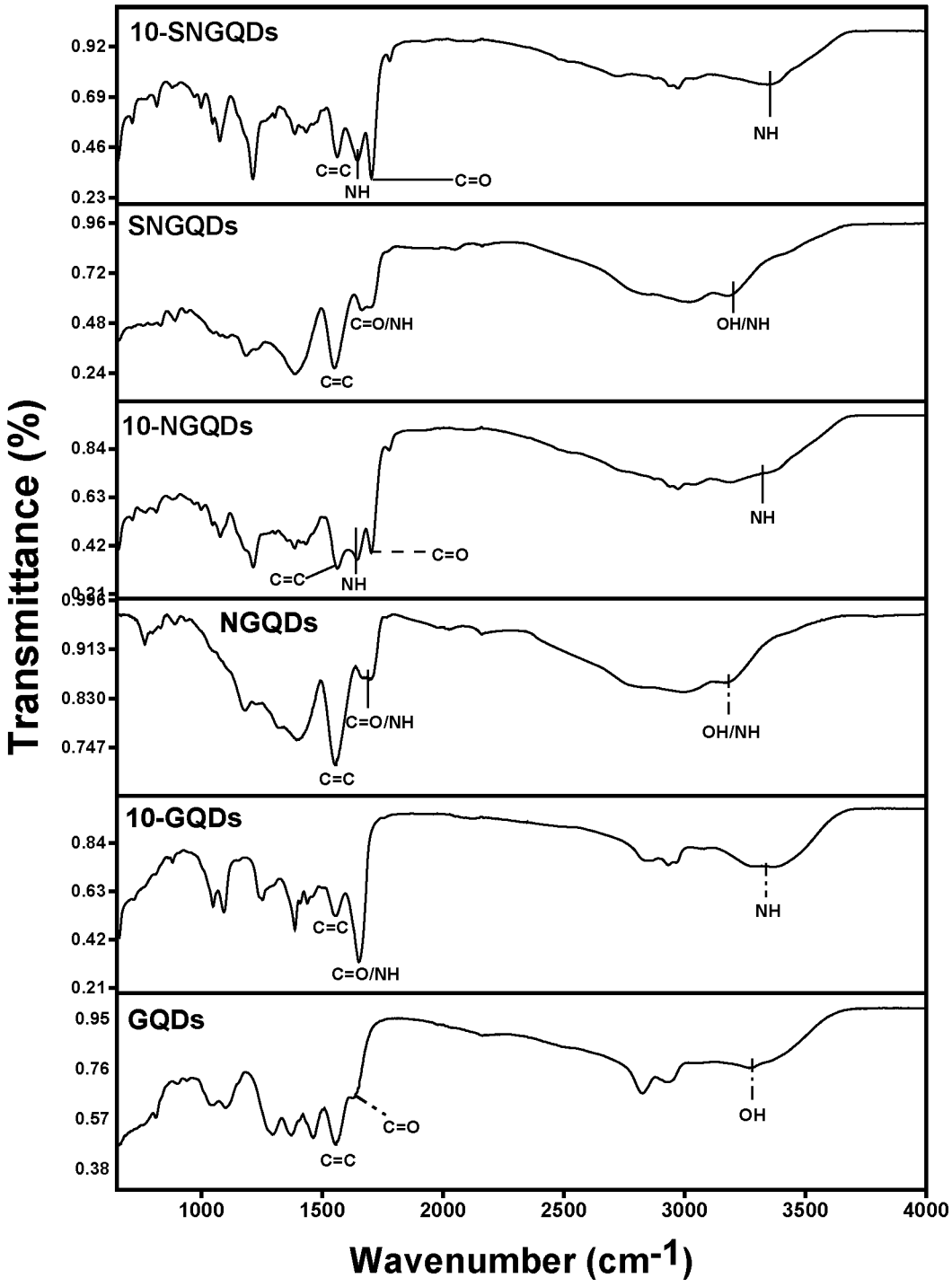

Figure 3.19: FT-IR spectra of bare GQDs, 10-GQDs, NGQDS, 10-NGQDs and SNGQDs and 10-SNGQDs.

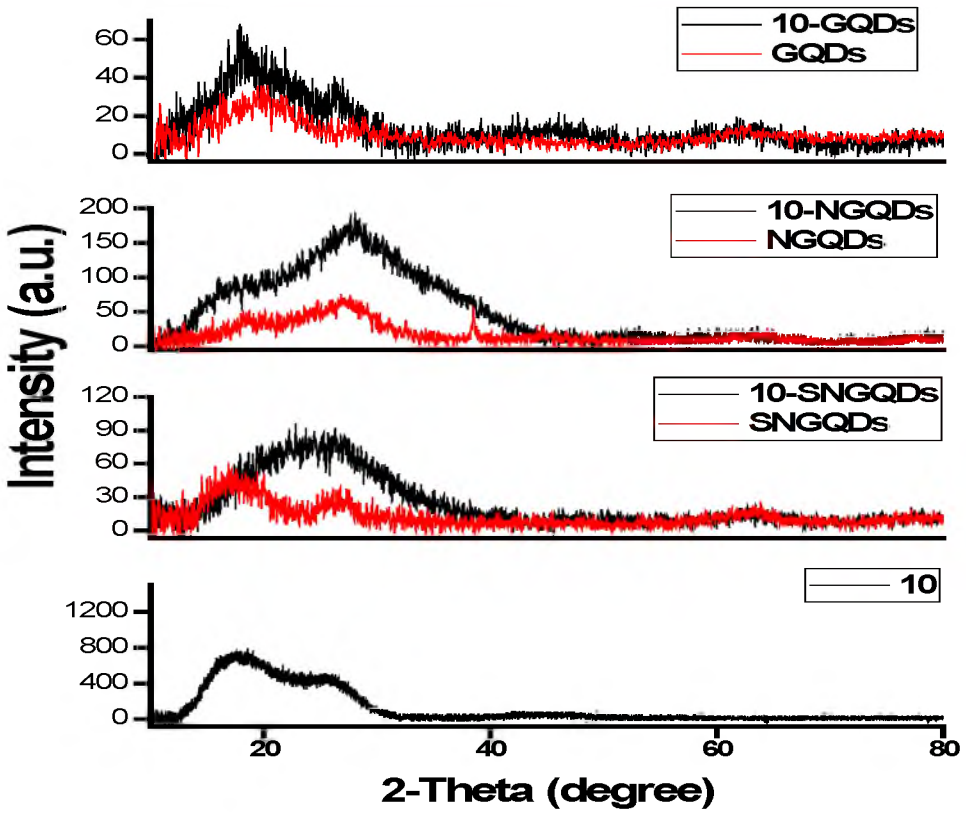

Figure 3.20: X-ray diffraction patterns of 10, SNGQDs, 10-SNGQDs, NGQDs, 10-NGQDs, GQDs and 10-GQDs.

3.2.2.2.3 TEM images

Transmission electron microscopy (TEM) micrographs showed that the as-prepared GQDs are monodispersed with fairly spherical morphology and average particle size of ~3 nm, **Figure 3.21**. The interparticle distances prevent aggregation of the nanoparticles. The conjugation of the GQDs to the phthalocyanines resulted in the formation of clusters due to interaction of neighbouring nanoparticles. Aggregation of graphene quantum dots in the presence of phthalocyanine can also arise due to π–π stacking interaction of the aromatic ring of the phthalocyanine with the graphene QDs, also among the GQDs.

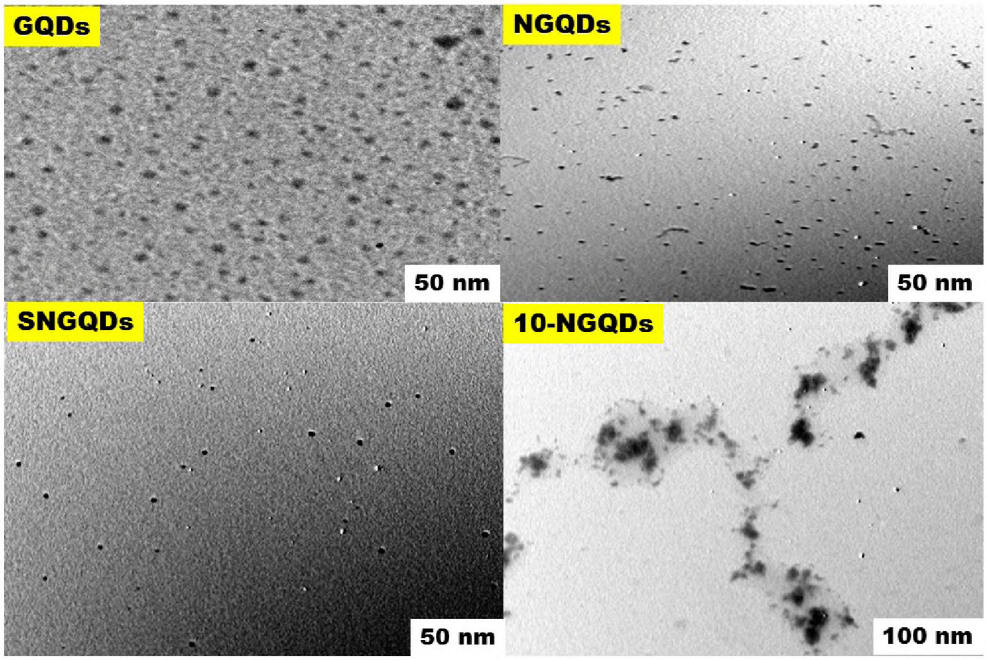

Figure 3.21: TEM images of pristine GQDs, NGQDs, SNGQDs and 10-NGQDs.

3.2.2.2.4 UV-Vis spectra

Figure 3.22A shows the UV-visible absorption and photoluminescence (PL) spectra of the as-prepared graphene QDs recorded in water. Absorption bands were observed at 334 nm for pristine GQDs and 341 nm for NGQDs. SNGQDs showed distinct absorption peak around 337 nm in addition to two other peaks positioned at 408 nm and 598 nm [198]. The photoluminescence (PL) spectra of NGQDs (blue dash dot line) and SNGQDs (red dash dot line) were slightly red-shifted compared to pristine GQDs (black dash dot line) due to the changes in chemical functionalities and defects on the graphene lattice by the heteroatoms [254]. The emission peaks of the GQDs were well resolved.

The absorption spectrum of **10** and when covalently linked to the QDs in DMSO are shown in **Figure 3.22B**. There was up to 5 nm shift to lower wavelengths for phthalocyanine-QDs nanocomposites, **Table 3.3**. Also, there is noticeable strong absorption in the B band region for the phthalocyanine-QDs nanocomposites compared to the free phthalocyanine, this corresponds to the region where the QDs absorb.

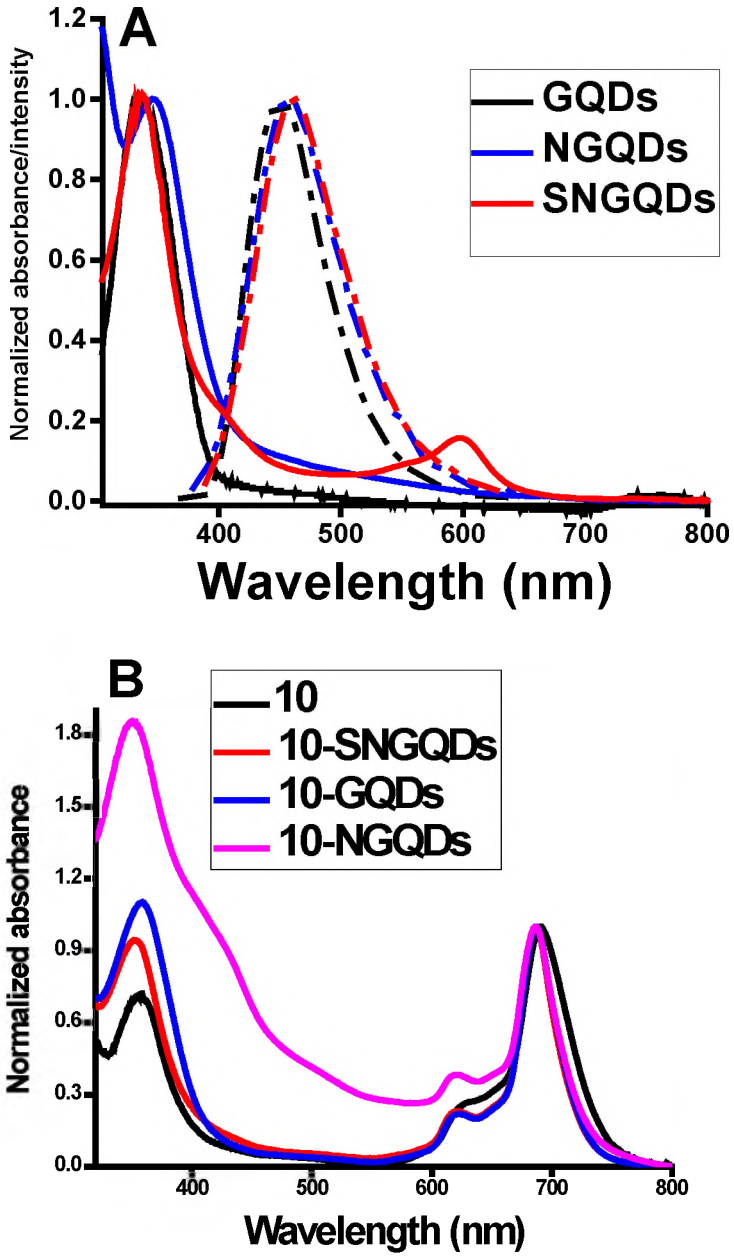

Figure 3.22: (A) Absorption (solid lines) and emission (dash dot lines) spectra of GQDs, NGQDs, and SNGQDs in water and (B) Absorption spectra of 10, 10-SNGQDs, 10-GQDs and 10-NGQDs composites in DMSO.

3.2.2.2.5 XPS spectra

X-ray photoelectron spectroscopy (XPS) was used to confirm the elemental compositions of pristine GQDs, NGQDs and SNGQDs before and after covalent bonding to **10**, **Figure 3.23**. The full survey scans of all the GQDs show expected atoms with NGQDs and SNGQDs showing addition of N, and N, S atoms, respectively which are not present in

pristine GQDs. The presence of Na auger peak at 298 eV in the XPS spectrum of GQDs is due to the NaOH used during its preparation. No other contaminating element(s) was detected in the XPS spectral of the QDs. The survey scans of **10-QDs** (using **10-SNGQDs** as example) showed the peaks due to C1s, S (2p and S 2s), N1s, and O1s, appearing along with Zn ($2p_{3/2}$ and Zn $2p_{1/2}$) in their respective peak positions.

Figure 3.24A shows the N1s spectrum of **10** which was deconvoluted into two chemically distinct peak positions at 399.11 eV and 400.97 eV, these peaks correspond to N–C of Pc (**10**) ring and N–H (from NH_2), respectively. Three distinct peaks corresponding to N–C, N–H and N–C=O were deconvoluted for the N1s of **10-GQDs** at 399.94, 401.12 and 402.13 eV, respectively, **Figure 3.24B**. The latter confirming the presence of the amide bond. N1s spectra of **10-SNGQDs** was deconvoluted to reveal the presence of pyridinic N, N-C/pyrrolic N, N-H and N–C=O at 399.25, 400.08, 401.06, and 401.97 eV, respectively, **Figure 3.24D**. The deconvolution of N1s spectrum of **10-NGQDs** (**Figure 3.24C**) gave similar peaks to those of **10-SNGQDs**, except that the N–C=O (due to amide bonding) shifted to higher binding energy at 403.10 eV. Pyridinic N and pyrrolic N peaks are due to the doping of graphene QDs with N-containing molecules [198,225].

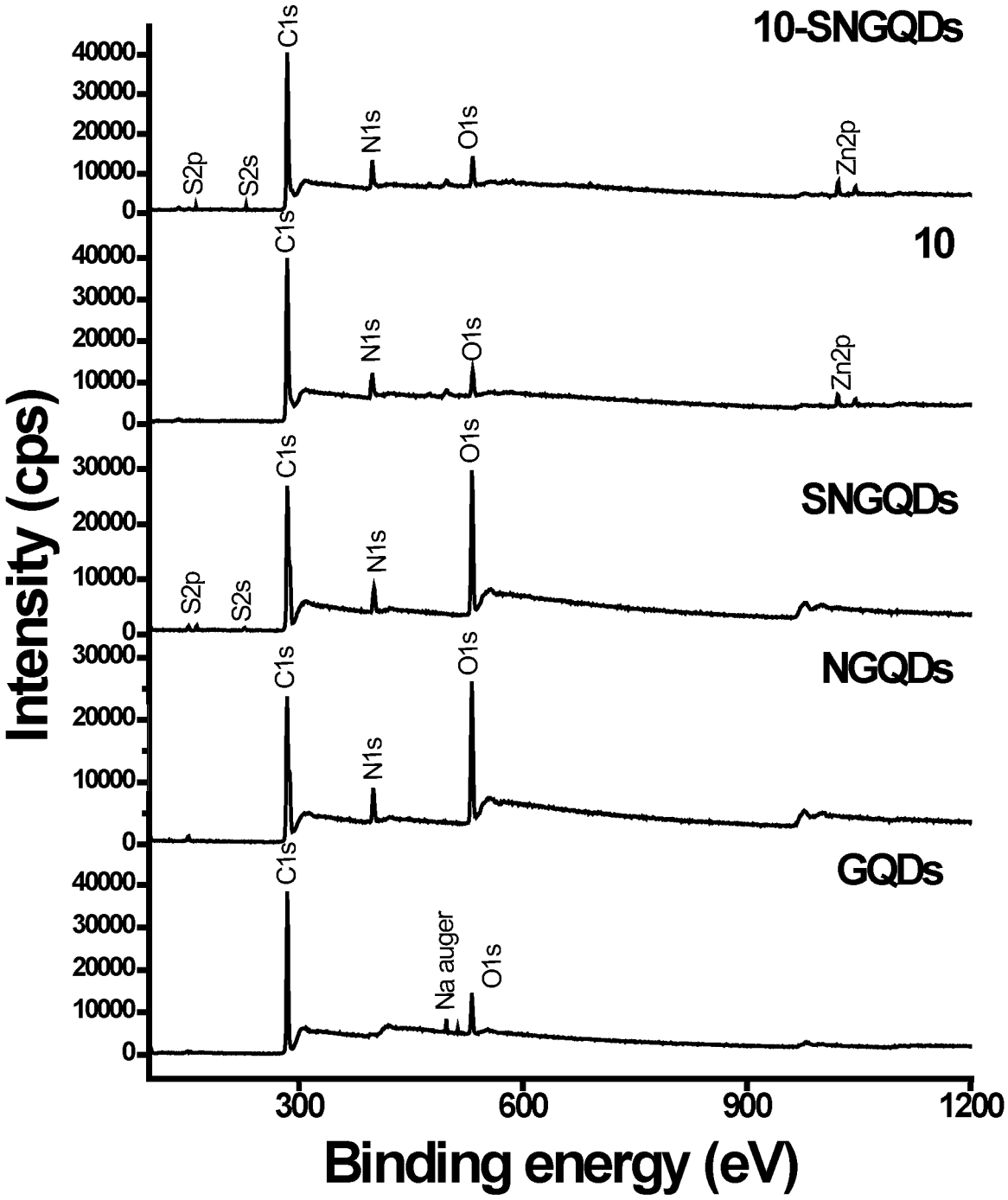

Figure 3.23: X-ray photoelectron wide-scan of (A) pristine GQDs, NGQDs and SNGQDs, (B) 10, and 10-SNGQDs.

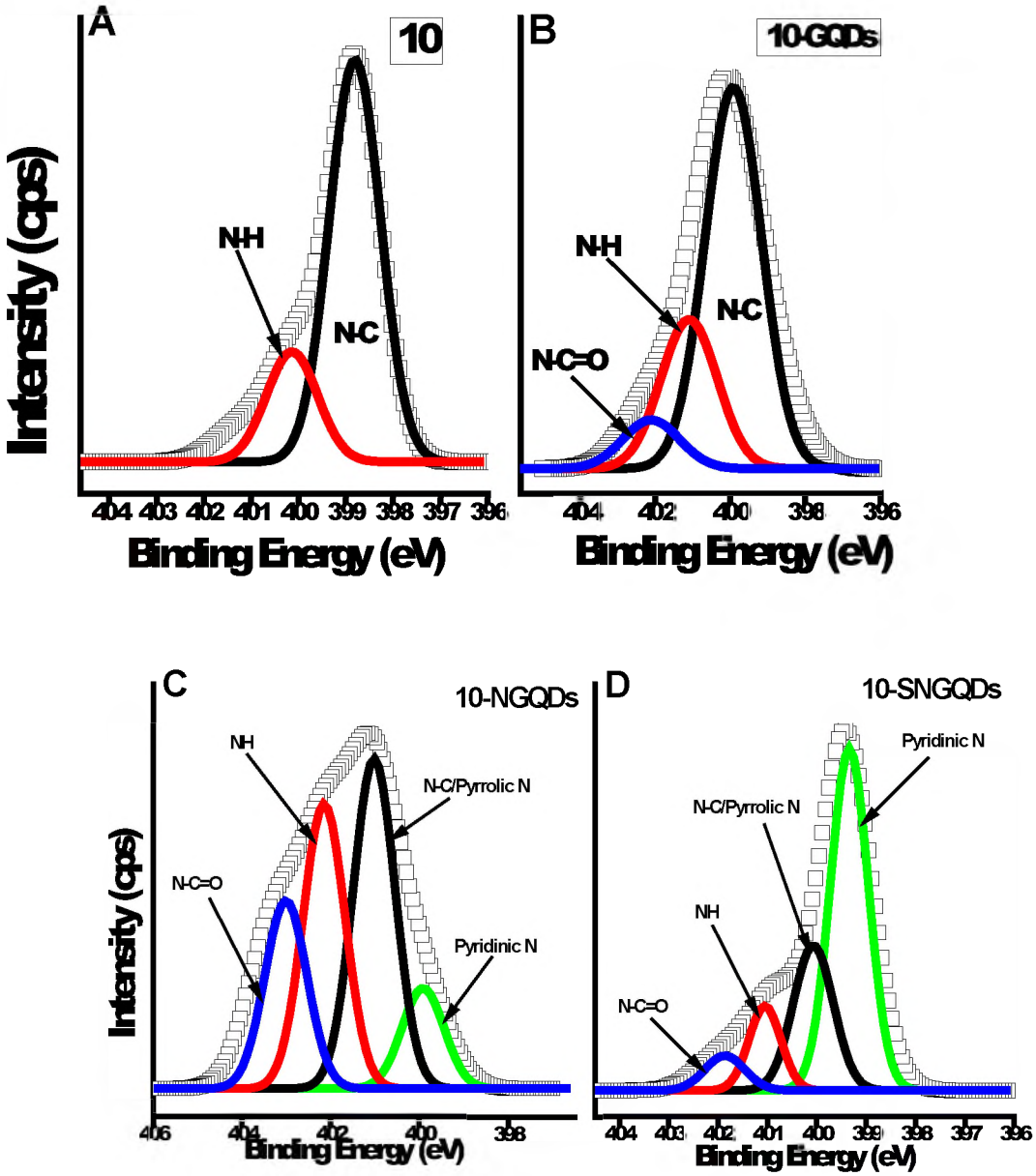

Figure 3.24: High resolution of deconvoluted N1s component for (A) 10, (B) 10-GQDs (C) 10-NGQDs, and (D) 10-SNGQDs.

3.2.2.3 Preparation of 10-Fe_3O_4-Ag and 10-Fe_3O_4@Ag (Schemes 3.9 and 3.10)

The synthesis of the Fe_3O_4 NPs precursor has been reported [223,224]. Core–shell nanoparticles of Fe_3O_4@Ag NPs were formed by deposition of the silver shell on Fe_3O_4 NPs in the presence of oleic acid and oleylamine dissolved in phenyl ether solution, following the procedure reported for Fe_3O_4@Au core–shell NPs [223]. Heterodimer

nanostructures of Fe_3O_4-Ag NPs were synthesized by reducing and growing Ag domains on the pre-synthesized Fe_3O_4 NPs seeds. The reduction and growth of Ag on the surface of seed nanoparticles of Fe_3O_4 NPs to form Fe_3O_4-Ag NPs proceeded under mild reaction conditions compared to the formation of Fe_3O_4@Ag NPs. The presence of capping ligands such as oleic acid and oleylamine on the surface of synthesized NPs endowed them high degree of dispersibility in many organic solvents such as toluene, hexane, chloroform, etc. Ligand exchange of oleic acid/oleylamine capped-nanoparticles with anchoring chemical groups such as thiols (**Schemes 3.9A** and **3.10A**) enabled further functionalization of the NPs to other molecules. Synthetic pathways for the preparation of **10-Fe_3O_4-Ag** and **10-Fe_3O_4@Ag** via amidation are represented in **Schemes 3.9B** and **3.10B**, respectively.

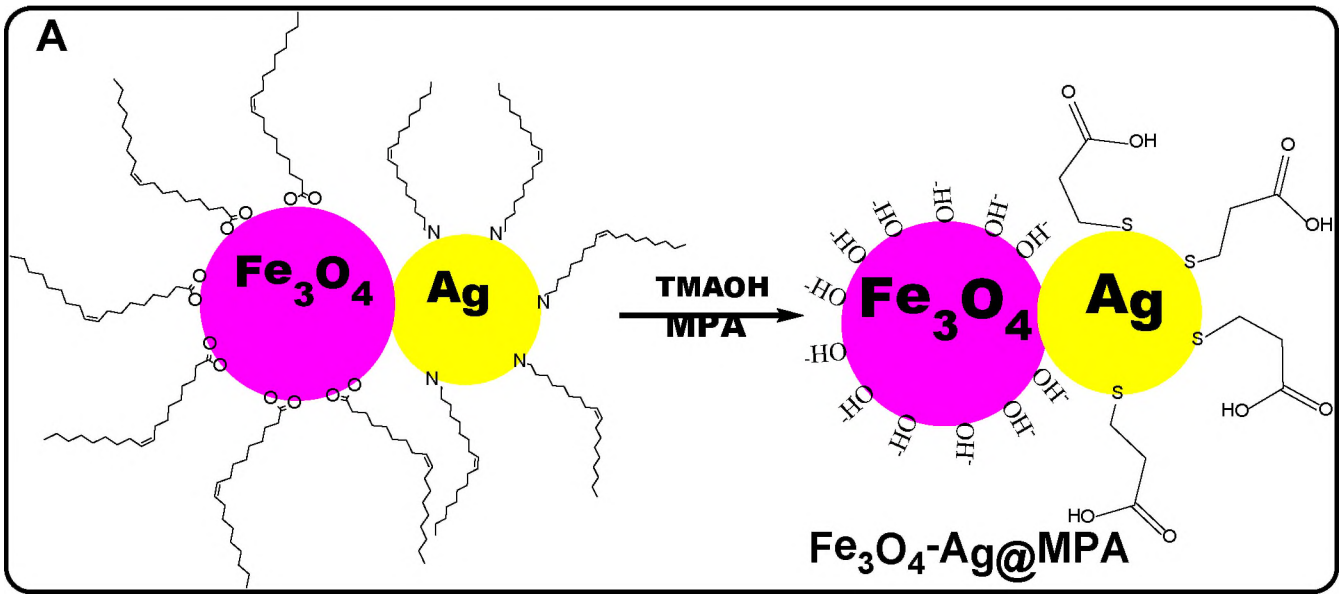

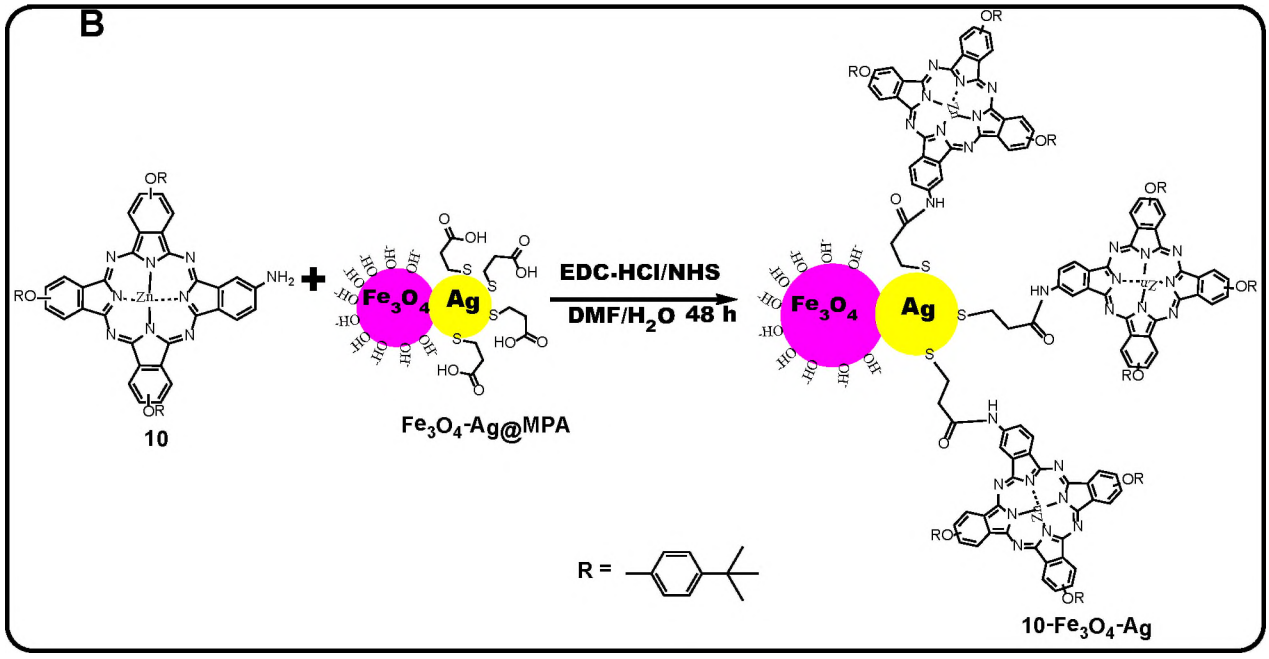

Scheme 3.9: (A) Schematic of the ligand-exchange bi-functionalization for Fe_3O_4-Ag with TMAOH/MPA (B) Covalent linking of MPA functionalized Fe_3O_4-Ag to complex 10.

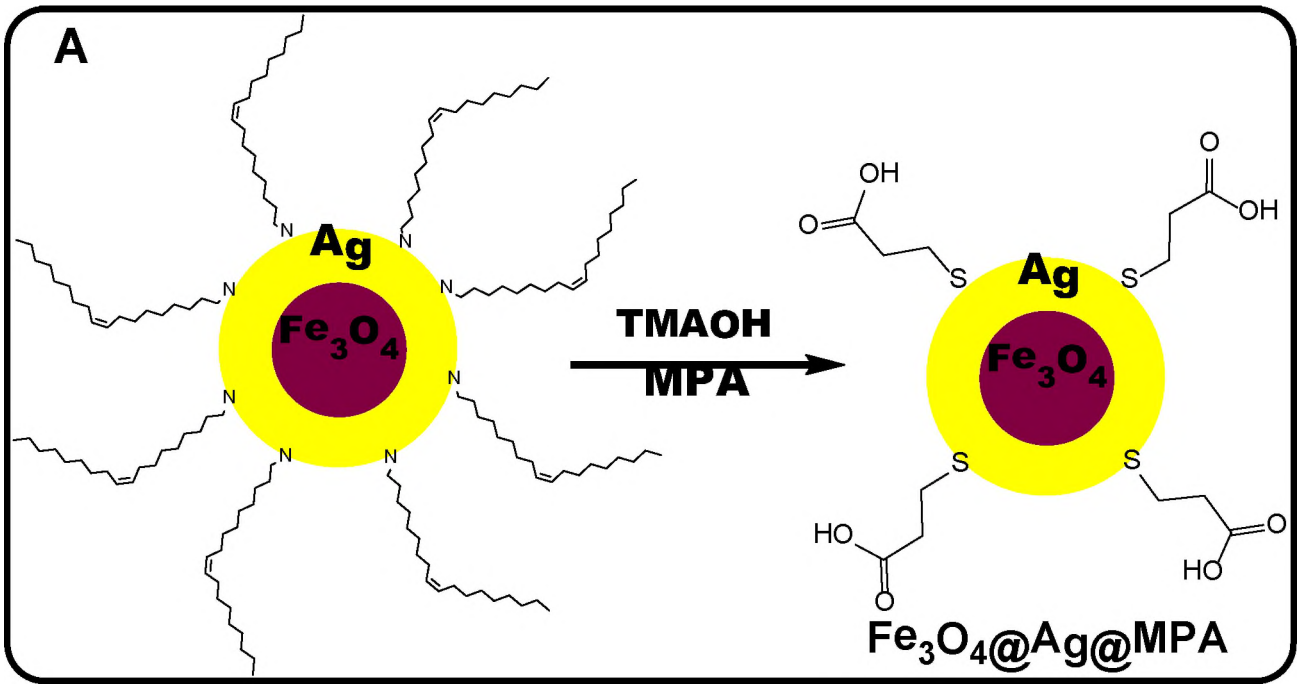

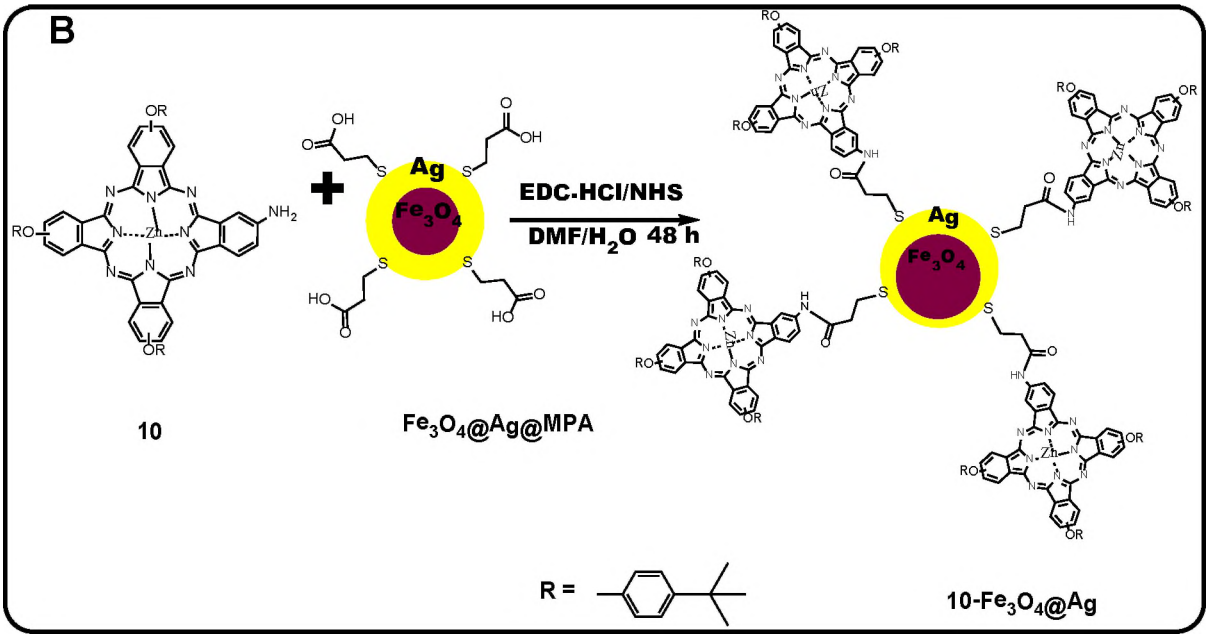

Scheme 3.10: (A) Schematic representation of the ligand-exchange for Fe_3O_4@Ag with TMAOH/MPA (B) Covalent linking of MPA functionalized Fe_3O_4@Ag to complex 10.

3.2.2.3.1 FTIR spectra

In the FTIR spectrum of Fe_3O_4 NPs alone, the characteristics peaks at ~3000 cm^{-1}, 2918 cm^{-1} and 2850 cm^{-1} are associated with =C-H, asymmetric and symmetric C-H vibrational modes of oleic acid and oleylamine attached to the surface of the nanoparticles (**Figure 3.25**). Significant reduction in the intense peaks of oleic acid/oleylamine was observed for Fe_3O_4@Ag and Fe_3O_4-Ag NPs after capping with MPA for Fe_3O_4@Ag@MPA and Fe_3O_4-Ag@MPA, respectively. MPA-capped NPs revealed broad OH and carbonyl stretching absorption bands around 3000-3250 cm^{-1} and 1690-1695 cm^{-1} suggesting successful ligand exchange with MPA on the surface of the NPs. The characteristic split vibrational bands of primary amine (NH stretch) at about 3230-3360 cm^{-1} and corresponding NH bend at 1598 cm^{-1} were observed in the spectrum of **10**. The amide peaks of NH stretch, C=O and NH bend were respectively observed at 3381 cm^{-1}, 1694 cm^{-1} and 1602 cm^{-1} for both **10-Fe_3O_4@Ag** and **10-Fe_3O_4-Ag**, indicating that the covalent linkages between carboxyl-functionalized NPs and amine of **10** were successful. Also, shifts in the carbonyl positions before and after amide linkages are pointers to the successful electronic interactions between **10** and the NPs.

3.2.2.3.2 XRD spectra

The X-ray diffraction patterns of synthesized magnetic-metallic nanoparticles before and after conjugation to **10** are shown in **Figure 3.26**. 11 and 10 crystalline diffraction peaks were observed in the X-ray diffraction patterns of Fe_3O_4-Ag@MPA and Fe_3O_4@Ag@MPA, respectively. These peaks are consistent with the diffraction patterns of pure synthetic magnetite (JCPDS Card No. 79 - 0417) and silver nanoparticles (JCPDS Card No 04-0783) in the literature [255-257]. The 6 (for Fe_3O_4-Ag@MPA) or 5 (for Fe_3O_4@Ag@MPA) peaks indexed to the fcc inverse spinel structure of Fe_3O_4 (o) have reflection positions at 30.40° (220), 35.41° (311), 43.30° (400), 56.7° (511), 62.92° (440) and 75.63° (622). The diffraction peak at 2θ =75.63° (622) is absent for Fe_3O_4@Ag@MPA due to the presence of Ag shell on the magnetic NPs. The Bragg's reflections of pure crystalline silver (*) were positioned at 2θ= 38.40° (111), 44.61° (200), 64.81° (220), 78.20° (311) and 82.10° (222). It is noteworthy to mention that the diffraction patterns for both Fe_3O_4 and Ag in Fe_3O_4-Ag@MPA are well resolved as expected for hybrid nanostructures, while the Fe_3O_4 peaks for the Fe_3O_4@Ag@MPA NPs were much more subdued due to the presence of Ag shell on the surface of the Fe_3O_4; similar observations have been reported in the literature [223,258].

Additional broad peak covering 2θ =17-20° in the XRD patterns of **10-Fe_3O_4@Ag** and **10-Fe_3O_4-Ag** revealed successful conjugation between the nanoparticles and phthalocyanine. This peak is weak for **10-Fe_3O_4-Ag**. Some crystallinity of magnetic-metallic NPs was lost after conjugation as evidenced from the broadening and reduction in the peaks of the composites as seen in **Figure 3.26**.

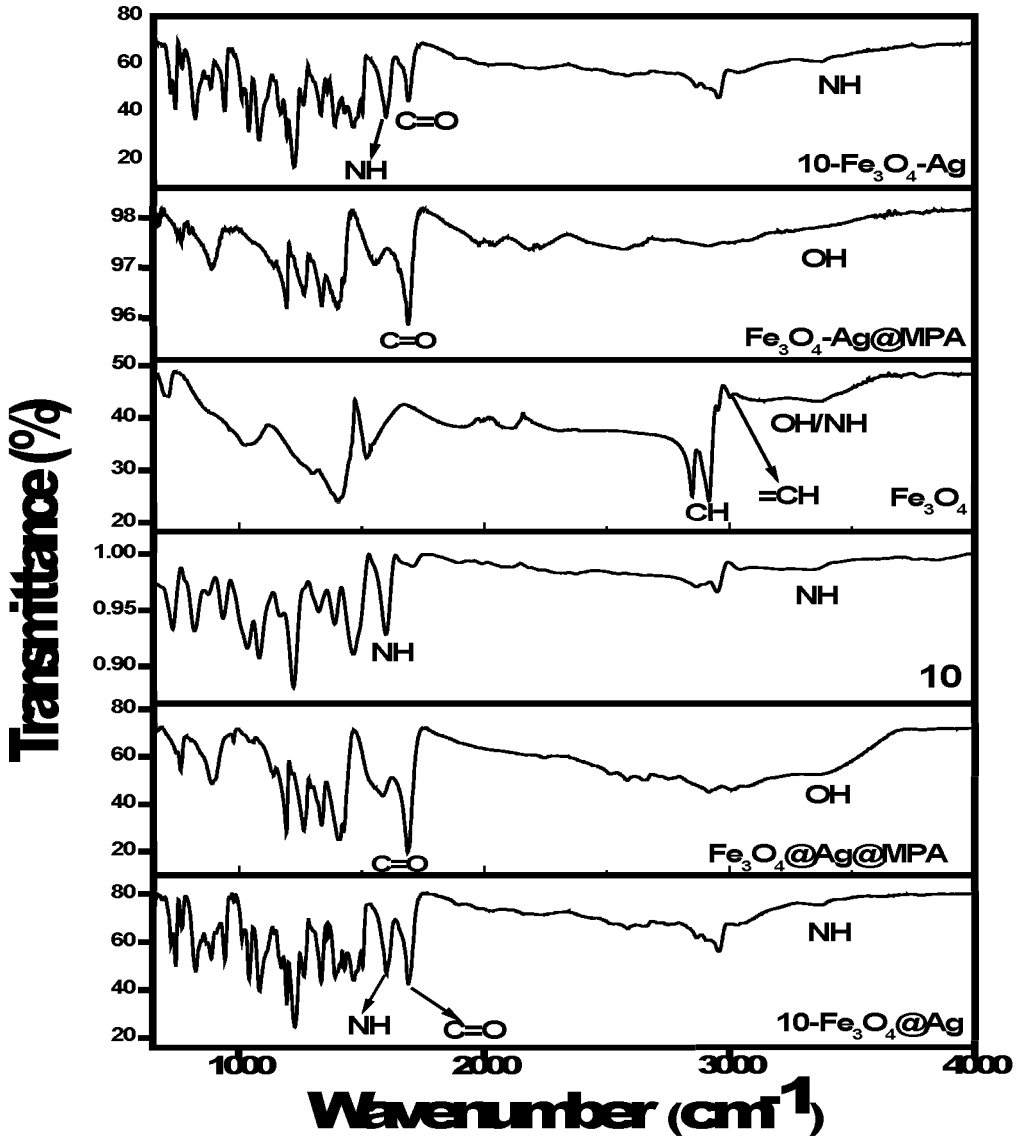

Figure 3.25: FT-IR spectra of bare Fe_3O_4, MPA-capped magnetic-metallic NPs, 10 and the conjugates.

3.2.2.3.3 EDX spectra

Elemental compositions of MPA capped nanoparticles and their conjugates to phthalocyanine, **10** were qualitatively verified using EDX spectroscopy in **Figure 3.27**. The EDX spectra of MPA capped nanoparticles confirmed characteristic peaks of Ag, Fe, and O appearing along with the C substrate peaks. The presence of S peak in the EDX pattern for Fe_3O_4-Ag@MPA and Fe_3O_4@Ag@MPA confirms

successful surface modification of NPs. Presence of Zn and N in the EDX spectra of the conjugates further confirmed the presence **10** in the composites. No other contaminating elements were detected in the samples.

3.2.2.3.4 TEM images

The TEM image of MPA capped Fe_3O_4@Ag NPs shows non-aggregated, quasi-spherically shaped nanoparticles with dark magnetic core and lighter Ag shell (see insert) suggesting successful encapsulation of the core Fe_3O_4 by Ag shell, **Figure 3.28**. Fe_3O_4@Ag core-shell NPs has an estimated particle size of 10 ± 1.2 nm (inset) while the core Fe_3O_4 was estimated to be in the range of 4-7 nm. In contrast to core-shell NPs, the TEM image of Fe_3O_4-Ag hybrid NPs clearly show that Ag domains were nucleated on the Fe_3O_4 particles resulting in a dumbbell shaped heterodimer particles (inset). The estimated size of the adsorbed Ag specie and Fe_3O_4 are 5 ± 1.2 nm and 6.5 ± 1.4 nm, respectively. Formation of Ag domains on Fe_3O_4 core are favoured by the strong reductants such as oleylamine and dodecanediol [259]. Significant increase in the particles sizes of the nanoparticles after covalent linking with **10** was observed, and it is attributed to the π–π stacking interaction of the aromatic ring of the phthalocyanine on adjacent nanoparticles.

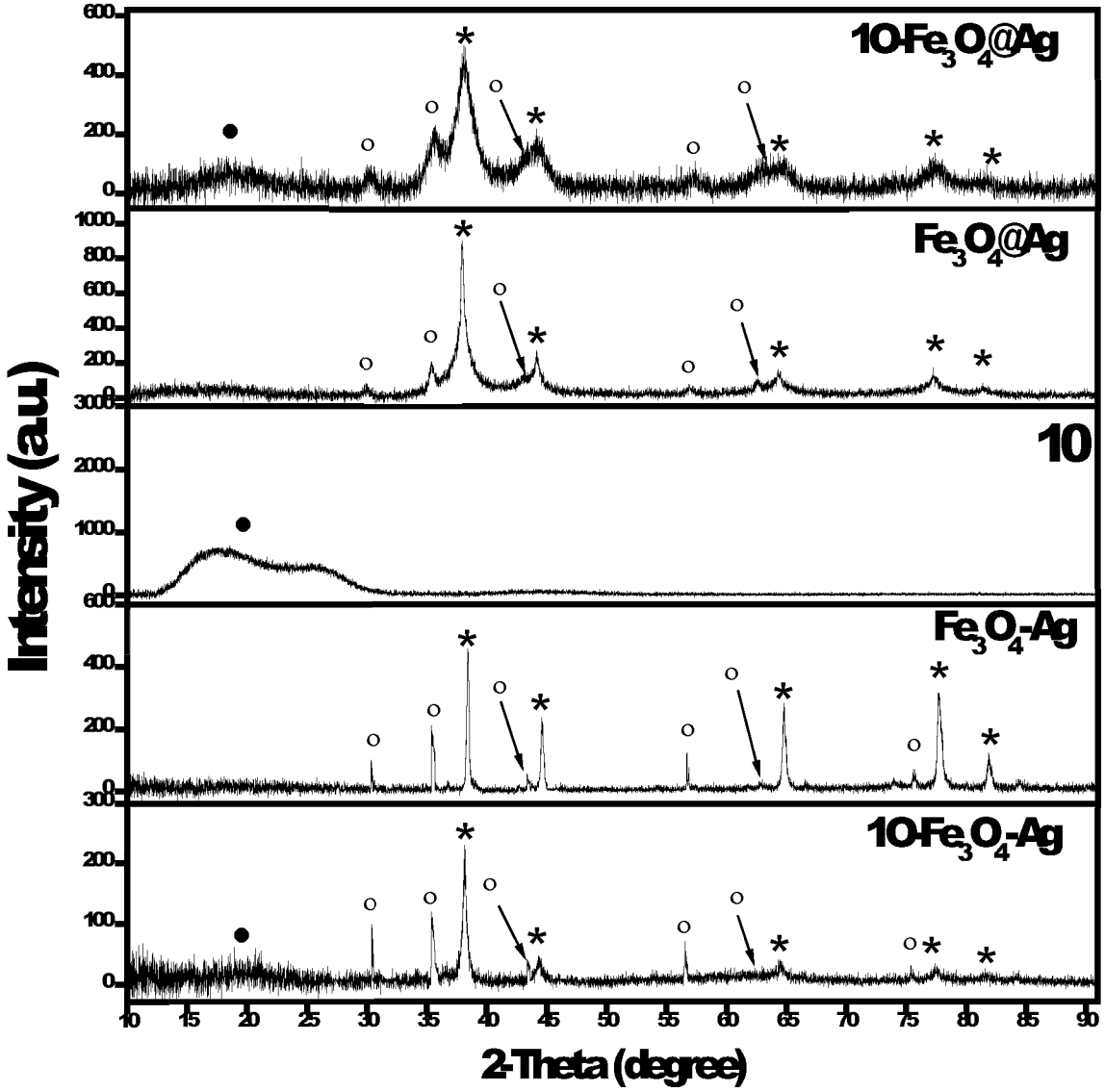

Figure 3.26: XRD spectra of Fe_3O_4-Ag@MPA, Fe_3O_4@Ag@MPA, 10, 10-Fe_3O_4-Ag and 10-Fe_3O_4@Ag.

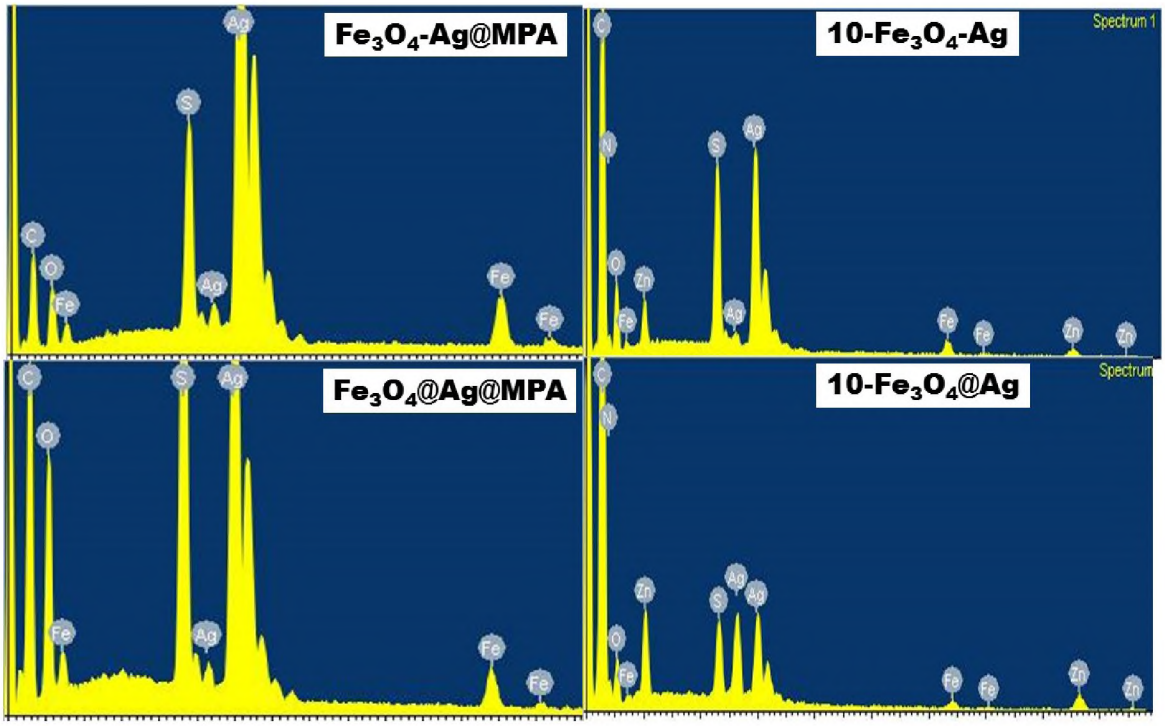

Figure 3.27: EDX spectra of Fe_3O_4-Ag@MPA, Fe_3O_4@Ag@MPA, 10-Fe_3O_4-Ag and 10-Fe_3O_4@Ag.

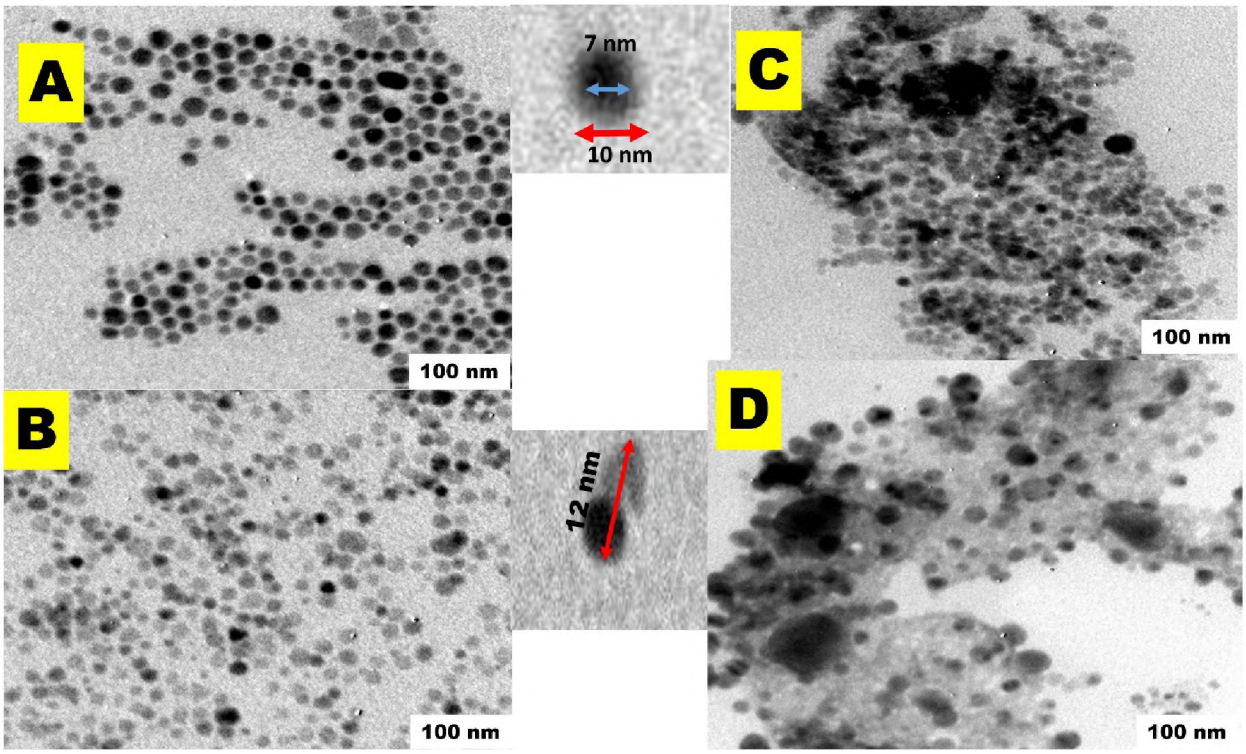

Figure 3.28: Transmission electron microscope (TEM) images of (A) Fe_3O_4@Ag@MPA (with insert on the right shows an isolated NP), (B) Fe_3O_4-Ag@MPA (with insert on the right shows an isolated NP), (C) 10-Fe_3O_4@Ag and (D) 10-Fe_3O_4-Ag.

3.2.2.3.5 UV-Vis spectra

Normalized UV-Vis spectra of Fe_3O_4@Ag and Fe_3O_4-Ag capped with MPA (Fe_3O_4@Ag@MPA and Fe_3O_4-Ag@MPA NPs) in water or oleic acid/oleylamine (represented as Fe_3O_4@Ag or Fe_3O_4-Ag NPs) in toluene, are presented in **Figure 3.29A**. Absorption spectra of oleic acid/oleylamine capped Fe_3O_4@Ag or Fe_3O_4-Ag NPs in toluene revealed single intense surface plasmon resonance (SPR) peaks at 414 nm and 429 nm, respectively. While the SPR peak of Fe_3O_4@Ag was observed close to the SPR positions of pure AgNPs [260], SPR peak of Fe_3O_4-Ag was shifted to longer wavelength by ~15 nm due to the contact between Ag and Fe_3O_4 which resulted in deficient electron population on Ag [261]. The absence of absorption peak in the spectrum of bare Fe_3O_4 (**Figure 3.29A**) shows that the observed SPR in Fe_3O_4-Ag and Fe_3O_4@Ag are due to the presence of Ag in the nanostructures. The SPR bands of both nanoparticles shifted to lower wavelength by 3-4 nm after ligand exchange with MPA without altering the shape of the SPR peaks.

Ground state electronic absorption spectra of **10** and the composites recorded in DMSO are shown in **Figure 3.29B** and summarized in **Table 3.3**. The Q bands of **10-Fe_3O_4@Ag** and **10-Fe_3O_4-Ag** were blue shifted to 683 nm and 685 nm, respectively, compared to **10** alone (**Table 3.3**). Similar blue shifts in Q bands of phthalocyanine in presence of magnetite NPs are well documented in literature [189,262]. Broad absorptions around 427-465 nm for **10-Fe_3O_4@Ag** and 461-505 nm for **10-Fe_3O_4-Ag** are the regions corresponding to SPR of Fe_3O_4@Ag and Fe_3O_4-Ag NPs, respectively.

Normalized absorption, fluorescence emission and excitation of the composites are shown in **Figure 3.30A** and **B**. The ground state and excited states of the conjugates have similar molecular geometries after excitation as seen from the monomeric Q bands of the absorption and excitation spectra. However, broad absorption bands due to the Fe_3O_4-Ag and Fe_3O_4@Ag SPR influence around 450-500 nm observed in the absorption spectra of **10-Fe_3O_4@Ag** and **10-Fe_3O_4-Ag** were conspicuously absent in their excitation spectra.

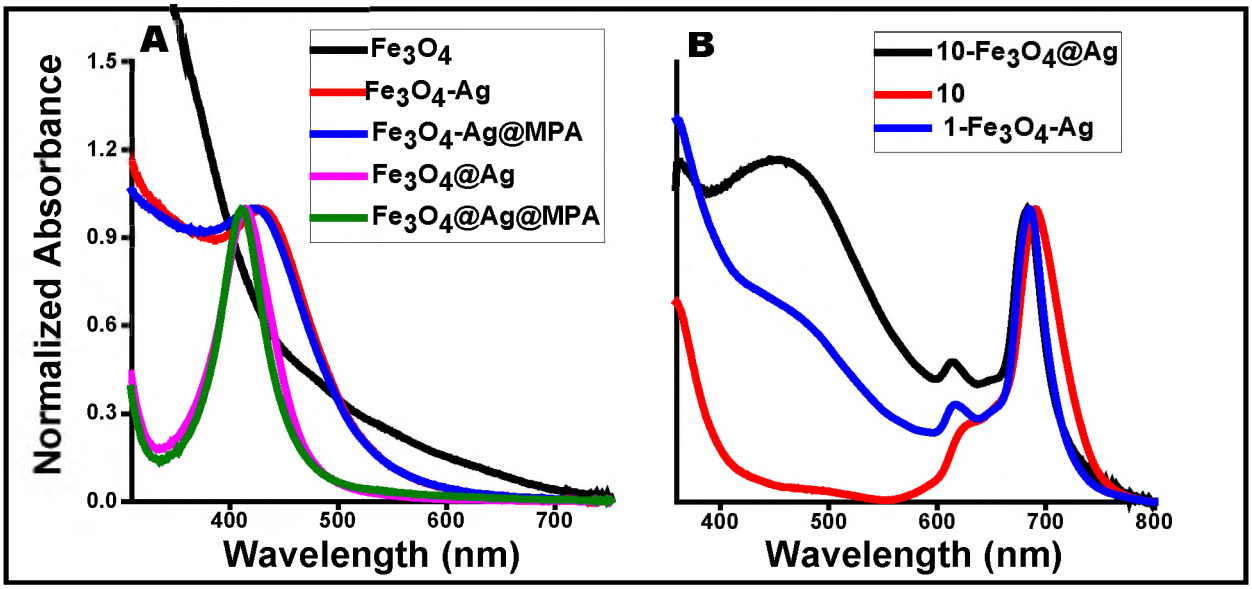

Figure 3.29: Absorption spectral of (A) bare Fe_3O_4, oleic acid/oleylamine capped Fe_3O_4@Ag and Fe_3O_4-Ag (in toluene), Fe_3O_4@Ag@MPA, and Fe_3O_4-Ag@MPA (in water), and (B) 10, 10-Fe_3O_4@Ag and 10-Fe_3O_4-Ag in DMSO.

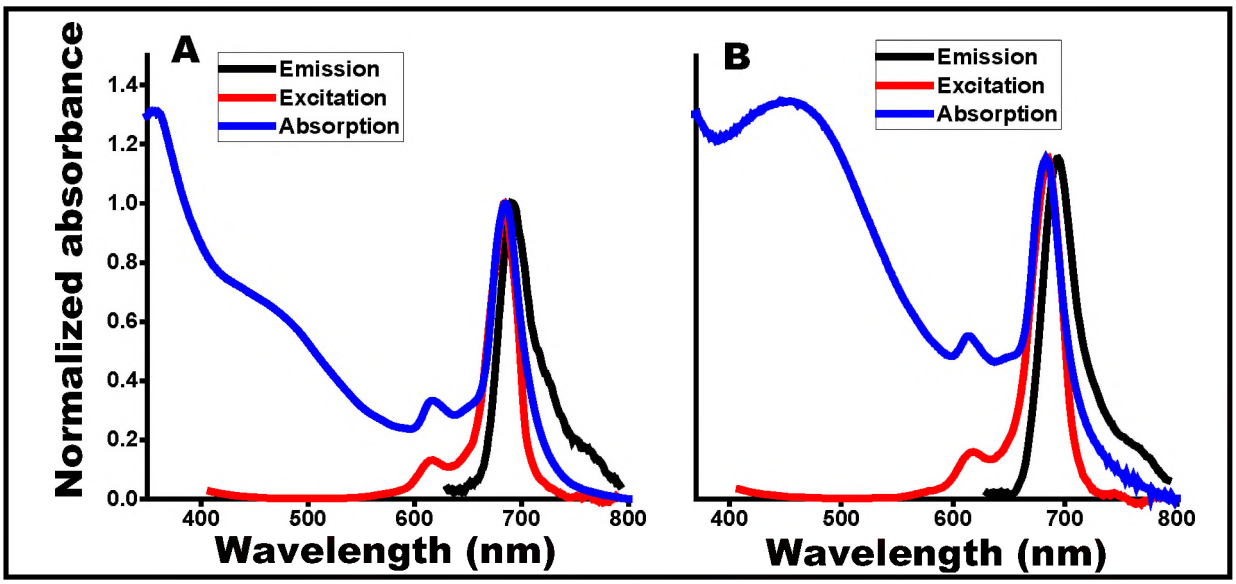

Figure 3.30: Absorption, fluorescence emission and excitation spectra of (A) 10-Fe_3O_4@Ag and (B) 10-Fe_3O_4-Ag in DMSO. Concentration 1.34 x 10^{-6} M. Excitation wavelength = 613 nm.

3.2.2.3.6 XPS spectra

Surface elemental compositions of Fe_3O_4@Ag@MPA and Fe_3O_4-Ag@MPA were investigated for the presence of Fe, Ag and S by X-ray photoelectron spectroscopy (XPS), **Figure 3.31A** and **B**. The presence of Ag 3d in the NPs was confirmed by binding energies at ≈368 eV (Ag $3d_{5/2}$) and ~374 eV (Ag $3d_{3/2}$) (**Table 3.4**), with a spin-orbit splitting of ca. 6 eV [263]. The region on the XPS spectra corresponding to Fe 2p were observed between 711 eV to 725 eV, these were assigned to Fe $2p_{3/2}$ and Fe $2p_{1/2}$, respectively, characteristic of Fe_3O_4 [264] in the nanostructures. The presence of S 2p and S 2s peaks in their respective peak positions and the absence of N1s peaks at 398 - 400 eV confirmed successful ligand exchange of the oleic acid/oleylamine for MPA prior to covalent linking.

Surface compositions of the conjugates and the free phthalocyanine were also investigated for possible amide linkage. **Figure 3.31C** and **D** showed the wide scan XPS spectra of the composites containing signals attributable to Ag 3d, Fe 2p, S 2p and S 2s in their respective peak positions. These peaks are also present in the spectra of the nanoparticles, but absent in the XPS spectrum of **10** (**Figure 3.31E**). The XPS spectra of **10-Fe_3O_4@Ag** and **10-Fe_3O_4-Ag** show additional N1s and Zn 2p peaks which can be ascribed to the presence of the linked phthalocyanine. The zinc 2p peaks of the phthalocyanine and the conjugates were positioned at ca. 1022 (Zn $2p_{3/2}$) and 1046 (Zn $2p_{1/2}$) eV with peak separation of ca. 24 eV, in agreement with the standard spin-orbit splitting of 22.97 eV of zinc(II) [265]. This shows successful stabilization of the nanoparticles with the phthalocyanine macrocycles. It is noteworthy to mention that the Fe 2p of **10-Fe_3O_4@Ag** almost disappeared in the spectrum due to further stabilization of the Fe_3O_4@Ag core-shell NPs with phthalocyanine macrocycles.

Table 3.4: XPS peak assignment for Fe_3O_4@Ag and Fe_3O_4-Ag

	XPS peak position (eV)					
	Ag 3d		Fe 2P		S	
	Ag $3d_{5/2}$	Ag $3d_{3/2}$	Fe $3p_{1/2}$	Fe $3p_{3/2}$	S 2p	S 2s
Fe_3O_4@Ag	368.1	373.6	725	711	163	227
Fe_3O_4-Ag	367.9	373.4	724.6	711	163	226.4

In order to prove amide bond formation between **10** and the MPA-capped nanoparticles; N1*s* XPS analysis of the conjugates were compared to that of **10**. **Figure 3.32** shows the deconvoluted N1*s* spectrum of **10** (also shown in **Figure 3.24**) into two chemically distinct peak positions at 399.11 eV and 400.97 eV as stated above, these peaks correspond to N–C (from Pc ring) and N–H (from NH_2), respectively. The N1*s* core level spectra of the conjugates were independently decomposed into three binding energies at 399.14 eV, 400.54 eV and 401.96 eV (for **10-Fe_3O_4@Ag**); and 399.69 eV, 400.99 eV and 401.85 eV (for **10-Fe_3O_4-Ag**). The deconvoluted high binding energy peaks at ca. 401.9 eV for the conjugates are attributed to the successful formation of amide bond between **10** and the carboxyl nanoparticles.

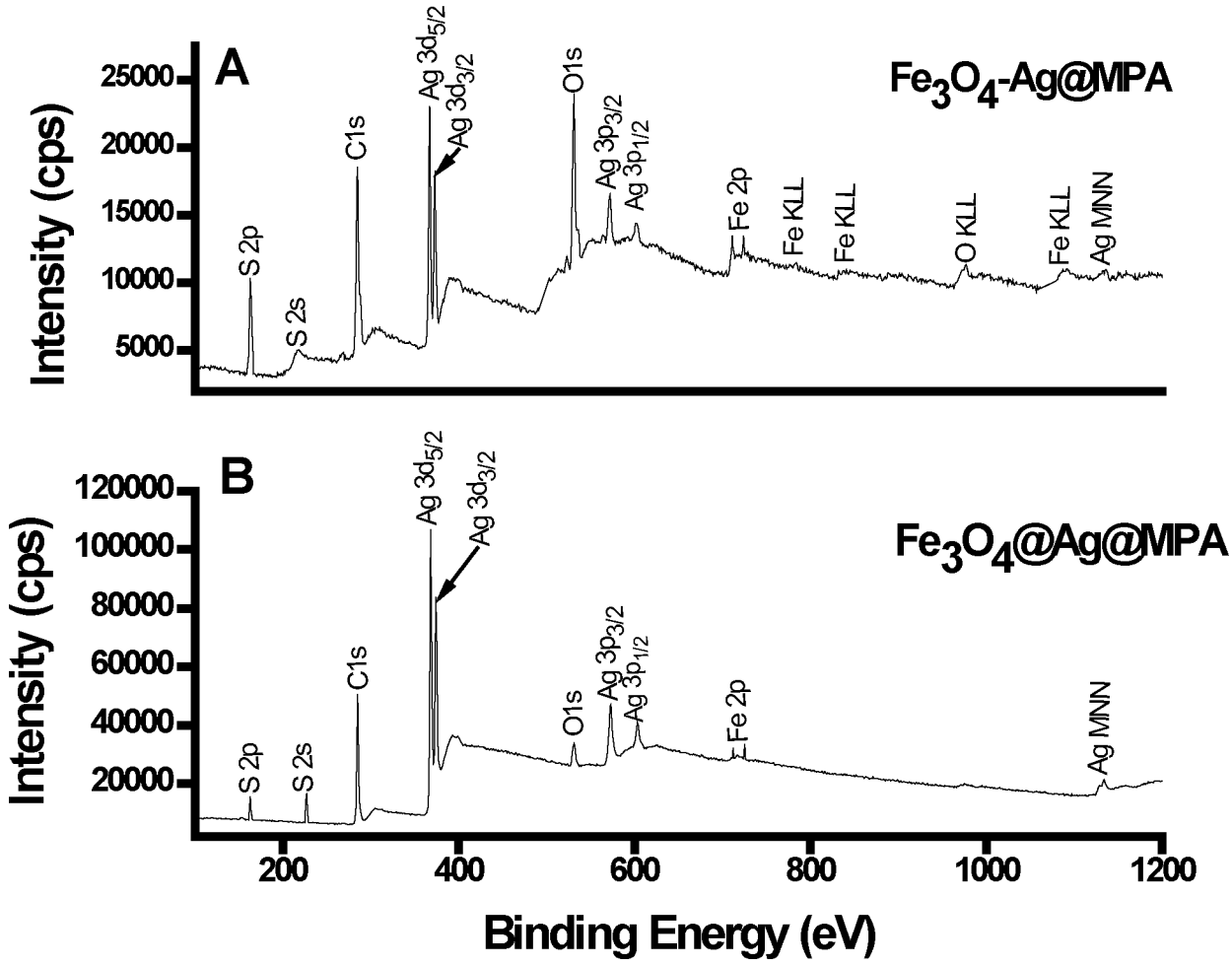

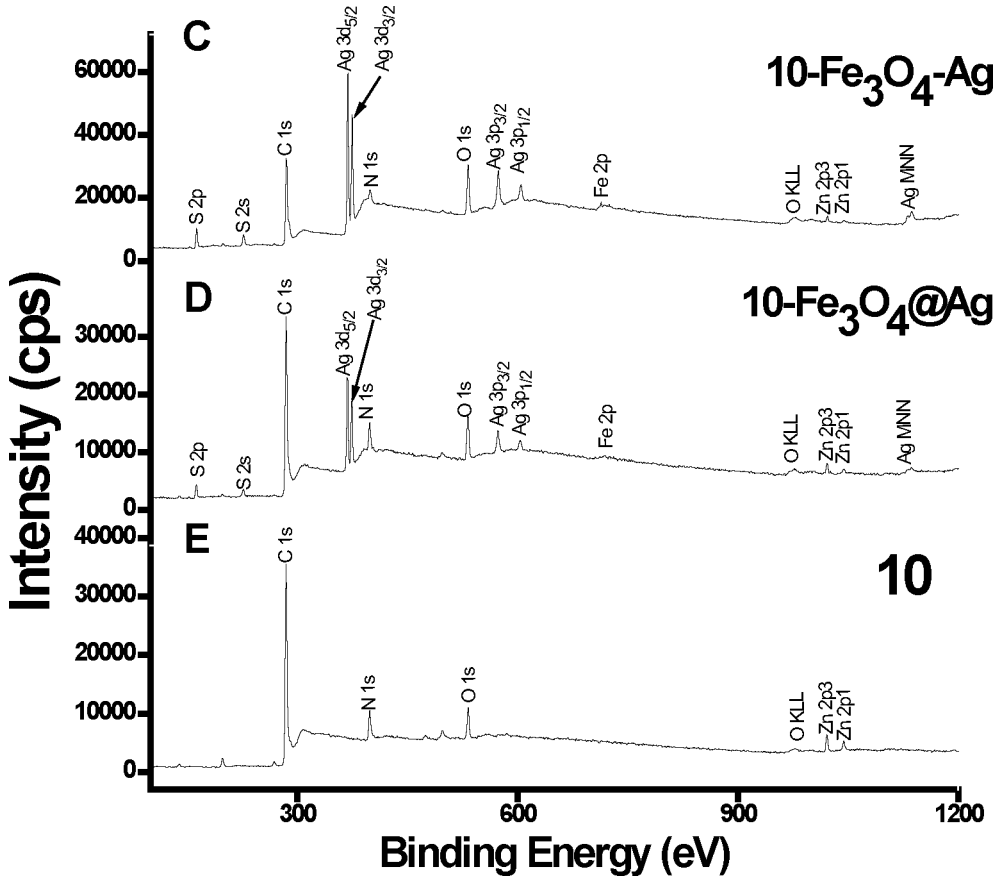

Figure 3.31: X-ray photoelectron wide-scan of (A) 10-Fe_3O_4-Ag@MPA, (B) Fe_3O_4@Ag@MPA, (C) 10-Fe_3O_4-Ag, (D) 10-Fe_3O_4@Ag and (E) 10

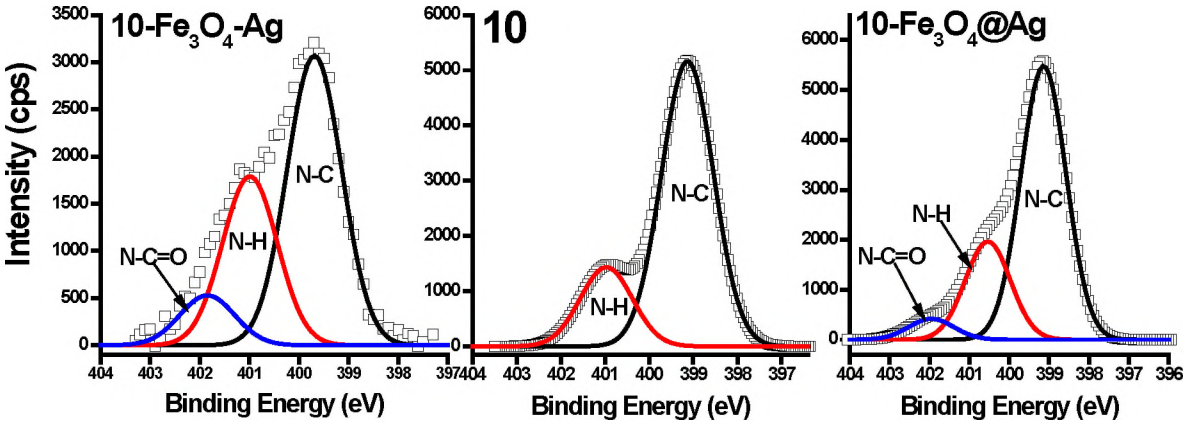

Figure 3.32: High resolution of deconvoluted N1s component for complex 10, 10-Fe_3O_4-Ag, and 10-Fe_3O_4@Ag

3.2.3 Characterizations of Ag_xAu_y and their conjugates with complex 11 (Scheme 3.11)

The surface of Ag-Au nano-alloys were functionalized with amino-rich complex **11** taking advantage of strong affinity for silver and gold by the amine and/or thiol groups, **Scheme 3.11** Ag_3Au_1 (3:1 Ag:Au) and Ag_1Au_3 (1:3 Ag:Au). Stronger bond(s) is expected between the terminal NH_2 of **11** and Ag_xAu_y nano-alloys than the sulphur atoms of mercapto rings as a result of likely restriction from pyrimidine rings. Evidence of successful conjugation of the phthalocyanine to the bimetallic nanoparticles was revealed in the UV-vis, EDS, TEM, XRD and XPS spectra.

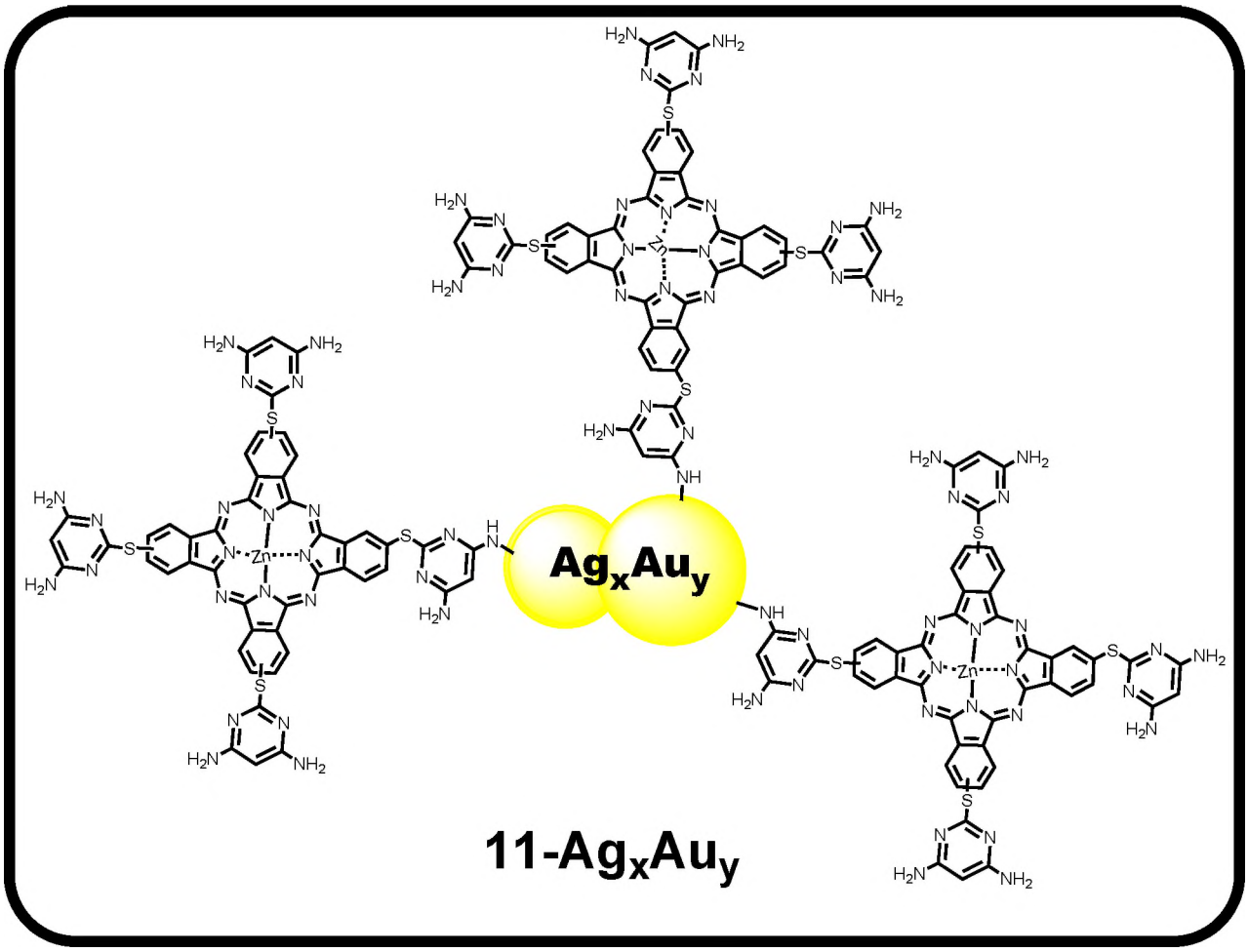

Scheme 3.11: Immobilization of ZnPc (11) on Ag_xAu_y via NH_2-Au bond.

3.2.3.1 XRD studies

The X-ray powder diffraction patterns of Ag_xAu_y alloys and when conjugated to **11** are shown in **Figure 3.33**. Theoretical XRD patterns of monometallic Ag and Au are similar and the same with the peak positions observed for nano-alloys of Ag_xAu_y. XRD patterns of Ag_xAu_y showed crystalline well-defined peaks assigned to 111, 200, 220, 311 and 222 planes, and in good agreement with the planes of face centered-cubic of metallic gold and silver [266,267]. XRD pattern of **11** showed a broad peak covering 2Θ= 17–27° indicating amorphous nature of phthalocyanines [250]. The additional broad peaks in XRD spectra of **11-Ag_xAu_y** near 22° is an indication that the phthalocyanine is present in the composites. Also, slight broadening of the peaks and reduction in the intensity of the XRD patterns for **11-Ag_xAu_y** were observed upon conjugation.

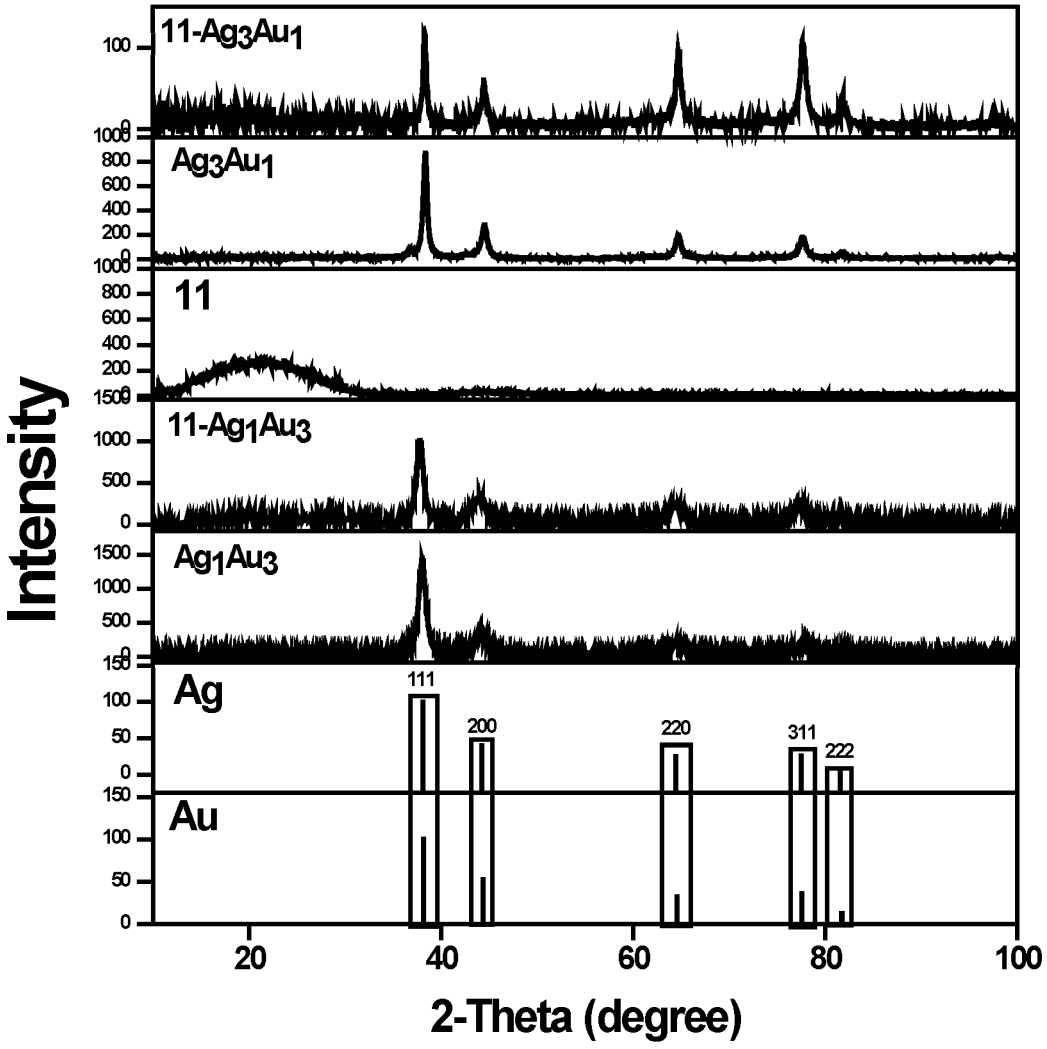

Figure 3.33: XRD patterns of Ag_3Au_1, 11-Ag_3Au_1, 11, Ag_1Au_3 and 11-Ag_1Au_3 with reference peaks for monometallic Ag and Au.

3.2.3.2 EDX spectra

Elemental composition of the bimetallic nanoparticles and the conjugates were qualitatively verified using energy dispersive spectroscopy (EDS) in **Figure 3.34**. The EDS spectra for Ag_xAu_y alone show peaks due to Ag and Au as expected. In addition, there are peaks due to Cl (from the $HAuCl_4.3H_2O$ used as starting material for NPs preparation), C and O are from diphenyl ether and oleic acid also used in the synthesis of NPs. The EDX spectra of **11-Ag_xAu_y** revealed characteristic C, N, S, Zn, Ag and Au peaks further confirming the presence of both complex **11** and the bimetallic nanoparticles as the major constituents of the composites.

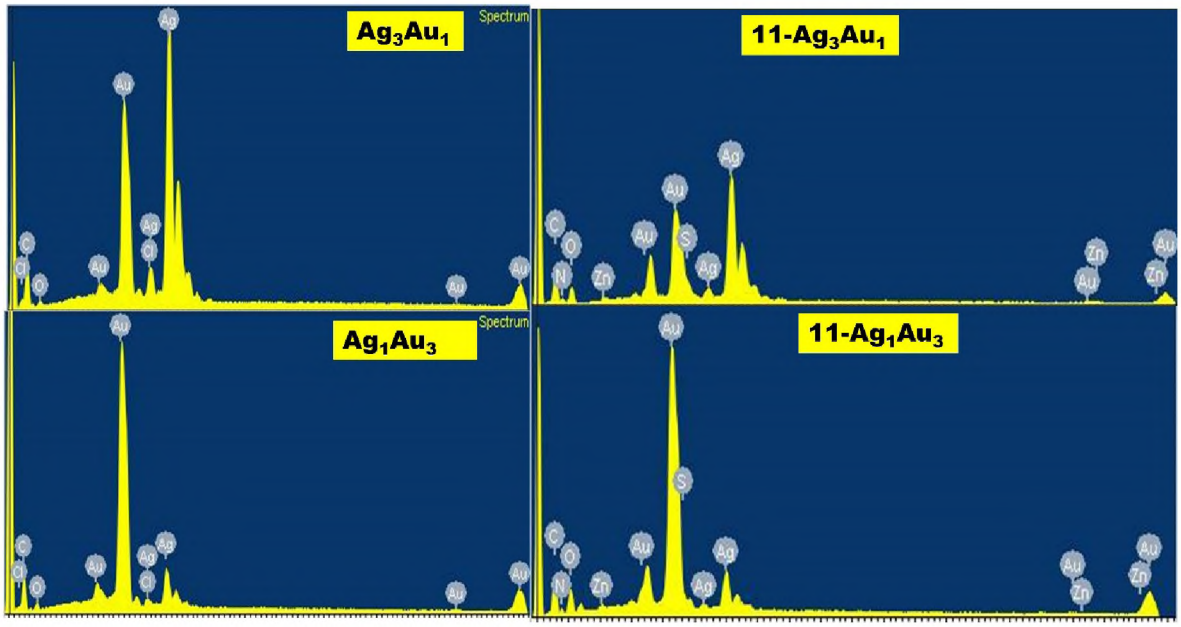

Figure 3.34 EDX spectra of Ag_3Au_1, 11-Ag_3Au_1, Ag_1Au_3 and 11-Ag_1Au_3.

3.2.3.3 TEM images

The TEM micrographs of the nano-alloy particles before and after conjugation to **11** are shown in **Figure 3.35**. The TEM images revealed monodisperse and nanosphere shaped alloy nanoparticles with estimated particle size of 9 nm for both NPs. Significant aggregation of Ag_xAu_y is observed following linking to **11**. Aggregation by $\pi - \pi$ stacking is well known in phthalocyanines [234]. For **11-Ag_xAu_y**, it is possible that phthalocyanines

from adjacent NPs interact, resulting in aggregation which is also evidenced by red shifting of the SPR bands below.

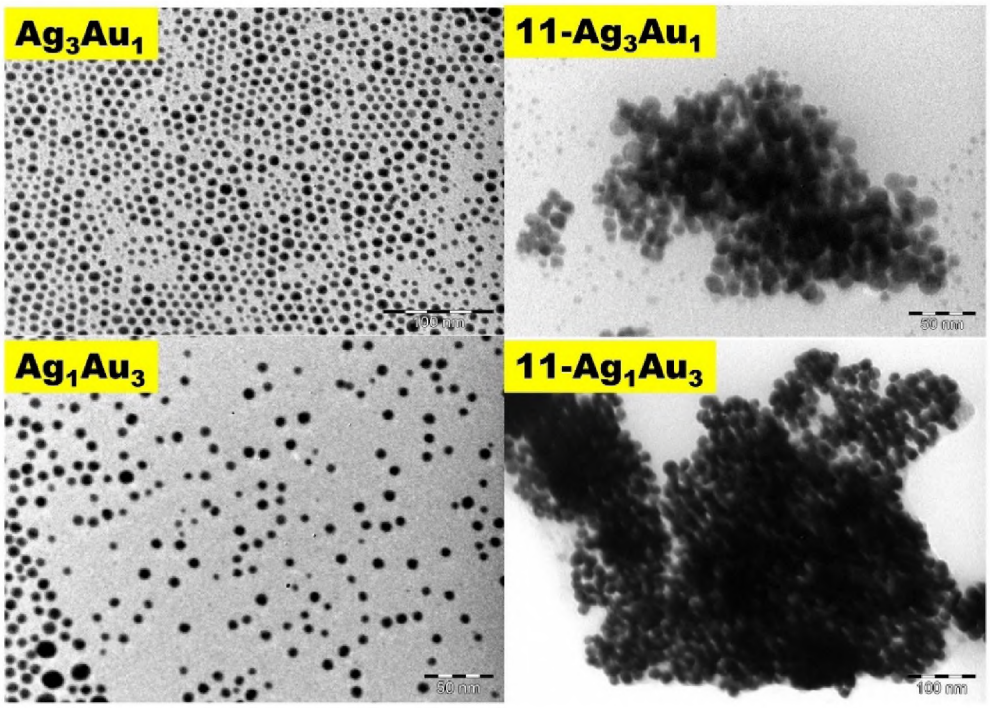

Figure 3.35: Transmission electron microscope (TEM) images of Ag_3Au_1, 11-Ag_3Au_1, Ag_1Au_3 and 11-Ag_1Au_3.

3.2.3.4 UV–vis electronic spectra

Electronic absorption spectra of **11**, **11-Ag_3Au_1**, **11-Ag_1Au_3** (in DMSO) and unconjugated Ag_3Au_1 and Ag_1Au_3 alloy nanoparticles (in hexane) are shown in **Figure 3.36A** and **B**. Simultaneous reduction of Ag and Au precursors by oleylamine resulted in the formation of gold–silver alloy NPs evidenced by the occurrence of one plasmon band in the UV–vis spectra [268]. The intense SPR peaks of Ag_3Au_1 and Ag_1Au_3 were observed at 423 nm and 482 nm, respectively, **Table 3.5**. The SPR peaks of the alloys are very close to the SPR positions of pure AgNPs and AuNPs, depending on the composition of Ag or Au present in the alloys [269]. No shifts in the Q bands of **11** occurred after conjugation to Ag_xAu_y, **Table 3.5**. Intense absorption band at 444 nm due Ag_3Au_1 SPR band contribution was observed for **11-Ag_3Au_1** in DMSO. Also, for **11-Ag_1Au_3**, contribution from Ag_1Au_3 SPR band was observed at 501 nm. The SPR bands of Ag_xAu_y in **11-Ag_xAu_y** measured in DMSO are red shifted by 19 and 21 nm compared to unconjugated Ag_xAu_y in hexane. The large shift

cannot be related only to solvent differences. It is known that the SPR band shifts with increasing particle size [172], hence the red shifting in **Figure 3.36** (**Table 3.5**) suggests aggregation.

Figure 3.37 shows the normalised absorption, fluorescence emission and excitation of **11-Ag_1Au_3** measured in DMSO at excitation wavelength of 612 nm. Emission spectra in all cases (**11-Ag_1Au_3** as a representative) are up to 10 nm red shifted from absorption spectra. Such shifts are typical of phthalocyanines [210].

Table 3.5: Absorption, emission, and excitation spectral data for 11, 11-Ag_3Au_1, 11-Ag_1Au_3 in DMSO.

Sample	Absorption (nm)	Emission, λ_{em} (nm)	Excitation, λ_{exc}(nm)
11	689 (Q band)	698	689
11-Ag_3Au_1	689 (Q band)	698	692
11-Ag_1Au_3	689 (Q band)	697	692
Ag_1Au_3	482 (501)[a] (SPR)	-	-
Ag_3Au_1	423 (444)[a] (SPR)	-	-

[a] Numbers in brackets are when Ag_xAu_y are conjugated to complex **11**.

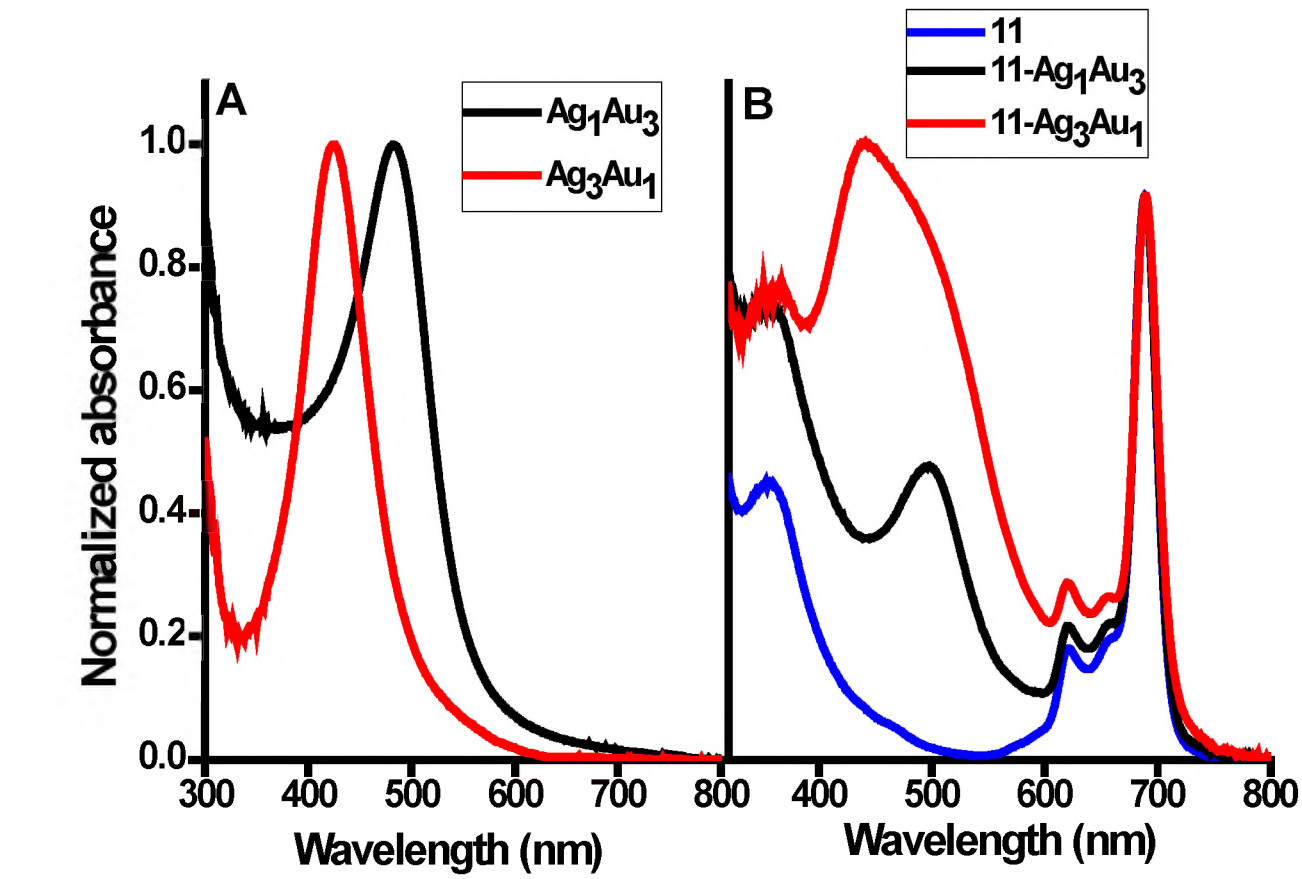

Figure 3.36: Absorption spectral (A) Ag_3Au_1 and Ag_1Au_3 in hexane and (B) 11, 11-Ag_3Au_1, 11-Ag_1Au_3 in DMSO.

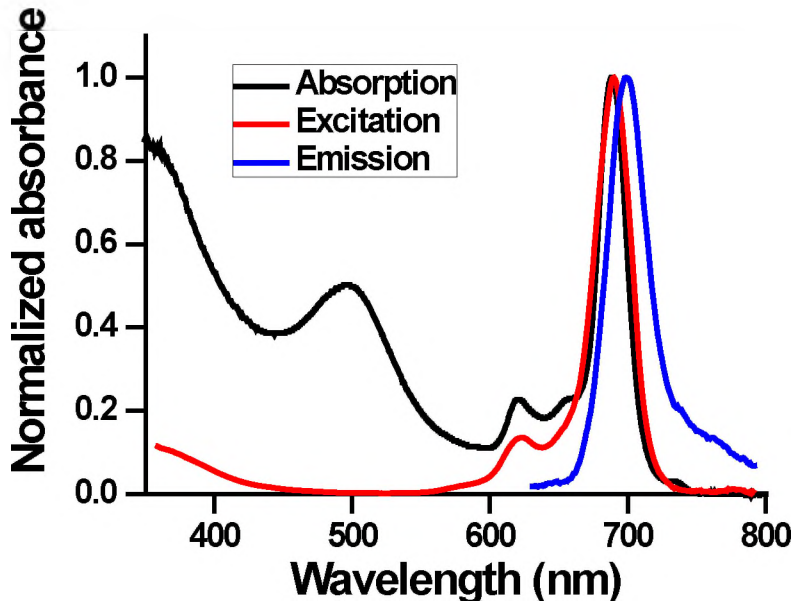

Figure 3.37. Absorption, fluorescence emission and excitation spectra of 11-Ag_1Au_3 in DMSO. Concentration 1.6 x 10^{-6} M. Excitation wavelength = 612 nm.

3.2.3.5 XPS studies

X-ray photoelectron spectroscopy (XPS), **Figure 3.38**, was carried out to confirm immobilization of phthalocyanine macrocycles on the surface of bimetallic plasmonic nanoparticles. The wide scan spectra of **11** (**Figure 3.38A**) shows the presence of signals attributable to S2p, S2s, C1s, N1s and Zn2p in their respective binding energy (BE) positions; the observed peaks were in good agreement with the elemental compositions of complex **11**. These peaks are also present in the XPS spectra of **11-Ag_xAu_y**, confirming successful immobilization of Zn-centered phthalocyanine on the bimetallic NPs. A close investigation on the bimetallic NPs shows that the intensity of Au4f in Au-rich (**11-Ag_1Au_3**) conjugate positioned at 82.6 eV is higher than Ag3d at 368.0 eV in the same conjugate. Similarly, Ag3d peak is higher than Au4f peak in the Ag rich **11-Ag_3Au_1**. This fairly agreed with the mole ratio of the Ag and Au precursors for each alloy. Possible points of attachment between the phthalocyanine and bimetallic surfaces were also investigated using deconvoluted N1s and S ($2p_{3/2}$ and $2p_{1/2}$) XPS spectra as shown in **Figure 3.38B** and **C**. The N1s spectrum of **11** was decomposed into two chemically distinct peaks at 399.13 eV and 400.97 eV corresponding to N-C (from Pc ring) and -NH_2 (unprotonated amine), respectively, **Figure 3.38B**. N1s core-level spectra of **11-Ag_1Au_3** were curve-fitted into two binding energies positioned at 399.61 eV and 401.09 eV, this corresponds to N-C and -NH, respectively. Similarly, N1s deconvoluted peaks for N-C and -NH for **11-Ag_3Au_1** peaks are respectively observed at 400.01 eV and 401.20 eV. The high binding energy peaks of **11-Ag_xAu_y** at ca. 401 eV (also present in **11** alone) are due to protonated amine/ amide species [270-272], suggesting successful conjugation of **11** to Ag_xAu_y NPs. The S2p deconvoluted spectra of **11** and the conjugates revealed two doublets, **Figure 3.38C**: the one at lower BE (ranging from 161.7 to 163.39 eV) and the other at higher BE (ranging from 165.01 to 167.22 eV) due to spin-orbit coupling [273]. For phthalocyanine alone, the first components appeared at 161.72 and 163.39 eV, corresponding to $S2p_{3/2}$ and $S2p_{1/2}$, respectively. Upon conjugation to Ag_xAu_y, the $S2p_{3/2}$ and $S2p_{1/2}$ peaks shifted to 162.08 and 163.38 eV for **11-Ag_1Au_3**; 161.95 and 163.25 eV for **11-Ag_3Au_1**, respectively. The BE at ≈162 corresponds to thiolated species immobilized on bimetallic NPs in **11-Ag_xAu_y** [274], and $S2p_{1/2}$ peaks at ≈163 eV are due to the physisorbed species on the NPs [273,275]. This is an indication that sulfur also took part in the formation of bond between **11** and Ag_xAu_y. The other unbounded thiols at higher binding energies (>164 eV) are attributed to S-C bonds of the Pc ring [276,277].

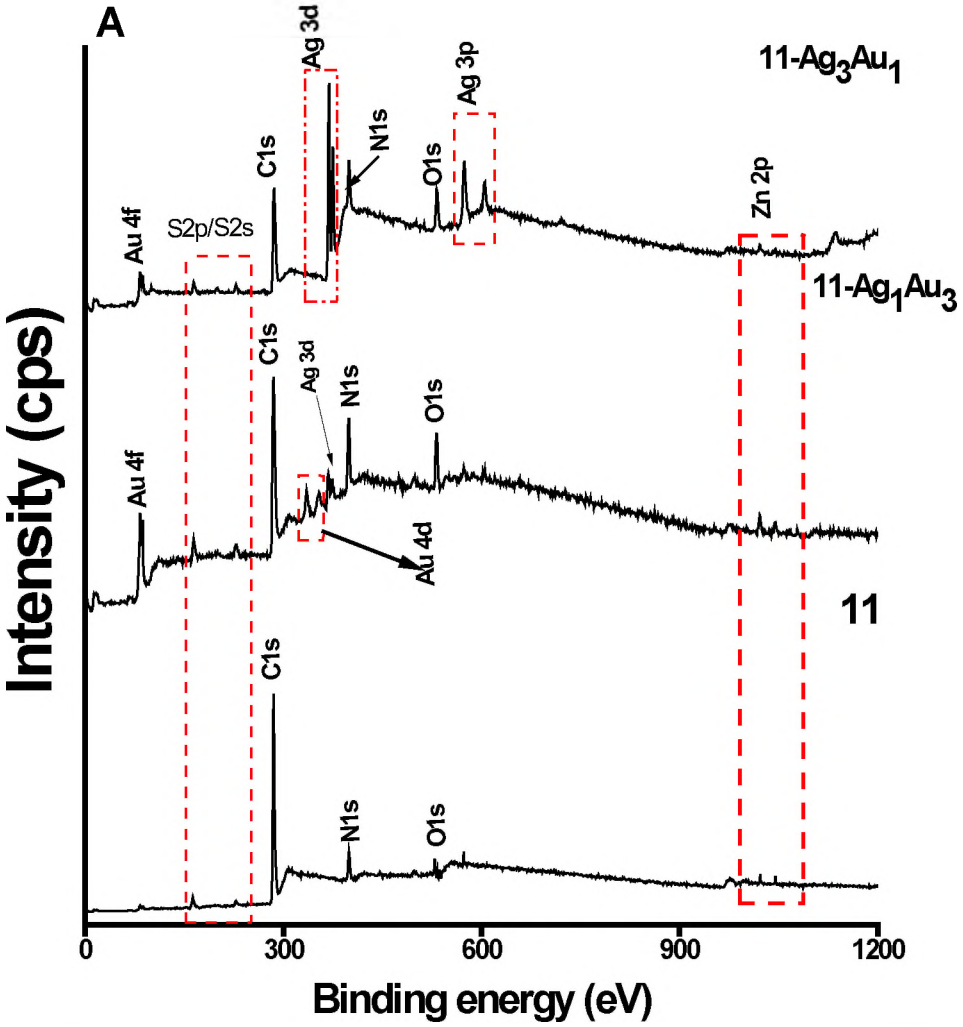
A
11-Ag3Au1
11-Ag1Au3
11
Ag 3d
Ag 3p
N1s
O1s
C1s
Zn 2p
Au 4f
S2p/S2s
Au 4d
Intensity (cps)
0
300
600
900
1200
Binding energy (eV)

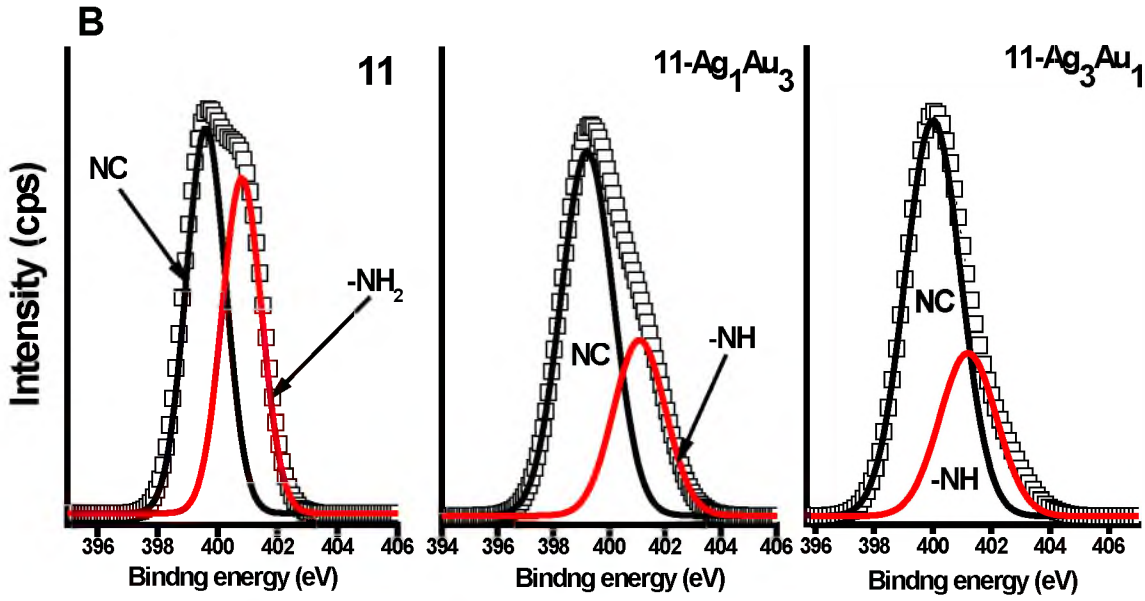
B
11
11-Ag1Au3
11-Ag3Au1
NC
-NH2
-NH
Intensity (cps)
396
398
400
402
404
406
394
Bindng energy (eV)

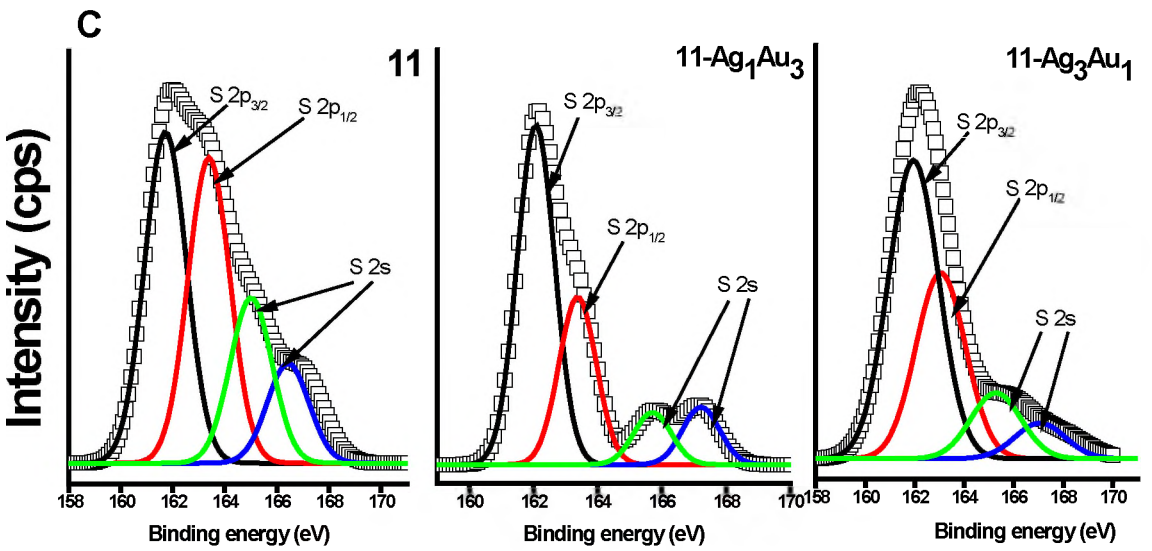

Figure 3.38: (A) X-ray photoelectron wide-scan spectra of 11, 11-Ag_1Au_3 and 11-Ag_3Au_1. High resolution XPS of deconvoluted spectra for (B) N1s and (C) S ($2p_{3/2}$ and $2p_{1/2}$) spectra for 11, 11-Ag_1Au_3 and 11-Ag_3Au_1.

3.3 Fabrication of MPc-polymer thin films using compounds 5 - 9

3.3.1 Characterizations of MPc-polymer composites of 5, 6 and 7 with poly(bisphenol A carbonate) (PBC)

The respective Pc molecules were mixed with PBC and sonicated in chloroform prior to immobilization on clean glass slides by drop-dry method. The concentrations of Pcs embedded in PCB polymer thin films are in the range of $4.5 \times 10^{-4} - 5.3 \times 10^{-4}$ M.

The UV–vis spectra of complexes **5**, **6** and **7** in solution and when embedded in PBC polymer thin films, **Figure 3.39A** and **B**. The complexes are monomeric in solution, **Figure 3.39A**. However, all the molecules exhibited aggregation with broadening of Q bands and Soret bands in thin films. The presence of the common H aggregates in Pcs is judged by the presence of a blue shifted peak due to the aggregate and a monomer peak at lower energies [234]. For **6-PBC**, the monomer peak (lower energy) is more intense than the aggregate peak (higher energy). **7-PBC** and **5-PBC** are more aggregated in solid state than **6-PBC**, since for the former two, the high-energy peak (due to the aggregate) is more intense than the peak due to the monomer. The spectra in thin films are broader compared to those in solution, **Figure 3.39B**. The broadening of the spectra of Pcs in solid states can be attributed to the intermolecular interaction and molecular deformation

[278,279], which results in the slight modification of the energy level configurations of the Pcs [120].

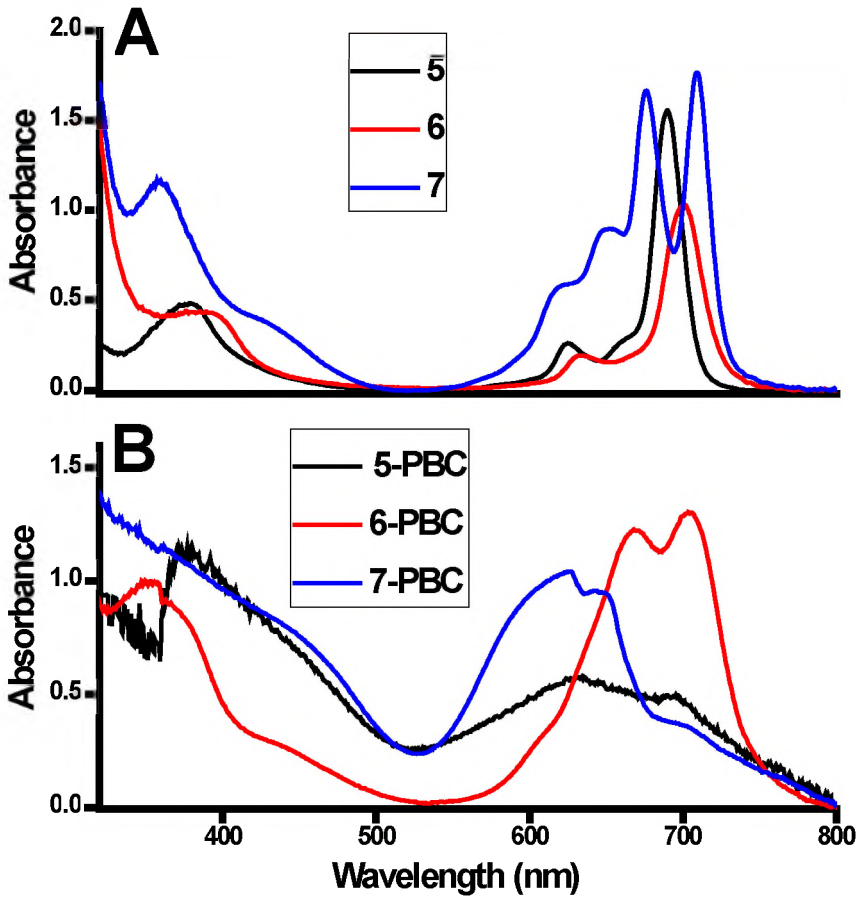

Figure 3.39: UV–vis spectra of (A) 5, 6 and 7 in $CHCl_3$ (B) 5, 6 and 7 in PBC thin films. (Concentrations of Pcs in films ~ 4.5×10^{-4} to 5.3×10^{-4} M).

3.3.2 Characterizations of MPc-polymer composites of 8 and 7 with polysulfone (PSU)

The UV–vis spectra of phthalocyanines **8-PSU** and **9-PSU** are shown in **Figure 3.40**, following immobilization on clean slide and placing in the sample compartment of the UV–vis spectrometer. The molecules exhibited aggregation with broadening of Q bands in thin films. The Q band for the monomer of **9-PSU** was observed at 687 nm complemented by the presence of a relatively intense absorption band near 622 nm, due to aggregation. In **8-PSU**, the split peaks were observed at 701 and 675 nm and the peak due to the aggregate at ≈630 nm, **Figure 3.40**.

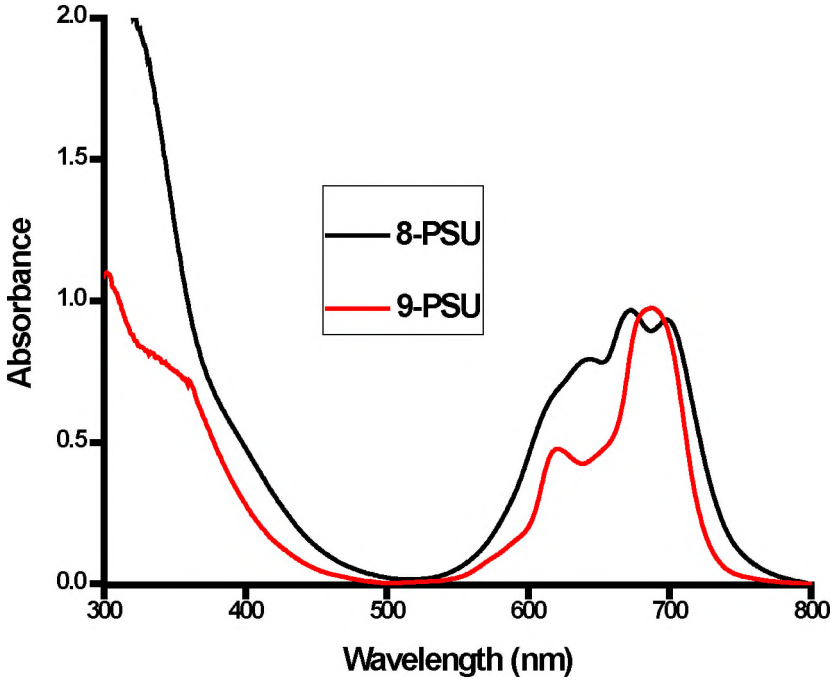

Figure 3.40: UV–visible spectra of 8-PSU and 9-PSU. Concentrations of Pcs in PSU 9.8 x 10^{-4} M.

The thin films (TF) of complex **10** (**10**/PAA-TF) and **10**-AuNPs (**10**-AuNPs/PAA-TF) composites were prepared by mixing the Pc or composites with PAA in DMF and baked at 100 °C to give compact coating surfaces. The UV-vis spectra of the doped Pc and the composites revealed aggregation in solid states with broadening of Q bands and Soret bands, the observed aggregation in solid states are also similar to the absorption spectra of Pcs (**5**, **6**, **7**, **8** and **9**) doped in PSU and PBC.

3.4 Conclusion for the chapter

Synthesis and characterizations of new phthalocyanine complexes **1**, **2**, **4**, **7**, **8**, **9** and **11** are reported in this chapter for the first time. The new complexes were characterized by FTIR, elemental analysis, ^{1}H NMR, UV-vis and mass spectroscopic techniques. Composites of complexes **10** and **11** with nanomaterials were characterized with several techniques including XPS, XRD, FTIR, EDX, TEM and UV-vis spectroscopies. The electronic absorption spectral of metallated Pc complexes showed monomeric behaviour in solution (DMSO and THF) evidenced by their single Q bands, typical of metallated phthalocyanines with D_{4h} symmetry. Unmetallated Pc complexes such as **7** and **8** revealed

splitting Q bands pattern consistent of Pcs with D_{2h} symmetry. However, Pc complexes such as **5**, **6**, **7**, **8** and **9** embedded in thin films exhibited aggregation with broadening of Q and Soret bands.

CHAPTER 4
PHOTOPHYSICAL PROPERTIES

This chapter describes the photophysical parameters such as fluorescence quantum yields and life-times, triplet quantum yields and life-times, fluorescence resonance energy transfer; fluorescence rate constants; and rate constants for intersystem crossings, of synthesized MPc molecules alone, and when conjugated to nanomaterials.

4.1 Photophysical properties of Pc derivatives without nanomaterials

4.1.1 Φ_F and τ_F

The fluorescence quantum yields (Φ_F) measured in DMSO for metal-free Pcs (**7** and **8**), InPc derivatives (**1**, **2** and **6**), ZnPc derivatives (**3**, **4**, **5**, **9**, **10** and **11**), and in THF for complexes **8** and **9** are summarized in **Table 4.1.** Fluorescence quantum yield (Φ_F) values are very low for complexes **1**, **2** and **6**, since Pcs with large metals such as In, fluoresce very weakly due to the heavy atom effects [280,281]. Results from **Table 4.1** show that Φ_F values obtained for InPc and ZnPc complexes in DMSO are lower than unsubstituted parent compounds; ClInPc (Φ_F = 0.018) [282], and ZnPc (Φ_F = 0.20 [69], respectively, suggesting quenching of fluorescence by their respective substituents on the peripheral positions.

The Φ_F values observed for complexes **8** and **9** in DMSO are lower than the values reported in THF, due to differences in solvent polarity, viscosity and refractive indexes [22,283,284]. Higher Φ_F values have been reported for Pcs in THF compared to DMSO [22], and this is attributed to low quenching abilities of THF for the excited singlet states. The low value of the fluorescence quantum yields of complex **8** in DMSO, compared to that in THF, is also attributed to the presence of some degree of aggregation of **8** in DMSO as shown in Chapter 3. Fluorescence quantum yield of complex **4** is lower than its ZnPc precursor (**3**), suggesting fluorescence quenching property of the triazole-fused nitrophenyl substituent in complex **4**. Electron withdrawing groups like NO_2 have tendency to diminish the fluorescence quantum yields [281], hence the lower quantum yield observed in **4**. Variation in the observed values of Φ_F of ZnPc complexes can be attributed to the differences in the molecular structures of the studied complexes. The lower quantum yield reported for complex **11** compared to **10** is due to the large numbers of amino group substituents in the former than the later, NH_2 groups are known to quench fluorescence [111].

The fluorescence lifetimes (τ_F) for the studied compounds were obtained from TCSPC technique by fitting the fluorescence decay data to a bi-exponential function for complexes **1** and **2**, and mono-exponential functions for other complexes. Average lifetimes for **1** and **2** are listed in **Table 4.1**. A bi-exponential decay may occur for Pcs due to the formation of aggregates which are non-fluorescent, but which can quench the monomer [284]. **Figure 4.1** shows the typical fluorescence decay profile of complex **2** in DMSO. The lifetimes reported for **1**, **2** and **6** are within the range reported for heavy atom based Pcs, and are much lower than other Pc molecules due to the reason given above for the Φ_F values, **Table 4.1**. Hence, complexes **1**, **2** and **6** are more favoured to populate the first triplet excited states than other complexes. The shorter τ_F for **4** corresponds to its lower Φ_F compared to **3**. Again, fluorescence lifetimes of complexes **8** and **9** were short in DMSO compared to when measured in THF due to the differences in solvent polarity and refractive indexes. Fluorescence lifetime of **11** also corresponds to lower quantum yields compared to complex **10**.

The fluorescence rate constant (k_F) is directly proportional to the fluorescence quantum yields (Φ_F) of the Pcs. However, the observed trends in the fluorescence rate constants for the studied complexes do not follow the same trend as the quantum yields.

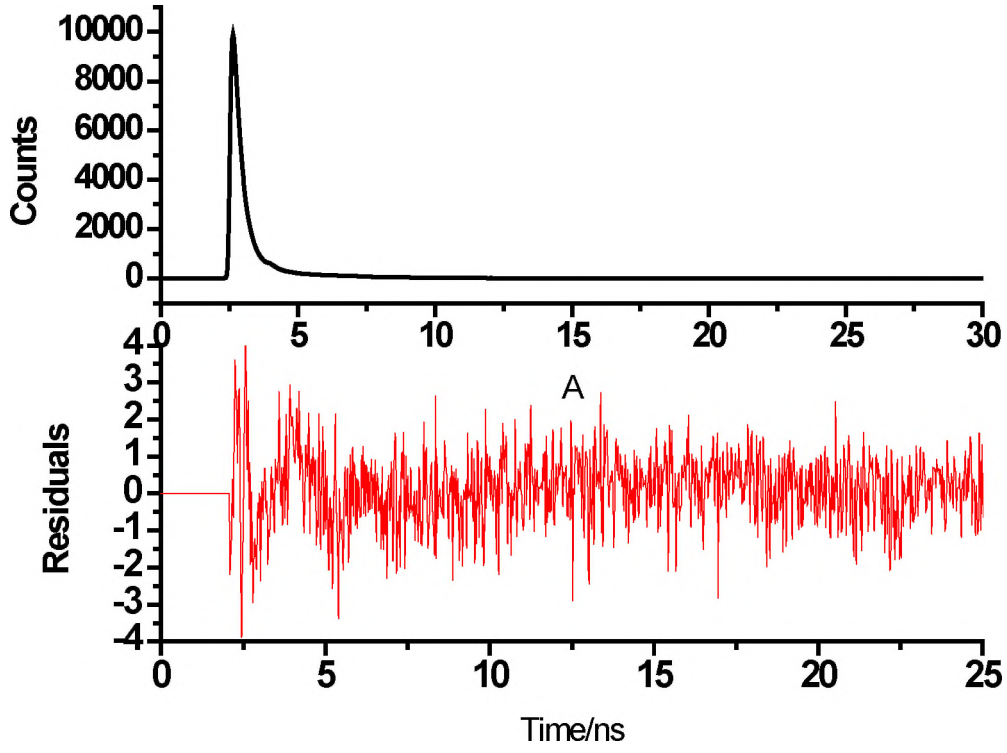

Figure 4.1: Fluorescence decay profile of 2 in DMSO. Excitation wavelength = 702 nm.

4.1.2 Φ_T, τ_T, k_{ISC} and τ_{ISC} values

Figure 4.2 shows a typical decay curve using complex **10** as an example. All complexes/conjugates gave bi-exponential decay curves, typical of Pcs at high concentration [285]. Triplet quantum yield (Φ_T) is a measure of the fraction of excited molecules that populate the metastable triplet excited states via spin-orbit coupling. In Table 4.2, large triplet quantum yields (Φ_T) values are recorded for complexes **1**, **2**, **6** and **11** in DMSO. High Φ_T values for **1**, **2** and **6** are due to the presence of heavy atom effect of indium. The highest Φ_T value reported for **11** compared to other ZnPc derivatives is due to the internal heavy atom effect induced by the sulphur-containing substituents in **11** as against the oxygen linkers in other ZnPc complexes [286]. The Φ_T observed for **8** was low at Φ_T = 0.60, due to the absence of central metal in the Pc ring; the value increased to Φ_T = 0.65 for **9** with the insertion of metal (Zn) in the cavity of the Pc. Also, larger triplet quantum yield (Φ_T) value was observed for **4** (0.77) compared to **3** (0.64), corresponding to the lower Φ_F value recorded for the former in Table 4.1. In general, Φ_T and Φ_F are competing processes, that is, the high value of Φ_T should correspond to low value of Φ_F and vice versa, Tables 4.1 and 4.2.

Triplet lifetimes values for the complexes in DMSO ranged from 63 to 350 μs with InPc complexes **1**, **2** and **6** having the shortest lifetime values expected for molecules with large triplet quantum yields. It is expected that **11** will have the shortest triplet lifetimes, since molecules with larger triplet quantum yields should have shorter triplet lifetimes [287], and vice versa. This is not the case for many of the ZnPc complexes listed in Table 4.2. It is safe to assume that the observed trends in **8** (H_2Pc) and **9** (ZnPc) are as a result of their different structural configurations upon excitation. Also, differences in the substituents of **4** and its precursor (**3**) could be the reason for the discrepancies.

The rate of intersystem crossing (k_{ISC}) observed for complexes **1**, **2** and **6** are the highest as expected for heavier atoms. The highest k_{ISC} values for **1**, **2** and **6** correspond to the lowest intersystem crossing lifetimes (τ_{ISC}), since τ_{ISC} and rate of intersystem crossing (k_{ISC}) to the triplet states are competing processes, as observed in Table 4.2. Combination of high rate of intersystem crossing (k_{ISC}) with low intersystem crossing lifetimes are required to populate the excited triplet states of organic macrocycles.

Table 4.1: Fluorescence data of InPcs, ZnPcs and metal-free Pc derivatives obtained in DMSO except otherwise stated

Sample	Solvent	Φ_F	τ_F (ns) ± 0.02	τ_{avF} (ns) ± 0.03	[a]k_F(s^{-1}) (10^7) ± 0.02
1	DMSO	0.012	0.31 2.85	0.37	3.2
2	DMSO	<0.01	0.32 2.72	0.36	2.5
3	DMSO	0.11	4.91	-	2.2
4	DMSO	0.09	2.49	-	3.6
5[b]	DMSO	0.03	1.3	-	23.1
6[c]	DMSO	0.029	0.26	-	11.1
7	$CHCl_3$	0.33	5.59		5.8
8	DMSO	0.16	2.56	-	6.3
8	THF	0.23	4.24	-	5.4
9	DMSO	0.17	1.67	-	10.2
9	THF	0.30	3.34	-	8.9
10	DMSO	0.18	2.73	-	6.5
11	DMSO	0.12	2.44	-	5.0

[a] $k_F = \Phi_F/\tau_{avF}$ or Φ_F/τ_F. [b] Data from reference [215], [c] Data from reference [216].

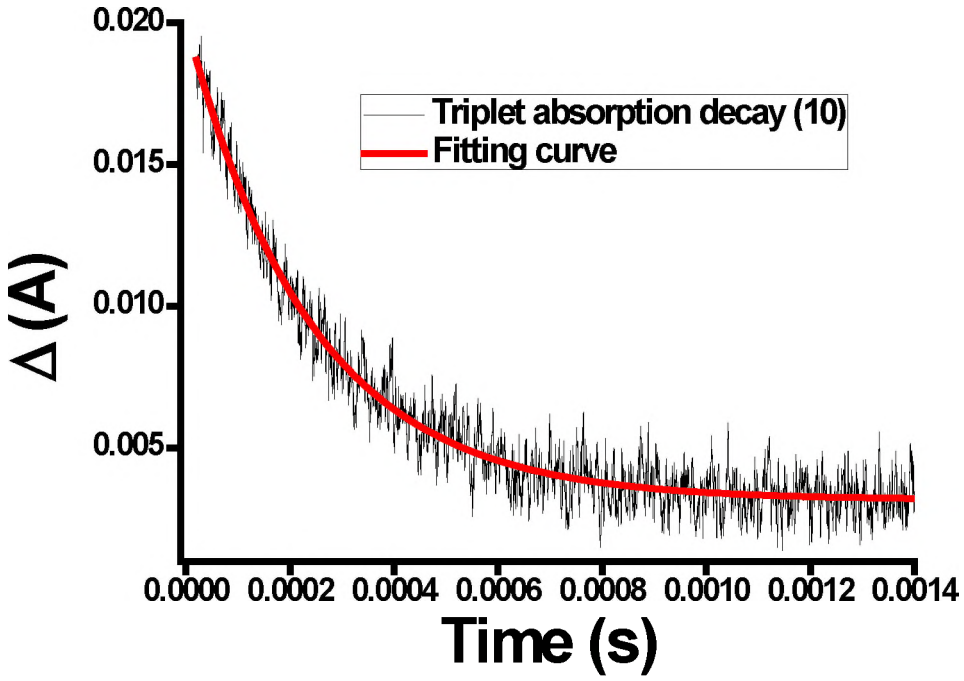

Figure 4.2: Triplet absorption decay curve 10 with the fitting curve in DMSO. Data were obtained at 475 nm using 675 nm excitation source.

Table 4.2: Φ_T, τ_T, k_{ISC} and τ_{ISC} of InPcs, ZnPcs and metal-free Pc derivatives obtained in DMSO.

Sample	Φ_T	τ_T (μs) ± 0.02	$k_{ISC}(s^{-1})$ $(10^9)^a$ ± 0.001	τ_{ISC}(ns)^b ± 0.003
1	0.82	75	2.22	0.45
2	0.84	66	2.33	0.43
3	0.64	251	0.13	7.67
4	0.77	283	0.31	3.23
5	0.75	229	0.58	1.70
6	0.86	63	3.30	0.30
8	0.60	307	0.23	4.30
9	0.65	310	0.39	2.60
10	0.73	240	0.27	3.70
11	0.83	350	0.34	2.90

[a] $k_{ISC} = \Phi_T/\tau_{avF}$ or Φ_T/τ_F, [b]$\tau_{ISC} = \tau_{avF}/\Phi_T$ or τ_F/Φ_T , [Complex **7** not soluble in DMSO, hence no triplet studies in chloroform]

4.2 Photophysical properties of 2-AuNPs and 3-AuNPs conjugates

4.2.1 Φ_F, τ_F, k_F and k_{ISC}

The fluorescence quantum yield (Φ_F) and lifetimes (τ_F) values of **2-** or **3-AuNPs** composites measured in DMSO are listed in **Table 4.3**, and compared with their respective unconjugated phthalocyanines **2** and **3**. Φ_F value of **2** alone is low due to the heavy atom effects of In central metal as reported above; the value is expected to drop further for **2-AuNPs** composites due to the combined effects of In and the metallic nanoparticles. The Φ_F value for **3-AuNPs** of 0.02 is 5.5 times lower than that of unconjugated **3**. Such significant reduction in the Φ_F is attributed to the heavy atom effects of AuNPs which are known for quenching of the excited singlet states of phthalocyanines.

Fluorescence lifetimes (τ_F) for the phthalocyanines-AuNPs composites were obtained from TCSPC technique by fitting the fluorescence decay data to a bi-

exponential function. In the presence of AuNPs, the presence of two lifetimes may reflect different orientations of the Pcs on the NPs. The average fluorescence lifetimes (τ_{avF}) of the conjugates were shortened compared to the unconjugated phthalocyanines alone. Again, this suggests quenching ability of Pcs fluorescence by the presence of the AuNPs, due to the heavy atom effect of Au.

Fluorescence and intersystem rate constants (k_F and k_{ISC}) were calculated from the values of Φ_F and Φ_T, respectively. Large k_{ISC} value is an indication of increased intersystem crossing (ISC) to triplet excited states. Hence, the rate of ISC is higher for both **2-AuNPs** and **3-AuNPs** composites than the corresponding **2** and **3**, respectively. This suggests that the triplet populations of **2** and **3** in presence of AuNPs increased with increasing rate of ISC. k_F value of **3** at 0.22 dropped to 0.052 after conjugating to AuNPs, while that of **2** dropped from 0.25 to 0.062 for **2-AuNPs**, suggesting that fluorescence pathway is more favoured for excited states of the **2** and **3** compared to the conjugates.

Table 4.3: Photophysical parameters for 2, 3, 2-AuNPs and 3-AuNPs recorded in DMSO.

Parameter/Samples	2	3	2-AuNPs	3-AuNPs
Φ_F	<0.01	0.11	< 0.01	0.02
τ_F (ns)[a] ± 0.0013	0.32 (98.39%) 2.72 (1.61%)	4.91	0.23 (97.54%) 1.50 (2.46%)	4.53 (81.37) 1.02 (18.63)
τ_{avF} (ns)[b] ± 0.013	0.36	-	0.26	3.87
Φ_T	0.84	0.64	0.92	0.77
τ_T (μs)	66	251	43.30	220
k_F (s^{-1}) (10^8)[c]	0.25	0.22	0.06	0.05
k_{ISC} (s^{-1}) (10^8)[d]	23.30	1.30	35.80	2
τ_{ISC}(ns)[e]	0.43	7.67	0.28	5.03

[a] Amplitudes in brackets, [b] Average lifetime used. [c] $k_F = \Phi_F/\tau_F$, [d] $k_{ISC} = \Phi_T/\tau_F$, [e] $\tau_{ISC} = \tau_{avF}/\Phi_T$ or τ_F/Φ_T.

4.2.2 Φ_T, τ_T and τ_{ISC}

Figure 4.3 shows the triplet absorption decay curves for **2**, **3** and their composites with AuNPs using laser flash photolysis in DMSO. Triplet quantum yields are

summarized in **Table 4.3**. A larger triplet quantum yield (Φ_T) value at 0.92 was observed for **2-AuNPs** as against 0.84 for **2** alone. Similarly, Φ_T of **3** increased from 0.64 to 0.77 after clicking with AuNPs. Higher triplet state absorptions of In and Zn phthalocyanines in the presence of the nanocrystals are due to the heavy metal effect of AuNPs. **Table 4.3** shows that the triplet lifetimes for the Pcs are longer that the values reported for their conjugates. The result is consistent for a molecule with smaller triplet quantum yield to have longer lifetime [287], and vice versa. Also, intersystem crossing lifetimes (τ_{ISC}) are lower for both **2** and **2-AuNPs** than **3** and its conjugates as expected for molecules with higher rate of intersystem crossing (k_{ISC}).

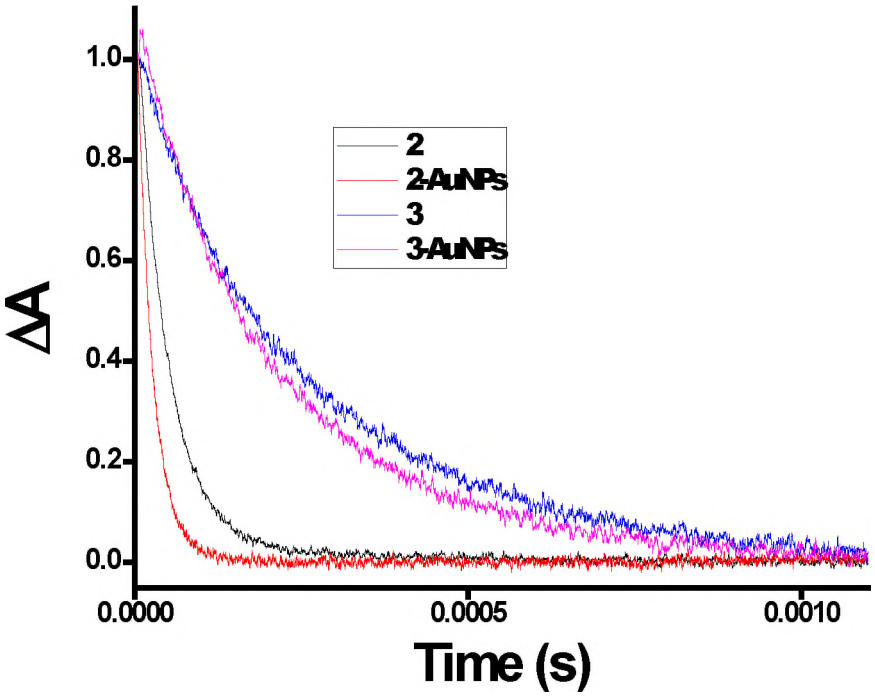

Figure 4.3: Triplet absorption decay curves for 2, 2-AuNPs, 3 and 3-AuNPs.

4.3 Complex 10 when covalently linked to nanomaterials or polymer

4.3.1 10-AuNPs and 10-PAA

4.3.1.1 Φ_F, τ_F and k_F values

The fluorescence lifetimes (Φ_F) and quantum yields (τ_F) of **10** alone and when conjugated to AuNPs and PAA in DMSO are summarized in **Table 4.4**. The fluorescence quantum yields of **10-AuNPs** and **10-PAA** composites are lower than the value observed for the **10** alone. The lowering of Φ_F values are expected for **10** in the presence of AuNPs is due the heavy atom effect of Au which encourages intersystem crossing to the triplet states, hence lowering fluorescence. The relatively larger Φ_F value of **10-PAA** than **10-AuNPs** reflects low quenching ability for the excited singlet state of **10** by the poly acrylic acid compared to AuNPs, due to the heavy atom effect of the latter. Fluorescence decay data of **10** and the composites were fitted to mono-exponential function, suggesting single fluorescence lifetimes (τ_F) for **10** and its conjugates. τ_F value of **10-AuNPs** is lower than for **10** alone and **10-PAA**, for reasons given above. Higher τ_F value for **10-PAA** compared to **10** alone could be attributed to nature or the length of the spacer between the Pc and the polymer [288]. The largest k_F value is observed for **10** alone, followed by **10-PAA** and the lowest for **10-AuNPs**.

4.3.1.2 Φ_T, τ_T, k_{ISC} and τ_{ISC} values

Figure 4.4 shows the triplet absorption decay curves for **10**, **10-AuNPs** and **10-PAA**. The highest triplet quantum yields (Φ_T) of 0.83 was recorded for **10-AuNPs** conjugate, followed by **10** alone with Φ_T of 0.73, and **10-PAA** composites recorded the lowest Φ_T value of 0.67, **Table 4.4**. The significant enhancement of the triplet state absorption of the **10** in presence of AuNPs is influenced by intersystem crossing induced by the heavy metal effect of Au atom as explained above. Triplet lifetimes of **10** and its conjugates ranged from 240 to 342 μs, with **10-AuNPs** showing the longest triplet lifetimes. **10-AuNPs** is expected to have the shortest triplet lifetimes considering its largest triplet quantum yields of 0.83. However, similar results have been reported for Pcs in presence of AuNPs which was attributed to the encapsulation of Pc molecules by AuNPs [220]. The largest value of k_{ISC} for **10-AuNPs** suggests an increased rate of ISC from an excited singlet to triplet states compared to **10** and **10-PAA**. The largest value of k_{ISC} for **10-AuNPs** also correspond to the lowest τ_{ISC} value at 3.02 ns compared to others.

Table 4.4: Photophysical parameters for 10, 10-AuNPs, 10-PAA, 10-Fe_3O_4@Ag and 10-Fe_3O_4-Ag recorded in DMSO.

Parameter/Samples	10	10-AuNPs	10-PAA	10-Fe_3O_4@Ag	10-Fe_3O_4-Ag
Φ_F	0.18	0.03	0.07	0.03	0.02
τ_F (ns)	2.73	2.56	2.80	2.54	2.41
Φ_T	0.73	0.83	0.67	0.81	0.88
τ_T (μs)	240	342	258	175	142
k_F (s^{-1}) (10^8)	0.6	0.14	0.24	0.11	0.09
k_{ISC} (s^{-1}) (10^9)	0.27	0.33	0.24	0.33	0.4
τ_{ISC} (ns)	3.74	3.02	4.18	3.14	2.74

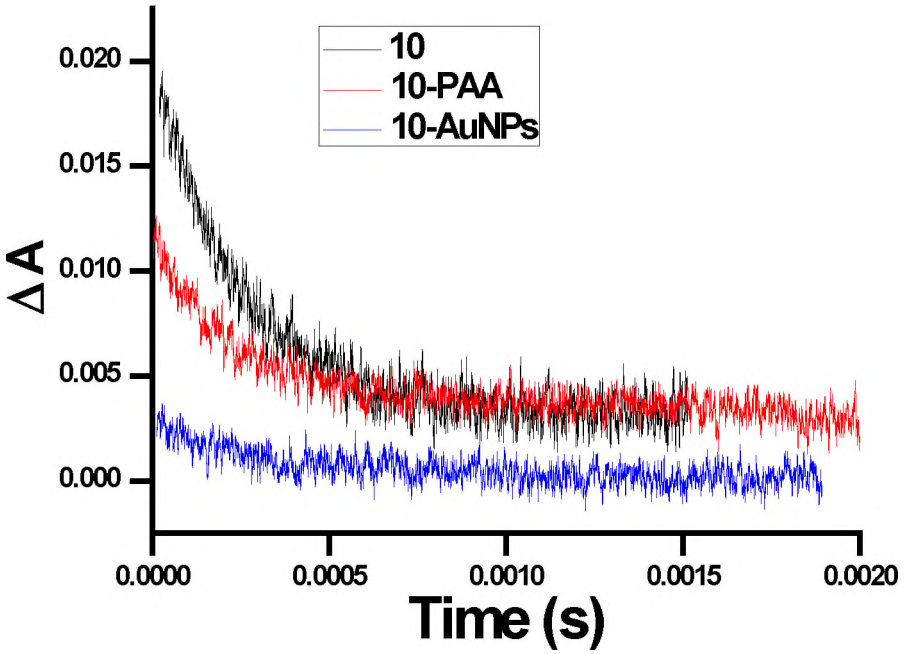

Figure 4.4: Triplet absorption decay curves for 10, 10-AuNPs and 10-PAA recorded in DMSO. Data were obtained at 475 nm using 675 nm excitation source.

4.3.2 10-Fe_3O_4@Ag and 10-Fe_3O_4-Ag

4.3.2.1 Φ_F, τ_F, k_F and k_{ISC}

The fluorescence quantum yields (Φ_F) of the conjugates are up to 7 to 8 times lower than the value reported for **10** due to heavy atom effects of the nanoparticles. **10-Fe_3O_4-Ag** gave a lower Φ_F value compared to **10-Fe_3O_4@Ag**, **Table 4.4.** Fluorescence decay data of the composites were fitted to mono-exponential function, suggesting single fluorescence lifetimes (τ_F) for the conjugates. Obtained τ_F value of **10-Fe_3O_4@Ag** was found to be 2.54 ns, this is slightly longer than the value observed for **10-Fe_3O_4-Ag** at 2.41 ns for reasons explained above. However, both conjugates have significantly lower τ_F values as compared to **10**. Large k_{ISC} value is an indication of increased ISC to triplet excited states. Hence, rate of ISC is highest for **10-Fe_3O_4-Ag** followed by **10-Fe_3O_4@Ag** and **10**. Fluorescence pathway is more favoured for excited states of **10** than ISC evidenced from the its largest k_F value compared to the conjugates.

4.3.2.2 Φ_T, τ_T and τ_{ISC}

Figure 4.5A shows the overlay triplet absorption decay curves for **10**, **10-Fe_3O_4@Ag** and **10-Fe_3O_4-Ag** investigated in DMSO at 675 nm cross-over wavelengths. Triplet quantum yields of the samples are also summarized in **Table 4.4**. Higher Φ_T was observed when **10** was conjugated to Fe_3O_4-Ag hybrid NPs than Fe_3O_4@Ag core-shell NPs which does not correspond to trends in Φ_F. Lower Φ_T value for **10-Fe_3O_4@Ag** could be due to the differences in the structural compositions of the nanoparticles, and their behaviour upon excitation. Also, this could be due to the effects of surface passivation of Fe_3O_4 core of the core-shell NPs by the Ag layer. Hence, photophysical properties of Fe_3O_4@Ag is more suppressed compared to Fe_3O_4-Ag hybrid nanostructures. Triplet lifetimes of the samples were determined by exponential fitting of the kinetic curves (**10-Fe_3O_4-Ag** as representative) using OriginPro 2016 in **Figure 4.5B**. Triplet lifetimes for **10** in the presence of Fe_3O_4@Ag and Fe_3O_4-Ag are 175 and 142 μs, respectively. Again, triplet absorption population of **10-Fe_3O_4-Ag** is more pronounced than **10-Fe_3O_4@Ag** evidenced for the lower τ_{ISC} value of the former. Generally, complex **10** showed improved photophysical properties when conjugated to both Fe_3O_4@Ag and Fe_3O_4-Ag than in the presence of AuNPs, this could be attributed to the

combined synergistic effects of Fe and Ag in lowering the fluorescence intensity of **10**, and consequently improving the triplet-triplet states absorption of the Pc in the triplet excited states.

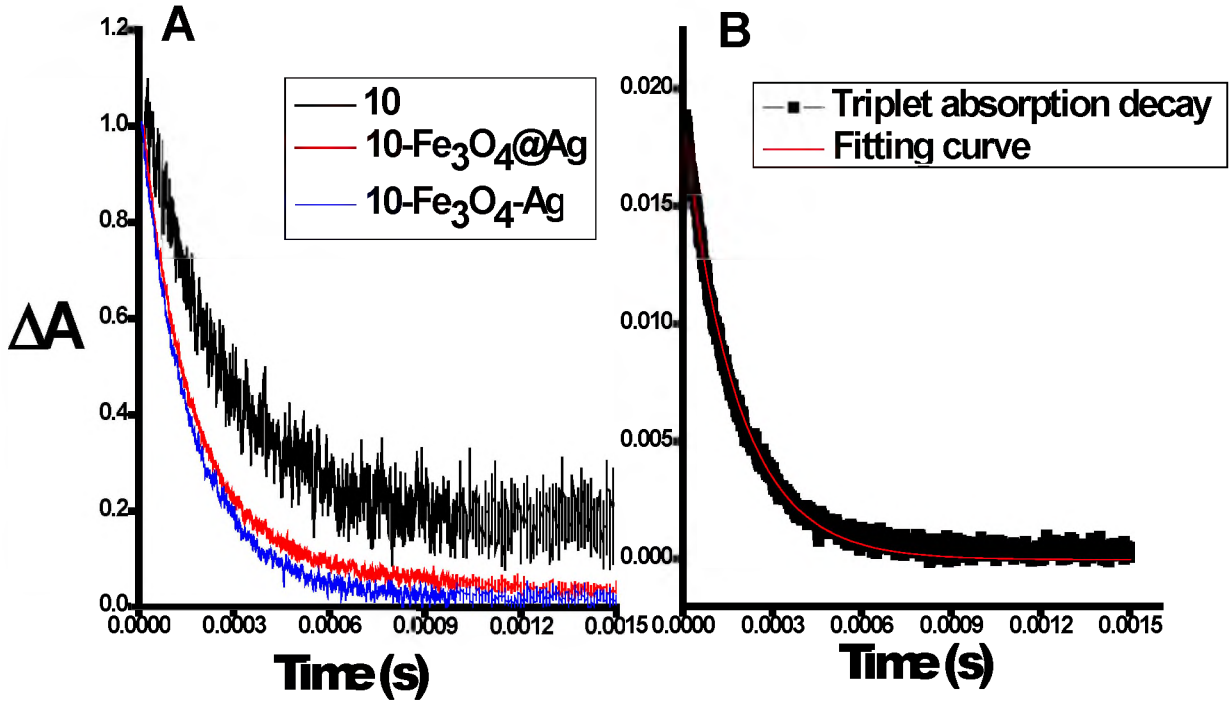

Figure 4.5: (A) Triplet absorption decay curves for (A) 10, 10-Fe_3O_4@Ag, and 10-Fe_3O_4-Ag and (B) 10-Fe_3O_4-Ag with exponential fitting curve.

4.3.3. 10-GQDs, 10-NGQDs and 10-SNGQDs

4.3.3.1 Φ_F, τ_F and FRET parameters

The photophysical parameters of graphene quantum dots, and their conjugates to complex **10** recorded in DMSO are summarized in **Table 4.5**. Fluorescence quantum yields ($\Phi_{F(QDs)}$) of QDs (GQDs, NGQDs and SNGQDs) alone in aqueous solution have been reported before [289]. Fluorescence quantum yields ($\Phi_{F(QDs)}$) of the conjugates at the wavelengths where QDs absorb were found to be up to 2.6 times lower than the QDs alone, **Table 4.5**. The decrease is due to Förster resonance energy transfer (FRET) and other energy transfer processes which has been reported to deactivate the emission of the QDs [290,291]. Fluorescence enhancement in the Pcs and fluorescence quenching in the quantum dots are the two competing processes that occur during interaction of Pcs with

quantum dots. Similarly, at the excitation wavelengths where the QDs absorb, the fluorescence lifetimes ($\tau_{F(QDs)}$) of the conjugates were observed to be significantly short compared to the lifetimes of the QDs (in brackets) alone, corresponding to decrease in quantum yields.

FRET efficiency for the conjugates were determined from the fluorescence quantum yields of the conjugates and unconjugated QDs at excitation wavelengths where QDs absorb as shown in **Eq. 1.3** [73].

The calculated FRET Eff ranged from 0.52 to 0.61, **Table 4.5**. The highest FRET efficiency value of 0.61 was obtained for SNGQDs with more red-shifted emission spectrum, and overlap slightly more with the UV-vis spectrum of **10** than GQDs and NGQDs, **Figure 4.6.** FRET efficiency values calculated for the QDs are only estimates, there other energy transfer processes that could be responsible for the decrease in the emission of the QDs in addition to FRET [76-78,288-292].

The $\Phi_{F(Pc)}$ of the **10-QDs** at the excitation wavelength of 613 nm where only Pc absorbs are larger than the unconjugated Pc (**10**). Reduction in Φ_F are mostly reported for metal-based nanomaterials when conjugated to phthalocyanines due to heavy atom effects of the nanoparticles, but there is no heavy atom effect for GQDs, hence decrease in Φ_F is not expected. However, increases in Φ_F for Pcs covalently linked to QDs and magnetic nanoparticles have been reported, and attributed to the nature or the length of the spacer [288]. Time resolved fluorescence data for **10** and **10-QDs** conjugates obeyed a mono-exponential decay. The increase in the $\Phi_{F(Pc)}$ values were complemented by increase in the fluorescence lifetimes ($\tau_{F(Pc)}$) for the conjugates measured at the excitation wavelengths of **10**.

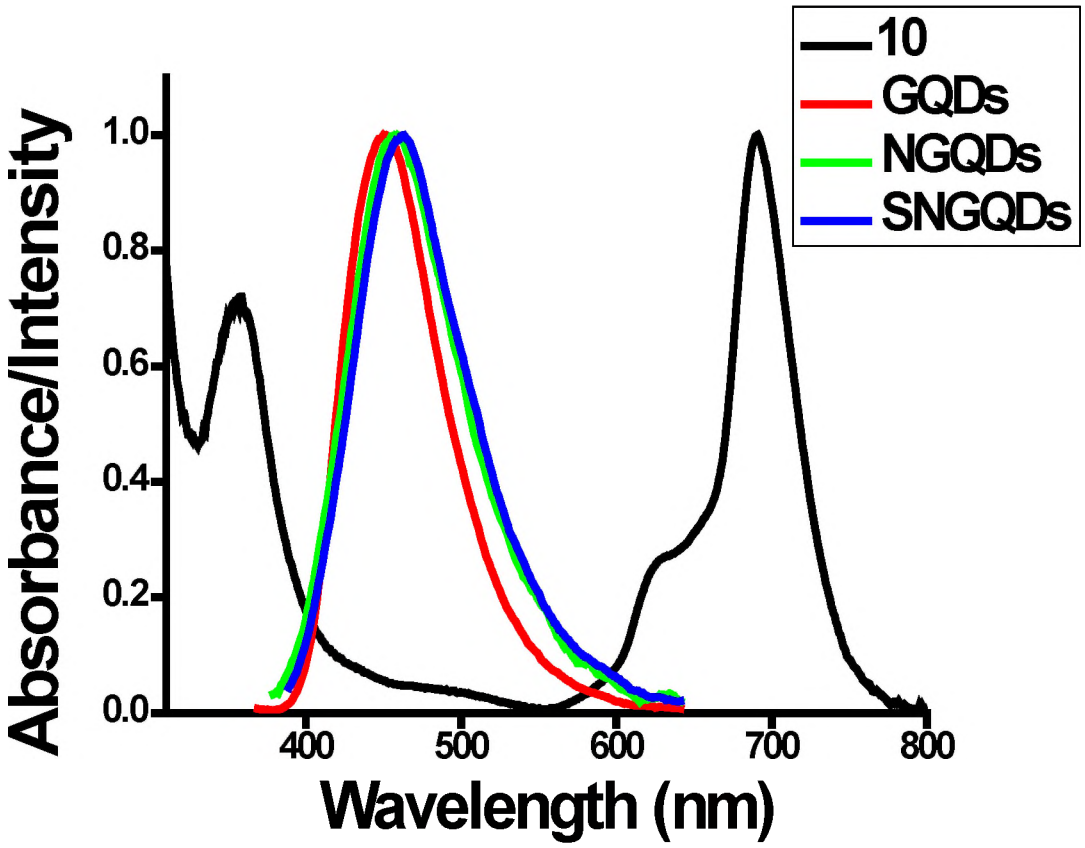

Figure 4.6: Absorption spectrum of 10 (in DMSO) and emission spectra of GQDs (λ_{exc} = 340 nm), NGQDs (λ_{exc} = 355 nm) and SNGQDs (λ_{exc} = 370 nm) in water.

4.3.3.2 Φ_T and τ_T

The triplet quantum yields absorption (Φ_T) and lifetimes recorded in DMSO at 675 nm cross-over wavelength are summarized in **Table 4.5**. The measured triplet quantum yields (Φ_T) of the samples are 0.73, 0.74, 0.77 and 0.79 for **10**, **10-GQDs**, **10-NGQDs** and **10-SNGQDs**, respectively. The observed trend was surprising since the QDs do not contain heavy metal atoms that can result in enhanced intersystem crossing to the triplet excited states via ISC [293,294]; as was observed in **Table 4.4** for **10** in the presence of AuNPs, Fe_3O_4@Ag and Fe_3O_4-Ag. The slight increase in Φ_T could be ascribed to the large conjugative systems of graphene QDs which significantly reduced the singlet-triplet splitting and thus enhance the probability of intersystem crossing [295]. Triplet lifetimes of the samples were determined by exponential fitting of the kinetic curves (**10-SNGQDs** as representative) in **Figure 4.7**. **Table 4.5** shows that the triplet lifetimes for **10** and its conjugates ranged from 187 to 240 μs.

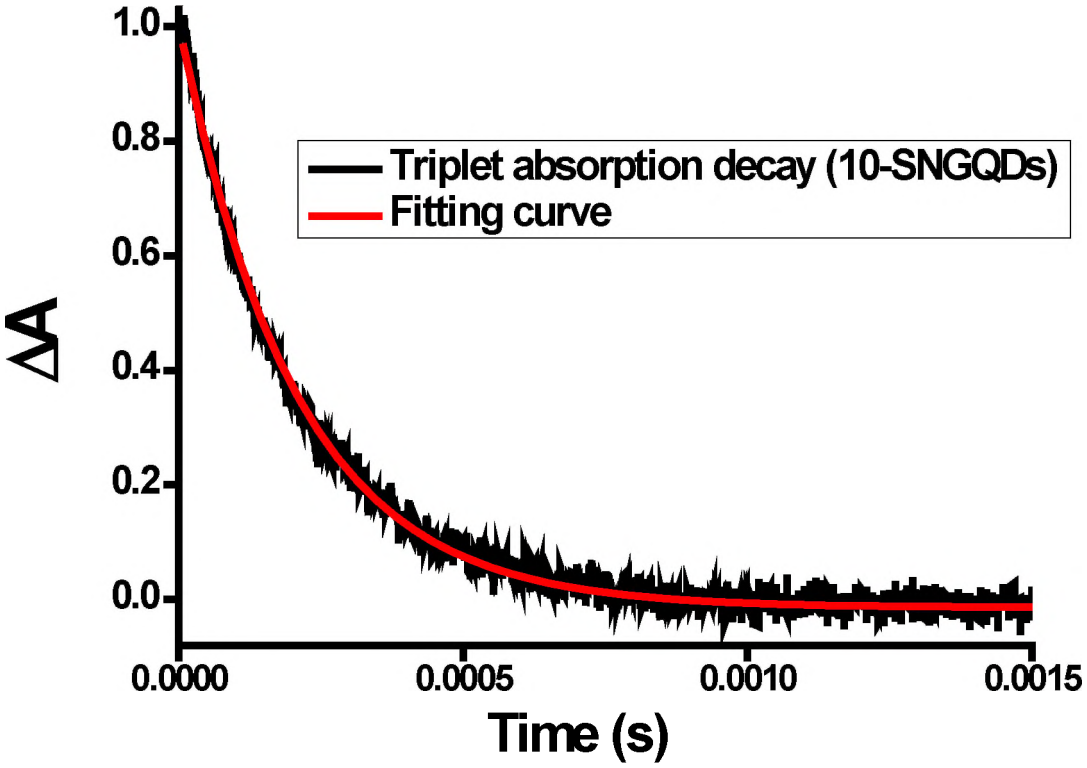

Figure 4.7: Triplet absorption decay curve of 10-SNGQDs with exponential fitting curve in red. Data were obtained at 475 nm using 675 nm excitation source.

Table 4.5: Photophysical parameters of graphene quantum dots, 10 and the conjugates recorded in DMSO.

Sample	λ_{abs}[a,b] (nm)	$\Phi_{F(Pc)}$[c]	$\Phi_{F(QDs)}$[b,d]	$\tau_{F(Pc)}$ (ns)[c]	$\tau_{F(QDs)}$[b] (ns)	τ_T (μs)	Φ_T	FRET Eff
10	691	0.18	-	2.73	-	240	0.73	-
10-GQDs	686 (334)	0.25	0.10 (0.21)	2.89	5.17 (5.7)	194	0.74	0.52
10-NGQDs	687 (341)	0.23	0.31 (0.77)	2.86	6.81 (7.8)	205	0.77	0.59
10-SNGQDs	687 (337)	0.20	0.31 (0.81)	2.84	3.96 (11.6)	187	0.79	0.61

[a] λ_{abs} = absorption wavelength. [b] values in brackets are for QDs alone in water. [c] Excitation where Pc absorbs. [d] Excitation where QDs absorb, values for $\Phi_{F(QDs)}$ alone are from reference [289].

4.3.4 11-Ag_3Au_1 and 11-Ag_1Au_3

Table 4.6 shows the fluorescence quantum yield (Φ_F) and lifetimes (τ_F) values of compound **11** and its conjugates studied in DMSO. The quantum yields of **11-Ag_1Au_3** and **11-Ag_3Au_1** composites are substantially lower than the value observed for **11** alone; this shows the significant quenching of the excited singlet states of **11** by bimetallic nanoparticles. The decrease in fluorescence quantum yields of **11** in the presence of Ag_xAu_y is attributed to the heavy atom effects of bimetallic nanoparticles which encourage intersystem crossing to the triplet states as discussed above. The Φ_F values for Pc (**11**) in the presence of Ag_xAu_y (**Table 4.6**) are larger than the values reported for **10** in the presence of AuNPs, or Fe_3O_4@Ag and Fe_3O_4-Ag (**Table 4.4**), since two heavy atoms are involved in the former. Time resolved fluorescence data, **Figure 4.8**, were fitted to mono-exponential functions for **11**. For the conjugates (**11-Ag_xAu_y**), a bi-exponential curve was obtained and average lifetimes are given in **Table 4.6**. The fluorescence lifetimes of **11-Ag_xAu_y** were shorter than **11** as expected, suggesting quenching of Pc fluorescence by the bimetallic nanoparticles.

The triplet decay curve is shown in **Figure 4.9**. The highest triplet quantum yields (Φ_T) of 0.95 was recorded for **11-Ag_1Au_3**, followed by **11-Ag_3Au_1** with Φ_T of 0.92, and **11** with the Φ_T value of 0.83. The significant enhancement of the Φ_T values is due to enhanced intersystem crossing as a result of the bimetallic nanoparticles. **11-Ag_1Au_3** containing more Au (a heavier atom than Ag), has a larger Φ_T value compared to **11-Ag_3Au_1**. The triplet lifetimes for **11** at 350 μs decreased significantly to 223 μs (for **11-Ag_3Au_1**) and 251 μs (**11-Ag_1Au_3**) after conjugation to bimetallic nanoparticles, corresponding to increase in Φ_T values.

11-Ag_xAu_y composites have larger k_{ISC} values ($\approx 0.4 \times 10^{-9}$ s^{-1}) with corresponding lower τ_{isc} values compared to complex **11**, suggesting increased ISC to triplet excited states. Rate of ISC is highest for **11-Ag_1Au_3** followed by **11-Ag_3Au_1** and **11** judging from the values of τ_{isc}. Also, fluorescence pathway is more favoured for excited states of **11** than ISC evidenced from the its largest k_F value compared to its composites (**11-Ag_xAu_y**).

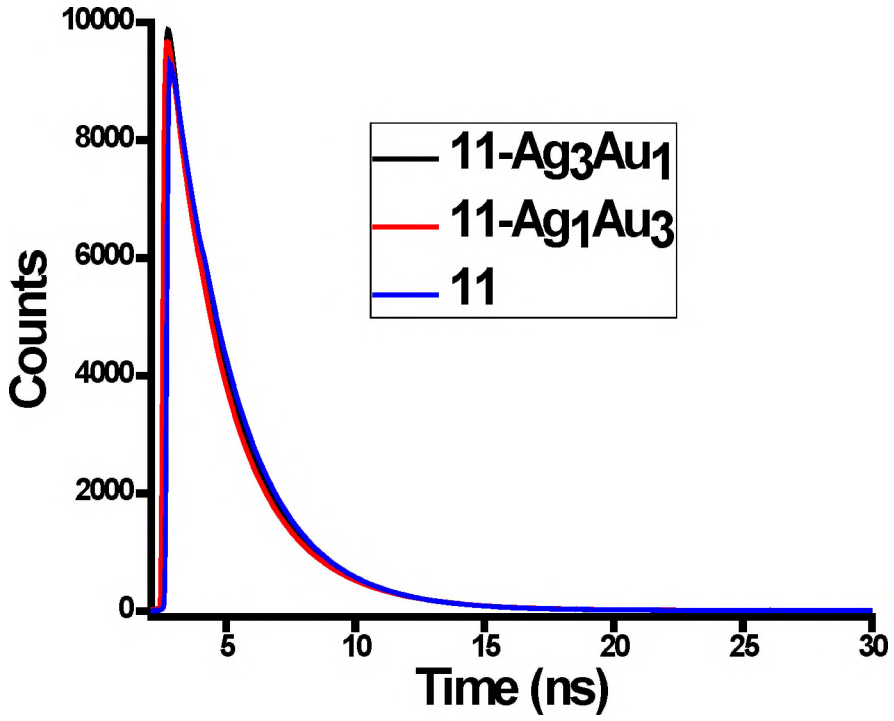

Figure 4.8: Fluorescence decay curves of 11, 11-Ag_1Au_3 and 11-Ag_3Au_1, absorbance of solution ≈ 0.05.

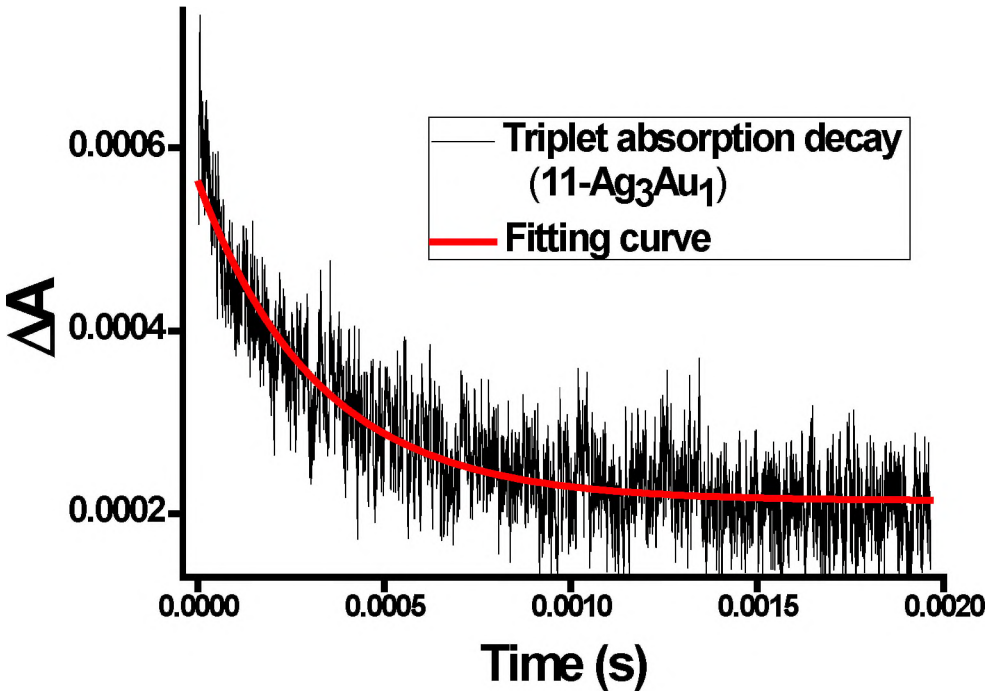

Figure 4.9: Triplet absorption decay curve of 11-Ag_3Au_1 with exponential fitting curve in red.

Table 4.6: Photophysical parameters of **11**, **11**-Ag_1Au_3 and **11**-Ag_3Au_1 recorded in DMSO.

Parameter/Samples	**11**	**11**-Ag_1Au_3	**11**-Ag_3Au_1
Φ_F	0.122	0.051	0.046
τ_F (ns) ± 0.001	2.44 (100%)	2.48 (87.54%) 0.56 (12.46%)	2.77 (72.83%) 0.98 (27.17%)
τ_{avF} (ns) ± 0.002	-	2.24	2.28
Φ_T	0.83	0.95	0.92
τ_T(μs)	350	251	223
k_F (s^{-1}) (10^8)	0.5	0.23	0.202
k_{ISC} (s^{-1}) (10^9)	0.34	0.42	0.40
τ_{ISC} (ns)	2.94	2.36	2.48

4.4 Conclusion to the chapter

Indium centred Pc complexes **1**, **2** and **6** showed improved triplet population compared to other molecules due to the heavy atom effects of In atom. Hence, complexes **1**, **2** and **6** are more favoured to populate the first triplet excited states than other complexes. Highest Φ_T value was reported for complex **11** compared to other ZnPc derivatives due to the internal heavy atom effect induced by the sulphur-containing substituents in **11** as against the oxygen linkers in other ZnPc complexes. Enhanced triplet absorptions of complexes **2**, **3**, **10** and **11** in presence of metal based nanomaterials were observed due to the heavy atom effects of metallic nanoparticles which are known for quenching of the excited singlet states of phthalocyanines. The slight increase in the fluorescence quantum yields of **10** in the presence of GQDs show that the excited singlet states of **10** was not quenched by the GQDs due to the absence of heavy metal atoms. However, the value of Φ_T for **10** was observed to improve slightly in the presence of GQDs due to the large conjugative systems of graphene QDs which significantly reduced the singlet-triplet splitting and thus enhance the probability of intersystem crossing.

CHAPTER 5
NONLINEAR OPTICAL STUDIES

5 Nonlinear optical (NLO) studies

This chapter describes nonlinear optical properties of phthalocyanine complexes, and when they are linked to nanomaterials or blended with polymers. An open-aperture (OA) Z-scan technique [207,296] which measures total transmittance through the sample as a function of incident laser was used to characterize the optical limiting potentials of the samples using a mode-locked Nd:YAG laser at 532 nm and 10 ns (FWHM) excitation conditions.

5.1 General mechanism and description of NLO parameters

The mechanism through which the NLO processes occur in organic macrocycles like MPcs include either simultaneous absorption of photons ($S_0 \rightarrow S_n$) via virtual states in the singlet excited states, or sequential absorption of photons ($T_1 \rightarrow T_n$) in the triplet excited states after ISC, **Figure 5.1** [83,297]. Both mechanisms are termed excitation state absorptions (ESA). The former ESA transitions ($S_0 \rightarrow S_n$) are negligible, and not considered in this work due to fast relaxation of the molecules from S_n to S_1, followed by quick transitions to either triplet states of T_1 via ISC or ground states (S_0) via fluorescence. ESA of $T_1 - T_n$ could give rise to reverse saturable absorption (RSA) when already excited molecules in triplet states sequentially absorb another photon, hence ESA-assisted RSA are only considered and discussed in this work.

Combination of phthalocyanines and nanomaterials or QDs would generate two-photon absorbing composites with different nonlinear absorption processes. Therefore, likely contributions due to free-carrier absorption (FCA), and/or nonlinear scattering (NLS) mechanisms are expected in addition to the RSA mechanisms. FCA could occur as a result of interference due to absorption from the composites at the excitation wavelength (532 nm) of the laser, while NLS occur as a result of formation of plasma or bubbles in the sample solution during irradiation [298]. NLS is a secondary nonlinear absorption, and as such not considered in this work.

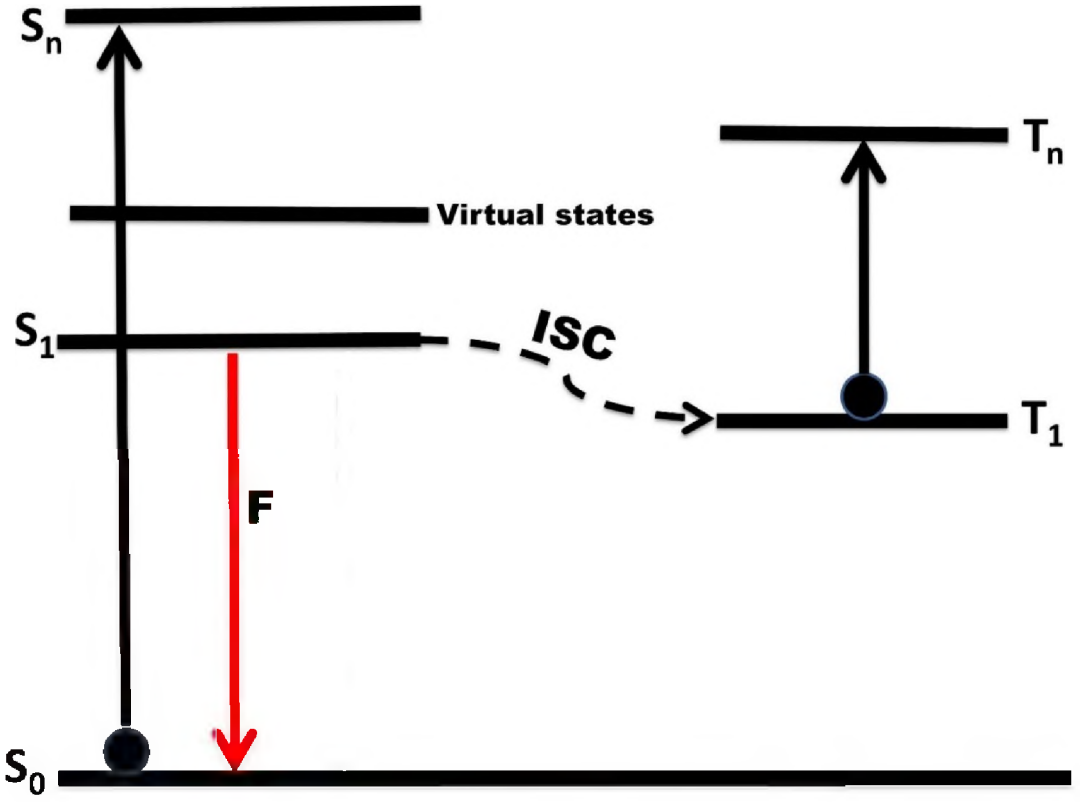

Figure 5.1: Simultaneous and sequential photon absorptions of excited state absorption (ESA) mechanisms, S_0 = singlet ground state, S_1 = singlet excited state, S_n = higher excited singlet state, F = fluorescence, ISC = intersystem crossing, T_1 = first triplet excited state and T_n = higher excited triplet state.

Nonlinear absorption (NLA) coefficient (β_{eff}); third-order susceptibility ($I_m[\chi^{(3)}]$); second-order hyperpolarizability (γ); limiting threshold intensity (I_{lim}) and excited to ground state absorption cross-sections ratio (k) are important nonlinear optical parameters. These parameters are used to characterize nonlinear absorptions in this work.

β_{eff} describe nonlinear optical effects induced as a result of laser light-matter interactions. The magnitude of the interactions was estimated in terms of cm/GW (from **Eq. 1.8**) and used throughout in this work. Values of β_{eff} can either be positive for molecules containing reverse saturable absorbers like Pcs, or negative for saturable absorbing materials like nanoparticles [205].

The imaginary third-order susceptibility, ($I_m[\chi^{(3)}]$), is a measure of fast response time of molecular material to the perturbation induced by the intense laser pulses. The second-order hyperpolarizability, γ, measures the interaction of the incident photon with the permanent dipole moments of the molecular materials. Both third-order susceptibility

($I_m[\chi^{(3)}]$) and hyperpolarizability (γ) (measured in esu), are evaluated in terms of nonlinear absorption (NLA) coefficients (β_{eff}), using **Eqs. 1.12** and **1.13** described in Chapter 1.

Limiting threshold intensity, (I_{lim}), is a measure of deviation of energy output by OL devices from incident laser light. Therefore, the larger the deviation from incident laser light (that is, the lower the I_{lim}), the better the material as optical limiters. I_{lim} for OL materials is measured when the input intensity is at 0.5 linear transmittance [299]. Generally, molecular material performs better as nonlinear optical device at I_{lim} value below 1.0.

5.2 Nonlinear optical studies of Pc complexes in the absence of NPs

Pc complexes with similar substituents or central metals at the same concentrations and absorbance are compared in solution, or when they are embedded on polymer supports. Nonlinear absorption behaviour of complexes **5**, **6** and **7** are studied in chloroform, complexes **8** and **9** were investigated and compared in DMSO and THF. Other MPc complexes and MPc-nanomaterial or polymer composites are studied only in DMSO. The choice of solvent was determined by solubility of the Pcs and/or composites.

5.2.1 Alkynyl indium phthalocyanine complexes (1 and 2)

Figure 5.2A shows a representative open aperture Z-scan for complex **2** recorded at 532 nm and 10 ns pulses using peak input intensity of ca. 60.0 MW/cm^2. For irradiance intensities at ca. 130.0 MW/cm^2 (**Figure 5.2B**), the normalized transmittance of complexes dropped below 0.5 making them good optical limiting materials [132,167,300]. The reduction in the linear transmission about the focus (z=0) is an indication of positive nonlinear absorption expected for molecules exhibiting reverse saturable absorption (RSA) profiles [90,167,206,296,300]. The observed RSA profiles for both samples are due to sequential photon absorptions at the triplet excited states.

Using two-photon absorption (2PA), estimated nonlinear absorption coefficients (β_{eff}) for **1** and **2** are respectively ≈ 427 cm/GW and 438 cm GW^{-1}, **Table 5.1**. In addition to 2PA, contributions from higher mechanisms such as three-photon absorptions (3PA) cannot be ruled out due to the ns pulses and the high peak intensities used [93,95,300-302].

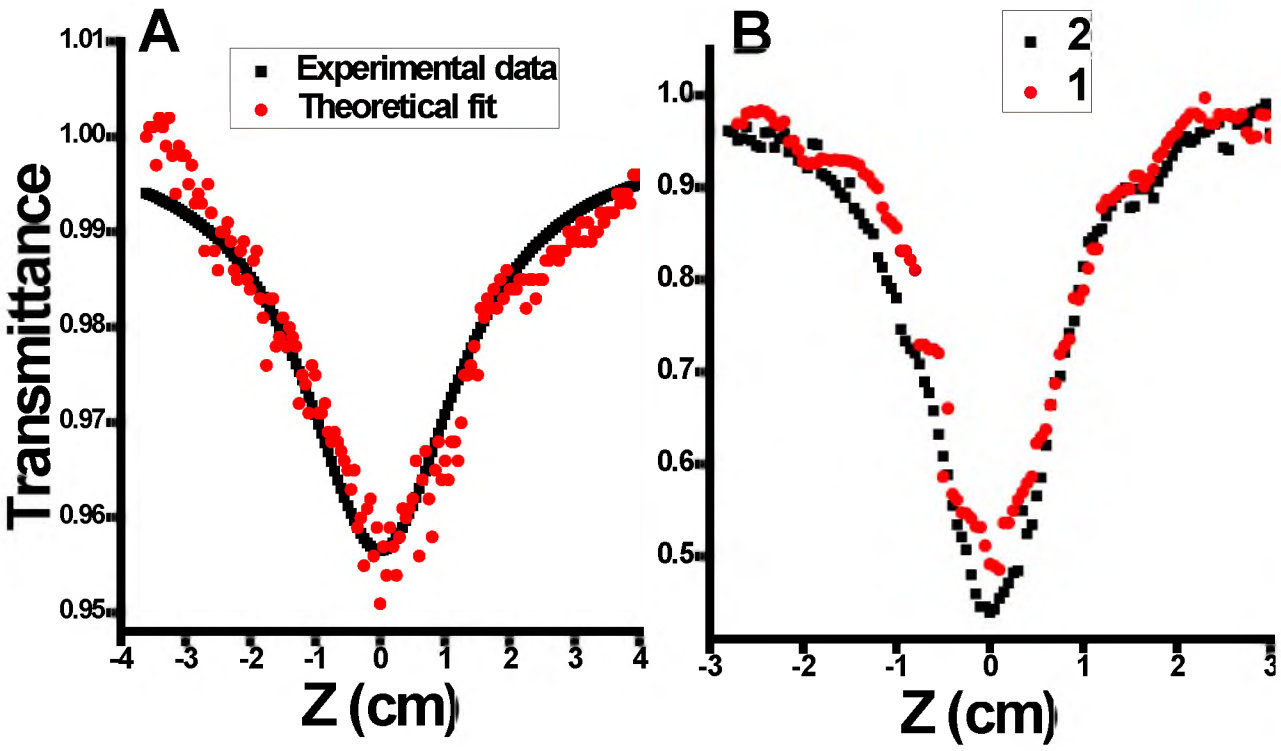

Figure 5.2: (A) Open aperture Z-scan for 2 in DMSO showing the fitting. The black solid curve is the theoretical fit, $I_{OO} \approx$ 60.0 MW/cm² (B) Representative open-aperture Z-scans of 1 and 2, $I_{OO} \approx$130.0 MW/cm².

Analytical absorption model **Eqs. 5.1** and **5.2** [209] was used to determine σ_T and verify the existence of 2PA mechanism for the two complexes.

$$\frac{T}{T_{linear}} = \frac{\ln[1+q]}{q} \quad (5.1)$$

where $q = \frac{\alpha\sigma_T}{2h\nu} I_o L_{eff}$ (5.2)

where σ_T is the excited state of absorption cross-section, I_O, L_{eff} and α are the input fluence, effective path length in the sample of length L and the linear absorption coefficient of the samples.

The excited state of absorption cross-section (σ_T) being larger than the ground state absorption cross-section (σ_O) is a condition which is primarily responsible for RSA occurring in the Pcs [297,303,304]. The incident pulses have duration of 10 ns compared to the shorter ISC lifetimes (τ_{ISC}) (<1 ns, **Table 5.1**) of the Pcs, resulting in the population of the triplet states T_1 via intersystem system crossing hence increase in σ_T. Also, both

complexes have high Φ_T (**Table 5.1**) that could ensure faster ISC to the triplet states, increased σ_T as well as [$T_1 \rightarrow T_n$] transitions.

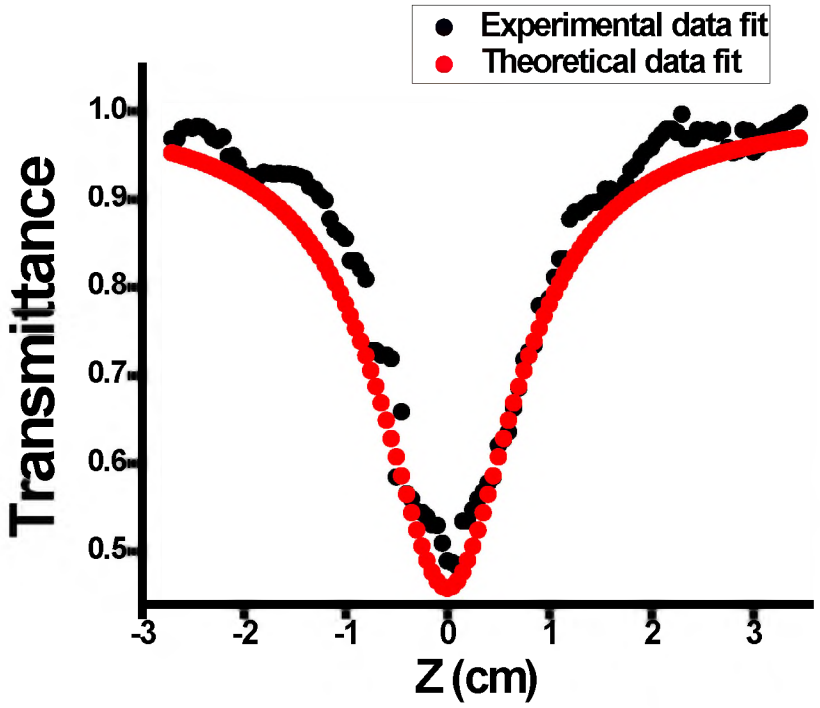

Figure 5.3: Representative open aperture Z-scan fits between experimental data and theoretical analytical of absorption model for 2 in DMSO using Eqs. 5.1 and 5.2.

Theoretical (**Figure 5.3**) OA Z-scan datasets were fitted to the experimental transmittance datasets (using **Eqs. 5.1** and **5.2**) while treating σ_T as a free parameter to obtain value of $R^2 \approx 0.9$. The values of σ_T for **1** and **2** were 8.8 $\times 10^{-17}$ cm^2 and 6.8 $\times 10^{-17}$ cm^2, respectively. Each of these values exceed ground state of absorption cross-section (σ_O =1.7 $\times 10^{-17}$ cm^2 for **1** and 1.97 $\times 10^{-17}$ cm^2 for **2**) by factors of 5 and 3, represented as k. These values are a very good indicator that RSA could be occurring for the Pcs. Saturation fluence (F_{sat}) curves of **1** and **2** are compared by plotting transmittance (T(z)) against the input fluence (I_o) (**Figure 5.4A**). The plots showed rapid decrease in transmittance as the input fluence increases. Similar observations ascribed to 2PA for organic compounds have been previously reported [209,305]. At I_o values higher than 0.18 J/cm^2, more rapid decrease of transmittance for **2** with respect to **1** was observed which can be attributed to the difference in carbon chain-lengths of the alkynyl substituents on the peripheral

positions of the Pcs. Thus, complex **2** showed better NLO property than **1** and this was in agreement with Φ_T value shown in **Table 4.2**.

Table 5.1: Nonlinear optical properties of 1, 2, 3, 4, 8, 9, 10 and 11 in DMSO at 532 nm wavelength and 10 ns pulses.

Complex	I_{oo} MW/cm²	β_{eff} (cm/GW)	$I_m[\chi^{(3)}]$/ esu	γ (esu)	k (σ_T/σ_O)	I_{lim} (J/cm²)	τ_{ISC} (ns)	Φ_T
1	130	427	2.10×10^{-9}	2.7×10^{-29}	5.17	0.55	0.45	0.82
2	130	438	2.15×10^{-9}	3.19×10^{-29}	3.46	0.48	0.43	0.84
3	247	89	2.09×10^{-11}	1.09×10^{-30}	5.9	0.42	7.67	0.64
4	247	149	3.53×10^{-9}	9.13×10^{-29}	4.9	0.27	3.73	0.77
8	99.7	360	8.47×10^{-10}	3.71×10^{-28}	38.6	0.58	4.3	0.60
9	99.7	427	1.00×10^{-9}	4.38×10^{-28}	38.6	0.64	2.6	0.65
10	44.1	165	3.86×10^{-11}	1.69×10^{-29}	47.6	0.89	3.74	0.73
11	55.4	209	4.91×10^{-11}	2.15×10^{-29}	621	0.28	2.9	0.83

Limiting intensity curves of the two alkynyl phthalocyanines are presented in **Figure 5.4B**. Low value of I_{lim} is an indication of good NLO response to the input intensity. From **Table 5.1**, complex **2** has lower I_{lim} value hence exhibits larger optical limiting response than **1**. However, I_{lim} values for both complexes were found to be among the lowest reported for phthalocyanines derivatives in recent literatures which ranged from 0.2 to 0.8 J cm^{-2} [112,116,300,306,307].

Estimated $I_m[\chi^{(3)}]$ and γ, (**Table 5.1**) values for both complexes are high and consistent for organic molecules as nonlinear optical materials [112,121,300,306,307].
Both $I_m[\chi^{(3)}]$ and γ are slightly larger for **2** compared to **1** hence the former is a better optical limiter. The obtained values of $I_m[\chi^{(3)}]$, γ, k and β_{eff} reported in this work compared favourably with different phthalocyanines (In-phthalocyanines inclusive) that have been reported before [108]. This suggests that both **1** and **2** have good prospects as optical limiters.

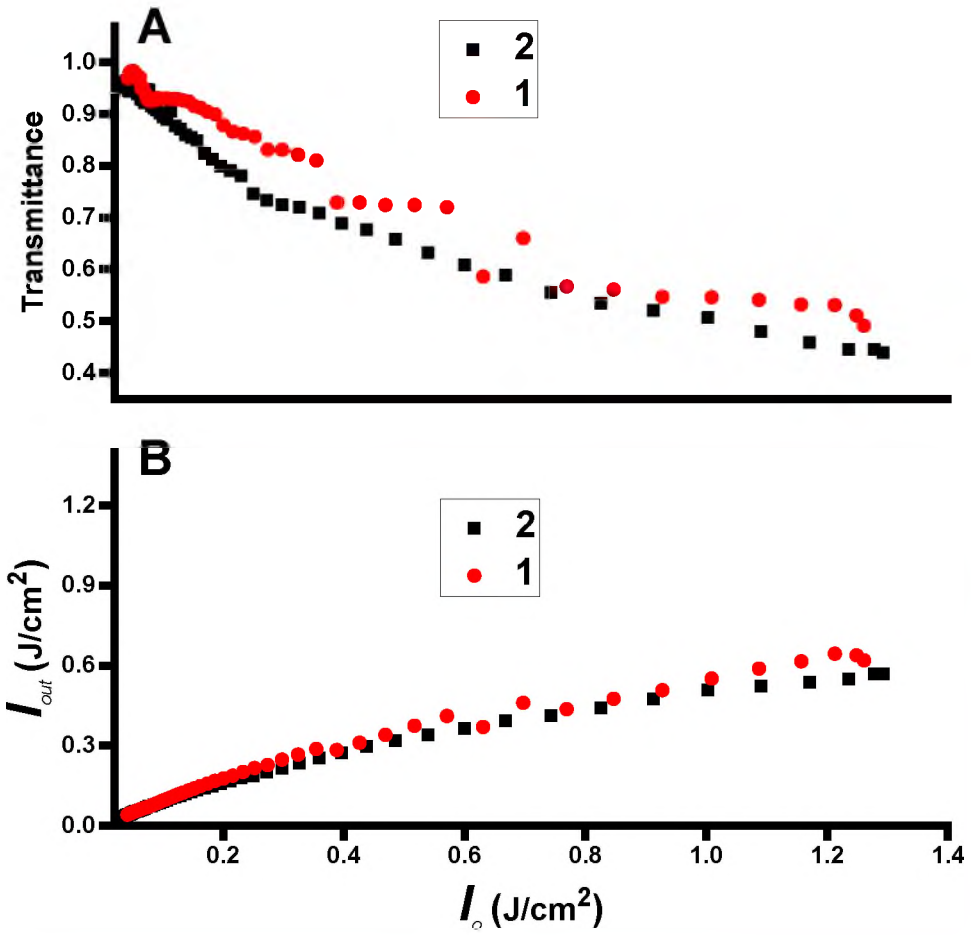

Figure 5.4: (A) Transmittance vs input fluence (I_o) curves for 1 (red) and 2 (black) in DMSO. (B) Output fluence (I_{out}) vs input fluence (I_O) for 1 ad 2. I_{OO} ≈130 MW/cm² for each sample.

5.2.2 ZnPc complexes 3 (alkynyl ZnPc) and 4 (triazole functionalized ZnPc)

5.2.2.1 Z-scan measurements

Figure 5.5 shows overlay open aperture Z-scans of complexes **3** and **4** measured in DMSO. Absorbance of the samples were maintained at 2 and irradiated at input intensity of ≈ 247.0 MW/cm²; the normalized transmittance for both compounds exhibited deep valley below 0.5 similar to the shapes of the Z-scan profiles observed for **1** and **2**, **Figure 5.5**. The nonlinear absorption coefficients (β_{eff}) for **3** and **4** are respectively ≈89 cm/GW and 149 cm/GW, **Table 5.1**. Larger β_{eff} value of **4** is an indication of stronger optical limiting (OL) potential due to the presence of α-substituted electron withdrawing NO_2

groups, and relatively larger Φ_T value, **Table 5.1**. As stated above, electron withdrawing groups have been previously reported to display effective OL properties in phthalocyanines molecules [159].

RSA as a dominant mechanism 532 nm and ns pulses was also tested by plotting β_{eff} against absorbance of each sample. **Figure 5.6** shows an increase in β_{eff} as the absorbance of the samples increases, for both compounds. This suggests direct relationship between β_{eff} and available number of molecules induced by RSA at the excited triplet states [95]. Compared to **1** and **2** (In based alkynyl Pcs), **3** and **4** have lower β_{eff} value at high I_{oo}, showing the importance of In compared to Zn as central metal for Pcs, **Table 5.1**.

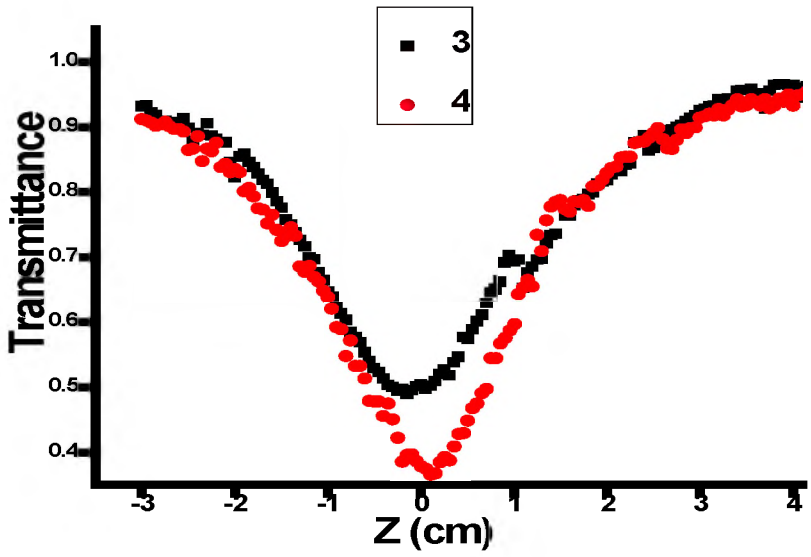

Figure 5.5: Representative open-aperture Z-scans of 3 and 4. $I_{oo} \approx 247$ MW/cm^2

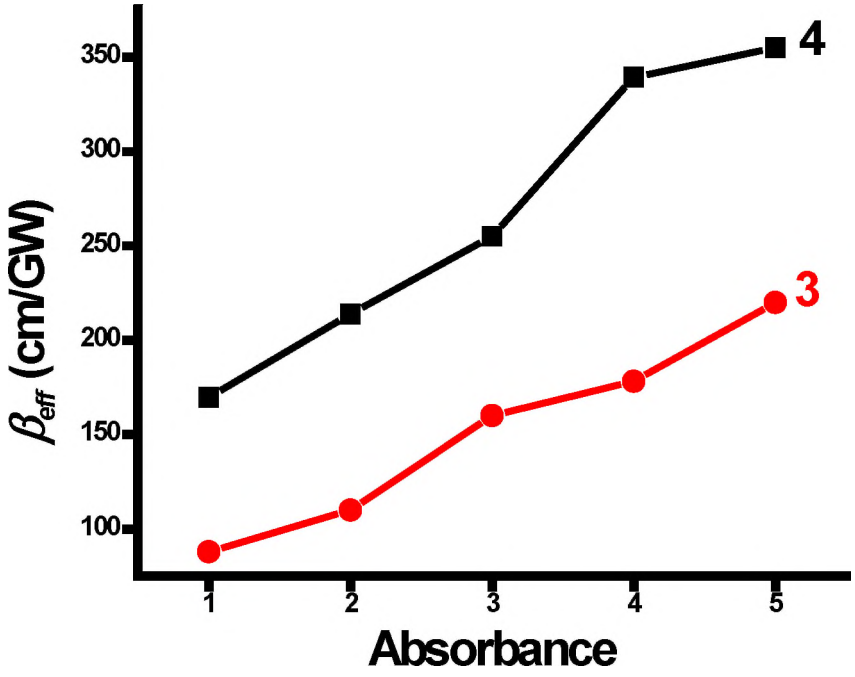

Figure 5.6: Plots showing the concentrations (absorbance) dependence β_{eff} for 4 and 3. $I_{00} \approx$ 67.4 MW/cm² for each independent measurement.

5.2.2.2 2PA vs 3PA mechanism

Possible contributions from higher mechanisms such as 3PA were verified by fitting experimental datasets to both 2PA and 3PA functions using **Eqs. 5.3A** and **B**, respectively. The open circles in the figure represent experimental data, the red and blue lines represent 2PA and 3PA fits, respectively, **Figure 5.7 A** and **B**.

$$T_Z = \frac{1}{1+\beta_2 L_{eff}(I_{00}/(1+(z/z_0)^2))} \qquad (5.3A)$$

$$T_Z = \frac{1}{1+2\beta_3 L_{3eff}(I_{00}/(1+(z/z_0)^2))} \qquad (5.3B)$$

where β_2 and β_3 are two-photons (2PA) and three-photons (3PA) absorption functions, respectively.

Judging from all the fits to the experimental data, it is evident that 2PA fitted well to the experimental data while 3PA fits were markedly different from the experimental data. This shows that 2PA and not 3PA, is the dominant mechanism for the observed RSA

behavior for both compounds at the ns pulses. Also, intensity dependence of β_2 under different experimental conditions were performed. The obtained 2PA coefficients for both compounds were plotted against the on-axis input intensities (I_{oo}) (**Figure 5.8A**). β_{eff} remained relatively constant with increasing intensities for both samples. It is believed that for the dominant mechanism, the values of β_n should remain constant with increasing I_{oo} [95,168]. It is evident that the dominant mechanism for the observed RSA is certainly 2PA. A plot of β_3 versus I_{oo} showed exponential decrease of β_3 as I_{oo} increases, **Figure 5.8B**. The decrease in β_3 as I_{oo} increases is attributed to the downward depletion of sequential photon absorbing species; opposite trend has been reported for molecules with 3PA induced RSA at fs pulses [300].

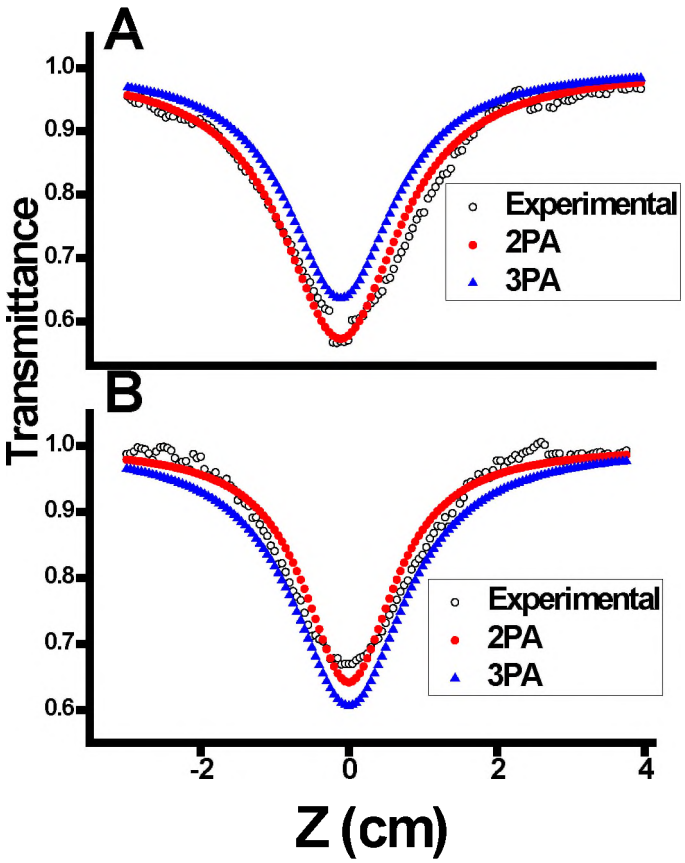

Figure 5.7: OA Z-scan curves for (A) 3 and (B) 4. $I_{oo} \approx$ 150 MW/cm^2 for both compounds. Open circles represent experimental data, red and blue lines represent 2PA and 3PA fits, respectively.

The plots of I_o against I_{out} for **4** and **3** clearly show deviation from linearity, an indication of good NLO responses to the input intensity, **Figure 5.9**. From **Table 5.1**, complex **4** has lower I_{lim} value hence exhibits larger optical limiting response than **3**. However, values of I_{lim} obtained for both compounds were found to be among the lowest reported for phthalocyanines derivatives in recent literature which ranged from 0.2 to 0.8 J/cm^2 [112,206,299]. Excited to ground state absorption cross-sections ratio (*k*) of both **3** and **4** are greater than unity, suggesting a direct consequence of ESA-assisted RSA mechanisms.

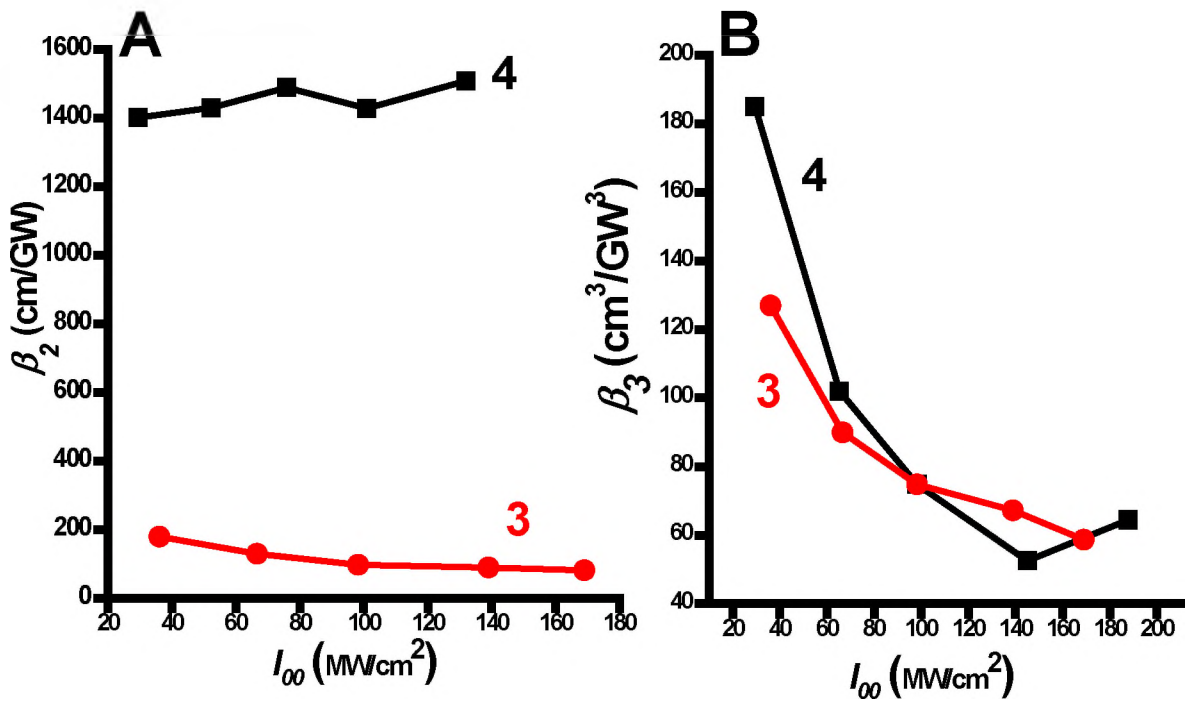

Figure 5.8: Plots showing the peak intensity (I_{00}) versus (A) β_2 and (B) β_3 for 4 and 3 obtained at 532 nm and 10 ns pulses.

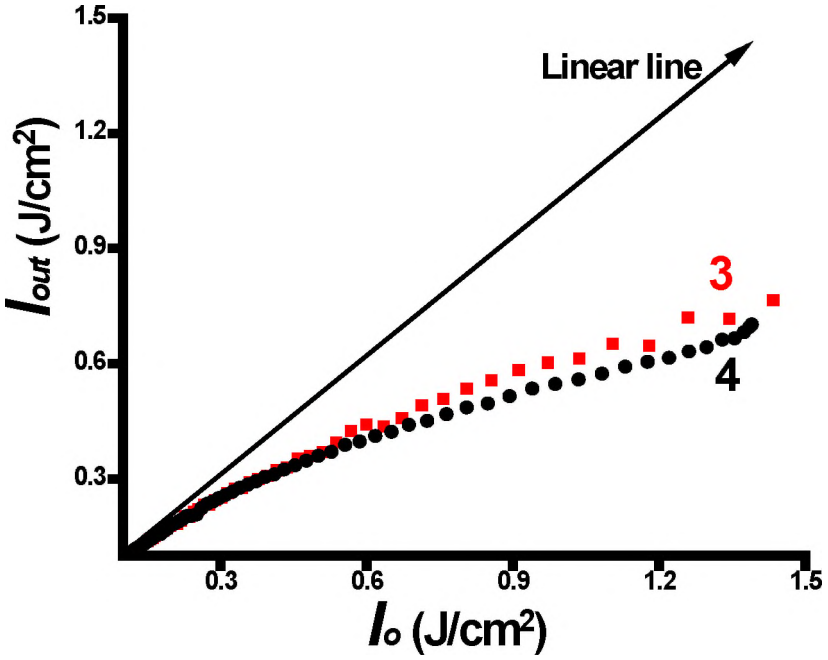

Figure 5.9: Output fluence (I_{out}) versus input fluence (I_O) for 3 and 4. The black line represent a case of linear transmission. $I_{OO} \approx$ 150 MW/cm² for each sample.

Estimated values for $I_m[\chi^{(3)}]$ and γ for **4** are higher than the values reported for the **3**. The superior nonlinear optical properties of **4** compared to **3**, could be attributed to the following factors; presence of high dipole moments induced by the electron withdrawing groups at the peripheral positions [159]; low ISC time and high triplet quantum yield [308] **Table 5.1**; and the expanded electron π electronsystem due to triazole-fused phenyl rings of **4**. The $I_m[\chi^{(3)}]$ values estimated for both **4** and **3** are larger by two to four orders of magnitude than the range reported for series of naphthalocyanines and phthalocyanine derivatives at 532–604 nm in DMF by Unnikrishnan et al. [309-312]. This implies that, complexes **3** and **4** possess ultra-fast response time to attenuate intense laser radiation compared to the aforementioned compounds. The γ values reported for **3** and **4** are also greater than those reported for ZnPcs (ranging from 7.60 to 8.32 $\times 10^{-31}$ esu) and CuPcs (ranging from 8.53 to 11.2 $\times 10^{-31}$ esu) dyads in DMF [313], LuTBPc (2.79 2 $\times 10^{-33}$ esu) [314], and other Pcs including InPcs [108]. The values of $I_m[\chi^{(3)}]$ and γ reported for **1** and **2** are within the same range as that of complex **4**, but larger by one to two orders of magnitude than the range reported **3**, **Table 5.1**.

5.2.3 Mercaptopyridine-substituted metal-free, Zn and In phthalocyanine complexes 5, 6 and 7 in solution and in thin films

5.2.3.1 Z-scan measurements in solution

Figure 5.10A–C show overlay of Z-scan spectra of **5**, **6**, and **7** in solution. Z-scan measurements carried out on the compounds at various input intensities showed reduction in the transmission about the focus of the lens. At $I_{oo} \geq 108$ GWcm^{-2}, a positive nonlinear absorption (NLA) signature is induced in the sample [132,167,300], attributed to the RSA behavior [90,167,206,296,300]. The absorbance of each sample was maintained at Abs ≈ 1.42 in $CHCl_3$, **Figure 5.10**. The Z-scan profile of **7** remained highly unstable (dip intensity changing) in the presence of different input intensities compared to **5** and **6**.

Using 2PA function, the best fit gave β_{eff} of 300 cm/GW for **7** at I_{oo} of 236 MW/cm^2 (**Figure 5.10, black line**), 372 cm/GW for **5** at I_{oo} of 273 MW/cm^2 (**Figure 5.10, black line**), and 432 cm/GW for **6** at I_{oo} of 214 MW/cm^2 (**Figure 5.10, black line**), **Table 5.2**. The estimated β_{eff} in solution for **7** is smallest followed by **5**, while the largest value was reported for **6**. This suggests better NLO behavior for **6** compared to **7** and **5**. The values were as expected, since inclusion of heavy metals in Pc leads to improved NLO and OL properties [315,316]. The presence of indium increased the triplet-state populations of **6** due to its heavier atom effect compared to zinc of complex **5** as discussed in Chapter 5 [317]. This explains the improved NLO properties of **6** compared to **5** and **7** (metal free), hence its larger β_{eff} value.

General trends for nonlinearity of the complexes in solution were also investigated at constant input intensity and varying concentrations. The measured β_{eff} values were plotted against the absorbance at $I_{oo} \approx 0.21$ GW/cm^2 (**Figure 5.11**). It can be clearly seen that β_{eff} increases in magnitude as the absorbance for each sample increases; complex **6** exhibits the largest effective NLA coefficient (β_{eff}) at 372 cm/GW. The increase in magnitude of the β_{eff} as the concentration increases suggests direct relationship between the β_{eff} and the available number of molecules induced by RSA at the excited triplet states [306].

Complexes **5**, **6** and **7** show larger β_{eff} values than **3** and **4** at input intensities ranging from 214 - 273 MW/cm^2, but smaller than both **1** and **2** measured at lower input intensity of 130 MW/cm^2, **Table 5.1**. Thus, the presence of alkynyl substituents and In central metal

enhanced the β_{eff} values. The effects of solvents $CHCl_3$ (for (**5**, **6** and **7**) and DMSO (for **1**, **2**, **3** and **4**) cannot be ruled out.

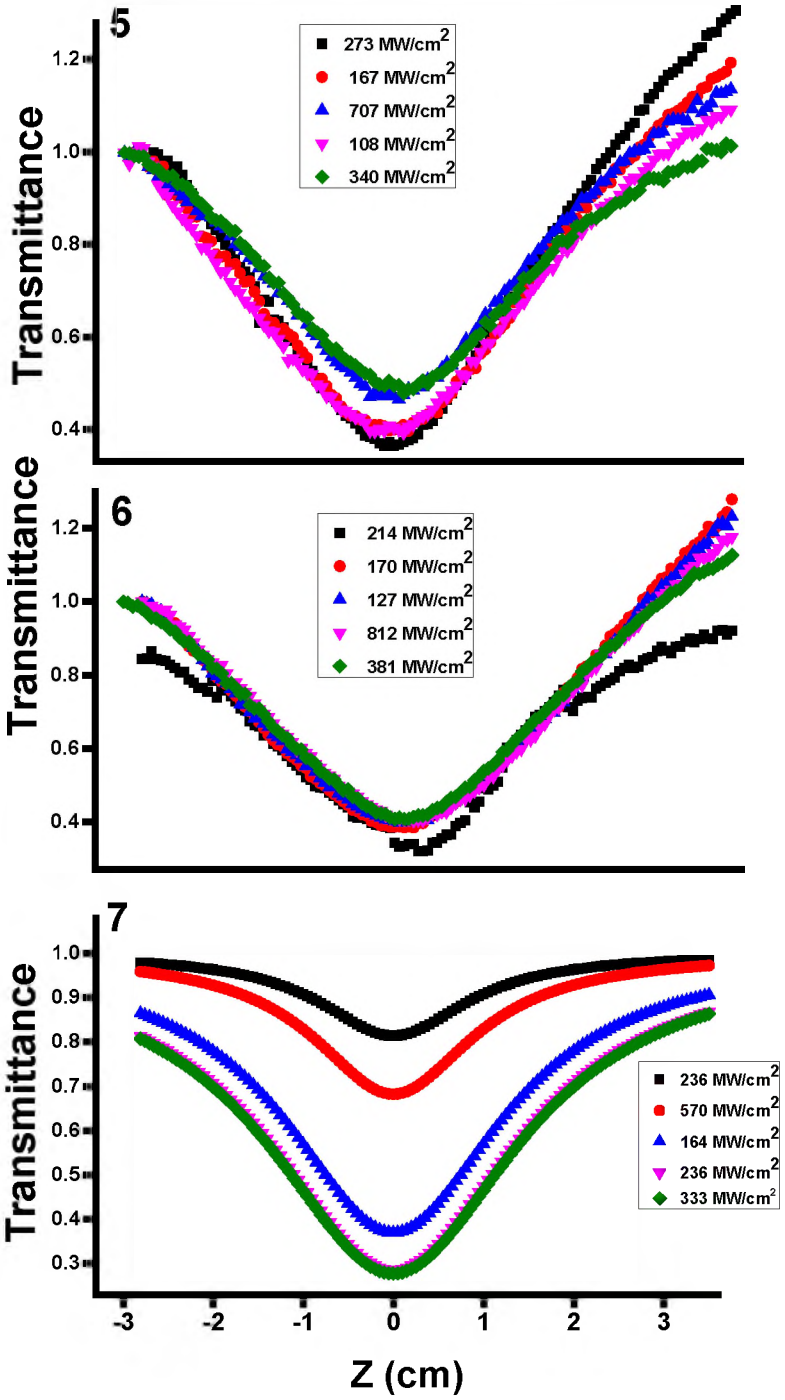

Figure 5.10: Plots showing OA Z-scan curves for evaluating β_{eff} for 5, 6, and 7. At ≈ 1.42 abs in $CHCl_3$.

The γ values in solution reported for **5**, **6** and **7** are greater than those reported for ZnPc, CuPc ~10^{-31} esu in DMF [313], and LuTBPc 10^{-33} esu [314]. The estimated γ values for **5**, **6**, and **7** in $CHCl_3$ are comparable to the copper complexes ($3.52 \times 10^{-29} - 7.6 \times 10^{-30}$ esu) measured in DMF [318], and are much higher than tert-butyl-substituted ZnPc at ~4.3×10^{-31} esu, implying that the molecules are good candidates as optical limiters. The estimated γ and $I_m\left[\chi^{(3)}\right]$ values for ZnPc (**5**) and metal free (**7**) Pcs in $CHCl_3$ are slightly larger than those reported for complex **3** in DMSO, but lower than the values reported for **1**, **2** and **4** in DMSO. Surprisingly, estimated values of γ and $I_m\left[\chi^{(3)}\right]$ for InPc (**6**) derivative in $CHCl_3$ are of lower order of magnitude compared to **1**, **2** and **4** measured in DMSO. The discrepancies could be due to differences in the polarity and refractive indexes of the solvent used for the NLO studies.

The $I_m\left[\chi^{(3)}\right]$ values estimated for **5**, **6**, and **7** in solution are larger by two to four orders of magnitude than the values reported for naphthalocyanine and phthalocyanine derivatives at 532–604 nm in DMF [309-314]. The measured $I_m\left[\chi^{(3)}\right]$ value for **6** in solution is larger by one to two orders of magnitude than the values reported for InPc (3.49×10^{-12} and 1.89×10^{-11} esu) [115], cadmium(II) polymeric cluster in DMF (8.03×10^{-12} esu) [319] and tert-butyl-substituted ZnPc at $\approx 4.3 \times 10^{-14}$ esu. The values of $I_m\left[\chi^{(3)}\right]$ reported for series of phthalocyanines in toluene and chloroform [108] are within the same range as **5** and **7** but lower than the value of reported for complex **6**.

5.2.3.2 Z-scan measurements in thin films.

The Z-scan profiles, **Figure 5.12A–C**, for the complexes in thin films were also fitted to 2PA processes, revealing RSA. At input intensity of ≈33 MW/cm^2, β_{eff} values of ≈2455 cm/GW, ≈4555 cm/GW, and ≈6213 cm/GW (**Table 5.2**) were obtained for **7-PBC**, **5-PBC**, and **6-PBC**, respectively. PBC alone showed no NLO behaviour. Complex **7** revealed fuzzy signals in both solution and on solid support, a characteristic of weaker nonlinear responses. The distinct and sharp signals observed for **5** and **6** in both solution and solid state is an indication of stronger nonlinear responses. However, indium phthalocyanine **6** outperforms other molecules in terms of the magnitude of the reduction in the normalized transmittance relative to input intensity. The substantial increase in the magnitude of β_{eff} values in thin films compared to solutions for each sample revealed the importance of Pc-polymer composites for NLO applications. The

choice of PBC as opposed to PSU used for **8** and **9**, and PAA used for **10** was based on relative solubilities of the Pcs and the polymers.

Table 5.2: NLO properties of samples 5, 6 and 7 in $CHCl_3$ and thin films.

Complex	I_{OO} (MW/cm²)	β_{eff}(cm/GW)	$I_m[\chi^{(3)}]$/esu	γ (esu)	I_{lim}(J/cm²)
5	273	372	8.73×10^{-11}	2.47×10^{-30}	0.57
6	214	432	1.97×10^{-10}	5.58×10^{-30}	0.46
7	236	300	7.04×10^{-11}	1.99×10^{-30}	0.88
5-PBC	33	4555	7.74×10^{-10}	8.37×10^{-29}	0.20
6-PBC	33	6213	1.46×10^{-9}	2.13×10^{-28}	0.11
7-PBC	33	2455	1.07×10^{-10}	3.02×10^{-29}	0.54

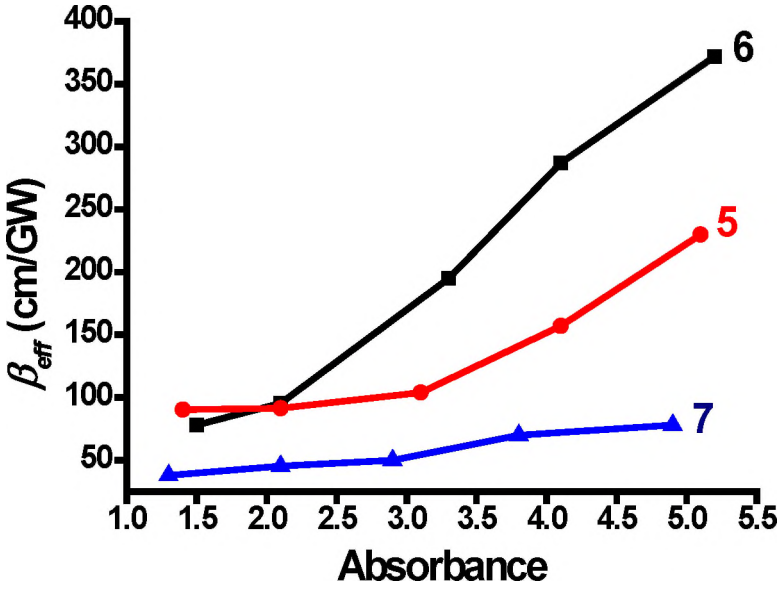

Figure 5.11: Plots showing the concentration dependence on β_{eff} for 5, 6, and 7. $I_{OO} \approx 0.21$ GW cm^{-2} for each independent measurement in $CHCl_3$.

The calculated $I_m[\chi^{(3)}]$and γ values for the samples, both in solution and in thin films, are presented in **Table 5.2**. Generally, the $I_m[\chi^{(3)}]$ and γ values in solution are lower than when embedded in thin films, **Table 5.2**. Of the thin films, the $I_m[\chi^{(3)}]$ value of 1.46×10^{-9} esu for **6-PBC** was the highest and the lowest value was obtained for metal-free phthalocyanine film (**7-PBC**, 1.07×10^{-10} esu). Since the substituents on the Pcs are all the same for the studied samples, it is safe to assume that the major factor responsible for the magnitude of $I_m[\chi^{(3)}]$ in MPc is the influence of central metals. Similarly, the same trend was also observed for γ values in solution and in their thin films.

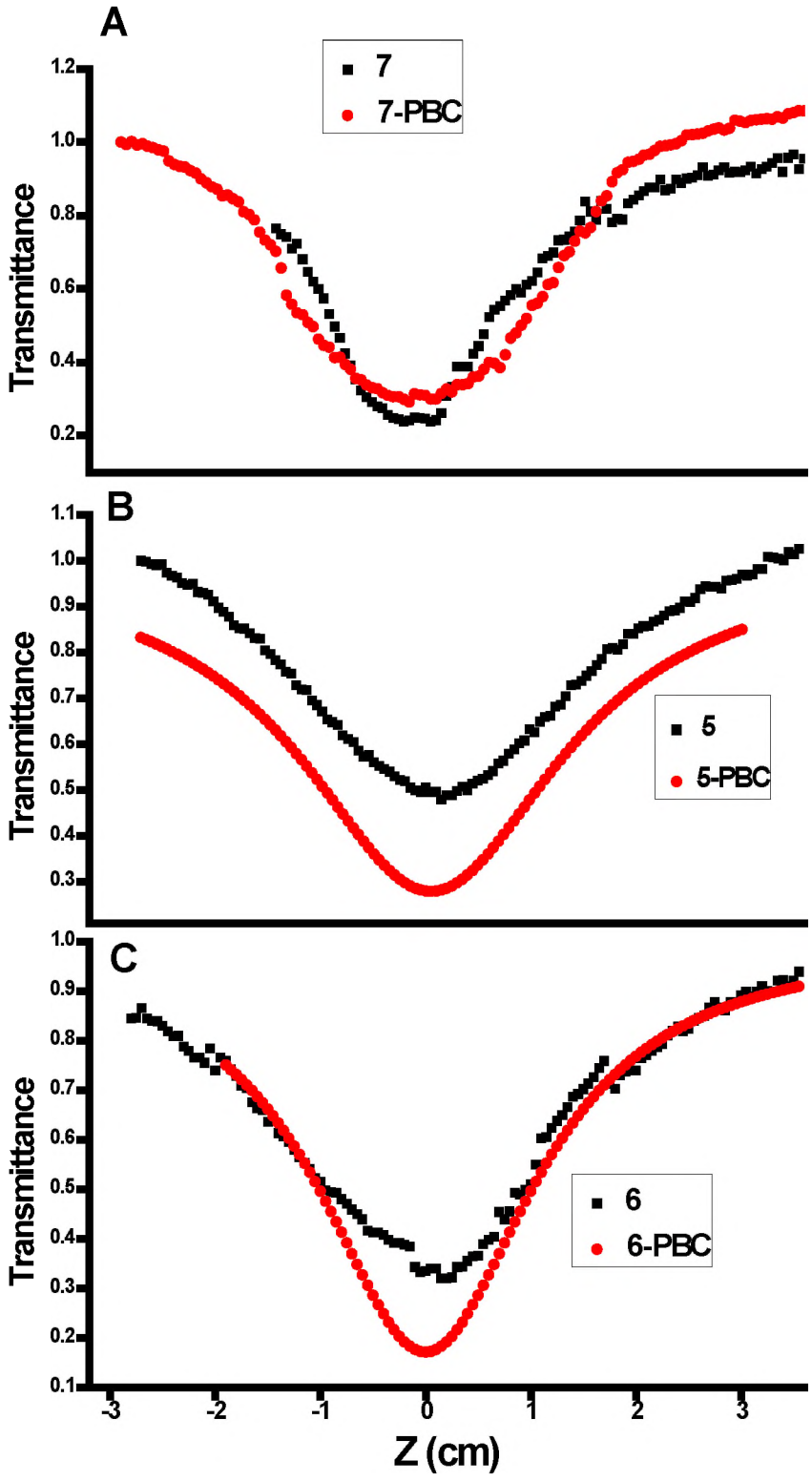

Figure 5.12: OA Z-scan curves for (A) 7 and 7-PBC, (B) 5 and 5-PBC, and (C) 6 and 6-PBC. $I_{OO} \approx 33$ MW cm^{-2}, Concentration = 1.0 × 10^{-4} M in $CHCl_3$.

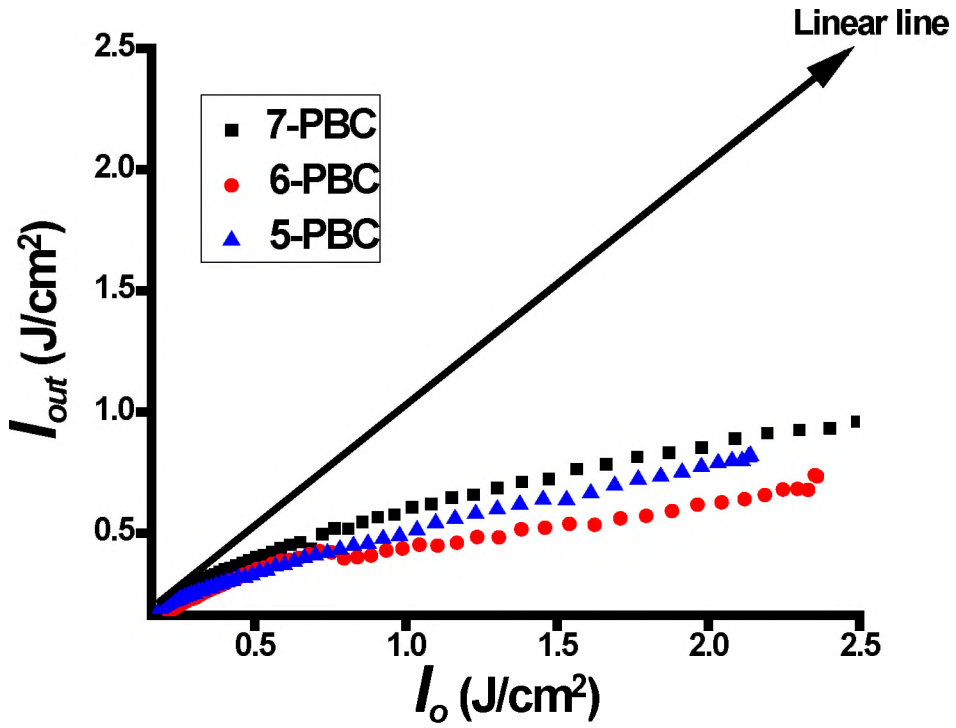

Figure 5.13: Output fluence (I_{out}) vs input fluence (I_o) for 7-PBC, 5-PBC, and 6-PBC. The black line represents a case of linear transmission. Peak intensity (I_{oo}) ≈ 33 MW cm^{-2} for each sample.

The $I_m[\chi^{(3)}]$ values of ~10^{-10} esu in thin films (Pc-PBC) were of the same order of magnitude for the trinuclear lanthanide phthalocyanines embedded in poly(bisphenol A carbonate) at 532 nm in DMF, as reported by Sekhosana et al. [124]. Rao et al. [120] reported $I_m[\chi^{(3)}]$ values of ≈10^{-10} esu for five different Pcs doped in PMMA polymers; these are lower by one order of magnitude compared to **6-PBC**. Reports [125] have shown that PMMA has poor mechanical strength and lower refractive index compared to PBC; hence, superior nonlinear transmittance is observed for Pc-PBC composites reported in this thesis.

Figure 5.13 shows a plot of incident laser intensity (I_o) against transmitted laser intensity (I_{out}) for **5-PBC**, **6-PBC**, and **7-PBC** at I_{oo}≈ 33 MW/cm^2. From **Table 5.2**, **6-PBC** has the lowest I_{lim} value of 0.11 J/cm^2; this translates to excellent OL response compared to **7-PBC** and **5-PBC**, considering the same approximate concentration. The metal-free phthalocyanine is outperformed by other samples and showed the least OL behaviour in

solution and in thin film. However, the I_{lim} values obtained for the samples are still within the acceptable limits.

5.2.4 Complexes 8 and 9 in solution and in thin films

5.2.4.1 Z-scan measurements in solution

Figure 5.14A shows the Z-scan plots of transmittance against the z-positions for compound **8** and **9** measured at concentration of ≈1.0 × 10^{-4} M in 0.2 cm quartz cell. The laser power was maintained at 2.0× 10^{3} W which translates to ≈ 99.7 MW/cm^2. At z = 0, the minimum transmission values of 0.35 and 0.47 were respectively measured for **8** in DMSO and THF. For compound **9**, transmission values of 0.42 and 0.43 were measured in DMSO and THF, respectively. Both samples revealed positive NLA with reverse saturable absorption (RSA) profiles [90,167,206,296,300].

Estimated nonlinear absorption coefficients (β_{eff}) of 360 cm/GW and 294 cm/GW were respectively measured for **8** in DMSO and THF, respectively, **Figure 5.14B**. β_{eff} values of 427 cm/GW and 386 cm/GW were respectively measured in DMSO and THF for complex **9**, **Table 5.3**. β_{eff} is larger for **8** in DMSO compared to THF. Complex **8** is aggregated in DMSO at the concentrations used for NLO. The spectra for the solution of **8** used for NLO was similar to **Figure 3.4B**, in Chapter 3, hence confirming aggregation. Thus the observed larger β_{eff} value suggests that aggregation improves NLO in solution.

Figure 5.15A shows overlay of OA Z-scan profiles of **8** in DMSO at different input intensities. The concentration of each sample was maintained at ≈1.0 × 10^{-4} M in solution, while the on-axis peak input intensity was varied from 14.8 to 99.7 MW/cm^2. For input intensities ranging from 14.8 to 55.1 MW/cm^2, no significant reduction in the transmittance along focal points was observed for compound **8** in DMSO. Interestingly, the transmittances dropped below 0.5 as input intensity increased from 67.2 to 99.7 MW/cm^2, suggesting better nonlinearity of complex **8** in DMSO at high laser power. It is noteworthy to mention that even though the formation of aggregates in DMSO impacts negatively on the NLO of **8** at low laser power, the nonlinear absorption observed at higher laser power is very impressive. **Figure 5.15B** shows the Z-scans profile of sample **8** in DMSO at the same concentration (2.5 × 10^{-7} M) used for the fluorescence studies. The reduction in transmittance was observed at low input intensity and at the low concentrations employed, which was not the case for larger concentration in **Figure 5.15A**. The estimated nonlinear absorption coefficients (β_{eff}) at the measured

concentration was 53.8 cm/GW at I_{00} 99.7 MW/cm^2, (**Table 5.3**). Thus a larger β_{eff} is obtained for complex **8** in the aggregated form and at the same I_{00} of 99.7 MW/cm^2, **Table 5.3**. β_{eff} values for **8** and **9** are in the same order of magnitude (in DMSO) as for **1**, **2** and **5** – **6**. Complexes **3** and **4** show lower β_{eff} values even at relatively higher input intensity.

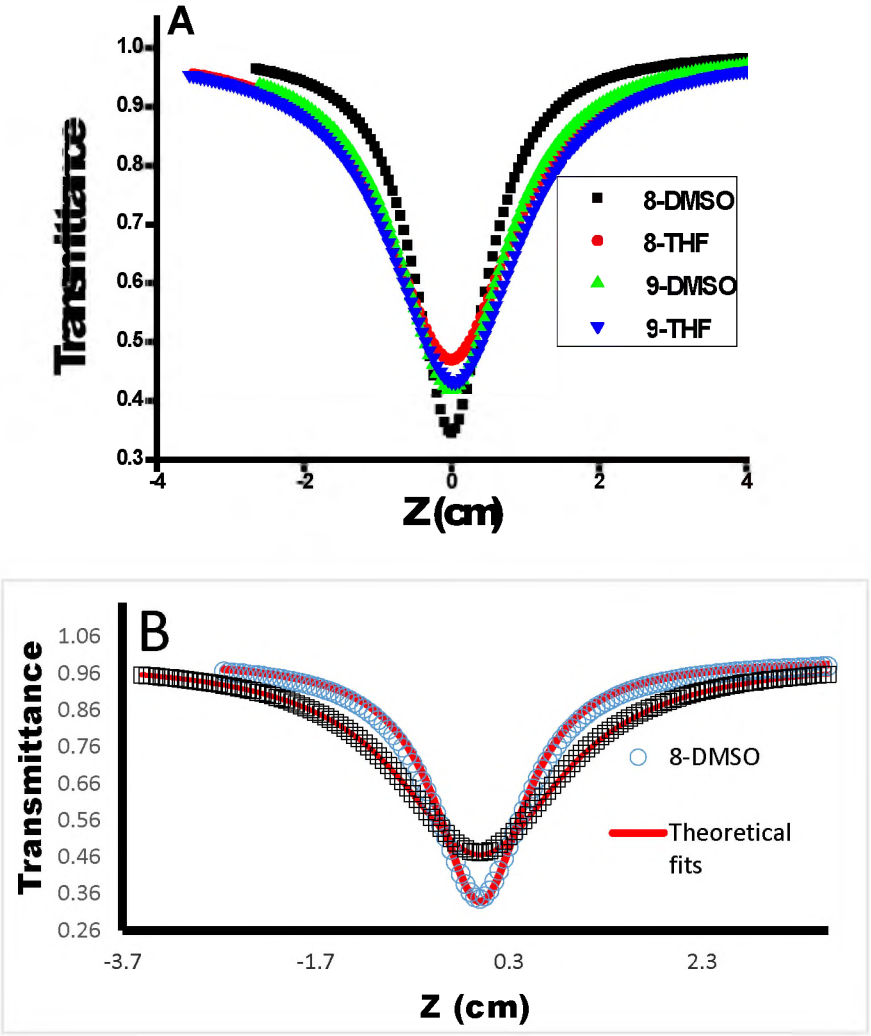

Figure 5.14: (A) Z-scans with normalized transmissions for 8 and 9 in THF and DMSO. (B) Z-scan curves for evaluating (β_{eff}) for 8 in THF and DMSO. Conc. = 1.0 × 10^{-4} M. (I_{00}) ≈ 99.7 MW/cm^2 for each independent measurement.

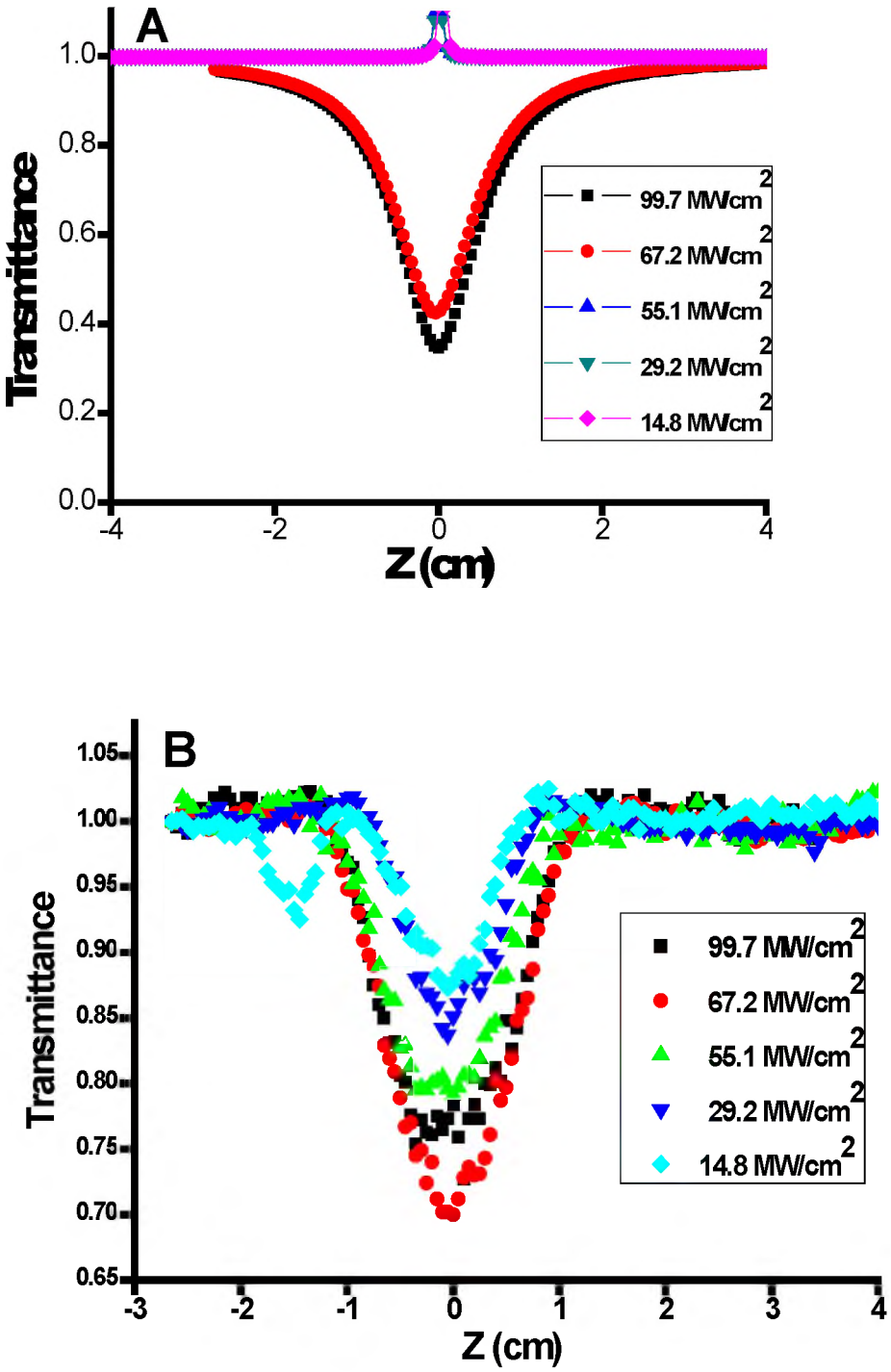

Figure 5.15: (A) Plots showing Z-scan curves for 8 in DMSO at a concentration of (A) 1.0 x 10^{-4} M and (B) 2.5 x 10^{-7} M. $I_{00} \approx$ 14.8 - 99.7 MW/cm^2 for each independent measurement.

Table 5.3: Nonlinear optical properties of 8 and 9 in solution and in thin films. Peak intensity for each measurement was ≈ 99.7 MW/cm²

Compound	Solvent	Concentration	β_{eff} cm/GW	$I_m[\chi^{(3)}]$/esu	γ (esu)	k (σ_T/σ_O)	I_{lim} J/cm²)
8	DMSO	1.0×10^{-4}	360	8.47×10^{-10}	3.71×10^{-28}	38.6	0.58
	THF	1.0×10^{-4}	294	6.24×10^{-10}	3.35×10^{-28}	39.3	0.72
	DMSO	2.5×10^{-7}	53.8	3.14×10^{-17}	2.64×10^{-34}	4.5	1.45
8-PSU			8610	2.02×10^{-8}	8.84×10^{-27}	210	0.04
9	DMSO	1.0×10^{-4}	427	1.00×10^{-9}	4.38×10^{-28}	38.6	0.64
	THF	1.0×10^{-4}	386	8.19×10^{-10}	4.40×10^{-28}	33.0	0.67
9-PSU			8900	2.09×10^{-8}	1.02×10^{-26}	250	0.05

The dominant mechanisms responsible for the nonlinearity of each complex (**8** and **9**) were investigated in DMSO using **Eqs. 5.1** and **5.2** to obtain σ_T [209]. **Figure 5.16** shows plots of β_{eff} and σ_T against sample concentrations at constant I_{00} ≈99.7 MW/cm². Both β_{eff} and σ_T increases in magnitude with positive slopes as the concentrations of each sample increases. The β_{eff} values increase with increasing concentration is an indication of direct relationship between the nonlinear response and the concentration of each sample [167]. The magnitude with which the σ_T of **8** and **9** are increasing with concentration is an indication of absorption of second photons by already excited molecules in the triplet states.

This observation is attributed to the rapid ISC of each molecule to the triplet excited states. Thus, the dominant mechanism for both molecules in DMSO is due to RSA assisted by excited state absorption in the triplet states. The population of an excited state absorption cross-section (σ_T) of a molecule being larger than the ground state cross-section (σ_0), is a condition primarily responsible for RSA occurring in the Pcs [297]. The absorption cross-sections ratios (k) for each sample are presented in **Tables 5.1** and **5.3**. These values are greater than 1, and a very good indicator that RSA could be occurring for the Pcs.

The γ values reported for these samples fall within the reported optimal range of hyperpolarizability values for phthalocyanines in solution [320]; this implies that they are good candidates as optical limiters. γ values estimated for sample **8** and **9** in solution are larger by at least two orders of magnitude than the values reported in literature for meso-

substituted porphyrins [321]; and series of porphyrin-heteropolyoxometalate hybrid systems [322], at 532 nm and 20 ps pulsed duration.

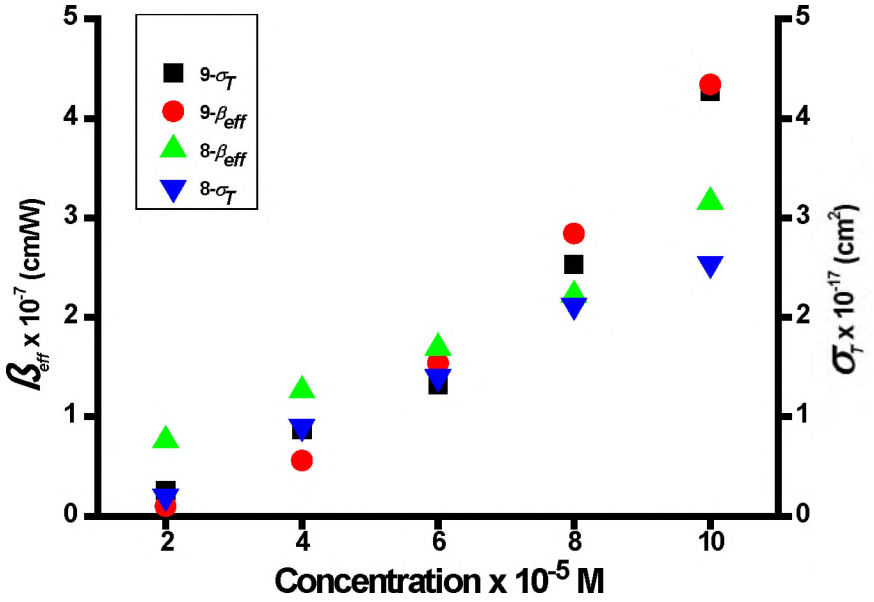

Figure 5.16: Plots of β_{eff} and σ_T increasing concentration for compound 8 and 9 in DMSO. I_{oo} = 99.7 MW/cm^2.

5.2.4.2 Z-scan measurements in thin films

Polysulfone on its own showed no NLO behavior. The overlay of the Z-scan profiles for the studied complexes **8** and **9** in thin films were measured at I_{00} of 99.7 MW/cm^2; revealing RSA like profiles, **Figure 5.17**. At this input intensity, the z-scan profiles for each host-guest system of Pc-PSU dropped to the lowest transmittance values at 0.13 and 0.15 for **8** and **9**, respectively. The obtained β_{eff} value rises to 8610 cm/GW for **8-PSU** and 8900 cm/GW for **9-PSU** (**Table 5.3**). The substantial increase in the magnitude of β_{eff} values in thin films compared to solutions can be attributed to the high resistance of polysulfone to laser radiation, and the effect of the aggregation of the samples on solid support. The effect of intermolecular interaction of the Pcs in solid states is particularly important to the enhanced NLO properties of the host-guest systems [323,324]. β_{eff} values of Pcs in PSU are higher than those reported for PBC even though different Pcs are used. polysulphone have been reported to be appreciably more stable to thermal and thermal-oxidative breakdown compared to polycarbonate and other polymers [325].

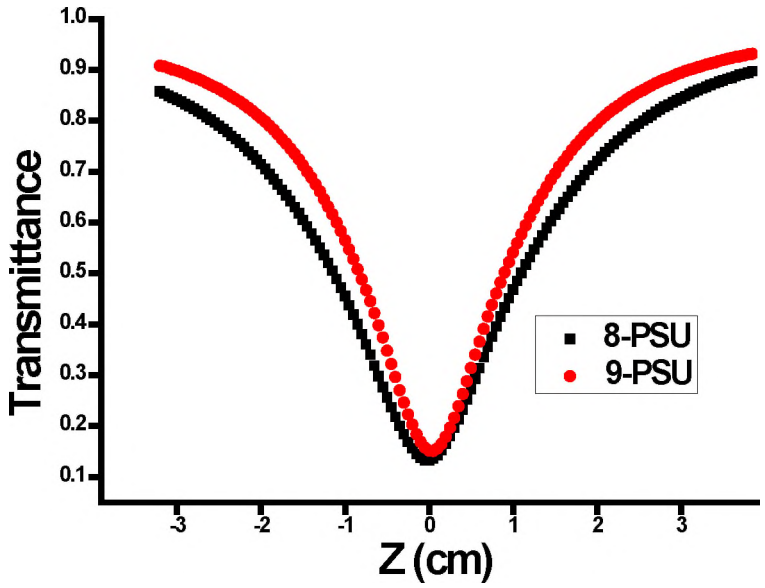

Figure 5.17: OA Z-scan curves for 8-PSU and 9-PSU. Peak input intensity (I_{oo}) = 99.7 MW/cm^2.

The calculated $I_m[\chi^{(3)}]$ and γ values for the samples, both in solution and thin films are presented in **Table 5.3**. The higher the values of $I_m[\chi^{(3)}]$ and/or γ, the better the compounds as optical limiters; values of $I_m[\chi^{(3)}]$ and γ were expected to vary in the same trend as observed for β_{eff}. Generally, the $I_m[\chi^{(3)}]$ values in solution for the studied samples are much lower than the corresponding values in thin films. Similarly, the same trend was also observed for γ values in solution and in their respective thin films. γ values for Pc-PSU composites (≈10^{-26} esu) are within the range reported for series of In, Ga and Zn phthalocyanine complexes in presence of nanomaterials, quantum dots and PMMA [326].

The $I_m[\chi^{(3)}]$ values of ≈10^{-8} esu, in thin films reported in this work was larger by two orders of magnitude compared to five different Pcs doped in PMMA polymers at 800 nm and 2 ps, as reported by Rao et al. [120]. The values in thin films are also remarkably larger than the values reported for transparent nanohybrids of TiO_2 doped on PMMA reported by Yuwono et al. [327]. Values of $I_m[\chi^{(3)}]$ and γ reported for **8** and **9** in PSU are remarkably larger than those reported for complexes **5**, **6** and **7** embedded in PBC (**Table 5.2**) for reasons given above for β_{eff}.

Figure 5.18 shows a plot of incident laser intensity (I_o) plotted against transmitted beam intensity (I_{out}) for **8** and **9** in solution and in thin films also at 532 nm and 10 ns pulsed duration. From **Table 5.3**, the I_{lim} values for **8** and **9** in DMSO at 0.5 linear transmittance were estimated at 0.58 J/cm^2 and 0.64 J/cm^2, respectively. The I_{lim} values of **8-PSU** and **9-PSU** are about the same at 0.04 J/cm^2 and 0.05 J/cm^2, respectively. This shows that even though complex **8** is metal free, it has the same optical limiting behavior as the Zn containing complex **9**. This shows that metal free Pcs cannot be ruled out as good NLO materials. The I_{lim} values obtained for the samples in solution are within the acceptable limits for optical limiters. The I_{lim} values for **8-PSU** and **9-PSU** are lower than the complexes studied in thin films due to the improved stability of polysulphone.

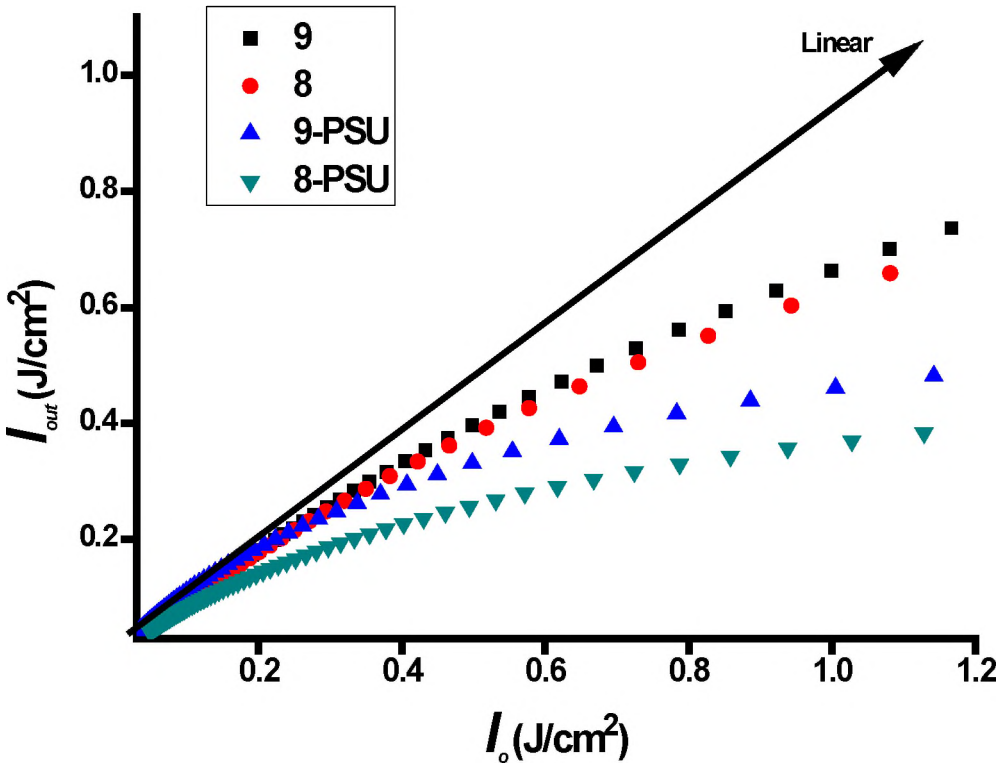

Figure 5.18: I_{out} versus I_o for 8, 9, 8-PSU and 9-PSU. Peak intensity, I_{OO} = 99.7 MW/cm^2 for each sample.

5.2.5 Complexes 10 and 11 in DMSO

Table 5.1 summarized the nonlinear optical parameters reported for complexes **10** and **11** in DMSO at laser input intensities of 44.1 MW/cm^2 and 55.4 MW/cm^2, respectively. Complex **10** was recorded at Abs of ≈ 0.76, while nonlinear optical characterizations of

11 were carried out at ≈ 0.5 Abs. The β_{eff} value obtained for complex **11** is larger than that of complex **10** also measured, this could be due to the plurality of the amino groups on complex **11** as observed in the improved Φ_T for **11** compared to **10**, **Table 5.1**. The $I_m[\chi^{(3)}]$ and γ values reported for **11** at 55.4 MW/cm^2 are within the same order of magnitude reported for complex **10**, in DMSO and at lower input intensity of 44.1 MW/cm^2.

5.3 Nonlinear optical studies of Pc-nanomaterial or polymer composites

5.3.1 Z scan behaviour of complexes 2 and 3 clicked to AuNPs

Open-aperture (OA) Z-scan technique was used to measure nonlinear optical absorptions of complexes **2** and **3** clicked to azide-derivatized AuNPs. The composite samples were all dissolved in DMSO and their linear absorption coefficients adjusted to ca. 1.0 cm^{-1} in 0.2 cm cuvette. **Figure 5.19A and B** show Z-scan profiles for **3**, **3-AuNPs**, **2** and **2-AuNPs**, exhibiting symmetrical minimum transmission around the focus. This corresponds to a reverse-saturable absorption (RSA) phenomenon [108], suggesting occurrence of multi-photon absorption processes due to the enhanced triplet excited-state to ground-state absorptions [98,328]. A plausible explanation to the transmission minimum exhibited by the samples is that, as the incident laser radiation increases, the transmitted beams from the samples decreases and reached a point at which it is clamped. At approximately the same irradiance of 0.08 GW/cm^2 (20.4 μJ), minimum transmission recorded for **3**, **3-AuNPs**, **2** and **2-AuNPs** are 0.66, 0.42, 0.56 and 0.30, respectively. Expectedly, **2** coupled to AuNPs gave the lowest transmission clamped at 30% compared to **3-AuNPs** observed at 42%, due to heavy indium metal in the former.

β_{eff} values of 374 cm/GW and 1392 cm/GW were respectively obtained for **2** and **2-AuNPs**, while β_{eff} values of 76 cm/GW and 630 cm/GW were also recorded for **3** and **3-AuNPs**, respectively, **Table 5.4**. Significant increase in the magnitude of β_{eff} values for phthalocyanines-AuNPs composites compared to unconjugated Pcs revealed the contribution of AuNPs in enhancing optical limiting performance of the later. Larger β_{eff} of **2-AuNPs** compared to **3-AuNPs** is a direct consequence of the combined heavy atom effects of In central metal and AuNPs which encouraged ISC for triplet absorption population. Also in the absence of AuNPs, **2** showed

impressive β_{eff} value compared to **3** due to heavier atom effects In imposed on former than later. Heavy atom-substituted Pcs are known to have enhanced NLO and OL properties than relatively lighter atoms [315,329]. Hence, the observed larger β_{eff} value of **2** compared to **3**.

Table 5.4: Nonlinear optical properties of 2, 3, 2-AuNPs and 3-AuNPs samples in DMSO. $I_{OO} \approx$ 0.08 GW/cm².

Sample	β_{eff} (cm/GW)	I_{lim}(J/cm²)	$I_{\mathrm{m}}[\chi^{(3)}]$(esu)	γ (esu)	$k(\frac{\sigma_T}{\sigma_0})$
3	76	0.63	0.91×10^{-11}	0.74×10^{-30}	6.2
3-AuNPs	630	0.31	9.77×10^{-9}	0.72×10^{-28}	301.2
2	374	0.20	1.14×10^{-10}	2.37×10^{-29}	7.8
2-AuNPs	1392	0.06	5.33×10^{-8}	1.80×10^{-27}	415

Note: values different from **Table 5.1**, since different intensities were used for the characterizations.

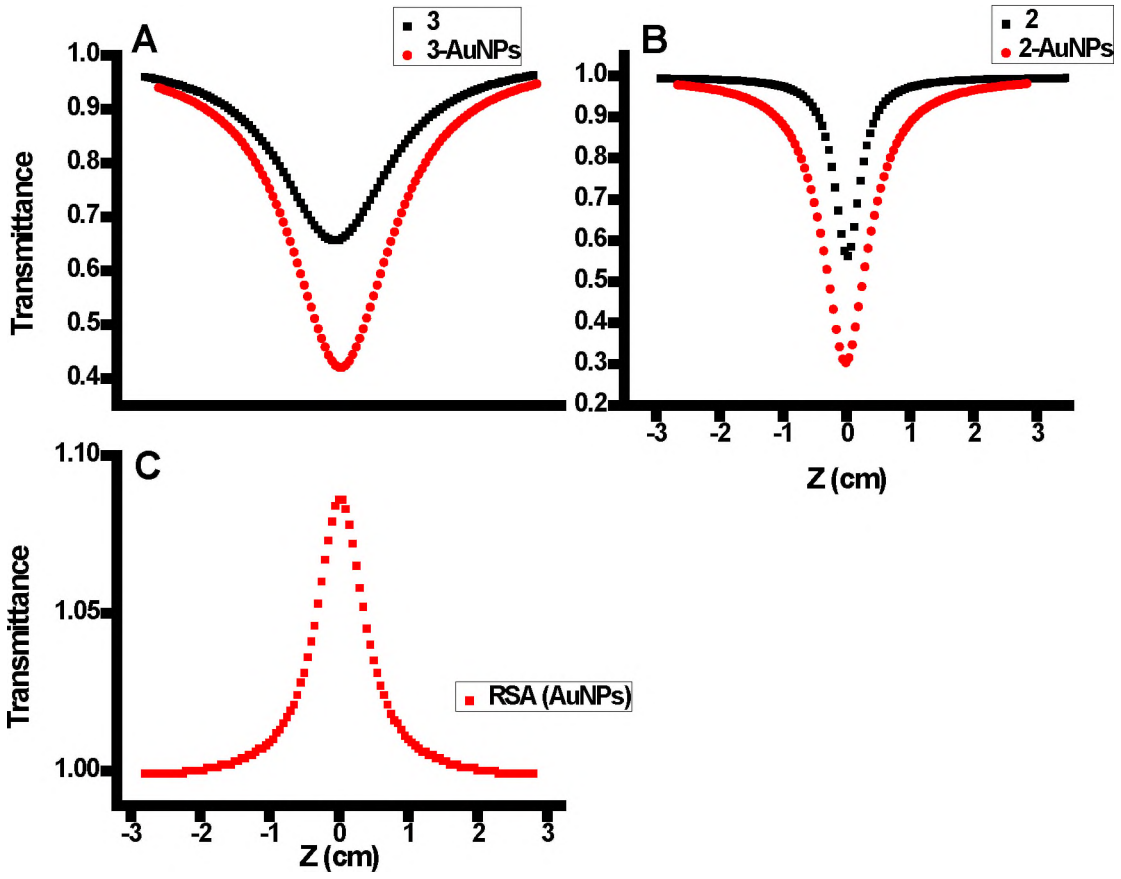

Figure 5.19: Z-scans transmittance plotted as a function of sample positions for (A) 3 and 3-AuNPs, (B) 2 and 2-AuNPs, and (C) AuNPs alone. Peak input intensity (I_{oo}) ≈ 0.08 GW/cm², Absorbance = 1.0 in DMSO.

Relationship between improved photophysical properties and enhanced nonlinear optical effects was established for the samples using absorption cross-sections ratio (k). σ_T was obtained by fitting the data to **Eqs. 5.1** and **5.2** [209].

Absorption cross-sections ratio (k) values for each sample was evaluated as ratio of excited state of absorption cross-section (σ_T) to ground state of absorption cross-section (σ_0). σ_T values exceeded the σ_0 by factors ranging from 6.2 to 415 with **2-AuNPs** having the largest k value followed by **3-AuNPs**, **Table 5.4**. This shows that triplet excited states of Pc-nanoparticle composites were populated with comparatively depleted ground state absorptions, due to the presence of AuNPs. The magnitude of k shows that improved photophysical properties of the composites also correspond to enhanced NLO effect of RSA.

The observed RSA for the phthalocyanines-AuNPs at input intensity of 0.08 GW/cm^2 (where AuNPs revealed SA, **Figure 5.19C**) showed that SA to RSA switching was greatly enhanced by the presence of the Pcs. Apart from being used to protect optical sensors and enhance night vision from intense laser pulses, the conjugation of the reverse saturable absorbers (**2** and **3**) to saturable absorbers (AuNPs) at low irradiances (< 0.5 GW/cm^2) can produce interesting optical limiting effects that can be found useful in technological applications such as optical switching, optical pulse compressor, and laser pulse narrowing [330].

For both Pcs, $I_m[\chi^{(3)}]$ and γ values in the presence of AuNPs are larger than the corresponding free phthalocyanines by up to 2 orders of magnitude, **Table 5.4**. At the same approximate concentrations, **2-AuNPs** relatively edged out **3-AuNPs** as OL material as evidenced from the calculated values of $I_m[\chi^{(3)}]$ and γ.

Figure 5.20 shows the plots of incident laser intensity (I_o) versus transmitted laser intensity (I_{out}) for the studied samples. The free phthalocyanines and their conjugates have their energy outputs deviated from linearity, an indicative of good NLO responses to the input intensity. From **Table 5.4**, the I_{lim} values for **2**, **3**, **2-AuNPs** and **3-AuNPs** in DMSO were estimated at 0.20 J/cm^2, 0.63 J/cm^2, 0.06 J/cm^2 and 0.31 J/cm^2, respectively. Thus, **2-AuNPs** shows the best optical limiting behaviour among the samples. The I_{lim} value of **2-AuNPs** is almost comparable to PSU thin films in **Table 5.3**.

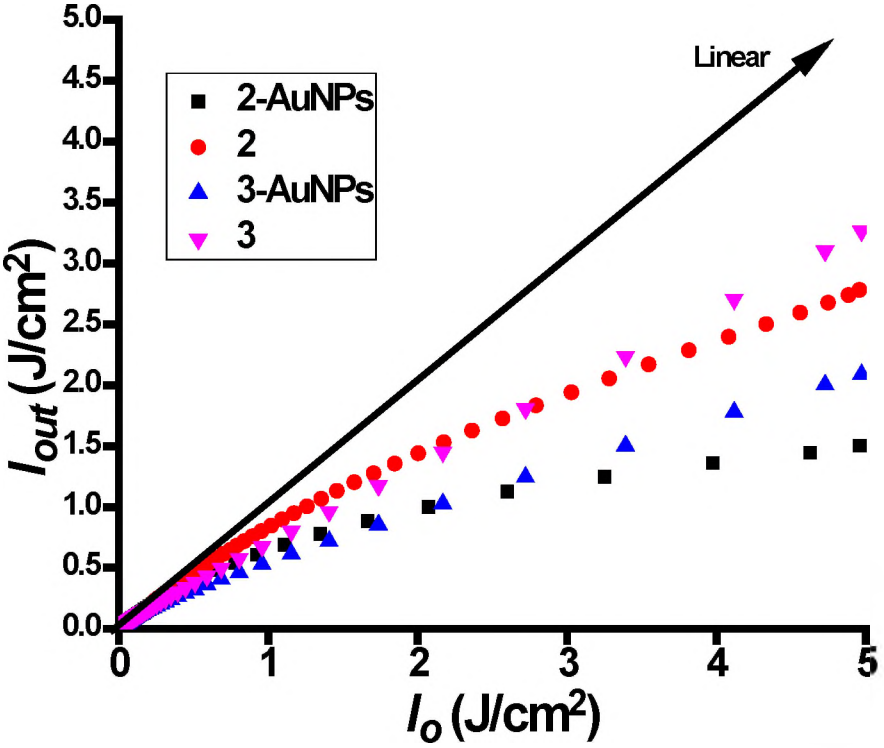

Figure 5.20: Output fluence (I_{out}) versus input fluence (I_o) for 3, 2, 3-AuNPs and 2-AuNPs in DMSO. Peak intensity (I_{oo}) ≈ 0.08 GW/cm² for independent sample.

5.3.2 Z scan behaviour of complex 10 conjugated to nanomaterials and polymer

Optical limiting behaviours of complex **10** covalently linked to AuNPs, PAA, Fe_3O_4@Ag, Fe_3O_4-Ag, GQDs, N-GQDs and SNGQDs are discussed in this section. In addition to nonlinear optical characterizations of **10-AuNPs** and **10-PAA** composites in solution, NLO studies were also done where **10** or **10-AuNPs** composite were also embedded into PAA as thin films (TF), without covalent linking to form either **10/PAA-TF** or **10-AuNPs/PAA-TF**.

5.3.2.1 NLO of 10, 10-AuNPs, 10-PAA in solution and in thin films

The samples were all excited using nanosecond pulses of mode-locked Nd:YAG laser system (λ= 532 nm, t = 10 ns, I_{oo} ≈ 44.1 MW/cm²). **Figure 5.21** shows the open aperture Z-scan plots of transmittance against the z-positions for the samples in solution (≈ 0.76 abs), and when embedded in PAA. The Z-scan profiles revealed reverse saturable absorptions evidenced from the reduction in their transmissions at the beam focus

[90,167,206,296,300]. Estimated β_{eff} in solution for **10** alone is the smallest followed closely by **10-PAA**, while the largest value was reported for **10-AuNPs, Table 5.5**, indicating enhanced OL behaviour of **10** in presence of AuNPs compared to PAA. At relatively low absorbance (ca. 0.76) and moderate peak intensity of ≈ 44.1 MW/cm^2, **10-PAA** showed an impressive NLO behaviour with absorption coefficient of 218 cm/GW. β_{eff} value of **10-PAA** is greater than or within the range reported for porphyrins linked to carbon nanostructures [331-333]. β_{eff} value of **10-AuNPs** is larger than the values reported for phthalocyanine combined with quantum dots, magnetite nanoparticles and graphene oxide [176,177,180].

The formation of the thin films resulted in highly enhanced β_{eff} values (**Table 5.5**) as is typical of thin films [124,334]. It should be noted that the films made the Pc highly aggregated, which may play a role in the enhanced nonlinear optical behavior over the solutions. There were insignificant changes in the spectra of the samples following Z-scan experiments, suggesting no changes to the chemical compositions of the samples after exposure to laser radiation.

The σ_T values calculated by fitting data to **Eqs. 5.1** and **5.2** for each sample exceeded ground state absorption cross-section σ_0 by factors of 47.6, 56.6 and 304 for **10**, **10-PAA** and **10-AuNPs**, respectively. The σ_T values for the thin films (for **10/PAA-TF** and **10-AuNPs/PAA-TF**) were much larger than those measured in solution. The population of an excited state absorption cross-section (σ_T) of a molecule being larger than the ground state cross-section (σ_0), is a condition primarily responsible for RSA occurring in the Pcs [297]. The largest absorption cross-sections ratio (*k*) for **10-AuNPs/PAA-TF** = 2.79 × 10^3 is a direct consequence of the magnitude of reduction of transmittance; this is a good indication of ESA-dependent RSA as predominant mechanism responsible for nonlinear absorption (NLA).

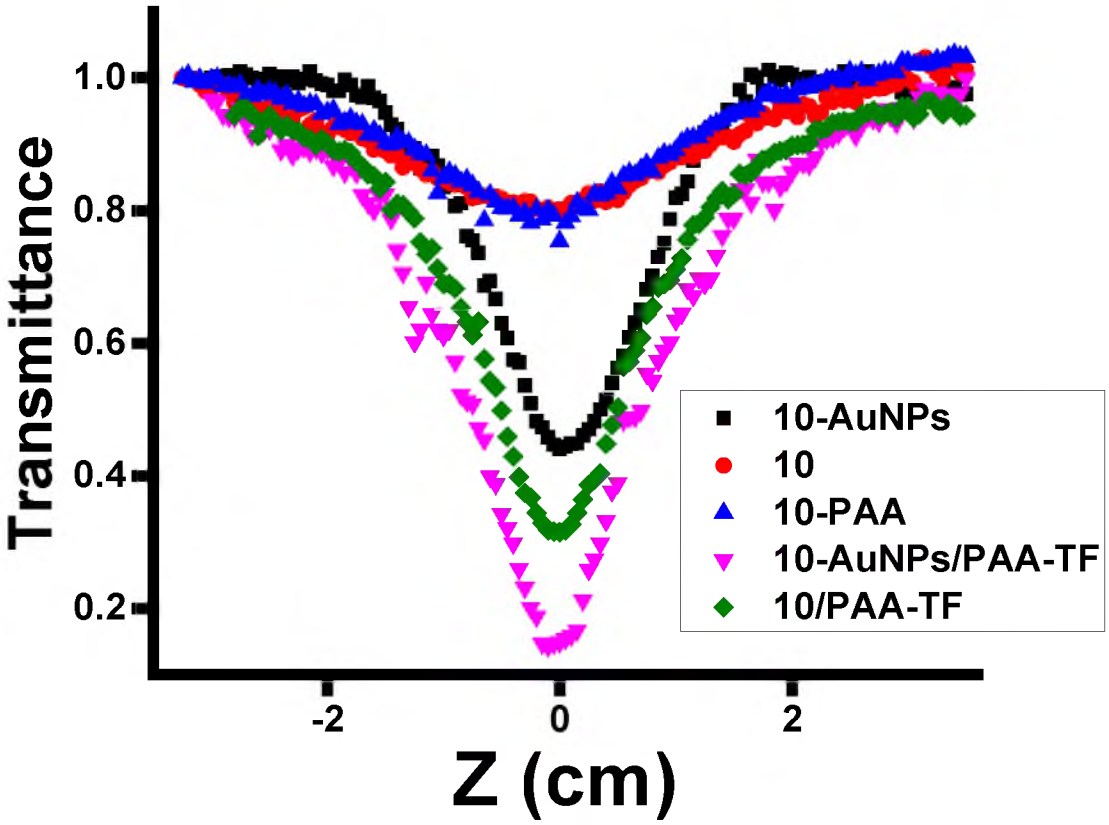

Figure 5.21: OA Z-scans profiles for 10, 10-PAA, 10-AuNPs in DMSO and in thin films (PAA).

Saturable absorption (SA) is known for AuNPs (**Figure 5.19C**), the observed SA for AuNPs was attributed to the photodegradation of the singlet excited states [335]. The intense absorption around 500 to 550 nm (from AuNPs) due to SPR observed for **10** conjugated to AuNPs rendered the contributions from 2PA negligible. Free carrier absorption has been reported to be phenomenologically similar to RSA, hence the NLO contributions from AuNPs can be estimated by fitting the experimental Z-scan data to FCA transmittance equation, (**Eq. 1.14**) [336]. Magnitude of FCA cross-section (σ_{FCA}) was estimated as 2.00 x 10^{-20} esu, this value falls within the same order of magnitude for those reported for a Pc linked to quantum dots [177].

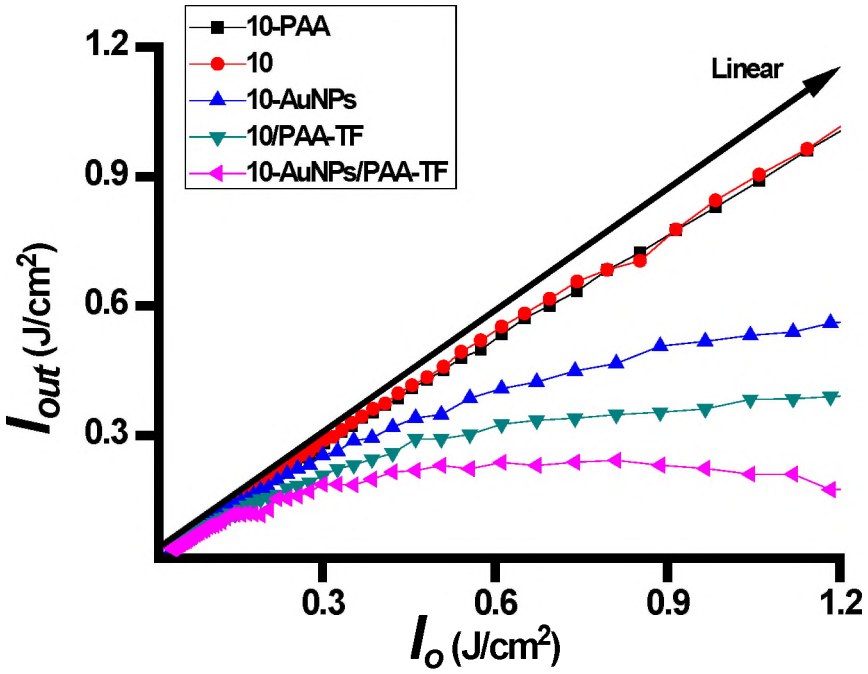

Figure 5.22: Output fluence (I_{out}) versus input fluence (I_o) for 10, 10-PAA, 10-AuNPs (in DMSO), 10/PAA-TF and 10-AuNPS/PAA-TF. (I_{oo}) = 44.1 MW/cm² for each sample.

The calculated $I_m[\chi^{(3)}]$ and γ values for the samples, both in solution and in thin films are presented in **Table 5.5**. $I_m[\chi^{(3)}]$ and γ values recorded for **10** and **10-PAA** composites in solution are within the same order of magnitude, and up to two orders of magnitude lower than the value reported for **10-AuNPs** conjugates in solution. The γ value for **10** alone is much higher than the values reported for symmetrical phthalocyanines in solution [93]. This shows that even at low concentration, complex **10** shows impressive NLO behaviour attributed to the increased molecular dipole moments of asymmetrical Pcs [132]. $I_m[\chi^{(3)}]$ value at $\approx 10^{-9}$ esu for **10-AuNPs**, is remarkably larger than the values reported for the same molecule linked to graphene oxide by two orders of magnitude [180]. The γ value reported for **10-AuNPs** when doped in PAA is at least one to two order of magnitude greater than values reported for series of In, Ga and Zn phthalocyanine complexes in presence of nanomaterials, quantum dots and PMMA [326]. Similarly, $I_m[\chi^{(3)}]$ values in thin films are also larger than the values reported for transparent nanohybrids of TiO_2 doped on PMMA reported by Yuwono et al. [327].

I_{lim} value of an OL materials is required to be sufficiently lower (below 1.0) as it measures the nonlinear response of the material to attenuate intense laser radiation. **Figure 5.22**

shows a plot of incident laser intensity (I_o) plotted against transmitted beam intensity (I_{out}) for **10**, **10-PAA** and **10-AuNPs** in solution and in thin films. From **Table 5.5**, the thin films of **10-AuNPs/PAA** and **10/PAA** have very low I_{lim} of 0.045 J/cm^2 and 0.063 J/cm^2, respectively. Again, the values of I_{lim} are lower for Pcs in PSU compared to the thin films of **10-AuNPs/PAA** and **10/PAA** (**Table 5.3**) due to the reason given above. In solution, the I_{lim} of **10**, **10-PAA** and **10-AuNPs** are respectively, 0.89 J/cm^2, 0.78 J/cm^2 and 0.13 J/cm^2.

5.3.2.2 NLO studies of 10-Fe_3O_4@Ag and 10-Fe_3O_4-Ag.

Figure 5.23A shows a representative overlay of open aperture (OA) Z-scan profiles for **10** in the presence of Fe_3O_4@Ag and Fe_3O_4-Ag, irradiated with nanosecond pulsed laser of peak input intensity of ≈ 44.1 MW/cm^2. At z=0, minimum transmissions (T(z)) of 0.75, 0.51 and 0.39 were recorded for **10**, **10-Fe_3O_4@Ag** and **10-Fe_3O_4-Ag**, respectively. The lower the T(z) of the sample the better the material as optical limiter, hence **10-Fe_3O_4-Ag** shows better OL properties than **10-Fe_3O_4@Ag**. **Figure 5.23B** shows the representative fitting of experimental to theoretical dataset for **10-Fe_3O_4-Ag**. The β_{eff} values increased from 165 cm/GW for **10** to ≈ 808 cm/GW (for **10-Fe_3O_4@Ag**) and 1,485 cm/GW (for **10-Fe_3O_4-Ag**), **Table 5.5**. The observed trend corresponds to larger Φ_T value for **10-Fe_3O_4-Ag** compared to **10-Fe_3O_4@Ag** in **Table 5.5**. Large values of Φ_T should translate into improved NLO properties [317]. The β_{eff} value for **10-Fe_3O_4@Ag** is larger than those reported for indium tetraamino phthalocyanine coordinated to silica coated magnetic particles or silica nanoparticles with β_{eff} of 400 cm/GW and 200 cm GW^{-1}, respectively [176]. This shows the importance of coating Fe_3O_4 with silver shell compared to silica NPs. Significant enhancement in the magneto-plasmonic optical responses of Fe_3O_4 in presence of silver or gold layer have been previously observed [185,194,337]. β_{eff} value reported for **10-Fe_3O_4-Ag** is greater than the value reported for **10-AuNPs**, this could be due to the size and compositions of the NPs.

Table 5.5: NLO properties of 10 and 10-NPs composites in DMSO and/or in thin films

Sample	Medium	β_{eff} (cm/GW)	$I_m[\chi^{(3)}]$ (esu)	γ(esu)	$k(\frac{\sigma_T}{\sigma_0})$	I_{lim} J/cm²	Φ_T
10	DMSO	165	3.86×10^{-11}	1.69×10^{-29}	47.6	0.89	0.73
10/PAA-TF	Thin Film	7290	1.71×10^{-8}	7.49×10^{-27}	908	0.063	
10-PAA	DMSO	218	5.11×10^{-11}	2.23×10^{-29}	56.6	0.78	0.67
10-AuNPs	DMSO	995	2.39×10^{-9}	1.02×10^{-27}	304	0.13	0.83
10-AuNPs/PAA-TF	Thin Film	18900	4.44×10^{-7}	1.94×10^{-25}	2.79×10^{3}	0.045	
10-Fe_3O_4@Ag	DMSO	808	1.99×10^{-9}	0.83×10^{-27}	312	0.11	0.81
10-Fe_3O_4-Ag	DMSO	1485	2.14×10^{-7}	0.94×10^{-24}	510	0.08	0.88
10-GQDs	DMSO	231	9.16×10^{-11}	7.01×10^{-29}	49.8	0.61	0.74
10-NGQDs	DMSO	288	1.32×10^{-10}	3.34×10^{-28}	59.4	0.58	0.77
10-SNGQDs	DMSO	320	3.42×10^{-10}	5.03×10^{-28}	63.2	0.55	0.79

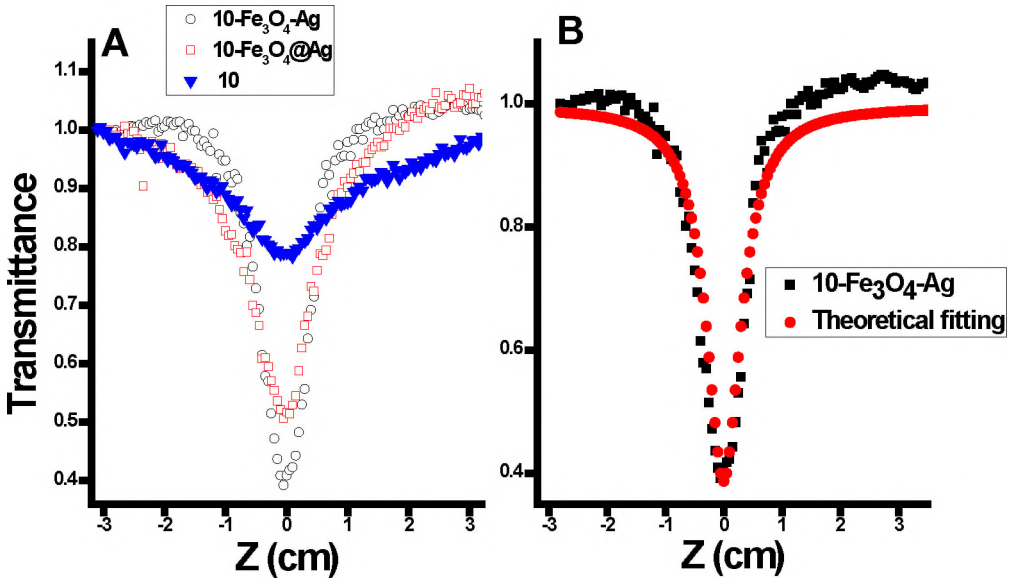

Figure 5.23: (A) OA Z-scans transmittance versus sample positions for 10, 10-Fe_3O_4@Ag and 10-Fe_3O_4-Ag and (B) Representative Z-scan for 10-Fe_3O_4-Ag (black) and the theoretical fitting in red, $I_{oo} \approx$ 44.1 MW/cm², Absorbance = 0.76 in DMSO.

Figure 5.24 shows the plot of β_{eff} versus absorbance ranging from 0.76A to 3.6A. As it can be seen, β_{eff} increases with positive slopes as the absorbance of each conjugate increases, suggesting direct relationship between the NLO responses and the concentration of each sample. This shows that as the concentration of the sample increases, the efficiency of the composites to shield light sensitive material also increases.

NLO responses of the oleic acid/oleylamine capped Fe_3O_4@Ag and Fe_3O_4-Ag in toluene were examined prior to surface ligands exchange. The nanoparticles switched from SA to RSA higher laser power (~110.3 MW/cm²) [160]. Interestingly, Fe_3O_4-Ag consistently shows better NLO behavior with minimum transmission at 0.81 compared to Fe_3O_4@Ag at 0.91, **Figure 5.25**; this shows both NPs maintained their NLO performances after conjugation. The lower NLO performance of Fe_3O_4@Ag core-shell could possibly due to the tensile effect exerted on the Ag shell by the core Fe_3O_4 due to differences in their lattice parameters [338]. Also, reduction in the saturation magnetization of Fe_3O_4@Ag core-shell NPs is more pronounced than in the Fe_3O_4-Ag heterodimer [339], this could lead to diminished NLO properties of Fe_3O_4@Ag core-shell NPs.

An attempt to excite the NPs at the same input intensity (44.1 MW/cm²) used for the complex **10** and the conjugates revealed saturable absorption behavior (figure not shown), suggesting that SA to RSA transition at low intensity was efficiently suppressed in the presence of **10** [160]. Upon conjugation to phthalocyanine, switching from one-photon absorption (SA) process to multi-photon absorption (RSA) process was observed (**Figure 5.23A**) for both Pc and the conjugates. Hence the predominant mechanisms for the observed NLA is due to MPA-assisted RSA.

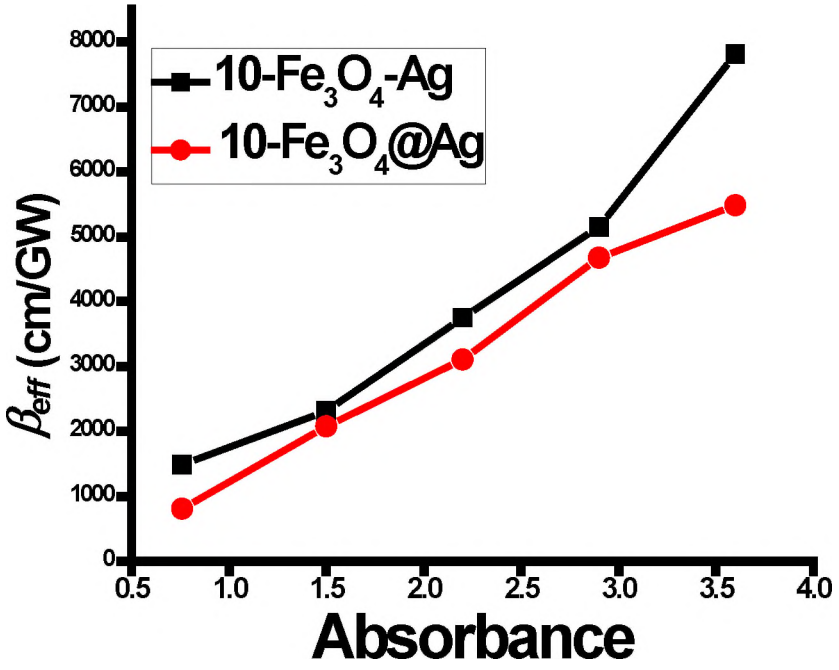

Figure 5.24: Absorbance dependence on β_{eff} for 10-Fe_3O_4@Ag and 10-Fe_3O_4-Ag, $I_{oo} \approx$ 110.3 MW/cm² for each independent measurement in DMSO.

Magnitude of absorption cross-sections ratio (*k*) for the conjugates were calculated using **Eqs. 5.1** and **5.2** [209]. Absorption cross-sections ratio (*k*) of 312 and 510 were reported for **10-Fe_3O_4@Ag** and **10-Fe_3O_4-Ag**, respectively. The magnitude of *k* shows that the NLO effect of the RSA is due to the excited triplet state populations with comparatively weaker ground state absorptions.

The imaginary third-order susceptibility, $I_m[\chi^{(3)}]$, value of **10** increased upon conjugation to the metallic NPs. Similarly, values of γ for the conjugates were up to 2 to 4 order of magnitude larger than **10** (**Table 5.5**). At the same approximate concentrations, **10-Fe_3O_4-Ag** was a much better NLO material compared to **10-Fe_3O_4@Ag** evidenced from the calculated values of $I_m[\chi^{(3)}]$ and γ.

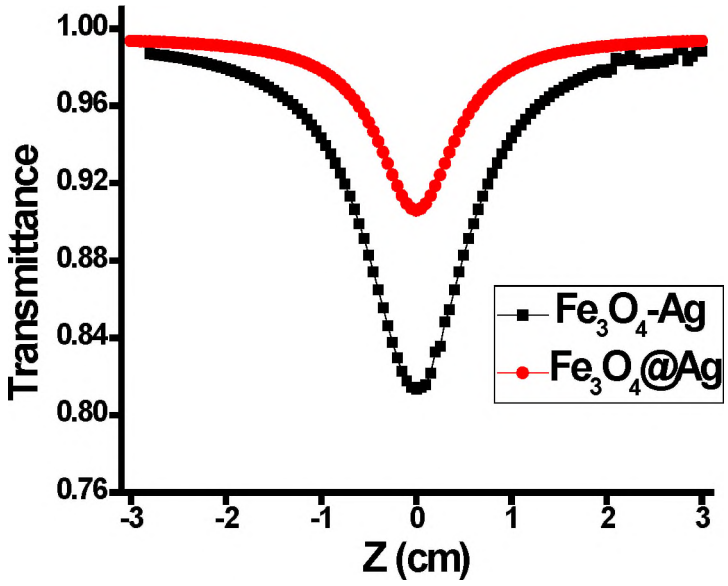

Figure 5.25: Open aperture Z-scans transmittance plotted as a function of sample positions for oleic acid/oleylamine capped Fe_3O_4@Ag and Fe_3O_4-Ag in toluene, $I_{oo} \approx$ 110.3 MW/cm^2.

Figure 5.26 shows the plots of incident laser intensity (I_o) versus transmitted laser intensity (I_{out}) for **10**, **10-Fe_3O_4@Ag** and **10-Fe_3O_4-Ag**. Both **10** and the conjugates have their energy outputs expectedly deviated from linearity, an indicative of better and good NLO responses to the input intensity [330]. However, the deviation of **10-Fe_3O_4-Ag** and **10-Fe_3O_4@Ag** were substantially lower compared to **10**, suggesting favourable effect of the magnetic-metallic nanoparticles on the nonlinearity of **10**. From **Table 5.5**, the I_{lim}, values for **10**, **10-Fe_3O_4@Ag** and **10-Fe_3O_4-Ag** in DMSO were estimated at 0.89 J/cm^2, 0.11 J/cm^2 and 0.08 J/cm^2, respectively. Superior NLO properties of **10-Fe_3O_4-Ag** may be a consequence of complex structure of **Fe_3O_4-Ag** with overall asymmetric electronic coupling between Ag and Fe_3O_4 as compared to symmetrical coupling of **Fe_3O_4@Ag** in **10-Fe_3O_4@Ag**.

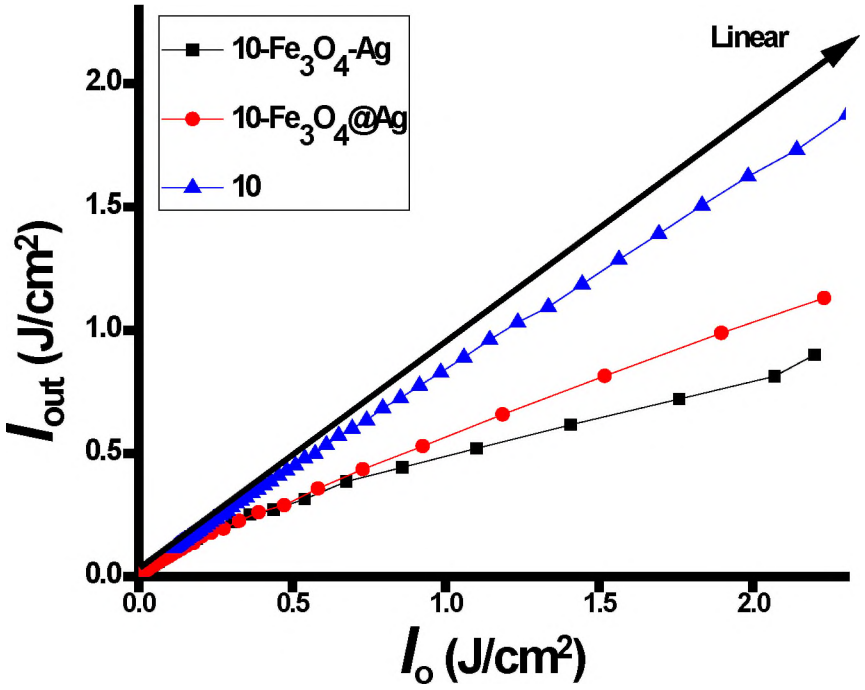

Figure 5.26: Output fluence (I_{out}) versus input fluence (I_o) for 10, 10-Fe_3O_4@Ag and 10-Fe_3O_4-Ag in DMSO. $I_{oo} \approx$ 44.1 MW/cm² for independent sample.

5.3.2.3 NLO of 10-GQDs, 10-NGQDs and 10-SNGQDs

Figure 5.27 shows the overlay open aperture Z-scan profiles for **10** and its composites with GQDs measured in DMSO at 2 absorbance. At constant irradiance intensity of ca. 0.08 GW/cm², the transmittance decreased along the sample positions (z) relative to the focal point (z=0). The reduction in the transmitted beam with increasing optical input intensity is an indication of positive nonlinear absorption [132,167,300], and presence of reverse saturable absorbers [90,167,206,296,300]. β_{eff} values for **10-NGQDs** and **10-SNGQDs** were larger than **10** and **10-GQDs**, **Table 5.5**. This could be as a result of increase in triplet absorption populations (increased triplet quantum yields) which could generate substantial NLO effect of reverse saturable absorption (RSA) [98,320,340,341]. β_{eff} of **10-GQD** composites are generally lower than that of **10-AuNPs**, **Fe_3O_4@Ag** or **10-Fe_3O_4@Ag** composites due to lack of heavy atom effects in the former, **Table 5.5**.

Bourlinos and co-workers reported on significantly enhanced nonlinear absorption for boron doped carbon dots compared to un-doped carbon dots at 532 nm, using 35 ps and 4 ns laser pulses [148]. Similarly, doping of quantum dots (graphene quantum dots

inclusive) with heteroatoms can endow the QDs with new or improved electronic states [198,342,343], photophysical and photoluminescence properties [198,344-347]. Hence, improved nonlinear absorbance (NLA) of **10-NGQDs** and **10-SNGQDs** could be due to the improved photophysical properties and formation of new electronic states that could lead to enhanced nonlinear absorptions [348].

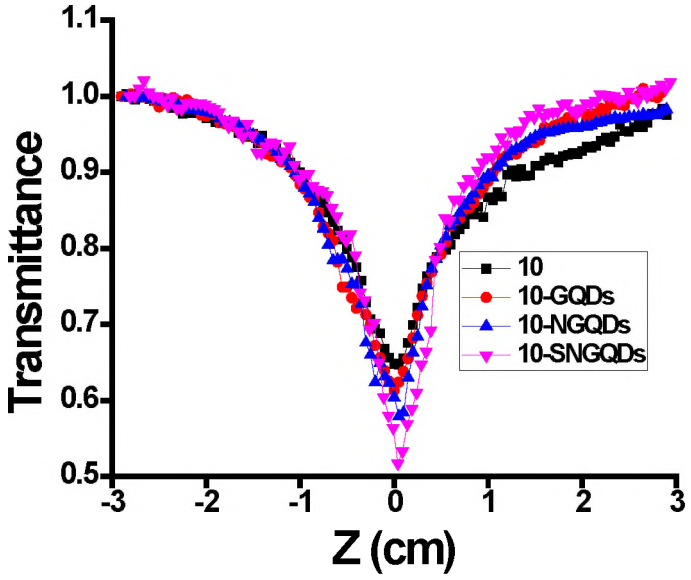

Figure 5.27: Open Aperture Z-scan signatures of the 10 and Pc-QDs conjugates Absorbance = 2.0, $I_{oo} \approx 0.08$ GW/cm².

The values of γ and $I_m[\chi^{(3)}]$ are expected to follow the same trend as observed for β_{eff}. From **Table 5.5**, the $I_m[\chi^{(3)}]$ value of **10** and **10-GQDs** are within the same range and up to one order of magnitude lower than the values for **10-NGQDs** and **10-SNGQDs.** Similar trends were also observed for values reported for γ. Larger γ and $I_m[\chi^{(3)}]$ values of **10-NGQDs** and **10-SNGQDs** could be attributed to the surface defects introduced on the graphene quantum dots after doping with S and/or N [198,200,225]. The $I_m[\chi^{(3)}]$ value of 17.62 ± 4.03 x 10^{-12} esu in DMF at 532 nm and 6 ns pulses [180] reported for **10** covalently linked to GO is up to 1 or 2 order of magnitude lower than the values reported for **10**-QDs conjugates in this work. The remarkably improved NLA for **10** in the presence of QDs can be ascribed to enhanced quantum confinement effect and the edge effects of graphene quantum dots compared to bulk graphene oxide [196,349]. Also,

differences from solvent polarities, Z-scan experimental conditions and procedures cannot be ruled out.

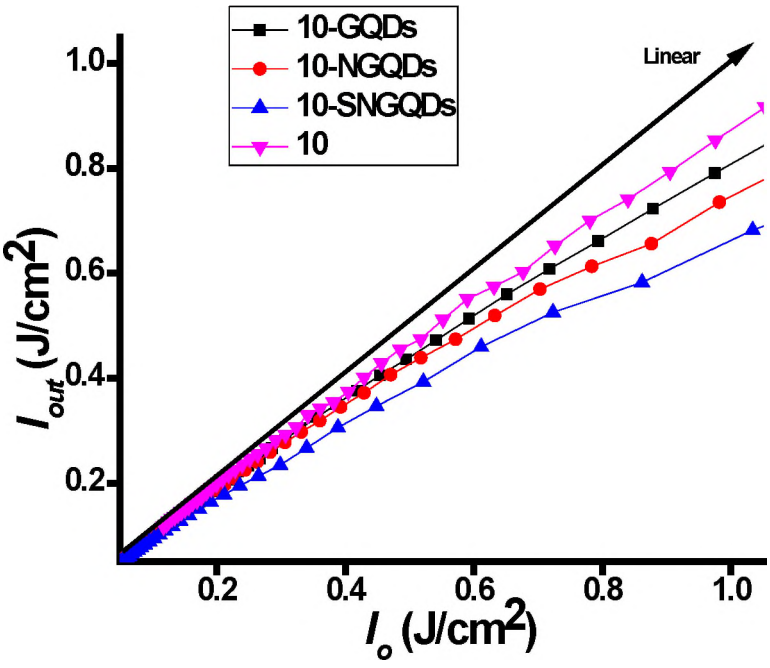

Figure 5.28: Output fluence (I_{out}) versus input fluence (I_o) for 10, 10-GQDs, 10-NGQDs and 10-SNGQDs. Peak intensity (I_{oo}) ≈ 0.08 GW cm^{-2} for each sample.

Figure 5.28 shows the plots of incident laser intensity (I_o) versus transmitted laser intensity (I_{out}) for **10** and **10**-QDs conjugates at input intensity of 0.08 GW/cm^2. Energy outputs of **10** conjugated to NGQDs and SNGQDs were substantially lower compared to **10** and **10**-GQDs. From **Table 5.6**, the I_{lim} values for **10**, **10**-GQDs, **10**-NGQDs and **10**-SNGQDs in DMSO were estimated at 0.77 J/cm^2, 0.61 J/cm^2, 0.58 J/cm^2 and 0.55 J/cm^2, respectively.

5.3.3 NLO characterizations of 11-$\mathbf{Ag_xAu_y}$ composites

Figure 5.29A shows plots of transmittance against the z-positions for the samples at an absorbance of ca 0.5A measured in 0.2 cm cuvette. The samples were found to exhibit reverse saturable absorption (RSA) behaviour [90,167,206,296,300]. **Figure 5.29B** shows the representative fitting of theoretical OA Z-scan (red) datasets to the experimental transmittance (black) data sets for **11** using **Eq. 1.10**. Estimated β_{eff} for **11**, **11**-$\mathbf{Ag_3Au_1}$ and **11**-$\mathbf{Ag_1Au_3}$ are respectively, 209 cm/GW, 910.5 cm/GW and 1108.8 cm/GW, **Table 5.6**. β_{eff} value is larger for the conjugates. The observed enhancement in β_{eff} values for **11**-$\mathbf{Ag_xAu_y}$ reported in this work, is attributed to the contributions from both **11** and the

bimetallic nanoparticles. NLO study on Ag-Au alloys by Papagiannouli et al. [269] showed that there is competition between saturable absorption (SA) and reverse saturable absorption (RSA) mechanisms for the bimetallic nanoparticles at different input intensities. They observed that a gold rich bimettalic nano-alloys switched from SA to RSA at ≈83 MW/cm^2 while Ag-rich alloys switched to RSA at high intensity of 220 MW/cm^2. Interestingly, NLO studies for **11-Ag_xAu_y** composites were carried out at lower intensity of ≈55.4 MW/cm^2. Each composite reported in this work revealed RSA as the predominant mechanism responsible for nonlinearity.

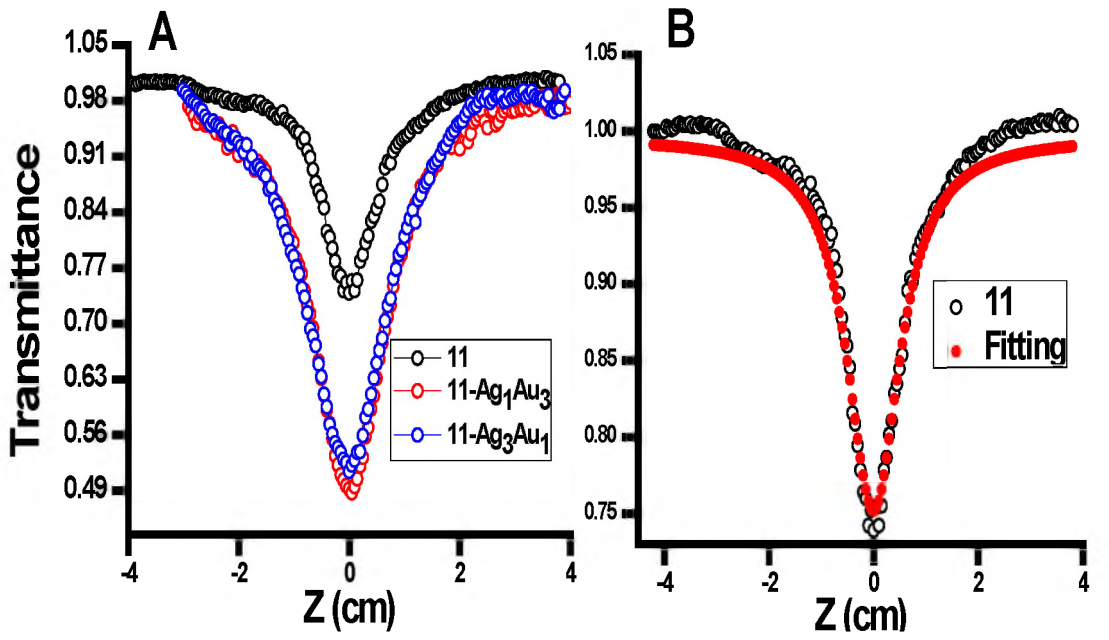

Figure 5.29: (A) OA Z-scans for 11, 11-Ag_1Au_3 and 11-Ag_3Au_1 (B) Representative open-aperture Z-scan of 11 (black) and the fitting in red, $I_{oo} \approx$ 55.4 MW/cm^2, Absorbance = 0.5 in DMSO.

The β_{eff} values for each sample at different absorbance were also plotted against the absorbance of the composites, **Figure 5.30**. β_{eff} increases in magnitude with positive slopes as the concentrations of each sample increases, suggesting direct relationship between the nonlinear optical responses and the concentration of each sample [167]. This shows that as the concentration of the sample increases, the efficiency of the material to act as a shield for light sensitive material also increases.

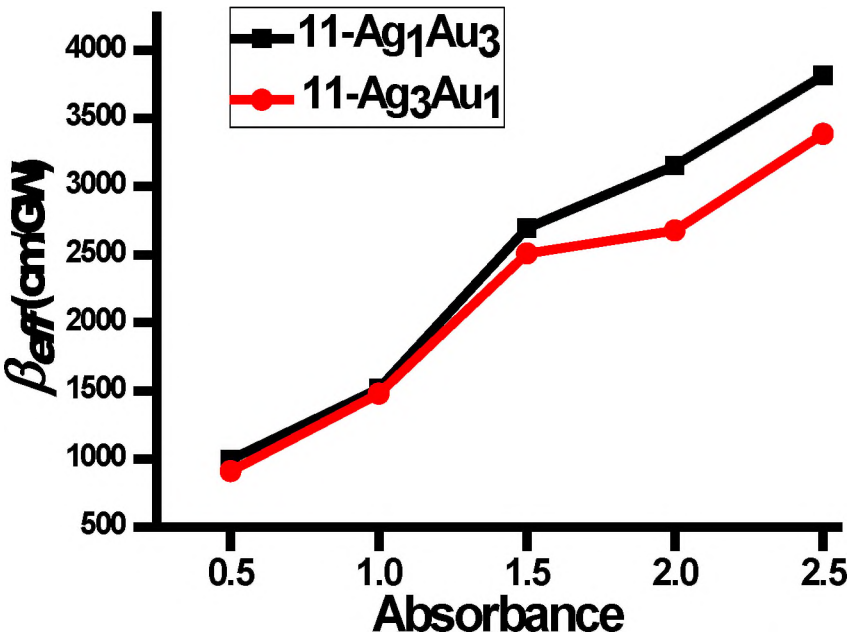

Figure 5.30: Plots showing the concentrations (absorbance) dependence on β_{eff} or 11-Ag_1Au_3 and 11-Ag_3Au_1. $I_{oo} \approx$ 55.4 MW/cm² for independent measurement in DMSO.

Table 5.6: Nonlinear optical properties of 11 and 11-Ag_xAu_y studied in DMSO

Sample	β_{eff} (cm/GW)	$I_m[\chi^{(3)}]$)/esu	γ (esu)	I_{lim}(J/cm²)	$k(\frac{\sigma_T}{\sigma_0})$	Φ_T
11	209	4.91×10^{-11}	2.15×10^{-29}	0.76	58.6	0.83
11-Ag_3Au_1	911	2.14×10^{-9}	9.35×10^{-28}	0.31	421	0.92
11-Ag_1Au_3	1109	2.6×10^{-9}	1.14×10^{-27}	0.28	621	0.95

Figure 5.31 shows the plots of incident laser intensity (I_o) versus transmitted laser intensity (I_{out}) for **11**, **11-Ag_1Au_3** and **11-Ag_3Au_1**. The plots clearly showed that all the samples including compound **11** expectedly deviated from linearity. However, the composites, **11-Ag_xAu_y** had their transmitted beams substantially much lower compared to **11** alone. This is indication of better NLO responses to the input intensity [330], and also showed the favourable effect of the bimetallic nanoparticles on the nonlinearity of **11**. From **Table 5.6**, the I_{lim} values for **11**, **11-Ag_1Au_3** and **11-Ag_3Au_1** in DMSO at 0.5 linear transmittance

were estimated at 0.76, 0.28 and 0.31 J/cm^2, respectively. The relatively low I_{lim} value of 0.76 J/cm^2 obtained for **11** in DMSO is still within the acceptable thresholds (< 1.0) required for protecting light sensitive materials.

Third-order susceptibility, ($I_m[\chi^{(3)}]$), values for **11-Ag_1Au_3**and **11-Ag_3Au_1** composites are within the same order of magnitude (≈ 10^{-9} esu), and up to two orders of magnitude larger than the value reported for **11** alone. The γ value of 2.15 × 10^{-29} esu for **11** alone is lower by one or two orders of magnitude than for **11-Ag_xAu_y** composites. However, γ value of **11** still falls within the optimal range of hyperpolarizability values reported for phthalocyanines in literature [320]. **11-Ag_1Au_3** is better than **11-Ag_3Au_1** as NLO material evidenced from the calculated values of $I_m[\chi^{(3)}]$ and γ, and also from the lowest value of I_{lim} discussed above.

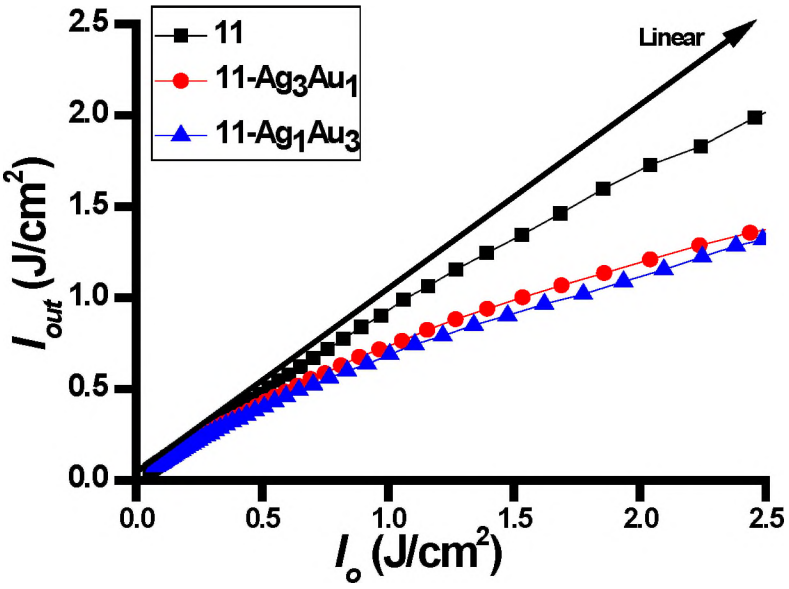

Figure 5.31: Output fluence (I_{out}) versus input fluence (I_o) for 11, 11-Ag_1 Au_3 and 11-Ag_3 Au_1. I_{oo} ≈ 55.4 MW/cm^2.

5.4 Conclusion for the chapter

Nonlinear optical characterizations of ZnPc, InPc and metal-free Pc complexes were studied using open aperture Z-scan techniques at 532 nm and 10 ns pulsed laser radiation. The samples were measured either in solution (DMSO, THF or $CHCl_3$) or when embedded in polymer mixtures. The analyses of the Z-scan data were fitted to a two-photon absorption mechanism (2PA), but the Pcs and Pc-nanomaterial or polymer

composites also possess the multi-photon absorption mechanisms aided by the triplet-triplet population to have RSA occur. Phthalocyanines complexes doped in polymer matrices (such as PSU, PBC and PAA) showed larger nonlinear absorption coefficients (β_{eff}), third-order susceptibility ($I_m[\chi^{(3)}]$) and second-order hyperpolarizability (γ), with an accompanying low values of intensity threshold (I_{lim}) than in solution. Aggregation was observed to impact negatively on the NLO behaviour of Pcs (**8** as a case study) at low laser power, and improved at relatively higher laser power. However, improved NLO behavior of Pcs in thin films due to aggregation were reported. Enhanced NLO and OL properties of complexes **2**, **3**, **10** and **11** in the presence of nanomaterials were observed compared to free phthalocyanines. Major factor responsible for the enhanced nonlinearities of **10** in the presence of NGQDs and SNGQDs were attributed to the surface defects caused by the presence of heteroatoms such as nitrogen (N) and sulfur (S).

CHAPTER 6
GENERAL CONCLUSIONS

This chapter summarizes the detailed syntheses, photophysical and nonlinear optical characterizations of phthalocyanine complexes and their composites with nanomaterials and/or polymers investigated in this thesis. Also, future prospects of the reported samples are reported in this chapter.

6.1 Conclusions

Syntheses and photophysical characterizations of new phthalocyanine complexes **1**, **2**, **4**, **7**, **8**, **9** and **11** are reported in this thesis for the first time. The results of the characterizations were in good agreement with their molecular structures, and confirmed the purity of the new molecules. Complexes **10** and **11** were conjugated to nanomaterials via covalent bonding as in the case of **10**, or NH_2-Au and/or Au-S bonding as in the case of **11**. Clickable azide-derivatized gold nanoparticles were synthesized and conjugated to alkyne moieties on **2** and **3** via azide-alkyne Huisgen cycloaddition reactions. The characterization results of the composites of **2**, **3**, **10** and **11** with nanomaterials were in good agreement with the expected results. Results were presented on the nonlinear optical properties of the studied samples using open aperture Z-scan techniques at 532 nm and 10 ns pulsed laser radiation, measured either in solution (DMSO, THF or $CHCl_3$) or when embedded in polymer mixtures. The analyses of the Z-scan data for the studied samples did fit to a two-photon absorption mechanism (2PA), but the Pcs and Pc-nanomaterial or polymer composites also possess the multi-photon absorption mechanisms aided by the triplet-triplet population to have RSA occur.

The results showed that;

- phthalocyanines (**5**, **6**, **7**, **8**, **9**, and **10**) doped in polymer matrices (such as PSU, PBC and PAA) showed larger nonlinear absorption coefficients (β_{eff}), third-order susceptibility ($I_m[\chi^{(3)}]$) and second-order hyperpolarizability (γ), with an accompanying low values of intensity threshold (I_{lim}) than in solution.
- Phthalocyanines (**8** and **9**) doped in PSU gave improved nonlinear optical properties compared to other Pcs in PBC and PAA due to the improved stability of PSU to thermal and thermal-oxidative breakdown than PBC and PAA.
- presence of electron withdrawing (NO_2) groups fused with triazole linkers in complex **4** provide excellent coexistent features like enhanced triplet absorptions and better optical limiting behavior than **3**.

- aggregation in DMSO negatively affected NLO behaviour of Pcs (**8** as a case study) at low laser power, and improved at relatively higher laser power. However, aggregation of Pcs in thin films improves NLO behavior of phthalocyanines.
- heavy atom-substituted Pcs (**6**) enhanced NLO and OL properties than relatively lighter atoms in complexes **5** and **7**.
- direct relationship between improved photophysical properties and enhanced nonlinear effects favoured by excited triplet absorption of the phthalocyanines (**2**, **3**, **10** and **11**) in presence of nanomaterials was established.
- exciting functional materials composed of appropriate saturable (nanomaterials) and reversed saturable (MPcs) can be developed at low laser intensity.
- major factor responsible for the enhanced nonlinearities of **10** in the presence of NGQDs and SNGQDs were fully described and attributed to the surface defects caused by the presence of heteroatoms such as nitrogen (N) and sulfur (S).

6.2 Future prospects

It would be interesting to see the nonlinear optical properties of the studied molecules or composites measured at different wavelengths (532-1064 nm) and with different laser pulsed durations (nanosecond, picosecond and femtosecond). The obtained information can be used to determine the specificity and sensitivity of the material(s) as optical limiters.

The optical limiting results observed for the Pc-nanomaterial composites are very impressive. It would be of great interest to study how optical limiting behaviour of the composites change at different particle sizes and shapes. Also, optical limiting behaviour of the composites as a function of the nanoparticles or Pcs concentration could be explored for nanoparticles that showed good optical limiting properties.

REFERENCES

1. A. von Braun, J. Tscherniac, Ber. Deut. Chem. Ges. **40** (1907) 2709.
2. H. de Diesbach, E. von de Weid, Helv. Chim. Acta. **10** (1927) 886.
3. R. P. Linstead, J. Chem. Soc. (1934) 1016.
4. R. P. Linstead, A.R. Lowe, J. Chem. Soc. (1934) 1022.
5. C. E. Dent, R.P. Linstead, J. Chem. Soc. (1934) 1027.
6. J. A. Elvidge, R.P. Linstead, J. Chem. Soc. (1955) 3526.
7. J. M. Robertson, J. Chem. Soc. (1935) 615.
8. J. M. Robertson, J. Chem. Soc. (1936) 1195.
9. J. M. Robertson, I. Woodward, J. Chem. Soc. (1937) 3536.
10. G.T. Byrne, R.P. Linstead, A. R. Lowe, J. Chem. Soc. (1934) 1017.
11. H. Ze. Gok, H. Kantekin, Yasar Gok, G. Herman, Dyes Pigm. **75** (2007) 606.
12. S. J. Lange, J.W. Sibert, A.G.M. Barrett, B.M. Hoffman, Tetrahedron **56** (2000) 7371.
13. Ö. Bekaroglu, J. Porphyrins Phthalocyanines **4** (2000) 465.
14. K. Ukei, Acta. Cryst. B **2** (1973) 2290.
15. J. W. Perry, K. Mansour, S. R. Marder, D. Alvarez Jr., K. J. Perry, I. Choong, J. Opt. Lett. **19** (1994) 625.
16. K. Tabata, K. Fukushima, K. Oda, I. Okura, J. Porphyrins Phthalocyanines 4 (2000) 278.
17. D. Atilla, V. Ahsen, J. Porphyrins Phthalocyanines **6** (2002) 593.
18. V. N. Nemykin, E.A. Lukyanets, Arkivoc **1** (2010) 136.
19. T. Shen, Z.-I. Yuan, H.-j. Xu, Dyes Pigm. **11** (1989) 77.
20. A. A. Chernonosov, E. A. Ermilov, B. Röder, L. I. Solovyova, O. S. Fedorova, Bioinorg. Chem. Appl. **2014** (2014) 7.
21. S. Çolak, S. Z. Yildiz, Turk. J. Chem. **38** (2014) 1153.
22. A. Ogunsipe, D. Maree, T. Nyokong, J. Mol. Struct. **650** (2003) 131.
23. J. D. Spikes, Photochem. Photobiol. **43** (1986) 691.
24. S. Z. Topal, Ü. İşci, U. Kumru, D. Atilla, A. G. Gürek, C. Hirel, M. Durmuş, J.-B. Tommasino, D. Luneau, S. Berber, F. Dumoulin, V. Ahsen, Dalton Trans. **43** (2014) 6897.
25. P. Gregory, in High-Technology Applications of Organic Colourant, Plenum Press, New York (1991).

26. N. B. McKeown, in Phthalocyanine Materials: Synthesis, Structure and Function; Cambridge University Press: Cambridge, U.K. (1998).

27. J. A. de Saja, M. L. Rodrìguez-Méndez, Adv. Colloid. Interfac. **116** (2005) 1.

28. M. Tian, T. Wada, H. Kimura-Sudab, H. Sasabea, J. Mater. Chem. **7** (1997) 861.

29. T. Nyokong, in J.H. Zagal, F. Bedioui F, Dodelet JP (Eds.), N4-Macrocyclic Metal Complexes, Springer, New York (2006).

30. E. A. Lukyanets, J. Porphyrins Phthalocyanines **3** (1999) 424.

31. C. M. Whitacre, D. K. Feyes, T. Satoh, J. Grossmann, J.W. Mulvihill, H. Mukhtar, N. L. Oleinick, Clin. Cancer Res. **6** (2000) 2021.

32. R. C. Baker, D. P. Wilkinson, J.J. Zhang, ECS Trans. **16** (2009) 43.

33. M. K. Nazeeruddin, R. Humphry-Baker, M. Grätzel, B. A. Murrer, Chem Commun. (1998) 719.

34. V. M. Vlasov, Russ. Chem. Rev. **72** (2003) 681.

35. P. A. Barrett, C. E. Dent, R. P. Linstead, J. Chem. Soc. (1936) 1719.

36. R. Huisgen, Angew. Chem. Int. Ed. Engl. **2** (1963) 565.

37. H. C. Kolb, M.G. Finn, K.B. Sharpless, Angew. Chem. Int. Ed. **40** (2001) 2004.

38. V. Rostovtsev, L. G. Green, W. Fokin and K. B. Sharpless, Angew. Chem., Int. Ed. **41** (2002) 2565.

39. U. Hahn, T. Torres, J. Porphyrins Phthalocyanines **15** (2011) 364.

40. B. N. Sena, H. Mert, H. Dinçer, A. Koca, Dyes Pigm. **100** (2014) 1.

41. H. Dinçer, H. Mert, B.N. Sen, A. Dag, S. Bayraktar, Dyes Pigm. **98** (2013) 246.

42. Y. Yilmaz, M. K. Sener, I. Erden, U. Avciata, Polyhedron **28** (2009) 3419.

43. S. G. Liu, Y. Q. Liu, Y. Xu, D. B. Zhu, A. C. Yu and X. S. Zhao, Langmuir **14** (1998) 690.

44. G. Rojo, G. De la Torre, J. Garcıa-Ruiz, I. Ledoux, J. Zyss, T. Torres, F. Agullo-Lopez, Chem. Phys. **245** (1999) 27.

45. G. J. Bryant, M. J. Cook, M. J. Haslam, R. M. Richardson, T. G. Ryan, A. J. Thorne, J. Mat. Chem. **4** (1994) 209.

46. K. E. Treacher, G. J. Clarkson, N. B. McKeown, Mol. Cryst. Liq. Cryst. **260** (1995) 255.

47. S. Osati, N. Safari, P. R. Jamaat, Inorg. Chim. Acta **363** (2010) 2180.

48. B. Ballesteros, G. de la Torre, C. Ehli, G. M. A. Rahman, F. Agullo-Rueda, D. M. Guldi, T. Torres, J. Am. Chem. Soc. **129** (2007) 5061.

49. N. Kobayashi, R. Kondo, S. Nakajima and T. Osa, J. Chem. Soc. **112** (1990) 9640.

50. S. Dabak, A. Gul, O. Bekaroglu, Chem. Ber. **127** (1994) 2009.

51. D. wohrle, G. Krawczyk, Polym. Bull. **15** (1986) 193.

52. J. Yang, T. C. Rogers, M. R. Van De Mark, J. Heterocycl. Chem. **30** (1993) 571.

53. J. V. Bakboord, M.J. Cook, E.J. Hamuryudan, J. Porphyrins Phthalocyanines **4** (2000) 510.

54. W. A. Nevin, W. Liu, S. Greenberg, M.R. Hempstead, S.M. Marcuccio, M. Melnik, C.C. Leznoff, A.B.P. Lever. Inorg. Chem. **26** (1987) 891.

55. M. Gouterman, In The Porphyrins, (Ed. D. Dolphin), Part A. Physical Chemistry, Academic Press, New York, (1978).

56. J. McHugh, M. Gouterman, C. Weiss, Theoret. Chim. Acta, **24** (1987) 246.

57. A. M. Schaffer, M. Gouterman, E.R. Davidson, Theoret. Chim. Acta **30** (1973) 9.

58. A. Jablonski, Z. Phys. **94** (1935) 38.

59. P. W. Atkins, in Physical Chemistry, P.W. Atkins (Ed.), Oxford University Press, Oxford, 6th Edition, (1998) Chapter 17.

60. K. Ishii, N. Kobayashi, in The Porphyrin Handbook, K.M. Kadish, K.M. Smith, R. Guilard, (Eds.), Elsevier Science, New York, Vol. 16 (2003) Chapter 102.

61. C. -M. Yang, C. -H. Wu, H. -H. Liao, K. -Y. Lai, H. -P. Cheng, S. -F. Horng, H.-F. Meng, J. -T. Shy, Appl. Phys. Lett. **90** (2007) 133509.

62. M. T. Vagnini, A. L. Smeigh, J. D. Blakemore, S. W. Eaton, N. D. Schley, F. D'Souza, R. H. Crabtree, G. W. Brudvig, D. T. Co, M. R. Wasielewski, PNAS **109** (2012) 15651.

63. L. B. Josefsen, R. W. Boyle, Theranostics **2** (2012) 916.

64. W. Sun, G. Wang, Y. Li, M. J. F. Calvete, D. Dini, M. Hanack, J. Phys. Chem. A **111** (2007) 3263.

65. R. Bonnett, in Chemical Aspects of Photodynamic Therapy (Advanced Chemistry Texts V.1); Gordon and Breach Science Publishers: Amsterdam, The Netherlands, (2000)

66. A. R. Simioni, F. L. Primo, A. C. Tedesco, J. Laser Appl. **24** (2012) 012004.

67. J. Fu, X. Y. Li, D. K. P. Ng, C. Wu, Langmuir **18** (2002) 3843.

68. T. W. J. Gadella Jr, R.M. Clegg, T.M. Jovin, Bioimaging **2** (1994) 139.

69. A. Ogunsipe, J.-Y. Chen, T. Nyokong, New. J. Chem. **28** (2004) 822.

70. H. C. Gerritsen, R. Sanders, A. Draaijer, Proc. SPI **2329** (1994) 260.

71. A. G. Ryder, S. Power, T. J. Glynn, J. J. Morrison, Proc. SPI **4529** (2001) 102.

72. T. Förster, Disc. Far. Soc. **27** (1959) 7.

73. J. R. Lakowicz, Principles of Fluorescence Spectroscopy, 3rd edn. Springer, NewYork, (2006).

74. J. Turro, in Modern Molecular Photochemistry, The Benjamin/Cummings Publishing Co., Inc. New York (1978).

75. M. M. Barroso, J. Histochem. Cystchem. **59** (2011) 237.

76. L. Stryer, Annu. Rev. Biochem. **47** (1978) 819.

77. J. S. Hsiao, B.P. Krueger, R.W. Wagner, T.E. Johnson, J.K. Delaney, D.C. Mauzerall, G.R. Fleming, J.S. Lindsey, D.F. Bocian, R.J. Donohoe, J. Am. Chem. Soc. **118** (1996) 11181.

78. E. Z. Chong, D.R. Matthews, H.D. Summers, K.L. Njoh, R.J. Errington, P.J. Smith, J. Biomed. Biotechnol. **2007** (2007) 1.

79. A.H. Clayton, K. Nectarios, H.C. Stephen, C.N. Edouard, Eur. Biophy. J. **34** (2005) 82.

80. L. De Boni, E. Piovesan, L. Gaffo, and C. R. Mendonca, J. Phys. Chem. A **112** (2008) 6803.

81. Y. Li, T. M. Pritchett, J. Huang, M. Ke, P. Shao, and W. Sun, J. Phys. Chem. A **112** (2008) 7200.

82. J. S. Shirk, R.G.S. Pong, F.J. Bartoli, A.W. Snow, Appl. Phys. Lett. **63** (1993) 1880.

83. R. L. Sutherland, in Handbook of Nonlinear Optics, 2nd Edn, Marcel Dekker, New York (2003).

84. R. Bonnet, R.J. Ridge, E.J. Land, R.S. Sinclair, D. Tait, T.G. Truscon, J. Chem. Soc. Faraday Trans. **78** (1982) 127.

85. S. L. Murov, I. Carmichael and G.L. Hug, Handbook of Photochemistry (2nd edn), M. Decker: New York (1993).

86. T. H. Tran-Thi, C. Desforge, C. Thiec, J. Phys. Chem. **93** (1989) 1226.

87. S. D'Souza, E. Antunes, C. Litwinski, T. Nyokong, J. Photochem. Photobiol. A: Chem. **220** (2011) 11.

88. R. Philip, G. Ravindra Kumar, P. Mathur, S. Ghosh. Chem. Phys. Lett. **313** (1999) 719.

89. J. E. Riggs, Y.P. Sun. J. Phys. Chem. A **103** (1999) 485.

90. M. Hanack, T. Schneider, M. Barthel, J. S. Shirk, S. R. Flom, R. G. S. Pong, Coord. Chem. Rev. **219–221** (2001) 235.

91. M. A. Díaz-García, J. Porphyrins Phthalocyanines **13** (2009) 652.

92. E. M. Maya, A.W. Snow, J.S. Shirk, S.R. Flom, R.G.S. Pong, G.L. Roberts, Polym. Prep. **42** (2001) 253.

93. Y. Chen, M. Hanack, Y. Araki, O. Ito, Chem. Soc. Rev. **34** (2005) 517.

94. G. de la Torre, P. Vazquez, F. Agulló-López and T. Torres, J. Mater. Chem. **8** (1998) 1671.

95. G. de la Torre, P. Vazquez, F. Agullo-Lopez, T. Torres, Chem. Rev. **104** (2004) 3723.

96. H. Zhang, D. E. Zelmon, L. G. Deng, H. K. Liu, B. K. Teo, J. Am. Chem. Soc. **123** (2001) 11300.

97. T.-H. Wei, T.-H. Huang, T.-C. Wen, Chem. Phys. Lett. **314** (1999) 403.

98. J. W. Perry, K. Mansour, I. Y. S. Lee, X. L. Wu, P. V. Bedworth, C. T. Chen, D. Ng, S.R. Marder, P. Miles, T. Wada, M. Tian and H. Sasabe, Science **273** (1996) 1533.

99. Y. Ipeka, H. Dince, A. Koca, Sens. Actuators, B **193** (2014) 830.

100. A. Hajri, S. Touaiti, B. Jamoussi, Adv. Optoelectron. **321563** (2013) 7.

101. S. R. Nxele, P. Mashazi, T. Nyokong, Electroanalysis **27** (2015) 2468.

102. A. M. Sevim, I. Özçesmeci, A. Gül, J. Porphyrins Phthalocyanines, **17** (2013) 540.

103. A. Fashina, E. Amuhaya, T. Nyokong, Spectrochim. Acta Mol. Biomol. Spectrosc. **140** (2015) 256.

104. D. Quinton, E. Antunes, S. Griveau, T. Nyokong, F. Bedioui, Inorg. Chem. Commun. **14** (2011) 330.

105. H. Yoshiyama, N. Shibata, T. Sato, S. Nakamura, T. Toru, Org. Biomol. Chem. **6** (2008) 4498.

106. S. Campidelli, B. Ballesteros, A. Filoramo, D. D. Dıaz, G. de la Torre, T. Torres, G. M. A. Rahman, C. Ehli, D. Kiessling, F. Werner, V. Sgobba, D. M. Guldi, C. Cioffi, M. Prato, J.-P. Bourgoin, J. Am. Chem. Soc. **130** (2008) 11503.

107. S. R. Nxele and T. Nyokong, Electrochim. Acta **194** (2016) 26.

108. S. M. O'Flaherty, S.V. Hold, M. J. Cook, T. Torres, Y. Chen, M. Hanack, W. J. Blau, Adv. Mater. **15** (2003) 19.

109. E. M. García-Frutos, S.M. O'Flaherty, E. M. Maya, G. de la Torre, W. Blau, P. Vázqueza, T. Torres, J. Mater. Chem. **13** (2003) 749.

110. I. V. Khudyakov, Y.A. Serebrennikov, N. Turro. J. Chem. Rev. **93** (1993) 537.

111. X. F. Zhang, X. Li, L. Niu, L. Sun, L. Liu, J. Fluoresc. **19** (2009) 947.

112. M. Yüksek, A. Elmali, M. Durmuş, H.G. Yaglioglu, H. Ünver, T. Nyokong, J. Opt. **12** (2010) 1.

113. H. Gu, S. Li, J. Wang, W. J. Blau, Y. Chen, Mater. Chem. Phys. **137** (2012) 188.

114. S. Tekin, H. G. Yaglioglu, A. Elmali, U., Kürüm, H. Yanık, D. A. Tekdas, M. Durmus and V. Ahsen, Mater. Chem. Phys. **138** (2013) 270.

115. K. Sanusi, T. Nyokong, Journal of J. Coord. Chem. **67** (2014) 2911.

116. K. Sanusi, E.K. Amuhaya, T. Nyokong. J. Phys. Chem. C **118** (2014) 7057.

117. K. Sanusi, T. Nyokong, J. Photochem. Photobiol. A: Chem. **303–304** (2015) 44.

118. V. Chauke, M. Durmus, T. Nyokong, J. Photochem. Photobiol. A: Chem. **192** (2007) 179.

119. M. C. Larciprete, R. Ostuni, A. Belardini, M. Alonzo, G. Leahu, E. Fazio, C. Sibilia, M. Bertolotti, Photon. Nanostr. Fundamen. Appl. **5** (2007) 73.

120. S. V. Rao, P. T. Anusha, T. S. Prashant, D. Swain, S. P. Tewari, Materials Sciences and Applications, **2** (2011) 299.

121. A. Auger, W. J. Blau, P. M. Burnham, I. Chambrier, M. J. Cook, B. Isare, F. Nekelson, S. M. O'Flaherty, J. Mater. Chem. **13** (2003) 1042.

122. W. M. Darwish, A. M. Darwish, E. A. Al-Ashkar, Polym. Adv. Technol. **26** (2015) 1014.

123. A. Slodek, D. Wohrle, J. J. Doyle, W. Blau, Macromol. Symp. **235** (2006) 9.

124. K.E. Sekhosana, E. Amuhaya, T. Nyokong. Polyhedron **85** (2015) 347.

125. C. Mkhize, J. Britton, T. Nyokong. Polyhedron **81** (2014) 607.

126. I. A. C. García, A. M. Sevim, A. de la Escosura, T. Torres, Org. Biomol. Chem. **11** (2013) 2237.

127. P. M. Burnham, M. J. Cook, L. A. Gerrard, M. J. Heeney, D. L. Hughes, Chem. Commun. (2003) 2064.

128. M. J. Cook, I. Chambrier, S. J. Cracknell, D. A. Mayes, D. A. Russell, Photochem. Photobiol. **62** (1995) 542.

129. K. Sakamoto, E. Ohno-Okumura, T. Kato, H. Soga, J. Porphyrins Phthalocyanines **14** (2010) 47.

130. D. Swain, V. K. Singh, N. V. Krishna, L. Giribabu, S. V. Rao, J. Porphyrins Phthalocyanines **18** (2014) 305.

131. R. S. S. Kumar, S. V. Rao, L. Giribabu, D. N. Rao, Opt. Mater. **31** (2009) 1042.

132. S. J. Mathews, S. C. Kumar, L. Giribabu, S. V. Rao, Opt. Commun. **280** (2007) 206.

133. C. Buzea, I. I. P. Blandino and K. Robbie, Biointerphases **2** (2007) 17.

134. E. Roduner, Chem. Soc. Rev. **35** (2006) 583.

135. D. Guo, G. Xie and J. Luo, J. Phys. D: Appl. Phys. **47** (2014) 013001.

136. W. T. Liu, J. Biosci. Bioeng. **102** (2006) 1.

137. S. E. McNeil, J. Leukoc. Biol. **78** (2005) 585.

138. N. L. Rosi, C. A. Mirkin, Chem. Rev. **105** (2005) 1547.

139. P.A. Hervieux, A. Benabbas, V. Halte, J.Y. Bigot, EPJ D **24** (2003) 185.

140. G. Weick, G. L. Ingold, R. A. Jalabert, D. Weinmann, Phys. Rev. B **74** (2006) 165421.

141. Y. Bigot, V. Halte, J.C. Merle, A. Daunois, J. Chem. Phys. **251** (2000) 181.

142. S. Shrestha, C. Yeung, C. Nunnerley, S. C. Tsang, Sens Actuators A Phys. **136**(2007) 191.

143. D. V. Goia, E. Matijevic, New J. Chem. **22** (1998) 1203.

144. A. C. Templeton, W. P. Wuelfing, R. W. Murray, Acc. Chem. Res. **33** (2000) 27.

145. Y. Li, Y. Wu and Beng S. Ong, J. Am. Chem. Soc. **127** (2005) 3266.

146. D. V. Talapin, J.-S. Lee, M. V. Kovalenko, El. V. Shevchenko, Chem. Rev. 110 (2010) 389.

147. S. S. Nair, J. Thomas, C. S. Suchand Sandeep, M. R. Anantharaman, R. Philip, Appl. Phys. Lett. **92** (2008) 171908.

148. A. B. Bourlinos, G. Trivizas, M. A. Karakassides, M. Baikousi, A. Kouloumpis, D. Gournis, A. Bakandritsos, K. Hola, O. Kozak, R. Zboril, I. Papagiannnouli, P. Aloukos, S. Couris, CARBON **83** (2015) 173.

149. T. Mthethwa, E. Antunes, T. Nyokong, Dalton Trans. **43** (2014) 8230.

150. T. P. Mthethwa, Y. Arslanoglu, E. Antunes, T. Nyokong, Polyhedron **38** (2012) 169.

151. C. Tshangana and T. Nyokong, J. Mol. Struct. **1089** (2015) 161.

152. P. Modisha, T. Nyokong and E. Antunes, J. Nanosci. Nanotechnol. **15** (2015) 3688.

153. P. Khoza and T. Nyokong, J. of Mol. Catal. A: Chem. **399** (2015) 25.

154. S. D'Souza, R. George, M. Göksel, D. Atilla, M. Durmus and T. Nyokong, Polyhedron **100** (2015) 296.

155. R. O. Ogbodu, T. Nyokong, Polyhedron **90** (2015) 175.

156. A. Chunder, T. Pal, S. I. Khondaker, L. Zhai, J. Phys. Chem. C **114** (2010) 15129.

157. X. Li, B. Wang, X. Wang, X. Zhou, Z. Chen, C. He, Z. Yu, Y. Wu, Nanoscale Res. Lett. **10** (2015) 373.

158. H. Tian, J. Oscarsson, E. Gabrielsson, S. K. Eriksson, R. Lindblad, B. Xu, Y. Hao, G. Boschloo, E. M. J. Johansson, J. M. Gardner, A. Hagfeldt, H. Rensmo, L. Sun, Sci. Rep. **4** (2014) 4282.

159. D. Dini, G. Y. Yang, M. Hanack, J. Chem. Phys. **119** (2003) 4857.

160. S.-J. Ding, F. Nan, D.-J. Yang, X.-L. Liu, Y.-L. Wang, L. Zhou, Z.-H. Hao, Q.-Q. Wang, Sci. Rep. **5** (2015) 9735.

161. H. I. Elim, J. Yang, J.-Y. Lee, J. Mi, W. Ji, Appl. Phys. Lett. **88** (2006) 083107.

162. M. Hari, S. Mathew, B. Nithyaja, S. Ani Joseph, V. P. N. Nampoori, P. Radhakrishnan, Opt. Quant. Electron **43** (2012) 49.

163. T. V. Murzina, I. A. Kolmychek, J. Wouters, T. Verbiest, O. A. Aktsipetrov, J. Opt. Soc. of Am. B: Opt. Phys. **29** (2012) 138.

164. Y.B. Band, D.J. Harter, R. Bavli, Chem. Phys. Lett. **126** (1986) 280.

165. J. Britton, C. Litwinski, E. Antunes, M. Durmuş, V. Chaukea, T. Nyokong, J. Macromol. Sci. A: Pure Appl. Chem. **50** (2013) 110.

166. Y. Chiu, U. Rambabu, M.-H. Hsu, H.-P.D. Shieh, C.-Y. Chen, H.-H. Lin, J. Appl. Phys. **94** (2003) 1996.

167. P.K. Hedge, A.V. Adhikari, M.G. Manjunatha, P. Poornesh, G. Umesh, Opt. Mater. **31** (2009) 1000.

168. P. Poornesh, G. Umesh, P.K. Hedge, M.G. Manjunatha, K.B. Manjunatha, A.V. Adhikari, Appl. Phys. B **97** (2009) 117.

169. S.K. Lor, H. Hiraoka, P, Yu, L. Cheng and G.K.L. Wong, J. Mater. Res. 10 (1995)

170. G. C. Papavassiliou, Prog. solid st. Chem. **12** (1980) 185.

171. A. Henglein, J. phys. Chem. **97** (1993) 8457.

172. S. K. Ghosh, T. Pal, Chem. Rev. **107** (2007) 4797.

173. K.-H. Su, Q.-H. Wei, X. Zhang, J. J. Mock, D. R. Smith, S. Schultz, Nano Lett. **3** (2003) 1087.

174. A. Majzik, L. Fülöp, E. Csapó, F. Bogár, T. Martinek, B. Penke, G. Bíró, I. Dékány, Colloids Surf., B: Biointerfaces **81** (2010) 235.

175. G. Dharanivasan, T. Rajamuthuramalingam, D. M. I. Jesse, N. Rajendiran, K. Kathiravan, Appl. Nanosci. **5** (2015) 39.

176. K. Sanusi, J. M. Stone, T. Nyokong, New J. Chem. **39** (2015) 1665.

177. K. Sanusi, S. Khene, T. Nyokong, Opt. Mater. **37** (2014) 572.

178. J. Britton, C. Litwinski, M. Durmus, V. Chauke, T. Nyokong, J. Porphyrins Phthalocyanines **15** (2011) 1239.

179. Z. Li, C. He, Z. Wang, Y. Gao, Y. Dong, C. Zhao, Z. Chen, Y. Wu, Weina Song, Photochem. Photobiol. Sci. **15** (2016) 910.

180. J. Zhu, Y. Li, Y. Chen, J. Wang, B. Zhang, J. Zhang, W. J. Blau, CARBON **49** (2011) 1900.

181. A. N. Gowda, M. Kumar, A. R. Thomas, R. Philip, S. Kumar, ChemistrySelect **1** (2016) 1361.

182. W. Song, C. He, W. Zhang, Y. Gao, Y. Yang, Y. Wu, Z. Chen, X. Li, Y. Dong, CARBON **77** (2014) 1020.

183. S. Dengler, C. Kubel, A. Schwenke, G. Ritt, B. Eberle, J. Opt. **14** (2012) 075203.

184. H. Chen, Y. Zhang, B. Zhang, L. Gao, Sci. Rep. **6** (2016) 21741.

185. V. Mamidala, G. Xing and W. Ji, J. Phys. Chem. C **114** (2010) 22466.

186. L. Blaney, Magnetite (Fe3O4): Properties, Synthesis, and Applications, The Lehigh Review **15** (2007) 33. http://preserve.lehigh.edu/cas-lehighreview-vol-15/5

187. W. Wu, Q. He and C. Jiang, Nanoscale Res. Lett. **3** (2008) 397.

188. A. Lak, M. Kraken, F. Ludwig, A. Kornowski, D. Eberbeck, S. Sievers, F. J. Litterst, H. Weller, M. Schilling, Nanoscale **5** (2013) 12286.

189. W. Wu, Z. Wu, T. Yu, C. Jiang, W.-S. Kim, Sci. Technol. Adv. Mater. **16** (2015) 023501.

190. M. Ando, k. Kadono, M. Haruta, T. Sakaguchi, M. Miya, Nature **374** (1995) 625.

191. B. L. Yu, C. S. Zhu, F. X. Gan, X. C. Wu, G. L. Zhang, G. Q. Tang, W. J. Chen, Opt. Mater. **8** (1997) 249.

192. D. Soga, S. Alves, A. Campos, F. A. Tourinho, J. Depeyrot, A. M. J. Figueiredo, Opt. Soc. Am. B **24** (2007) 49.

193. B. L. Yu, C. S. Zhu, F. X. Gan, Physica E **8** (2000) 360.

194. Y. Q. Li, G. Zhang, A.V. Nurmikko, S.H. Sun, Nano Lett. **5** (2005) 1689-1692.

195. X. Li, M. Rui, J. Song, Z. Shen, H. Zeng, Adv. Funct. Mater. **25** (2015) 4929.

196. F. Zhang, F. Liu, C. Wang, X. Xin, J. Liu, S. Guo, J. Zhang, ACS Appl. Mater. Interfaces **8** (2016) 2104.

197. Y. Li, Y. Zhao, H. Cheng, Y. Hu, G. Shi, L. Dai and L. Qu, J. Am. Chem. Soc. **134** (2012) 15.

198. D. Qu, M. Zheng, P. Du, Y. Zhou, L. Zhang, D. Li, H. Tan, Z. Zhao, Z. Xied, Z. Sun, Nanoscale **5** (2013) 12272.

199. L. T. Qu, Y. Liu, J. B. Baek, L. M. Dai, ACS Nano **4** (2010)1321.

200. D. Qu, Z. Sun, M. Zheng, J. Li, Y. Zhang, G. Zhang, H. Zhao, X. Liu and Z. Xie, Adv. Opt. Mater. **3** (2015) 360.

201. McGraw-Hill in Encyclopedia of Science and Technology (5th ed.). McGraw-Hill Education, (1993).

202. J. A. Miragliotta, Johns Hopkins APL Technical Digest, **16** (1995) 348.

203. P. A. Franken, A. E. Hill, C. W. Peters, G. Weinreich, Phys. Rev. Lett. **7** (1961) 118.

204. D. Dini, M. Barthel, M. Hanack, Eur. J. Org. Chem. (2001) 3759.

205. A. Salah, M. Bakr, S. Hassabelnaby, I. Azzouz, Y. Badr, OPJ **5** (2015) 125.

206. M. Sheik-Bahae, A.A. Said, T.H. Wei, D.J. Hagan, E.W. Van Stryland, IEEE J. Quantum Electron. **26** (1990) 760.

207. E. W. Van Stryland, M. Sheik-Bahae, in Characterization Techniques and Tabulations for Organic Nonlinear Materials, M. G. Kuzyk and C. W. Dirk, Eds., page 655-692, Marcel Dekker, Inc. (1998).

208. D. Dini, M. Hanack, in: K.M. Kadish, K.M. Smith, R. Guilard (Eds.), The Porphyrin Handbook: Physical Properties of Phthalocyanine-based Materials, 17, Academic Press, USA, 2003, pp. 2.

209. T. Pritchett, in Models for Saturable and Reverse Saturable Absorption in Materials for Optical Limiting, Army Research Laboratory, Sensors and Electron Devices Directorate, Adelphi, MD (2002) 20783.

210. A. Fashina, E. Antunes, T. Nyokong, Polyhedron **53** (2013) 278.

211. N. Sehlotho, M. Durmuş, V. Ahsen, T. Nyokong, Inorg. Chem. Commun. **11** (2008) 479.

212. H.G. Yaglioglu, M. Arslana, S. Abdurrahmanoglu, H. Unver, A. Elmalia, O. Bekaroglu, J, Phys. Chem. Solids **69** (2008) 161.

213. S. Pagoti, S. Surana, A. Chauhan, B. Parasar, J. Dasha, Catal. Sci. Technol. **3** (2013) 584.

214. D. Wöhrle, O. Tsaryova, A. Semioshkin, D. Gabel, O. Suvorova, J. Organometal. Chem. **747** (2013) 98.

215. N. Saydan, M. Durmuş, M.G. Dizge, H. Yaman, A.G. Gürek, E. Antunes, T. Nyokong, V. Ahsen. J. Porphyrins Phthalocyanines **13** (2009) 681.

216. M. Durmuş, V. Ahsen. J. Inorg. Biochem. **104** (2010) 297.

217. X. Yu, C. Zhan and Y. Huang, Chin. J. Org. Chem. **32** (2012) 770.

218. S. V. Kudrevich, H. Ali and J. E. van Lier, J. Chem. Soc. Perkin Trans. **1** (1994) 2774.

219. M. Brust, M. Walker, D. Bethell, D.J. Schiffrin, R. Whyman, J. Chem. Soc. Chem. Commun. (1994) 801.

220. N. Masilela, T. Nyokong, J. Photochem. Photobiol. A **223** (2011) 124.

221. J. Hannant, J. H. Hedley, J. Pate, A. Walli, S. A. F. Al-Said, M. Galindo, B. A. Connolly, B. R. Horrocks, A. Houlton, A. R. Pike, Chem. Commun. **46** (2010) 5870.

222. S. Liu, G. Chen, P.N. Prasad, M. T. Swihart, Chem. Mater. **23** (2011) 4098.

223. I. Robinson, L.D. Tung, S. Maenosono, C. Walti, N.T.K. Thanh, Nanoscale **2** (2010) 2624.

224. J. Jiang, H. Gu, H. Shao, E. Devlin, G.C. Papaefthymiou, J.Y. Ying, Adv. Mater. **20** (2008) 4403.

225. D. Qu, M. Zheng, L. Zhang, H. Zhao, Z. Xie, X. Jing, E.H. Raid, H. Fan, Z. Sun, Sci. Rep. **4** (2014) 5294.

226. R. Ban, J. Li, J. Cao, P. Zhang, J. Zhang, J.-J. Zhu, Anal. Methods **5** (2013) 5929.

227. N. Nombona, E. Antunes, C. Litwinski, T. Nyokong, Dalton Trans. **40** (2011) 11876.

228. J. G Young, W. Onyebuagu, J. Org. Chem. **55** (1990) 681.

229. C. C. Leznoff, M. Hu, C. R. McArthur, Y. Qin, J. E. van Lier, Can. J. Chem. **72** (1994) 1990.

230. A. Y. Tolbin, V. E. Pushkarev, G. F. Nikitin, L. G. Tomilova, Tetrahedron Lett. **69** (2009) 4848.

231. T. Ceyhan, Ö. Bekaroglu, Monatsh. Chem. **133** (2002) 71.

232. S. Dabak, Ö. Bekaroglu, New J. Chem. **21** (1997) 267.

233. M. Patel, R. Vaidya, M. Dave, S.G. Patel, A.T. Oza, Indian J. Pure Appl. Phys. **42** (2004) 79.

234. M.J. Stillman, T. Nyokong, In: C.C. Leznoff, A.B.P Lever (Eds.), Phthalocyanines: Properties and Applications, vol. 1, VCH Publishers, New York (1989).

235. T. Nyokong, Electronic spectral and electrochemical behavior of near infrared absorbing metallophthalocyanines, struct bond. Springer Berlin Heidelberg; (2010).

236. S.Y. Al-Raqa, Dyes Pigments **77** (2008) 259.

237. E. Glimsdal, M. Carlsson, T. Kindahl, M. Lindgren, C. Lopes, B. Eliasson, J. Phys. Chem. A **114** (2010) 3431.

238. W. Freyer, S. Mueller, K. Teuchner, J. Photochem. Photobiol. A: Chem. **163** (2004) 231.

239. E.C. Kaya, M. Durmus, E. Yanmaz, H. Kantekin, Turk. J. Chem. **38** (2014) 1118.

240. T.Y. Suman, S.R. Radhika Rajasree, R. Ramkumar, C. Rajthilak, P. Perumal, Spectrochim. Acta A: Mol. Biomol. Spectrosc. **118** (2014) 11.

241. A.W. Snow, J.R. Griffith, N.P. Marullo, Macromolecules **17** (1984) 1614.

242. M. Ashjari, S. Dehfuly, D. Fatehi, R. Shabanid, M. Koruji, RSC Adv. **5** (2015) 104621.

243. S. Y. Moon, S. Tanaka, T. Sekino, Nanoscale Res Lett. **5** (2010) 813.

244. Y. Luan, Y. Qi, H. Gao, N. Zheng, G. Wang, J. Mater. Chem. A **2** (2014) 20588.

245. G. Qin, C. Santos, W. Zhang, Y. Li, A. Kumar, U. J. Erasquin, K. Liu, P. Muradov, B. W. Trautner, C. Cai, J. Am. Chem. Soc. **132** (2010) 16432.

246. W. Li, Y. Xu, Y. Zhou, W. Ma, S. Wang, Y. Dai, Nanoscale Res. Lett. **7** (2012) 485.

247. M. James, S. Ciampi, T. A. Darwish, T. L. Hanley, S. O. Sylvester, J. J. Gooding, Langmuir **27** (2011) 10753.

248. S. K. Vashist, Diagnostics **2** (2012) 23.

249. J. R. Dunetz, J. Magano, G. A. Weisenburger, Org. Process Res. Dev. **20** (2016) 140.

250. R. Prabakaran, R. Kesavamoorthy, G.L.N. Reddy, F.P. Xavier, Phys. Stat. Sol. B **229** (2002) 1175.

251. D. Pan, J. Zhang, Z. Li, M. Wu, Adv. Mater. **22** (2010) 734.

252. L. Tang, R.Ji, X.Cao, J.Lin, H.Jiang, X.Li, K.S. Teng, C.M. Luk, S. Zeng, J. Hao, S. P. Lau, ACS Nano **6** (2012) 5102.

253. B. N. Achar, K. S. Lokesh, J. Organomet. Chem. **689** (2004) 2601.

254. X. T. Zheng, K. Q. Ananthanarayanan, P. Luo, P. Chen, Small **11** (2015) 1620.

255. B. Chudasama, A. K. Vala, N. Andhariya, R. V. Upadhyay, R. V. Mehta, Nano Res. (2009) 955.

256. P. Gong, H. M. Li, X. X. He, K. M. Wang, J. B. Hu, W. H. Tan, S. C. Zhang, X.H. Yang, Nanotechnology **18** (2007) 285604.

257. H. El Ghandoor, H. M. Zidan, M. M. H. Khalil, M. I. M. Ismail, Int. J. Electrochem. Sci. **7** (2012) 5734.

258. X. W. Teng, D. Black, N. J. Watkins, Y. L. Gao and H. Yang, Nano Lett. **3** (2003) 261.

259. Y. Mao, P. Yi, Z. Deng, J. Ge, CrystEngComm**15** (2013) 3575.

260. L. Zhang, Y.-H. Dou, H.-C. Gu, J. Colloid Interface Sci. **297** (2006) 660.

261. H. Yu, M. Chen, P. M. Rice, S. X. Wang, R. L. White, S. H. Sun, Nano Lett. **5** (2005) 379.

262. P. Modisha, T. Nyokong, E. Antunes, J. Mol. Catal. A: Chem. **380** (2013) 131.

263. D. Lutzenkirchen-Hecht, H. H. Strehblow, Surf. Interface Anal.**41** (2009) 820.

264. T. Yamashita, P. Hayes, Appl. Surf. Sci.**254** (2008) 2441.

265. C. Lee, G.-W. Lee, W. Kang, D.-K. Lee, M. J. Ko, K. Kim, N.-G. Park, Bull. Korean Chem. Soc. **31** (2010) 3093.

266. M.H. Majles Ara, Z. Dehghani, R. Sahraei, A. Daneshfar, Z. Javadi, F. Divsar, J. Quant. Spectrosc. Radiat. Transfer **113** (2012) 366.

267. D. Zanchet, B.D. Hall, D. Ugarte, J. Phys. Chem. B **104** (2000) 11013.

268. H.M. Chen, R.S. Liu, L.-Y. Jang, J.-F. Lee, S.F. Hu, Chem. Phys. Lett. **421** (2006) 118.

269. I. Papagiannouli, P. Aloukos, D. Rioux, M. Meunier, S. Couris, J. Phys. Chem. C **119** (2015) 6861.

270. S.K. Das, C. Dickinson, F. Lafir, D.F. Broughamc, E. Marsili, Green Chem. **14** (2012) 1322.

271. T. Ramanathan, F.T. Fisher, R.S. Ruoff, L.C. Brinson, Chem. Mater. **17** (2005) 1290.

272. J.-S. Lim, S.-M. Kim, S.-Y. Lee, E.A. Stach, J.N. Culver, M.T. Harris, Nano Lett. **10** (2010) 3863.

273. D.G. Castner, K. Hinds, D.W. Grainger, Langmuir **12** (1996) 5083.

274. T. Weidner, F. Bretthauer, N. Ballav, H. Motschmann, H. Orendi, C. Bruhn, U. Siemeling, M. Zharnikov, Langmuir **24** (2008) 11691.

275. M. Zharnikov, S. Frey, K. Heister, M. Grunze, Langmuir **16** (2000) 2697.

276. C.M. Pradier, M. Salmain, L. Zheng, G. Jaouen, Surf. Sci. **502** (2002) 193.

277. C.M. Yam, C.M. Pradier, M. Salmain, P. Marcus, G. Jaouen, J. Colloid Interface Sci. **235** (2001) 183.

278. A. Gadalla, J.-B. Beaufrand, M. Bowen, S. Boukari, E. Beaurepaire, O. Crégut, M. Gallart, B. Hönerlage, P. Gilliot. J. Phys. Chem. C **114** (2010) 17854.

279. A. Gadalla, O. Crégut, M. Gallart, B. Hönerlage, J.-B. Beaufrand, M. Bowen, S. Boukari, E. Beaurepaire, P. Gilliot. J. Phys. Chem. C **114** (2010) 4086.

280. M. Durmuş, T. Nyokong, Polyhedron **26** (2007) 3323.

281. D. N. Satyanarayana, Electronic Absorption Spectroscopy and Related Techniques, University Press India Limited, New Delhi (2001).

282. M. Durmus, T. Nyokong, Photochem. Photobiol. Sci. **6** (2007) 659.

283. G. Gümrükçü, G. K. KaraoLlan, A. Erdogmus, A. Gül, U. Avciata, Journal of Chemistry (2014) 1.

284. J.A. Lacey, D. Philips, Photochem. Photobiol. Sci. **1** (2002) 378.

285. M.G. Debacker, O. Deleplanque, B. Van Vlierberge, F.X. Sauvage, Laser Chem. **8** (1988) 1.

286. Z. Iqbal, A. Ogunsipe, T. Nyokong, A. Lyubimtsev, M. Hanack, T. Ziegler, J. Porphyrins Phthalocyanines **16** (2012) 413.

287. J.R. Darwent, P. Douglas, A. Harriman, G. Porter, M.C. Richoux, Coord. Chem. Rev. **44** (1982) 83.

288. S.A. Corr, A.O'. Byrne, Y.K. Gunko, S. Ghosh, D.F. Brougham, S. Mitchell, Y. Volkov, A. Prina-Mello, Chem. Commun. (2006) 4474.

289. O.J. Achadu, T. Nyokong, J. Fluoresc. **26** (2016) 283.

290. E.I. Zenkevich, A.P. Stupak, D. Kowerko, C. von Borczyskowski, Chem. Phys. **406** (2012) 21.

291. T. Blaudeck, E.T. Zenkevich, F. Cichos, C. von Borczyskowski, J. Phys. Chem. C **112** (2008) 20251.

292. C.L. Takanishi, E.A. Bykova, W. Cheng, J. Zheng, Brain Res. **1091** (2006) 132.

293. M.L. Mueller, X. Yan, J.A. McGuire, L. Li, Nano Lett. **10** (2010) 2679.

294. C.A. Masmanidis, H.H. Jaffe, R.L. Ellis, J. Phys. Chem. **79** (1975) 2052.

295. R. Englman, J. Jortner, J. Lumin. **12** (1970) 134.

296. M. Sheik-Bahae, A.A. Said, E.W. Stryland, Opt. Lett. **14** (1989) 955.

297. L.W. Tutt, T.F. Boggess, Prog. Quant. Electr. **17** (1993) 299.

298. A. A. Chastov, 0. L. Lebedev, Zh. Eksp. Teor. Fiz. **58** (1970) 848.

299. Y. Chen, L. Gao, M. Feng, L. Gu, N. He, J. Wang, Y. Araki, W. J. Blau, O. Ito, Mini-Rev. Org. Chem. **66** (2009) 55.

300. R.S.S. Kumar, S.V. Rao, L. Giribabu, D.N. Rao, Chem. Phys. Lett. **447** (2007) 274.

301. M. Hanack, D. Dini, M. Barthel, S. Vagin, Chem. Rec. **2** (2002) 129

302. M. Hercher, Appl. Opt. **9** (1967) 947.

303. H.S. Nalwa, J.S. Shirk, in: C.C. Cliznoff, A.B.P. Lever (Eds.), Phthalocyanines: Properties and Applications, vol. 4, VCH, New York, (1996).

304. P.L. Chen, I.V. Tomov, A.S. Dvornikov, M. Nakashima, J.F. Roach, D.M. Alabran, P.M. Rentzepis, J. Phys. Chem. **100** (1996) 17507.

305. S.H. Guang, R. Gvishi, P.N. Prasad, B.A. Reinhardt, Opt. Commun. **117** (1995) 133.

306. S.O. Sanusi, E. Antunes, T. Nyokong, J. Porphyrins Phthalocyanines**17** (2013) 920.

307. J. Wang, M. Sheik-Bahae, A.A. Said, D.J. Hagan, E.W. Van Stryland, J. Opt. Soc. Am. B **11** (1994) 1009.

308. F. Guo, W. Sun, Inorg. Chem. **44** (2005) 4055.

309. K.P. Unnikrishnan, J. Thomas, V.P.N. Nampoori, C.P.G. Vallabhan, Opt. Commun. **217** (2003) 269.

310. K.P. Unnikrishnan, J. Thomas, V.P.N. Nampoori, C.P.G. Vallabhan, Synth. Metals **139** (2003) 371.

311. K.P. Unnikrishnan, J. Thomas, V.P.N. Nampoori, C.P.G. Vallabhan, Appl. Phys. B **75** (2002) 871.

312. K.P. Unnikrishnan, J. Thomas, V.P.N. Nampoori, C.P.G. Vallabhan, Chem. Phys. **79** (2002) 209.

313. Z. Li, Z. Chen, S. Xu, X. Zhou, F. Zhang, In In Third-Order Optical Nonlinearities of Novel Phthalocyanines and Related Compounds, Laser Systems for Applications, Dr Krzysztof Jakubczak (Ed.), InTech. Publ., Rijeka, (2011) (Chapter 13).

314. L. Liu, C. Tai, A.T. Hu, T. Wei, J. Porphyrins Phthalocyanines **8** (2004) 984.

315. C. Piechocki, J. Simon, J.J. André, D. Guillon, P. Petit, A. Skoulios, P. Weber. Chem. Phys. Lett. **122** (1985) 124.

316. K. Sanusi, E. Antunes, T. Nyokong. Dalton Trans. **43** (2014) 999.

317. J.W. Perry, K. Mansour, S.R. Marder, K.J. Perry, D. Alvarez Jr., I. Choong. Opt. Lett. **19** (1994) 625.

318. C. An, X. Feng, N. Zhao, P. Liu, T. Wang, Z. Lian. J. Coord. Chem. **67** (2014) 3623.

319. Y. Li, W. Pan, P. Hong, Z. Zhang, K. Li. J. Coord. Chem. **67** (2014) 2630.

320. J.S. Shirk, R.G.S. Pong, S.R. Flom, H. Heckmann, M. Hanack, J. Phys. Chem. **104** (2000) 1438.

321. G. Ao, Z. Xiao, X. Qian, Z. Li, Y. Wang, X. Zhang, Y. Song, Molecules **20** (2015) 5554.

322. Z.H. Shi, Y.S. Zhou, L.J. Zhang, S.U. Hassan, N.N. Qu, J. Phys. Chem. C **118** (2014) 6413.

323. M. Hosoda, T. Wada, A. Yamada, A.F. Garito, H. Sasabe, Jpn. J. Appl. Phys. **30** (1991) L1486.

324. A.W. Snow, N.L. Jarvis, J. Am. Chem. Soc. **106** (1984) 4706.

325. A. Davis, Macromol. Chem. Phys. **132** (1970) 23.

326. J. Britton, M. Durmus, S. Khene, V. Chauke, T. Nyokong, J. Porphyrins Phthalocyanines**17** (2013) 691.

327. A.H. Yuwono, J. Xue, J. Wang, H.I. Elim, W. Ji, Y. Li, T.J. White, J. Mater. Chem. **13** (2003) 1475.

328. P. Wang, S. Zhang, P. Wu, C. Ye, H. Liu and F. Xi, Chem. Phys. Lett. **340** (2001) 261.

329. J. Wang, Y. Chen, R. Li, H. Dong, L. Zhang, M. Lotya, J. N. Coleman, W. J. Blau, Nonlinear optical properties of graphene and carbon nanotube composites, carbon nanotubes - synthesis, characterization, applications, Dr. Siva Yellampalli (Ed.) (2011).

330. D. Dini, S. Vagin, M. Hanack, V. Amendola, M. Meneghetti, Chem. Commun. (2005) 3796.

331. Z.-B. Liu, J.-G. Tian, Z. Guo, D.-M. Ren, F. Du, J.-Y. Zheng, Y.-S. Chen, Adv. Mater. **20** (2008) 511.

332. Z.-B. Liu, Y.-F. Xu, X.-Y. Zhang, X.-L. Zhang, Y.-S. Chen, J.-G. Tian, J. Phys. Chem. B **113** (2009) 9681.

333. J. Wang, W.J. Blau, Chem Phys. Lett. **465** (2008) 265.

334. S. Tekin, U. Kürüm, M. Durmuş, H.G. Yaglioglu, T. Nyokong, A. Elmali, Opt. Commun. **283** (2010) 4749.

335. L. De Boni, E.L. Wood, C. Toro, F.E. Hernandez, Plasmonics **3** (2008) 171.

336. W. Jia, E.P. Douglas, F. Guo, W. Sun, Appl. Phys. Lett. **85** (2004) 6326.

337. P.K. Jain, Y.H. Xiao, R. Walsworth, A.E. Cohen, Nano Lett. **9** (2009) 1644.

338. H. Liu, J. Yang, J. Mater. Chem. A **2** (2014) 7075.

339. J. Huang, Y. Sun, S. Huang, K. Yu, Q. Zhao, F. Peng, H. Yu, H. Wang, J. Yang, J. Mater. Chem. **21** (2011) 17930.

340. W. Blau, H. Byrne, W.M. Dennis, J.M. Kelly, Opt. Commun. **56** (1985) 25.

341. J.S. Shirk, S.R. Flom, J.R. Lindle, F.J. Bartoli, A.W. Snow, M.E. Boyle, MRS Symp. Proc. **328** (1994) 661.

342. J. Gu, X. Zhang, A. Pang, J. Yang, Nanotechnology **27** (2016) 165704.

343. X. Li, S.P. Lau, L. Tang, R. Ji, P. Yang, Nanoscale **6** (2014) 5323.

344. Q. Liu, B. Guo, Z. Rao, B. Zhang, J. R. Gong, Nano Lett. **13** (2013) 2436.

345. L. Cao, M. J. Meziani, S. Sahu, Y.-P. Sun, Acc. Chem. Res. **46** (2012) 171.

346. S. Liu, J. Tian, L. Wang, Y. Zhang, X. Qin, Y. Luo, A. M. Asiri, A. O. Al-Youbi, X. Sun, Adv. Mater. **24** (2012) 2037.

347. Y. Wang, Y. Shao, D. W. Matson, J. Li, Y. Lin, ACS Nano **4** (2010) 1790.

348. K. Imakita, M. Ito, M. Fujii, S. Hayashi, Opt. Express **17** (2009) 7368.

349. M. Hassan, E. Haque, K.R. Reddy, A.I. Minett, J. Chenc, V.G. Gomes, Nanoscale **6** (2014) 11988.